UNIVERSITY OF
NEWCASTLE

UNIVERSITY OF
NEWCASTLE UPON TUNE
School of Mechanical and System Engineering
Stephenson Building
Newcastle upon Tyne NE1 7RU

Microstructure and Fatigue Strength of High Performance Gear Steels

By

Fouad B. Abudaia

A thesis submitted as a requirement for the degree of Doctor of Philosophy at the University of Newcastle upon Tyne

February 2003

Preface

Declaration

This Thesis records the work carried out in the Faculty of mechanical and system engineering University of Newcastle upon Tyne between October 1999 and December 2002 and is original except where acknowledged by reference.

No portion of this work is being, nor has been submitted for a degree or other qualification at any other university.

Acknowledgements

I would like to thank Professor J.T. Evans for his supervision, guidance and generosity with time through out the period of this work. His encouragement was a great motive during this research.

I would like to thank Dr. B.A. Shaw for the supervision, guidance and support throughout this work.

Thanks are also due to all members of the Design Unit at University of Newcastle for all the assistance and help. Special thanks to Chris Aylott and Phil Wilson for their valuable assistance and patience.

Also I would like to thank all the technicians in the workshop and strength Lab in Stephenson building and technician Colin Henry in Hershel building at the school of mechanical and system engineering.

I would like to thank also Marilyn Kay Dodd -the department and Prof. Evans secretary- for all the effort and time organisation.

Abstract

Observations on some steels used in high performance gears are presented in this thesis. The object was to understand how microstructure and residual stress influenced mechanical properties, particularly fatigue strength. The investigations were carried out using fatigue testing, metallographic techniques, shot peening, hardness testing and X-ray diffraction to determine residual stress and the amount of retained austenite. The work is divided into two main parts. In the first part, the opportunity was taken of investigating a batch of case-carburised gears manufactured from 17CrNiMo6 steel that contained an abnormally high level of retained austenite. . The benefits or otherwise of retained austenite is a matter of some controversy in the literature and this was an opportunity of testing the effect of high retained austenite in gears. In the second part, the properties of a recently formulated through hardening steel was investigated. The steel is inexpensive and capable of being fully hardened by air-cooling. It is believed that use of the material could reduce the cost of gear manufacture by eliminating the carburisation process, oil quenching and the subsequent need to correct distortions that arise from quenching.

Gears were manufactured using 17CrNiMo6 steel. After carburization, one batch was found to have an abnormally high level of retained austenite (40 to 60%). Normally, gears with this level of retained austenite would be rejected. Nevertheless, gears from this batch were found to have surface and bending fatigue strengths that were not very different from those with much lower retained austenite contents. Despite the fact that the material is relatively soft, it was found that a very thin surface layer had hardened during back-to-back gear testing, probably by strain-induced transformation of the retained austenite. It was deduced that this thin layer of hardened material is sufficient to maintain a good level of surface contact fatigue strength.

The second part of the work includes a basic study of the through-hardening steel. The study includes heat treatment and hardness, estimation of fracture toughness and the development of residual stress during heat treatment. Specialised standing contact fatigue (SCF) tests were also done using this material. The SCF test consists of cyclic loading of a hard ball in contact with the surface of the specimen, which is meant to simulate asperity contact in surface contact fatigue. Radial cracks or ring cracks or both are nucleated just outside the indentation circle in these tests, depending on the load and the development of plasticity. The stresses near the indentation were modelled using Finite Element analysis and were found to be consistent with the experimental results. Finally, the effect of residual compressive stress induced by shot peeing was studied using the SCF test. It was found that shot peening suppressed the formation of radial cracks.

Contents

CHAPTER 1

Introduction

1.1 Background

This thesis is about some of the materials used in high performance gears. The research described below was done in collaboration with the Design Unit, a self-funding research group in the author's department. The Design Unit is the premier group in the UK for gear design, metrology and research. Amongst the range of work undertaken by the Design Unit is a very large programme of testing funded by producers and users of gears in the UK, Europe and the USA. These large programmes of work address the following questions: what are the mechanisms of failure of gears ? How is failure influenced by the materials used ? How does the design and accuracy of the gears, the lubricants used in operation and the treatments used in their manufacture interact in determine performance ?

The research on testing high performance gear materials has generated a very large number of results and a correspondingly large number of specimens. In this thesis we present the results of research on two of the gear materials used in the large testing programme.

Gears are used to transmit rotary motion between shafts; they are usually cylindrical in shape. There are many different gear designs. For example, spur gears have straight teeth, which are parallel to the axis of rotation, whereas the teeth in helical gears are inclined to the rotation axis. Both types of these gears are used to transmit motion between parallel shafts. Helical gears owe their higher ability to transmit heavy loads at higher speed to the gradual engagement of teeth and the smooth transfer of load from one tooth to another. Figure 1.1 shows different types of gears.

During the transmission operation, gears are subjected to different types of stresses. Accordingly, failure in gears varies in mechanism and the location where failure occurs. Because of the cyclic nature of loading, fatigue failure is a common form of

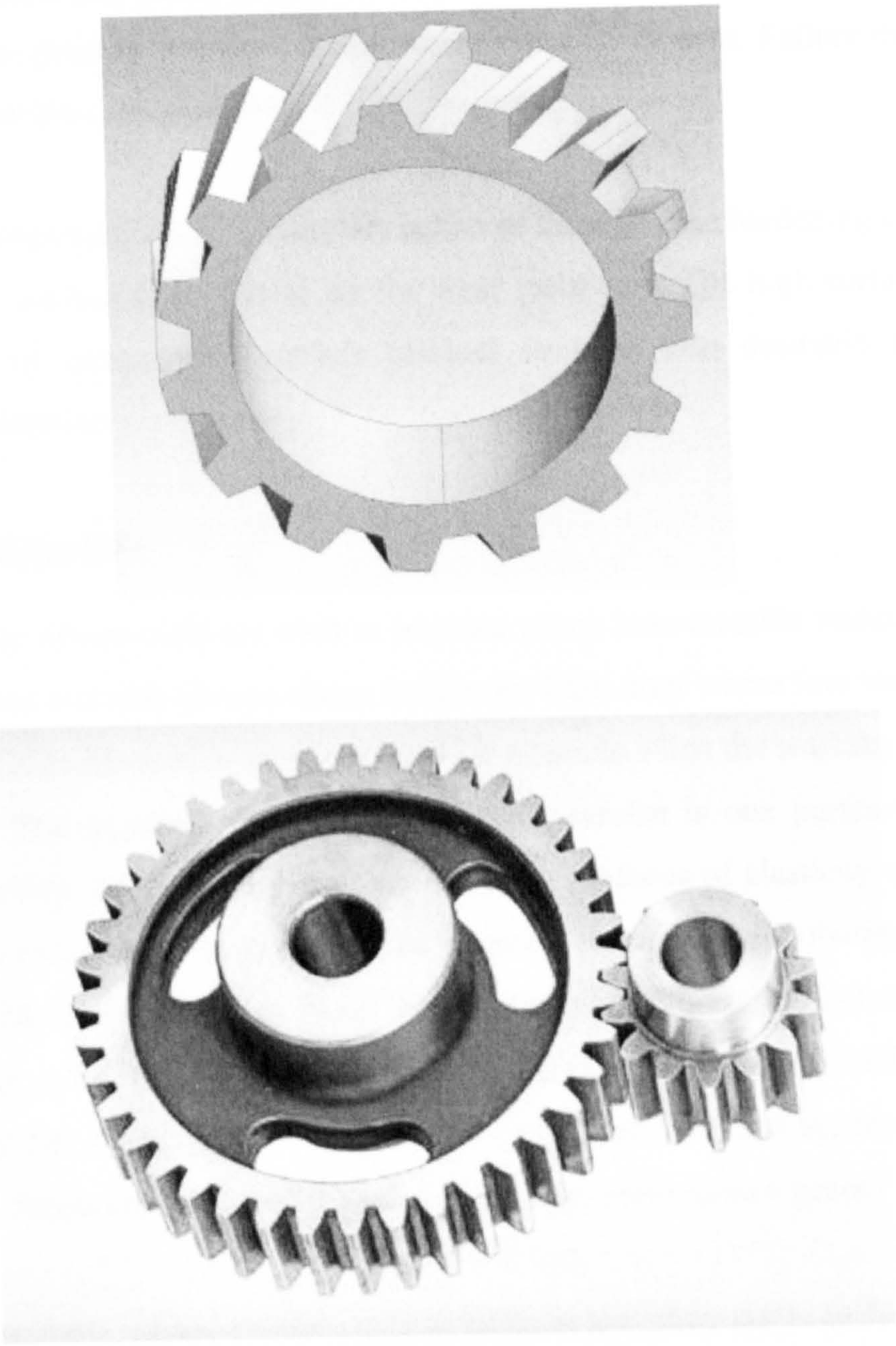

Fig.1.1 Examples of helical and spur gears

failures in gears. Beside fatigue failure, gears also fail by wearing of flank surfaces due to contact of involutes flanks during service. However, this is also a form of fatigue Therefore gears must be designed against these types of failures. Failure mechanisms are discussed in more detail below.

In steel gears high performance is usually achieved through case hardening of low alloy steels. A hard surface is beneficial for the wear resistance. The high surface strength accompanied by compressive surface residual stress is also desirable to improve resistance against fatigue failures.

1.2 Gear Materials

A wide variety of materials are used to produce gears. Non-metallic materials such as plastics, ferrous and non-ferrous alloys are use for light duty where low torque is to be transmitted. Gears made of bronzes are used for example when the working atmosphere is corrosive. The imposed stress on gears during service is one parameter for gear material selection. Polymers for example have low modulus of elasticity and strength. This helps to reduce the Hertzian or surface contact stresses by distributing stresses on larger area. Steels on the other hand with higher strength enable higher torque and greater power to be transmitted. Gears made from different types of steels are in use. This is due to the wide range of strengths that can be achieved and the range of cost of the material. Steels are the material of choice for high performance gears.

To take an example, nickel-chromium-molybdenum low alloy steels such as SAE 4320 and SAE 8620 alloys are widely used as gear materials. These alloys contain about 0.5 to 0.8% Cr and 0.2% Mo with nickel content about 1.8 % in the former and reduced to 0.55 % in the latter alloy. Both these steels are carburizing grades with a basic carbon content of 0.2 %. Higher levels of strength and toughness are achieved by addition of silicon and vanadium to alloys of medium carbon content. We note that the steels selected for gear manufacture have changed in recent years. For instance EN36 was once used widely for large case carburised marine gears. The high nickel content ($\approx$ 3.5 %) produces a high level of hardenability and experience showed that EN36 gave relatively little problems to manufacturers (for example it was reported to be resistant to grinding burns). On the other hand nickel is an expensive element and cost factors

have lead to the replacement of EN36 with alternative alloys in many applications. At the other end of the scale, SAE 8620 is lean in nickel, but its hardenability is adequate for the production of small gears. Consequently, SAE 8620 is favoured by automobile manufacturers for automotive gears.

1.3 Surface Hardening of Gears

High performance gears have to be able to resist fatigue. Higher levels of hardness and tensile strength are required for the high fatigue resistance. A rule of thumb often quoted is that the fatigue strength of ferrous materials is approximately one half the tensile strength. Therefore, increasing strength by quenching and tempering is beneficial for fatigue resistance. However, this approach is valid for steels only up to a tensile strength of about 1200 MPa. With higher carbon contents the fatigue strength of quenched and tempered steels shows a wide range of variations and the lower bound of the fatigue strength shows no increase with hardness. An example is shown in Fig.1.2.

The results in Fig.1.2 can be interpreted in the following way. Fatigue crack nucleation requires some degree of cyclic plastic deformation even if this occurs on a localised, microscopic scale. (Laufer and Roberts, 1966). It follows that fatigue strength will rise in proportion to the tensile strength. However, at strength levels above 1200 MPa, fatigue is increasingly susceptible to the strain concentration effects of small microscopic defects, such as cracked or incompletely bonded non-metallic inclusions. Therefore the lower bound fatigue strength tends not to rise with hardness.

If the lower bound fatigue strength is adopted for design, there is not much point using steels with a hardness level much greater than 400 Hv if conventional fatigue resistance only is required. However, gears also have to resist surface contact fatigue and this is the reason for applying surface hardening treatments such as case hardening (carburizing and nitriding) or induction hardening.

The aim of any surface hardening process is to obtain a hard and more wear resistance surface. Induced compressive residual stress at and near the surface improves the resistance against fatigue failure. The toughness of the core material does not deteriorate by application of these processes. A combination of hard strong surface and

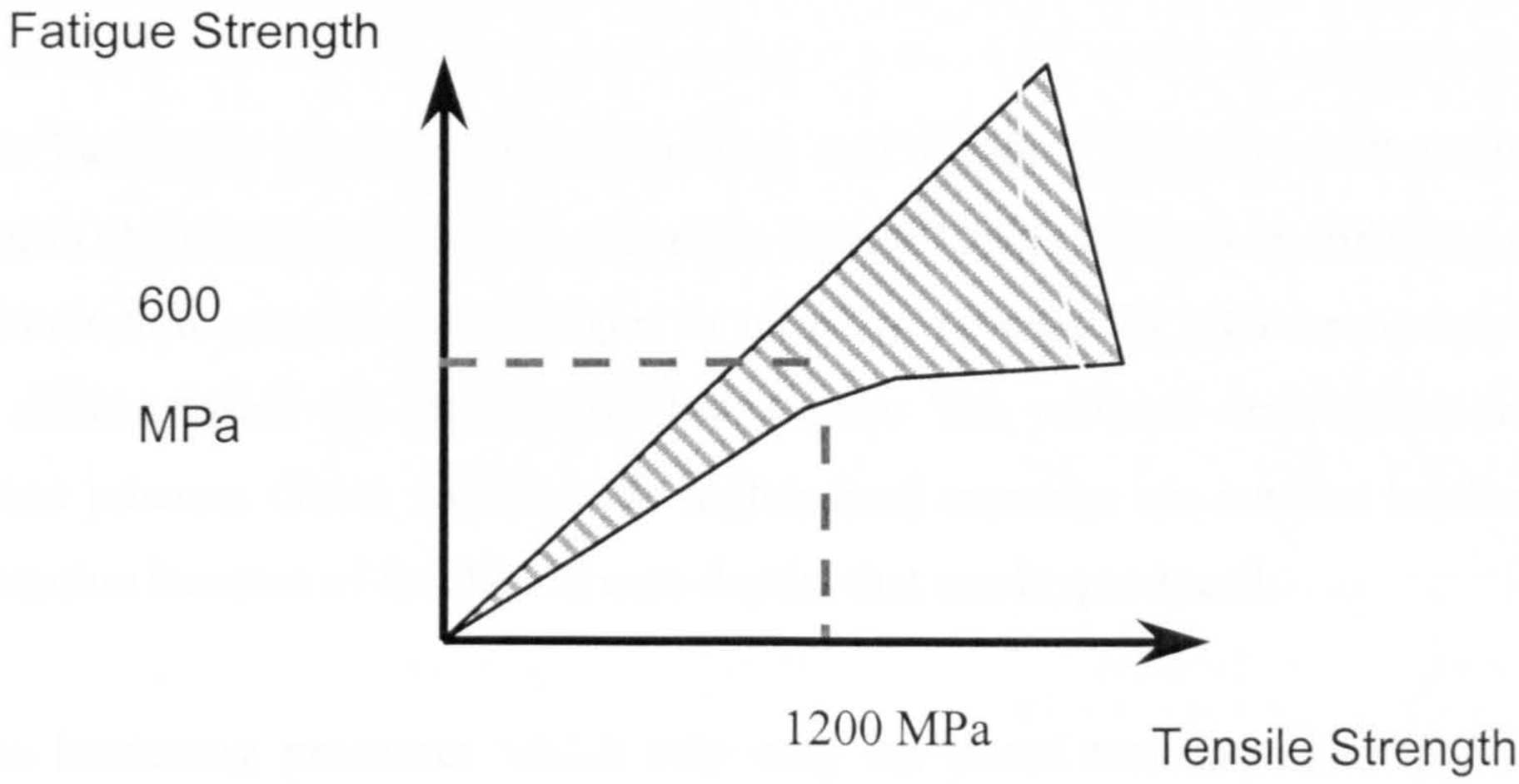

Fig. 1.2 Scatter band showing the relation between fatigue strength and tensile strength for a wide range of steels (taken from (Hertzberg, 1996)

ductile tough core is regarded as desirable for a material intended for use in gear applications. The tougher core is useful for resisting secondary loading such as when a gear is shrink fitted onto a shaft.

Surface hardening processes in carburizing and nitriding depend on the alteration induced in chemical compositions at surface layers. This is attained by diffusing carbon in carburization process and nitrogen in nitriding process. In either process nascent atoms diffuse inside the steel to shallow depths. The end use decides the required treatment process. Gears required for higher load capacity are surface hardened by carburization because of the thicker case depths that can be produced.

In case hardening processes which rely only on phase transformation for surface hardening such as induction hardening, the surface layer is selectively heated followed by rapid cooling. Phase transformation which produces martensitic structure in the surface layers is responsible for surface hardening in this cased.

The hardening mechanisms in nitriding and carburizing processes are entirely different to each other. In nitriding, the increase in surface hardness of carbon steel is due to the formation of a hard layer of ε iron nitride (Fe_3N) and in alloy steels is attributed to the interaction between nitrogen and nitrides forming elements such as Al and Cr to form hard stable nitrides such as (AlN). Nitriding is carried out at temperature range of 500 to 575°C. In this temperature range the steel is ferritic therefore no phase transformation is involved in the process. The case depth produced by nitriding is shallow, a depth of about 0.5 mm could be attained with prolonged nitriding time. (Thelning, 1975). The hard or compound layer also improves the corrosion resistance in moist atmospheres. The most common nitriding process is gas nitriding which involve dissociation of ammonia gas (NH_3) to form nitrogen and hydrogen. Other methods like solid and liquid salt bath nitriding are also used.

Hardening of case carburised steel is achieved by producing the martensitic structure with high carbon content in surface layers. The hardness of the martensite phase increases as the carbon content increases. In plain carbon steel the maximum hardness is obtained at carbon content of 0.8 %. The decline of hardness with increasing carbon

content beyond this level is attributed to the retention of the softer austenite phase (retained austenite) within the structure. In alloy steels, peak hardness is attained at lower carbon content than the specified above. Steels commonly used for carburization contain 0.1 to 0.25 % basic carbon. The steel is carburised in the temperature range of 900 to 930°C and then quenched from the austenite field to produce martensitic structure. The case depth increases with carbon potential and time. Case depths produced by carburization are in the order of 0.5 to 1 mm and therefore are capable of carrying higher loads than cases produced by nitriding. However, longer times and higher temperature are necessary for the deep case carburization. Carburization is usually carried out in two stages. The first is the carburizing stage and the second is the diffusion stage during which carbon is diffused to greater depths without increasing the surface carbon content. Quenching and tempering follows and one disadvantage of case carburizing is the distortion that can occur during quenching. Thus, it is conventional to achieve final tolerance in gears by final grinding after heat treatment.

1.4 Lubrication

Lubrication plays a critical role in preventing damage and failure in gears especially in the heavy duty gears. Loaded gear flanks during running undergo rolling contact combined with sliding in some areas along the flank surface. In dry (un-lubricated) gears surface contact between mating surfaces is confined to asperities points where contact stresses are concentrated. In lubricated gears an oil film is formed between mating surfaces. When the film thickness is larger than asperities height there is full film lubrication and no metal contact occurs. The film thickness-to-surface roughness ratio λ is large (λ greater than 2). This is known as Elastohydrodynamic lubrication or (EHL). Metal-to-metal contact start to occur as the oil film thickness decreases or the surface roughness increases. At very small ratio (λ is less than 1) the condition is known as boundary lubrication and contact occurs through absorbed oil layer. The mixed lubrication is the condition when partial metal to-metal contact occurs. (Dudley's Gear Handbook 2nd edition, 1992). Of course, the oil film thickness depends on a number of factors including the viscosity of the oil and the velocity of rolling or sliding of surfaces. It follows that the λ factor is not constant at all times in gear operation. If the temperature rises, the oil viscosity will fall and λ decreases. Equally, during start up, the velocity is low and λ is small until the full operating speed is

reached. For this reason, EP additives are used in gear lubricants to avoid scuffing during 'start up' condition during gear operation.

1.5 Modes of Failures in Gears

Fatigue is the predominant failure type in gears. Even micropitting, which results in wear, is a form of fatigue failure. The cyclic loading of contact stresses and bending stresses produce various types of fatigue failure as shown schematically in Fig.1.3. Gears fail by one or more of the following modes: micro-pitting wear, pitting, scuffing or bending fatigue.

Pitting and Micropitting are attributed to surface contact stresses. The common feature of these types is the loss of material from the flank surface but location of damage along flank surface is distinctive for each type. The origin of the damage can be traced back to formation of surface cracks or severe wear mainly due to unfavourable lubrication condition between mating surfaces. The scale and the extent of the damage in each type are related to applied load, surface roughness and working conditions. Scuffing is the only form of fatigue that is not associated with the growth of fatigue cracks. Root bending fatigue failure is generally catastrophic as it results in complete detachment of a tooth without warning. (Bull *et al.*, 1999)

1.5.1 Micropitting

This is a fatigue failure caused by fluctuating surface contact stresses. In the gear flank where rolling and sliding motion prevails the surface is susceptible to micropitting i.e in the addendum and dedendum areas but not along the pitch circle. Micropitted areas have a dull, evenly grey appearance (Hohn *et al.*, 1996). A numerous small pits (~ 10 μm) are produced by tiny shallowly inclined surface cracks in the damaged areas. (Olver, 1995). Asperity contact between mating surfaces produces local micro-Hertzian stresses. Plastic deformation at asperities points of contacts is a fundamental cause of micropitting formation. (Olver, 1984). Berth *et al.* (1980) concluded that when pressures on asperities are in the elastic level the rate of formation of micropits with time tends to zero. Therefore surface roughness is an important cause for micro-pitting formation. Severe micropitting results in wear and profile deviation and affects the

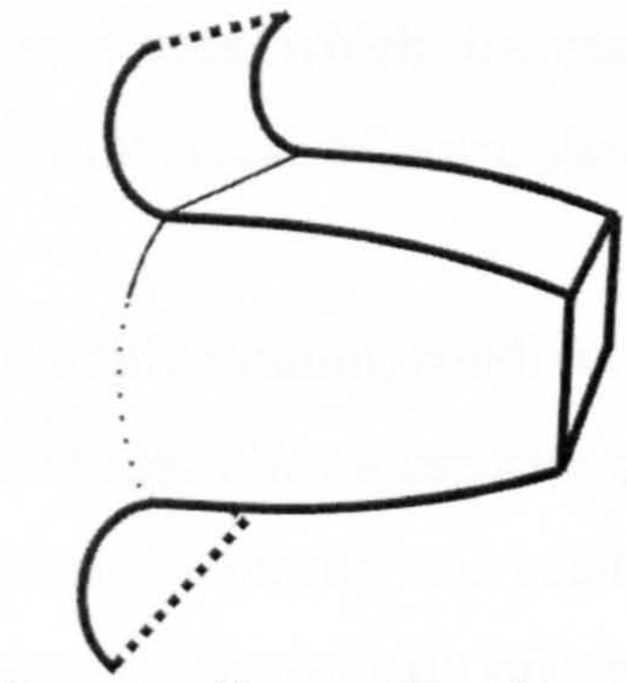

Bending Fatigue

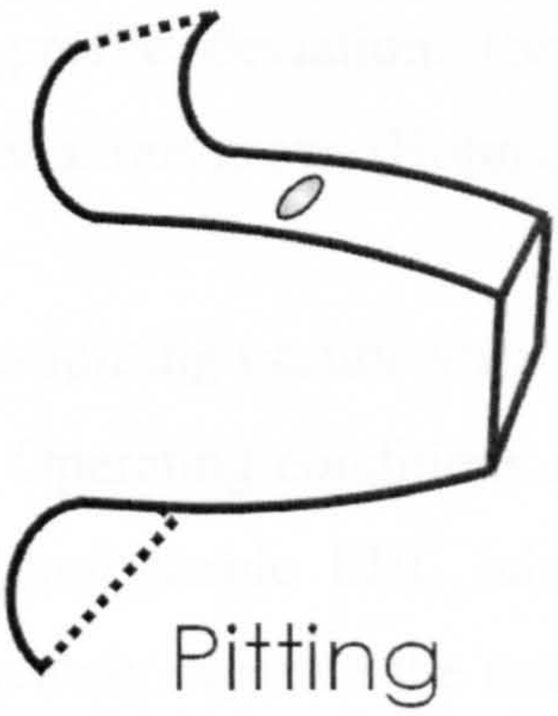

Pitting

Micropitting

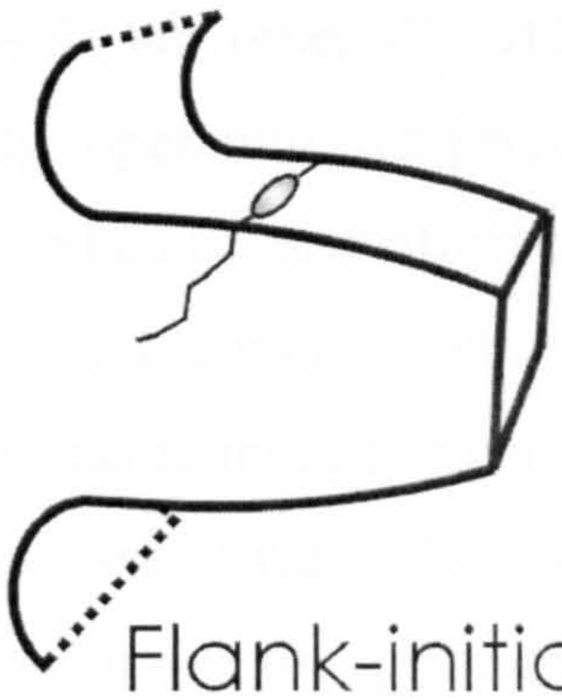

Flank-initiated Bending

Fig.1.3 Illustration of different types of failure in gears. Bending fatigue is caused by cyclic loading at the tip of the tooth. Pitting and micropitting are caused by surface contact. Flank initiated bending fatigue is produced by cyclic tip loading acting on a crack originally produced by surface contact

dynamic forces which increase with increasing profile deviation. (Schonnenbeck, 1984). An increase of noise also occurs as profile deviations grow. (Hohn *et al.*, 1996).

Unfavourable running condition responsible for micropitting occurs when the lubricant film thickness allows asperity contact and friction. Operating conditions influence the micropitting capacity are related to the ElastoHydrodynamic EHL lubrication film thickness. High viscosity of lubricant tends to adequately separate the mating surfaces at a given load. Certain lubricant additives are beneficial in avoiding micropitting such as lead containing compounds. (Hohn *et al.*, 1996) but other EP additives may be detrimental. Viscosity decreases with increasing operating temperature, therefore higher temperature reduces the film thickness and had an adverse affect on micropitting formation. Tooth flanks with high surface roughness are more prone to micropitting than smooth surfaces. The effect of surface roughness is more pronounced when low viscosity lubricants are used. (Emmert, 1994). However Olver (1995) pointed out that although micropitting is caused by surface roughness, the phenomenon requires persistent roughness. Sulphide stringers and non-metallic inclusions have minor effect in micropit or microcrack development. (Hoeprich, 2000).

1.5.2 Pitting

As the micropitting load capacity increases through optimising the above mentioned conditions the external load necessary for crack formation increases. This concurs with decrease in number of cracks formed. At higher number of cycles these cracks grow to higher depths resulting in pit formation that are less in number but larger in size and depth. (Hohn *et al.*, 1996). Macropits are formed near the pitch circle. (Way and Pittsbugh, 1935) or in the area of negative sliding toward the tooth root area of the gear flank. (Hohn *et al.*, 1996). In laboratory tests the failure criteria due to pitting are set such that when 1 % of the total active surface area of gear teeth is covered or 4 % of the active surface of any one tooth, failure is deemed to have occurred. We note that the difference between micropitting and macro-scale pitting may be one of perception, rather than basic mechanism. Micropitting is most prominent away from the pitch line where the slide-to-roll ratio is high. Micropitting also results in material removal (wear). It may be that macroscale pitting does not occur in this region because the

fatigue cracks are eliminated by wear before cracks grow to macroscopic size features. (Winter and Weiss, 1981). The surface contact fatigue curves are plotted as the stress versus the logarithm numbers of cycles to failure at that stress, analogous to the S-N curve for conventional fatigue. Stress is defined as Hertzian contact stress.

1.5.3 Scuffing

The wear of tooth flanks produced by scuffing is another form of lubricated-related tooth failure. Local welding of contact surfaces or adhesive wear occurs when the oil film breaks down. Mixed or boundary lubrication develop at high temperature or at the beginning of gear running before adequate oil film is formed. Damage by scuffing occurs in a very short time when interaction between mating surfaces takes place. (Dudley's Gear hand book, 2nd edition, 1992). This is usually near the tips of the teeth where sliding is most pronounced. It should be noted that scuffing is most likely to occur during the start up period of gear operation, before full hydrodynamic lubrication has been established. For this reason extreme pressure (EP) additives are used in gear lubrication to prevent the damage associated with start up. However, there is increasing evidence that although EP additives are desirable in preventing scuffing, some EP additives make micropitting worse. It is noteworthy that bearing manufacturers avoid EP additives where possible. Of course bearings do not suffer from scuffing damage because contact predominantly involves rolling rather than sliding.

1.5.4 Root Bending Fatigue

This type of gear failures results in complete fracture of a gear tooth or a number of adjacent teeth. The failure mechanism corresponds with conventional fatigue failure under tensile stress which encompasses crack initiation, propagation and final overload fracture. The gear tooth can be regarded as a short cantilever beam loaded on the tooth surface of the active flank. (Fernandes, 1996). The highest tensile stress occurs at the tooth root due to stress concentrations. Because of the cyclic nature of loading in gears fatigue cracks initiate at teeth radii. The tooth root is not the only location where bending fatigue fracture can start. Micro-pits which usually develop early on the flank surface can give rise to flank initiated bending fatigue failure. (Bull *et al.*, 1999).

In carburized steels, the most potent sites for crack initiation includes surface oxides, inclusions, corners, surface discontinuities, or at prior austenite grain boundaries. (Krauss, 1991). Studies of fatigue fracture surface of carburised polished specimens showed that the fracture surface consist of intergranular crack at the surface followed by transgranular region and then a region of overload intergranular cracking which changes gradually to microvoid coalescence fracture toward the specimen core. (Apple and Krauss, 1973; Zaccone *et al.*, 1989). Formation of intergranular cracks was attributed to phosphorous segregation and cementite formation on prior austenite grain boundaries. (Ando and Krauss, 1981).

Surface treatment improves bending fatigue strength. Sung-Ki Lyu *et al.* (1998) concluded that chemical polishing about 20-30 μm after shot peening resulted in bending strength levels that are superior to carburised gears. Cavallaro *et al.* (1995) investigate the effect of peening and cryogenic treatment on bending fatigue strength. They found that residual stresses induced in the near-surface layers by glass bead peening improve the bending fatigue limit. However deterioration after cryogenic treatment was attributed to decrease in retained austenite level and consequently the decrease in K_{1C}.

1.6 Residual Stresses

Residual stresses are those stresses remaining in a part after all manufacturing operations are completed, with no external load applied.

Austenite to martensite transformation is accompanied by an increase in volume. Compressive residual stresses can be induced in the hardened case due to the constraint imposed by the core material on the case. Carbon concentration gradient exists from the outer surface toward the boundary region between the case and the core material. This results in delayed transformation in the outer layers relative to the boundary region. The last part to transform will be in state of compressive residual stress (Ebert, 1978).

In nitriding process no phase transformation takes place after cooling. Compressive residual stresses in the ferrite phase resulted from diffusing of nitrogen atoms into interstitial positions in the ferrite phase. Stress induced in nitrided case is lower than

compressive residual stresses induced in carburized case. As a carburised case is deeper with higher compressive residual stresses than a nitrided case, the capacity for carburised case to bear load is higher than that achieved with nitrided case (Leslie, 1981).

However, the work presented in this thesis shows that the compressive stress from these sources is not large. Much larger compressive stresses can be induced by shot peening.

1.7 Shot Peening

Shot peening is a cold work process aimed to improve metallic material resistance against fatigue failure through induction of surface compressive residual stresses. The method involves impingement of a stream of shots towards the metal surface at high velocity under controlled conditions. (Metal handbook, 9th edition, vol. 5). Incipient metal surface stretching occurs as a result of shot impact on the surface, but the material beneath the surface layers tends to constraint surface plastic deformation. Thus high compressive stresses parallel to the surface are induced in the outer layers. Beneath the effected layers smaller tensile stresses are induced.

Shots made from steel are designated by numbers in the range S70 to S930 according to MIL-S-13165 standard. The shot number is approximately the same as the nominal diameter of the individual pellets in ten thousands of an inch. The peening intensity depends on the velocity, hardness, size, weight and angle of impingement of shots against the metal surface. High levels of compressive residual stresses are achieved by shot peening. This stress level approach half the material yield strength, therefore it is higher for harder material. The surface stress is compressive but the maximum value of the induced compressive stress occurs at shallow depth below the surface. The compressive residual stress beneath this depth then decreases before changes to tensile stresses at higher depths.

1.8 Stresses due to Contact Loading

Power transmission by gears is accomplished through a couple of a drive and driven gears. Teeth of both gears contact along the active profile. The path of contact start at

the tip of the driven gear tooth then goes through the pitch line and end at tip of the driving gear tooth. (Dudley's Gear Handbook 2nd edition, 1992). Only at the pitch line is the contact purely rolling. At either side of the pitch line the contact involves relative sliding.

The above mentioned process generates two main types of stresses, namely the surface contact stress at the surface and subsurface of tooth flank and the bending stress at tooth root. Due to the periodicity of the process, both types of the stress could lead to fatigue failures. The first of the two could results in pitting and / or spalling and the second in fatigue cracks at the tooth root.

Contact loading under the action of distributed tangential and normal forces results in a complicated state of stress. Different positions relative to the point or line of contact are subjected to shear, normal and hydrostatic pressure superimposed in different combinations. The dominant stress field is compressive although smaller levels of tensile stress occur in regions near the contact surface.

Smith *et al.* (1953) analysed the stresses generated when two long cylinders of the same material whose longitudinal axes are parallel and pressed against each other with one or both are rotating. They estimated the maximum principal stresses near the contact area and the range of stresses experienced by a number of points in the cross section throughout one cycle of application and release of the load. By taking the coefficient of friction (f) in consideration they predicted that the maximum shearing stress occurs at a point in the surface when (f) become greater than 1/9 instead of being underneath the surface when (f) is less than 1/9. At value of 1/3 for the coefficient of friction the maximum shear stress is increased by 43 percent. The normal stress at the surface in the longitudinal direction σx is found to be in the range between a maximum compression of 1.2 po [1]to maximum tension of 0.67 po.

---

[1] $p_0 = 2P / \pi a$

P is the normal load per unit length in the y direction

a is the half width of the contact area

Note that these calculations of stress follow the Hertz method which assumes perfectly smooth surfaces. In reality, surfaces are not smooth and contain local asperities. Asperity contact gives rise to much higher short range stresses than is calculated in the Hertzian calculation. Owing to the difficulty of knowing the details of asperity contact, the Hertzian stress is used as the control variable in surface contact fatigue tests. However, it must be accepted that the microstresses produced by asperity contact will give rise to localised plastic deformation on microscale.

1.9 Residual Stress and Fatigue

Fatigue failure is the failure due to cyclic loading even if the load is below the yield strength or the ultimate strength of the material.

Conditions where components subjected to fluctuating stresses are commonly encountered. Failure due to alternating stresses and large number of cycles could occur even if the highest applied load is below the safe values.

The fatigue strength or the stress level a component can withstand decreases with increasing number of cycles. The plot of fatigue strength versus the number of cycles is known as the S-N diagram. Test specimens or real components can be used to produce S-N diagrams. Fatigue failures classified according to number of cycles termed as low cycle fatigue when failure occurs below 10^4 cycles and high cycle fatigue on greater number of cycles. For ferrous materials, classification as finite life and infinite life is distinguishable. This is due to the fact that the S-N curve for ferrous materials show a distinct 'Knee' where the curve appears to be horizontal at greater than 5×10^5 cycles. Thus, it is argued that ferrous materials exhibit a fatigue limit, below which stress fatigue will not occur. This stress level is the material endurance limit or fatigue limit.

Fatigue failure can be enhanced or accelerated by other factors such as corrosive environment or high temperature. Corrosion fatigue and creep fatigue are assigned respectively to fatigue failure when these factors played a role in the failure mechanism

The lifetime of a component working under fluctuating stress is affected by the stress cycle. Complete reverse stress cycle has stress range or stress amplitude greater than a cycle that alternates between the same highest stress and zero. Therefore it is important

to define the stress cycle in terms of the highest (σ_{max}) and lowest (σ_{min}) applied stress. The following equations define the mean stress (σ_m) and the stress amplitude (σ_a)

$$\sigma_m = \frac{\sigma_{max} + \sigma_{min}}{2} \tag{1.1}$$

$$\sigma_a = \frac{\sigma_{max} - \sigma_{min}}{2} \tag{1.2}$$

The influences of mean stress and stress amplitude on fatigue failure criterion is shown in the following empirical equation proposed by Goodman.

$$\Delta\sigma = \Delta\sigma_o\left[1 - (\bar{\sigma}/\sigma_u)\right] \tag{1.3}$$

Where

$\Delta\sigma = \sigma_{max} - \sigma_{min}$ and $\bar{\sigma} = \left(\frac{\sigma_{max} + \sigma_{min}}{2}\right)$. $\Delta\sigma_o$ is the fatigue limit in completely reversed cycling. The Goodman relation indicates that a residual compressive stress will increase the fatigue limit since $\bar{\sigma}$ will be negative.

A simple illustration shows the effect of residual stress. Imagine that the results of fully reversed bending fatigue are compared with and without a residual compressive stress. If a compressive stress equal to $-\sigma_R$ exists, the fatigue strength is

$$\Delta\sigma = \Delta\sigma_o\left[1 + (\sigma_R/\sigma_u)\right] \tag{1.4}$$

If $\sigma_R = \frac{1}{2}\sigma_u$ then

$$\Delta\sigma = \frac{3}{2}\Delta\sigma_o \tag{1.5}$$

The fatigue strength will have been increased by 50 %. Of course this outcome will depend on the nature of the material. Less hard steels often do not derive the benefits of shot peening because residual stresses may "shake down" during fatigue loading if small scale cyclic plasticity occurs. However, case hardened steels often retain the

benefits of shot peening because of the high strength of the case material which remains in the elastic range during load cycling.

Another approach to assess fatigue strength is based on strain. Ideally the plastic strain in cycle is plotted versus the number of load reversals foe failure (log-log scale). In low cycle fatigue, plastic strain is dominant and the relation between $\Delta \varepsilon_p$ and N_f is given by the Manson-Coffin relation

$$\frac{\Delta \varepsilon_p}{2} = \varepsilon_f' (2N_f)^c \qquad (1.6)$$

where $\frac{\Delta \varepsilon_p}{2}$ is plastic strain amplitude

ε_f' is the fatigue ductility coefficient, defined by the strain intercept at one load reversal ($2N_f = 1$)

N_f is number of cycles to failure

c is the fatigue ductility exponent, a material property in the range – 0.5 to – 0.7

At high cycle fatigue, elastic strain is dominant and the relation is given by

$$\frac{\Delta \varepsilon_e E}{2} = \sigma_f' (2N_f)^b \qquad (1.7)$$

where $\frac{\Delta \varepsilon_e}{2}$ is the elastic strain amplitude

E is modulus of elasticity

σ_f' is fatigue strength coefficient, defined by the stress intercept at one load reversal ($2N_f = 1$)

b is fatigue strength component

The fatigue resistance of a material subjected to a strain in the elastic and plastic range is estimated by superposition the contribution from both strains as

$$\frac{\Delta \varepsilon_T}{2} = \frac{\Delta \varepsilon_e}{2} + \frac{\Delta \varepsilon_p}{2} = \frac{\sigma'_f}{E}(2N_f)^b + \varepsilon'_f(2N_f)^c \qquad (1.8)$$

The problem in applying this relation is in being able to separate the elastic and plastic components of total strain. In engineering applications this may not be possible

1.10 Air Hardening Steel

Alloying elements when added in sufficient amount enable full hardness to be achieved in thick sections. The retardation of austenite transformation to ferrite, pearlite or bainite allowed the steel to be air hardened. The most effective elements to enhance hardenability include carbon, Mo, Cr, Mn and Si. Some tool steels are designed to achieve full hardening by air cooling. Air hardening medium alloy cold work tool steel is designated as group (A). (Metal handbook 9th ed. vol. 3). These alloys contain about 5 % Cr, and 1% of Mn and Mo. Carbon content is high and some grades contain more than 1 %. By avoiding drastic cooling in quenchants, distortion is minimised and cooling cracks are less liable to occur. Structural air hardening steels are also available.

One of the steels tested in the present research was air hardening steel developed by the Ovako steel company (Sweden). There are considerable economic advantages in using a steel of this type, given that cost of case carburizing is considerable. However, to realise these advantages, the steel must not contain expensive alloying elements and the steel must be soft enough before hardening to be machined using conventional hobbing or other gear shaping techniques. It is claimed that the Ovako air hardening steels meet these requirements.

1.11 The Austenite to Martensite Transformation in Steel

The formation of austenite by quenching steel from the austenite region is basic to the technological value of engineering steels. By varying the carbon content and subsequent tempering treatment, a wide range of properties can be achieved in which hardness can be "traded off" against toughness to match mechanical properties with design requirement.

Martensitic transformation is a type of reaction which proceeds through cooperative atomic movement to produce martensite structure. The martensite phase can be found in a wide range of ferrous and non-ferrous alloys.

In carbon and low alloy steels martensite is formed after rapid cooling (quenching) from the austenite field. When there is insufficient time for eutectoidal diffusion controlled decomposition to occur, the austenite transforms to martensite. This transformation thereby is diffusionless produced by lattice deformation but with no change in composition. Fig. 1.4 shows a general time-temperature transformation (ttt) diagram. The cooling rate should be fast enough so that the superimposed cooling curve must avoid the nose of the ttt diagram if martensite is to be produced.

The interstitial carbon atoms occupy the octahedral sites in the tetragonal martensite that are inherited from the octahedral positions in fcc austenite. These interstitial carbon atoms create substantial strains or dipole distortion. The interaction between the strain fields of mobile dislocations with the lattice strain due to carbon atoms causes the high strength of the un-aged martensite structure.

The martensite phase in steel owes its technological importance due to its strength and hardness. Because these mechanical properties are desirable in many engineering applications, the hardening process in steel has received great attention. However because increasing strength and hardness is accompanied by a loss of ductility, tempering is usually employed following the hardening process. Tempering of carbon and low alloy steels is accomplished by heating at intermediate temperatures to restore some of ductility and toughness despite of the decrease in strength.

During cooling, the martensite starts to form at characteristic temperature, this temperature is termed as M_s or martensite start temperature. The amount of transformed martensite continuously increases as the temperature decrease. This kind of transformation is known as athermal martensitic transformation, which covers most of the martensitic transformations in steels. The martensite finish temperature or M_f temperature is reached when further cooling does not increase the amount of transformed martensite. In practise some retained austenite usually coexists with martensite even at temperature below M_f.

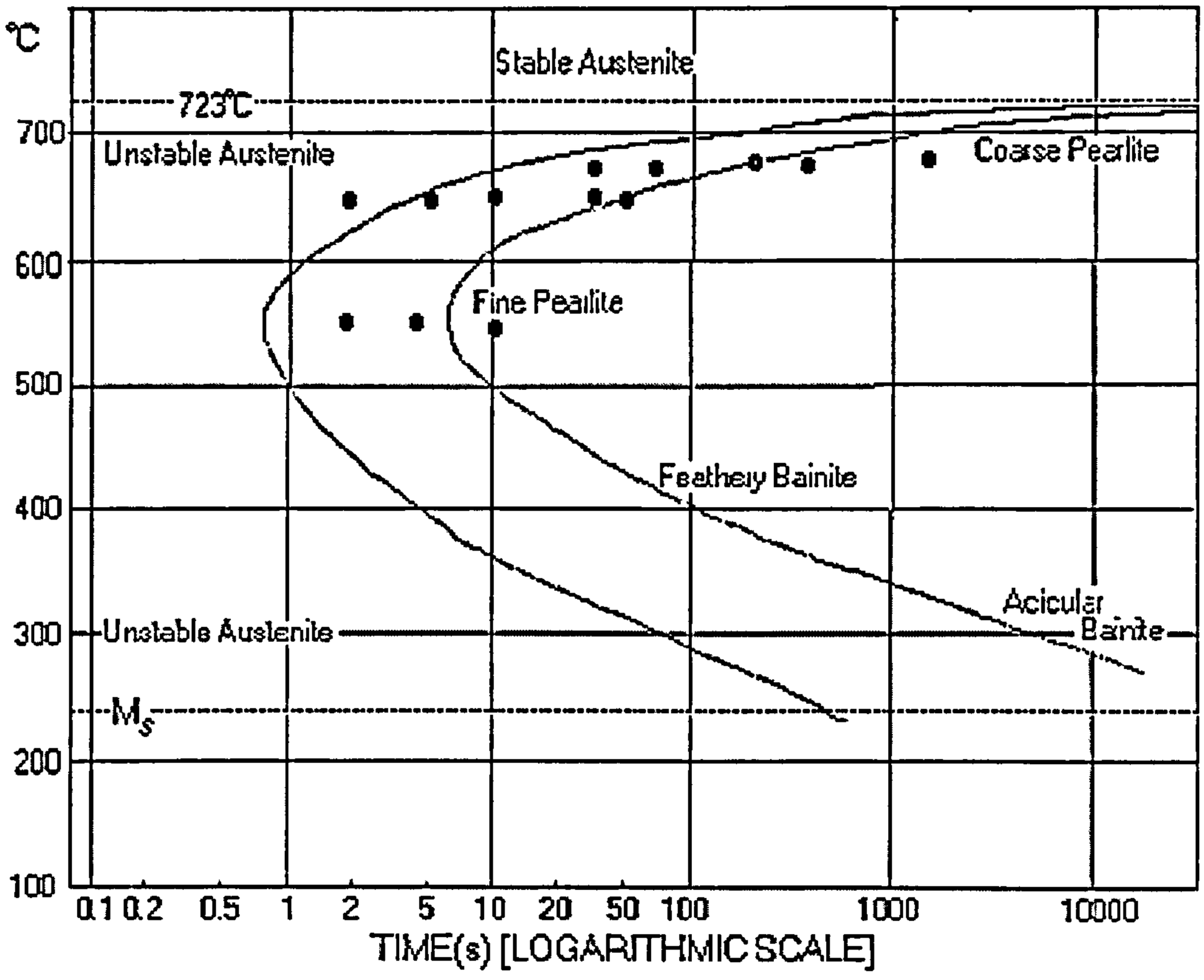

Fig. 1.4 Time-temperature-transformation diagram
for euotectoid plain carbon steel

The M_s temperature depends on the composition of the steel. In carbon and low alloy steels M_s decreases with increasing carbon content and most of the alloying elements that enter into solid solution in the austenite phase. (Honeycombe, 1981). The carbon content affects also the martensite morphology. In low and medium carbon steels lath martensite is formed. Lath martensite consist of packet contains parallel crystals of martensite. The crystals contain large number of tangled dislocations. The packets gathered in groups or blocks. Small amounts of austenite are retained between the laths. Plate martensite is formed when the carbon content is higher than 1.0 wt % and mixed morphologies is produced when the carbon content is around 0.8 wt %. Figure 1.5 shows the effect of carbon content on M_s temperature and amount and type of retained austenite. Plate martensite is distinguished from lath martensite as these plates are non-parallel and highly twinned. Austenite is retained between the plates. The amount of the retained austenite coexists with plate martensite is higher than with the lath martensite. (Marder and Krauss, 1967). Plate martensite is associated with harder steel composition. However, the formation of intersecting martensite plates is known to produce microcracks. To avoid this, the length of individual plates must be limited by having a small austenite grain size. An important feature in harder steel is the presence of grain refining elements and compounds to prevent growth of austenite grains during carburization.

1.12 Stabilisation of Retained Austenite

Martensite transformation occurs over a temperature range as mentioned earlier. The early transformed martensite induces internal stresses in the un-transformed austenite. The regions exposed to compressive stresses suppress the transformation and lower the M_s temperature. Diffusion of carbon and nitrogen to the retained austenite from transformed regions stabilises the un-transformed austenite. The term stabilisation of retained austenite refers to the impediment to further martensite transformation. (Mohanty, 1995) or that the retained austenite becomes more difficult to transform when subject to a sub-zero heat treatment. (Thelning, 1975).

The process of stabilisation of austenite encompasses several mechanisms. Chemical and mechanical stabilisation involves change in the chemical composition and effect of

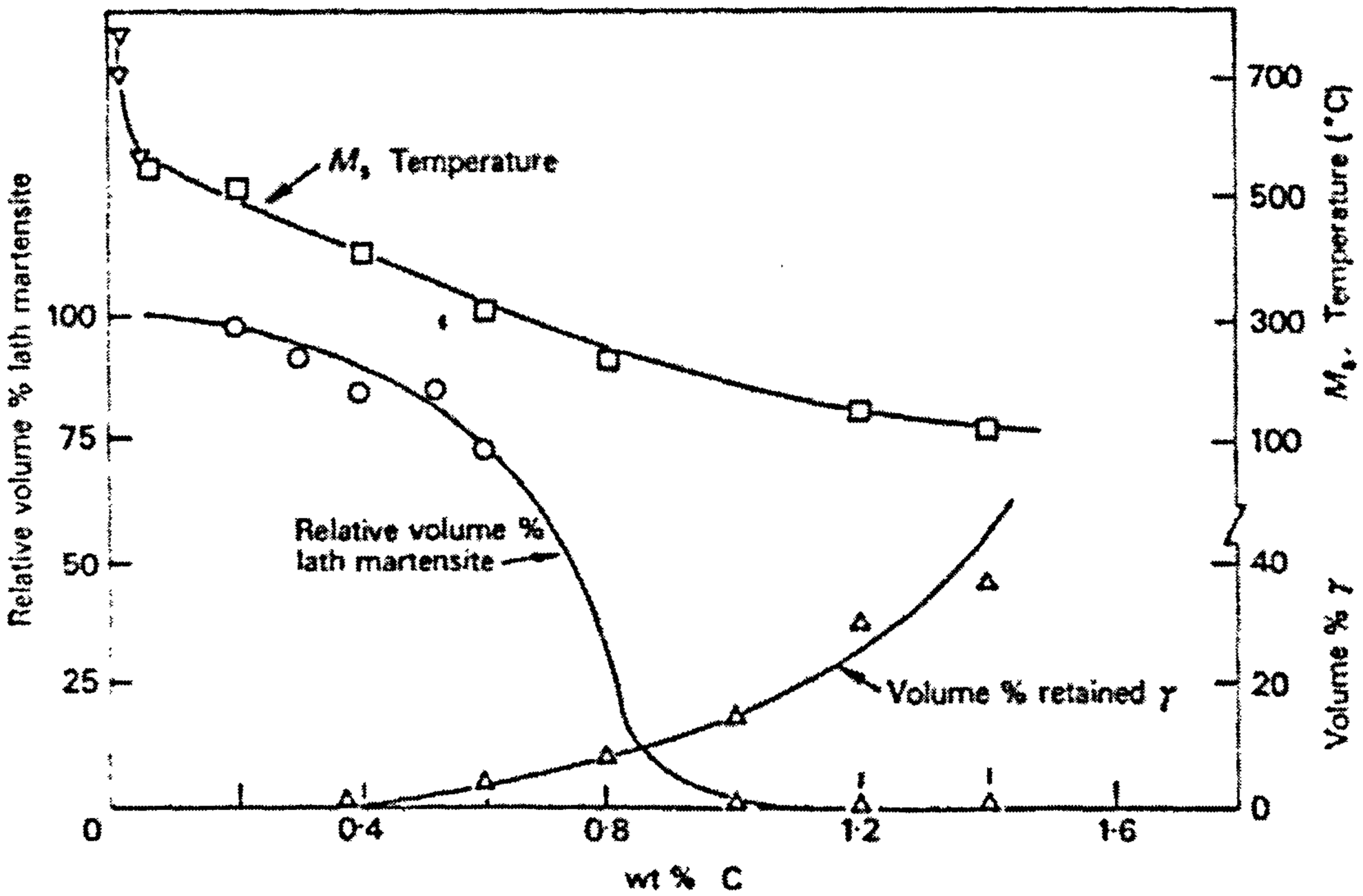

Fig.1.5 Shows the effect of carbon content on M_s temperature and amount and type of transformed martensite. (after Honeycombe, 1981)

stresses respectively. This discussion will be focused on thermal stabilisation through isothermal holding below M_s temperature. Nishiyama (1978) states several mechanisms are responsible for stabilisation. The mechanisms thought to operate in thermal stabilisation are related to diffusion and interaction of interstitial atoms with dislocations and boundaries. Stabilisation of retained austenite in ball bearing chromium steel was studied by Okamoto and Odaka (1952) They expressed stabilisation as the decrease in the M_s temperature (θ°C). They showed that interruption of quenching for 1 hour below the M_s temperature lowers the subsequent M_s temperature. Stabilisation mechanisms were attributed to pinning of pre-existing martensite nuclei in the austenite phase during ageing by diffusion of interstitial atoms to the dislocation arrays at boundaries between nuclei and the austenite matrix. (Kinsman and Shyne, 1966). Nishiyma (1978) added that pinning of other potent nucleation sites such as $\gamma/\overline{\alpha}$ boundaries and lattice imperfections also took place by interstitial atom diffusion. Okamoto and Odaka (1952) also studied the effect of temper-ageing on transformation of retained austenite. They quenched chromium steel from 1000°C to room temperature to give partial transformation and then aged the steel at various temperatures. The stabilisation effect by ageing at 10°C was found to increase steadily with ageing time. At 200°C the effect is higher and shifted to shorter times. However at this temperature the effect declined with increasing ageing time after passing a peak value before it increases abruptly again. The stabilisation mechanism is attributed to the diffusion of interstitial atoms to the nucleation sites and the austenite phase. Formation of carbide clusters may be responsible for the decrease in the stabilisation effect. At later stages formation of bainite promotes stabilisation due to diffusion of interstitial atoms from the supersaturated bainite to the retained austenite.

1.13 Crystallography of Martensite

Martensite is a supersaturated solid solution of carbon in iron. The crystal structure of martensite in carbon and low alloy steel is a body centred tetragonal (bct). Carbon atoms occupy the octahedral sites in the bct lattice. The interstitial carbon atoms in bct lattice giving rise to unsymmetrical distortion resulting in tetragonality of the lattice,

which increases with carbon content. The c/a ratio of the bct lattice varies with carbon content as shown in Fig.1.6 and by the following equation.

$$c/a = 1 + 0.045(wt\%C)$$

Martensite laths or plates form inside the austenite grains and grow in a number of orientation variants. Martensite plates are able to grow at speeds approaching the speed of sound; therefore some sort of highly mobile interface is required. This interface is the habit plane or the plane that is common to both phases. Across the habit plane coherency is maintained and all directions (and angular separations) are unchanged during transformation. The habit plane varies with steel composition. When the carbon content is between 0.5 and 1.4 wt % the habit plane is $\{225\}_\gamma$.

In low carbon and alloy steels the orientation relationship is such that the closest packed planes are approximately parallel i.e. $\{111\}_\gamma$ is parallel to $\{110\}_{\bar{\alpha}}$ and $[011]_\gamma$ is parallel to $[111]_{\bar{\alpha}}$.

Bain showed that bct unit cell could be obtained from fcc unit cell with the minimum of atomic movement if one axis is contracted by 20% and the other two expanded by 12%. This Bain strain or homogeneous shape deformation when combined with a fine scale inhomogeneous deformation leads to the interface being undistorted.

Frank (1953) proposed a model for the $\{225\}_\gamma$ habit plane. He showed that lattice misfit is minimised if the $(111)_\gamma$ plane is inclined with small angle less than 1° to the $(101)_{\bar{\alpha}}$ plane and both these planes are inclined to the$(522)_\gamma$ habit plane by 25°. The $[011]_\gamma$ and $[11\bar{1}]_{\bar{\alpha}}$ are lying in the $(522)_\gamma$ habit plane and are parallel to its intersection with the two closed packed planes. The small difference in interatomic distance between the $[01\bar{1}]_\gamma$ and the $[11\bar{1}]_{\bar{\alpha}}$ could be accommodated by lattice strain. Complete matching along successive planes at the interface is achieved if screw dislocations are generated with a Burgers vector of (a/6) $[011]_\gamma$ at the interface. The interdislocation distance corresponding to six layers of $(011)_\gamma$ planes. This $(011)_\gamma$ plane becomes the $(112)_{\bar{\alpha}}$ plane. The plate is thus formed within two sets of opposite sign screw dislocations. Edge dislocations at the upper and lower region of the plate connect the screw dislocations. The martensite plate is enclosed within a dislocation loop. New

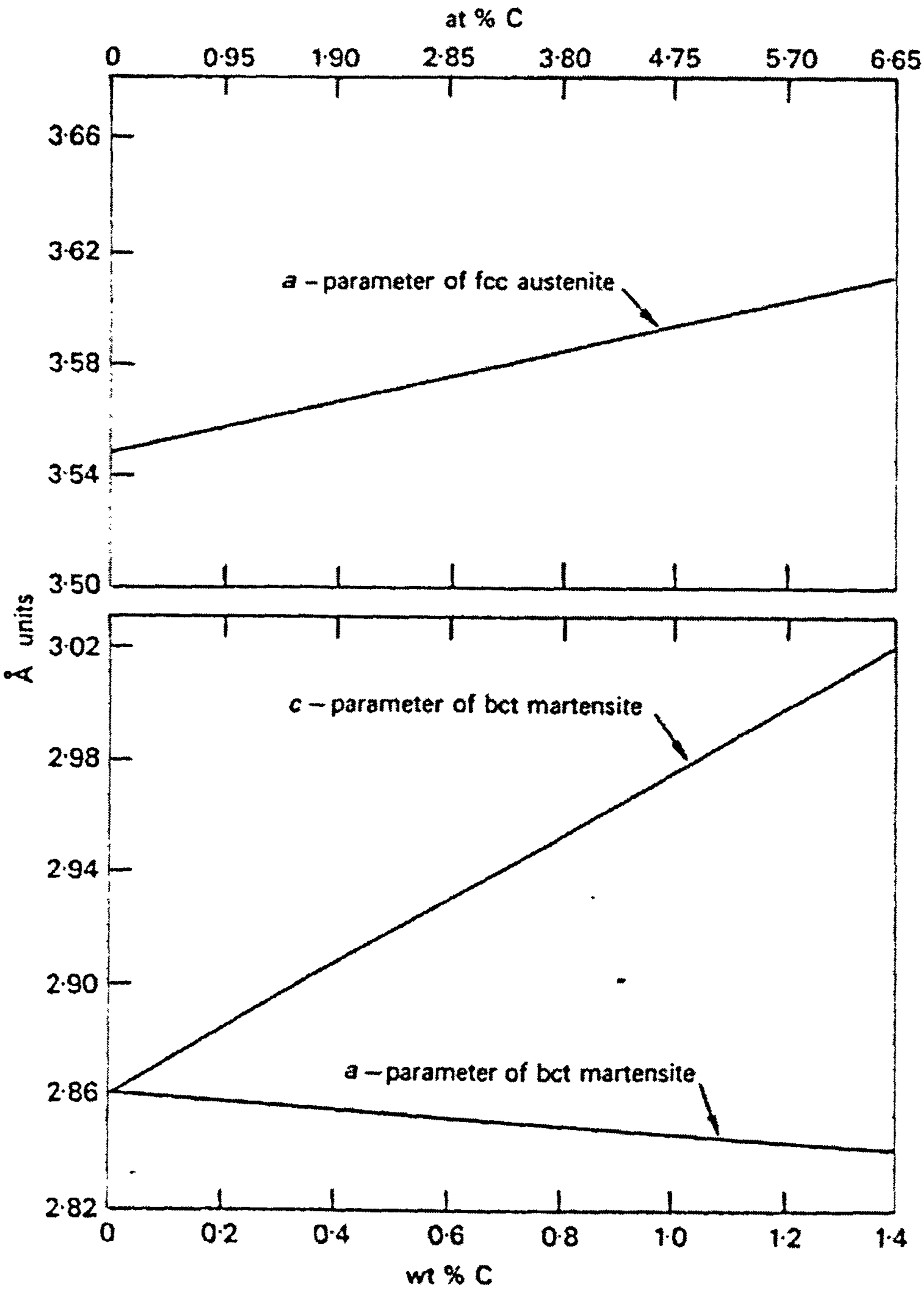

Fig.1.6 Shows the effect of carbon content on the c/a ratio of the martensite bct unit cell (after Honeycombe, 1981)

dislocation loops must be created successively for the plate to grow. Put in it's the most simple way, a martensite plate forms by a process of shear combined with a volume increase. This is discussed in further detail in (Chapter 5).

1.14 Strength of Martensite

The hardness of martensite in carbon steels depends on the carbon content. Thus the tetragonality increased by carbon is correlated with the increase in hardness. The effect of carbon content on the hardness has been reported in many investigations. (Krauss, 1999; Honeycombe, 1981). Apart from some scatter in these results the trend of hardness increases with increasing carbon content is very uniform. This scatter could be attributed among other factors, including prior austenite grain size, amount of retained austenite or amount of dissolved carbon in austenite (Krauss, 1999).

The effect of carbon is more pronounced at lower carbon content where hardness rises with increasing carbon up to about 0.5 wt %. Makinson *et al* (1998) found that the effect of carbon extended to higher levels when nanohardness measurements were carriedout on individual martensite crystals. The nanohardness measurements showed higher values than those obtained with microhardness. In the latter the measurements integrate deformation response of larger volumes of microstructure including retained austenite.

Winchell and Cohen (1962) designed a method of investigation which in principle was able to distinguish between solid solution hardening produced by carbon and the effects of clustering or carbon precipitation hardening. They claim that a large fraction of the strength of martensite is due to solid solution hardening. Since martensite is highly saturated with carbon, precipitation can occur in a very short time at temperatures a little above room temperature and can not normally be prevented even by very fast quenching. This effect is called autotempering. Winchell and Cohen (1962) were able to avoid autotempering by using iron-nickel-carbon alloy with $M_s \sim$ -35°C. Thus they were able to measure the hardening due to solution hardening without carbon atom clustering or precipitation. The hardness / flow stress was found to increase linearly with $C^{1/4}$ (where C is the carbon concentration) but appeared to saturate when the carbon content was above 0.4 %.

A disadvantage of the Winchell and Cohen (1962) experiments was that their specimens with higher carbon contained appreciable quantities of retained austenite. The data had to be corrected for this effect. Chilton and Kelly (1968) avoided this difficulty by subzero cooling the iron-nickel-carbon martensite to eliminate retained austenite. The results confirmed that solid solution hardening produces large proportion of the strength of untempered martensite by carbon.

In Fe-Ni-C steel Cohen (1968) showed that the dependency of 0.2% offset flow stress on carbon content was could be expressed as

$$\sigma_{0.2}(\text{MPa}) = 461 + 1.31 \times 103(\text{wt\%C})^{1/2}$$

Cohen (1968) measured the flow stress at 0.2% and 0.6% strain and he showed that the strain hardening also increased with carbon content.

In plain carbon and low alloy steels with an M_s temperature well above room temperature, carbon atom diffusion is possible and segregation to dislocation and lath boundaries occurs during quenching. Also clustering and precipitation can occur (autotempering) In these steels, the 0.2% offset flow stress depend on carbon content according to the following equation (Speich and Warlimont, 1968).

$$\sigma_{0.2}(\text{MPa}) = 413 + 1.72 \times 103(\text{wt\%C})^{1/2}$$

This equation is in good agreement with experimental results except when the carbon content is below 0.013 wt. %. This was attributed to the low hardenability of the steel with low carbon content.

Norstrom (1976) found that the dislocation density in lath martensite increases with carbon content. They developed an equation for the yield strength of low carbon martensitic steel including the effect of the dislocation density and the carbon content. Leslie and Sober (1967) showed that there is a contribution from strain hardening and dynamic strain ageing to the strength of martensitic structure of 4340 steel.

1.15 Fracture of Martensitic Steel

Martensite in high strength plain carbon and low alloy steels has poor toughness. The low ductility in steels which have been lightly tempered or untempered is due in part to the existence of easy fracture paths such as one provided by prior austenite grain boundaries. (Hyde *et al.*, 1998). Another factor in the low toughness of martensite is the formation of microcracks during the quench. Marder and Krauss (1967) found microcracks with C > 0.75%. Bowen *et al.* (1967) found cracks 1-6 μm long at martensite boundaries. Marder and Benssober (1968) showed that cracks probably originate when transformed martensite plates intersect. A reduced prior austenite grain size is important in preventing microcrack formation by this mechanism.

In carbon steel with carbon content greater than 0.5 wt % C fracture proceeds intergranularly due to phosphorous segregation and cementite formation on austenite grain boundaries (Hyde *et al.*, 1998) With lower carbon content fracture could be a mixture of cleavage and regions of microvoids.

1.16 Stress Induced and Strain Induced Martensite Transformation

Retained austenite can be transformed to martensite above the M_s temperature if tensile stress is imposed on it. The transformation by the aid of stress occurs within a specific range of temperature. The highest temperature in this range is termed M_d temperature, the temperature above which no transformation to martensite occurs (Olson, 1982).

In the temperature range between M_s and M_d there are two modes of transformations which produce martensite from retained austenite. These two types of martensite are the stress-assisted martensite and the strain-induced martensite. The distinction between these two types is characterised by differences in morphology, distribution and the temperature at which martensite is formed. (Maxwell *et al.*, 1974 a).

An approximate boundary between the two modes is designated as M_s^σ below, which the stress-assisted mechanism is responsible for transformation. The strain-induced transformation predominates between M_s^σ and M_d (Olson, 1982).

In the strain-induced transformation mode, yielding (as observed in a tensile test) is initiated by slip process whereas in the stress-assisted transformation the observed yielding is initiated by the onset of martensitic transformation (Olson and Cohen, 1972).

Strain-induced transformation can take place only if the applied stress reaches or exceeds the yield stress (σ_y) of the austenite. Because this type of transformation is induced by plastic deformation, the slip bands or intersection of these bands becomes the new nucleation sites for the martensite phase. Maxwell *et al.* (1974 a) found that strain induced martensite formed along the slip bands of austenite as a fine parallel laths on the $\{111\}_\gamma$ planes of the austenite. The stress required to induce transformation in the strain-induced mode rises above the yield stress of the austenite as the temperature increases (Olson and Cohen, 1972).

In the stress-assisted transformation range, below M_s^σ temperature, the stress to initiate transformation decreases as the temperature decreases and approaches zero as the M_s temperature is approached (Olson and Cohen, 1972).

The energy supplement by the applied stress compensates for the decrease in the chemical free energy when the temperature is above Ms allowing transformation to occur on the same sites when cooling only would induce transformation (Patel and Cohen, 1953).

The Clausius-Clapeyron equation estimates the change in the equilibrium temperature with pressure for the reactions involve a volume change. Martensite formation is associated with about 4% increase in volume. Accordingly high hydrostatic pressure is expected to decrease the M_s temperature and hydrostatic tension would increase the M_s temperature (Karaman *et al.*, 1998).

Neu and Sehitoglu (1992) studied the transformation of retained austenite in carburized SAE 4320 steel with 35% retained austenite, they found that stress-assisted transformation occurs under tensile loading. This transformation is responsible for the apparent initial yielding as observed in a tensile test. Under compressive loading, no or very little transformation occurs and the yielding observed was as a result of the slip process.

Patel and Cohen (1953) showed for Iron-Nickel-carbon alloy that M_s temperature rose by tensile loading and is lowered by hydrostatic pressure. Karaman *et al.* (1998) found that retained austenite is less stable under tensile loading than under compression. They found also that the greater the initial amounts of the retained austenite the lower the flow stress and the earlier the transformation starts.

Neu and Sehitoglu (1992) found for carburized SAE 4320 steel that stress-induced transformation of retained austenite occurs under cyclic loading. Transformation was found to saturate under constant stress amplitude and further transformation then occurs only when the stress is raised above the level of the previous cycles. The anisotropy of the transformation strain was less for cyclic loading than under monotonic loading. They perform torsion test on the same steel and found that stress-induced transformation also occurs by shear loading.

Maxwell *et al.* (1974 a) showed that the stress-assisted martensite in Iron-Nickel-Carbon alloys has the same morphology as the plate martensite formed spontaneously below M_s with the exception that it is somewhat finer and less regularly shaped than that formed by cooling only. As the temperature increases the martensite plates becomes smaller, less regular in shape and the transformed amount decreases.

Neu and Sehitoglu (1991) showed that stress-induced transformation can occur at temperature up to 40°C above the quenching temperature for the SAE 4320 carburized steel. At a temperature of 60°C above the quenching temperature they did not observe any stress-induced transformation.

Mechanical induced transformation of retained austenite is affected by the chemical composition of the steel, processing history, test temperature, M_s temperature and the fraction of the retained austenite (Karaman *et al.*, 1998; Neu and Sehitoglu, 1992).

1.17 Microstructure in the Case of Case Carburized Steel

Carburization of the gear materials has the benefit of introducing a relatively deep, hard case. Martensite constitutes the large proportion of the case microstructure, which gives a high strength and hardness. The high hardness associated with carburized case improves the wear resistance of the gear material.

A carbon concentration gradient exists from the surface inward to the core. Quenching the steel from the austenite field generates complex residual stresses owing to thermal stresses and phase transformations. Because neither the carbon concentration nor the cooling rate are uniform through out the thickness, differences in the microstructure and residual stresses exists across the case of the hardened steel.

Carbon is known for its effect on the M_s temperature (austenite stabiliser) and martensite morphology, therefore martensite undergoes change in morphology through the thickness as well the percentage of the retained austenite coexisting with the martensite phase.

The last area of the case undergoes transformation to martensite is believed to have the highest compressive residual stress. If the amount of the transformed martensite is small, the compressive stress will be low. Areas of the case that contain non-martensitic phases are unable to produce high compressive residual stresses (Diesburg, 1978).

At the intermediate carbon region of the carburised case austenite may decomposes to form bainite.

It has been shown that compressive residual stress in the core decreases as the carbon content increases (Kern, 1968).

The presence of alloying elements alters the hardenability and the relative amounts of the constituents in the case material.

1.18 Internal Oxidation

Internal oxidation is the formation of oxides of other elements within the metal surface during carburizing heat treatment. The iron is not oxidised but other elements such as

silicon and chromium are. This phenomenon was observed about forty years ago. The internally oxidised layer has harmful effects on mechanical properties of carburized components. Post heat treatment machining or grinding can be used to remove the oxidised layer. However, post-heat treatment grinding adds cost to manufacturing process.

The constituents in normal carburizing media used for gas carburization (H_2O, CO_2 and CO) are the source of the oxygen. As case hardening steels usually contain alloying elements, oxides of these elements are readily formed at the carburizing temperature whilst the iron matrix is unaffected. Internal oxidation is also refereed to as surface oxidation because oxides are formed in intergranular and intragranular locations (Evanson *et al.*, 2000).

Alloying elements in case hardening steels improve hardenability and reduce the non-martensitic products in the case material. The presence of non-martensitic products adversely affects the fatigue strength of carburized components. Depletion of these alloying elements near the surface due to surface oxidation promotes non-martensitic transformation. Resistance to fatigue failure in carburized components rely on the high compressive residual stresses induced in the case material accompanies the formation of the martensite phase. Therefore formation of non-martensitic products lowers the level of surface compressive residual stress, produces cases with lower hardness and deteriorates fatigue properties (Dowling *et al.*, 1995). The effect of internal oxidation extends beyond the oxide layer. This is because as the surface layers become depleted in alloying elements a concentration gradient is set up. Diffusion towards the surface region render deeper regions impoverish in alloying elements. Loss of alloying elements from the solution decreases the hardenability as mentioned earlier (Fischer, 1978). Metal oxides near the surface have a harmful effect on fatigue performance as they may provide potent sites for fatigue cracks (Evanson *et al.*, 2000). Surface cracking could take place in case of severe grain boundary oxidation (Fischer, 1978). It should be noted that internal oxidation rarely occurs in a uniform layers. Rather, the prior austenite grain boundary regions are internally oxidised to greater depth than the bulk. This arises because diffusion of oxygen in the steel is faster in grain boundaries at temperature of carburization.

Alloying elements such as Ti, Cr, Mn, V and Si have greater affinity for oxygen than iron. Elements that form stable carbides at carburizing temperatures such as Ti and V do not oxidise (Turkdogan, 1989). Fischer (1978) studied the effect of alloying elements content in various combinations on internal oxidation. He found that alloys of pure Fe-Ni and Fe-Mo do not produce surface oxides. In Fe-Cr and Fe-Mn alloys, oxides are formed only when the alloying element content exceeds a minimum amount of 1.3 % for Cr and 0.8 % for Mn. However he found that the oxidation behaviour of Cr and Mn is largely enhanced with addition of silicon. Alloys of Fe-Ni-Mo were not immune against oxidation in the presence of silicon.

Reducing depth of oxide layers is possible through decreasing CO_2 content. However avoiding internal oxidation with the current employed carburizing methods is difficult to achieve. Therefore Fischer (1978) proposed implementing new methods which involve the use of oxygen-free carbon compounds as carburizing media in conjunction with vacuum furnaces to avoid internal oxidation. These new methods have not been widely implemented because of additional cost.

The desirability of avoiding internal oxidation is another advantage of the Ovako 677 steel. The Ovako 677 steel is heat treated but not carburized. Of course surface oxidation can occur during heat treatment, but because of the shorter heat treatment time the depth of any internally oxidised layer is very small compared with that which occurs in carburization (5-100 μm).

1.19 Influence of Retained Austenite on Fatigue Strength of Carburized Gears

In general fatigue strength is related to the monotonic tensile strength. As a rule of thumb, fatigue strength increases in proportion to the tensile strength.

In the literature there is some confusion about the effect of retained austenite on the mechanical behaviour of steels containing retained austenite. Some authors ,eg. Castleman *et al.* (1952); Bailey *et al.* (1952), claimed deterioration in the tensile strength and fatigue strength of the carburized case when austenite is retained in the microstructure. Frankel *et al.* (1960) concluded that when the percentage of the retained

austenite exceeds 10-15 % it has a minimal effect on strength and below this level fatigue strength decreases. More recent investigations indicate the beneficial effect of retained austenite on the fatigue resistance of the carburized steels. Zaccone *et al.* (1987) investigated the effect of retained austenite on the elastic limit and the strain hardening of austenite-martensite composite. They performed tensile tests in the microstrain regime and compression tests in the macrostrain regime. They found that the elastic limit decreases as the retained austenite content increases and steels with higher retained austenite has a higher stain hardening rate. They made a correlation between the observed higher fatigue strength in the low cycle fatigue and the higher strain hardening rate for steels with larger amount of retained austenite. Higher strain hardening rate results from strain induced transformation. Fatigue cracks initiated under high strains at prior austenite grain boundaries therefore; higher strain hardening rates retard the fatigue crack initiation mechanism.

Richman and Landgraf (1975) attributed the enhanced fatigue resistance in high carbon steels with higher percentage of retained austenite to the cyclic hardening and the development of mean compressive stresses. These changes are due to deformation induced transformation of the initial retained austenite which produces a more ductile martensite than the thermally formed martensite. Zaccone *et al.* (1989) found that the amount of cyclic hardening increases as the retained austenite level increases. This improves the low cycle fatigue resistance of the steel with higher retained austenite. The fatigue resistance is reversed in the high cycle fatigue.

Da Silva *et al.* (1999) attributed the improvement in the fatigue life for SAE 8620 steel to both the capacity of the retained austenite to transform to martensite during local plastic deformation and the evolution of compressive stresses associated with the transformation, the level of which is dependent on the carbon content before transformation.

Maxwell *et al.* (1974 b) studied the influence of mechanically induced martensite on the mechanical behaviour of Fe-Ni-C alloys. They concluded that the formation of stress assisted, plate martensite increases the flow stress and the work hardening rate, and substantial amounts of retained austenite must transform to give appreciable effect. With higher carbon content the effect is more pronounced. When the carbon content is 0.6 % it required about 25 vol. % of plate martensite to give appreciable effect and 40

vol. % of plate martensite for the alloy with 0.2 % carbon content. They found that Transformation Induced Plasticity (TRIP) steels exhibits a TRIP effect over a much wider temperature range than the Fe-Ni-C alloys do which transform to stress assisted plate martensite during transformation.

Lou *et al.* (1990) attributed a reduction in the fatigue crack growth rate to the compressive residual stresses generate during transformation in the plastic zone ahead of the crack tip.

Szpunar and Bielanik (1984) explained the increase in the fatigue strength of carburized steels with retained austenite through the consumption of part of the work done by the applied force to transform the retained austenite. As a result of that the effect of the external applied force to propagate the fatigue crack decreases.

The influence of retained austenite is not clear as indicated in the above references. It seems likely that the effect of retained austenite is different in the different fatigue regimes. It is also likely that moderate amounts of retained austenite (15%) do not have a deleterious effect on properties. Nevertheless it is standard practice in the aerospace industries to eliminate retained austenite from steel gears. This is done by sub-zero cooling after quenching. In contrast retained austenite is tolerated (and even used) by bearing manufacturers, i.e. materials with retained austenite content of 40% are specified in some applications. It would be satisfying if the reasons for these different approaches could be understood on a scientific basis.

CHAPTER 2

Materials and Methods

The materials, heat treatments and experimental methods are described in this chapter

2.1 Materials

2.1.1 Gear Steel 17CrNiMo6

This steel (ISO: Standard 683, 17CrNiMo6) has low carbon content in the as-received condition (Table 2.1) and can be case hardened by carburization. This steel was available for investigation in the form of carburized helical gears.

Carburizing was carried out at 925°C using a boost diffuse cycle and direct quench from 840°C in oil (QUENCHALL 23WS) at ambient temperature up to 50°C. Heat treatment were carried out by Heat Tech, who were collaborators in the project.
The 17CrNiMo6 steel was tested as an intact gear and later in sections taken from tested gears. In fact, as explained in more detail in (Chapter 1), this batch of gears was carburised incorrectly, resulting in a much higher level of retained austenite than specified for final properties. The specified surface carbon content after carburization was between 0.7 and 0.8%. Table 2.2 shows the gear specification and Table 2.3 shows the gear dimensions

Test gears were tested for surface contact fatigue in back-to-back gear rigs. In this test four gears were mounted in the test rig, each two gears were meshed together as shown in Fig.2.1 and schematically in Fig.2.2. The gear position in the test rig determines which flank side is being tested. All tests were carried out at a constant speed of 3000 rpm with ZFG oil with 4% EP additive used as a lubricant. After the required speed was attained a specified torque was applied to the two shafts through a hydraulic actuator. This has the effect of loading the gear teeth as if the gears were being driven by a motor against a load. The advantage of this is that relatively little power is required to drive the rig. Effectively, power is recirculated between the two shafts. The

Table (2.1) Chemical composition of the 17CrNiMo6 steel (wt %)

C	Ni	Cr	Si	Mn	Mo	S	Cu	P	Sn	Al	N	V
0.17	1.5	1.66	0.27	0.5	0.28	.0093	.15	.008	.011	.023	.007	.004

Table (2.2) Gear heat treatment specifications

Parameter	**Specification**
Case depth to 550HV Pitch line Root Fillet	 1.25 mm to 1.75 mm 60% Min of pitchline minimum
Surface carbon content	0.6±0.05%
Case hardness	650-750 HV 10kg
Decarburization 100μm below surface	<40 HV drop
Carbide	<15 μm
Retained Austenite	15% visual max
Intergranular Oxidation(Root Fillet)	< 20 μm

Table (2.3) Gear dimensions

Gear Property	**Value**
Helix angle (degrees)	30°
Number of teeth	23
Module (mm)	6.0
Gear ratio	1:1
Centre distance (mm)	160
DIN quality	5
Face width (mm)	38
Base circle diameter	150.350
Addendum (mm)	6.0
Tip diameter(mm)	172.0
Root diameter (mm)	142.7
Base pith error (μm)	7.0
Form error (μm)	8.5
Tip relief μm/mm	70 μm over 0.8 mm
Total error (μm)	9.5

Fig.2.1 Gear test rig for back-to-back surface contact fatigue test

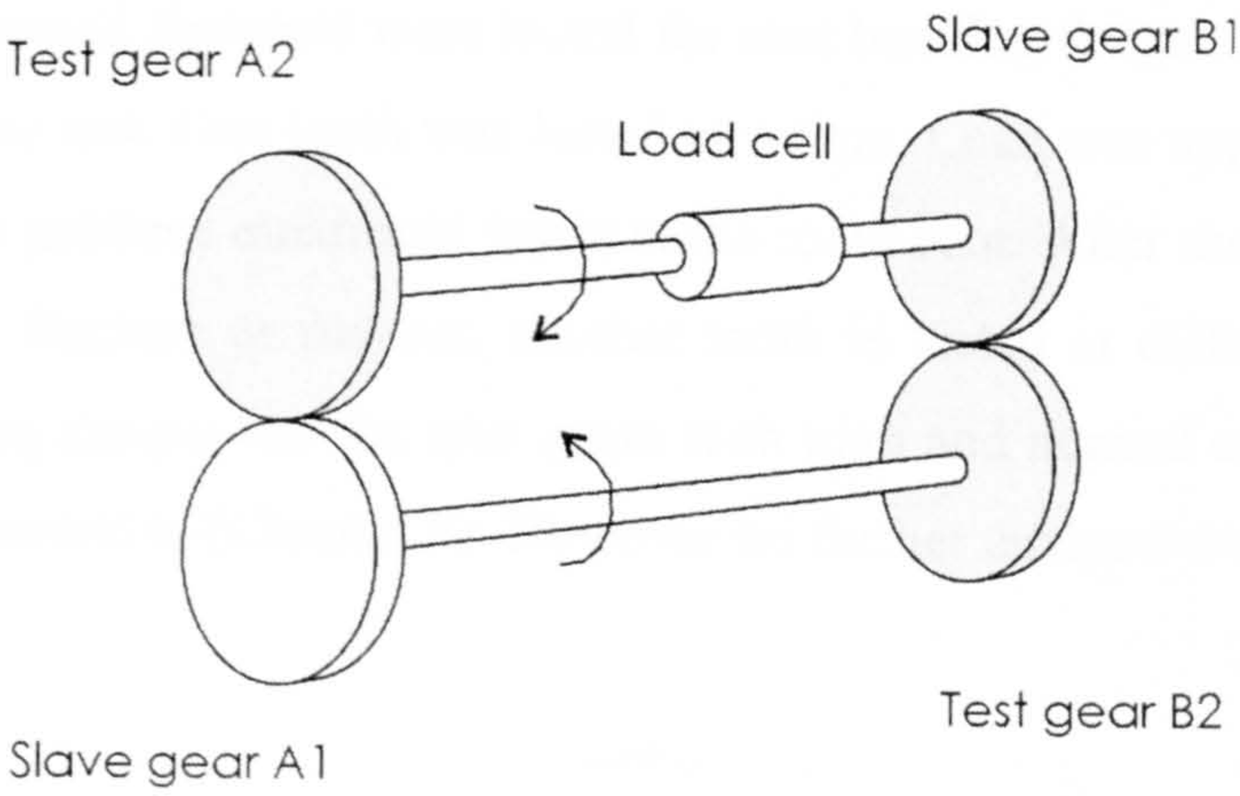

Fig.2.2 Schematic diagram for back to back test

tested gears were frequently checked for any damage. The test was stopped if the failure criterion was met or obvious fracture took place. Otherwise the test was continued to a specific number of cycles (usually 10^8 run out).

After the test was completed the applied torque and the corresponding Hertzian contact stress and the number of cycles were recorded. Calculation of bending stress for spur gears and contact stress for helical gears were made according to the implementation of ISO: 6336-1: 1996. When a sufficient amount of data was collected the S-N curve was plotted. The surface contact fatigue plot shows the number of cycles to failure as a function of the nominal Hertzian stress. "Failure"in surface contact fatigue is defined as that stage when 4% of the total involute flank area is pitted.

One gear was selected for microstructural examinations. This gear had been tested for 32 million cycles in the back-to-back test on the left flank only. The applied torque was 3500Nm equivalent to a Hertzian contact stress of 1455 MPa. The contact stress is the maximum stress operating in the area of contact between the involute flanks. As explained below in (Chapter 3) the opportunity was taken using this batch of gears to assess the effect of high retained austenite on surface contact fatigue. It should be noted that the Hertzian contact stress is calculated on the assumption that the gears are perfectly smooth and does not take account of the asperity contact.

Spur gears made with the same steel and same carburization scheme and containing high levels of retained austenite were tested for root bending fatigue. Figure 2.3 shows the test rig for this test. One tooth was tested at a time. Load was applied and pulsated at the tooth tip to produce maximum stress at the tooth root. After the test ended either because of tooth fracture or run-out, another tooth is tested at different testing load. Results of bending fatigue test for spur gears with high and normal content of retained austenite are presented in (Chapter 3). However no further analysis were carried out for spur gears.

Retained austenite and residual stresses using X-ray diffraction, portable hardness and magnetic Barkhausen emission (MBE) measurements were carried out on four teeth. These teeth were 90° apart on the gear and both flanks (run and un-run flanks) were

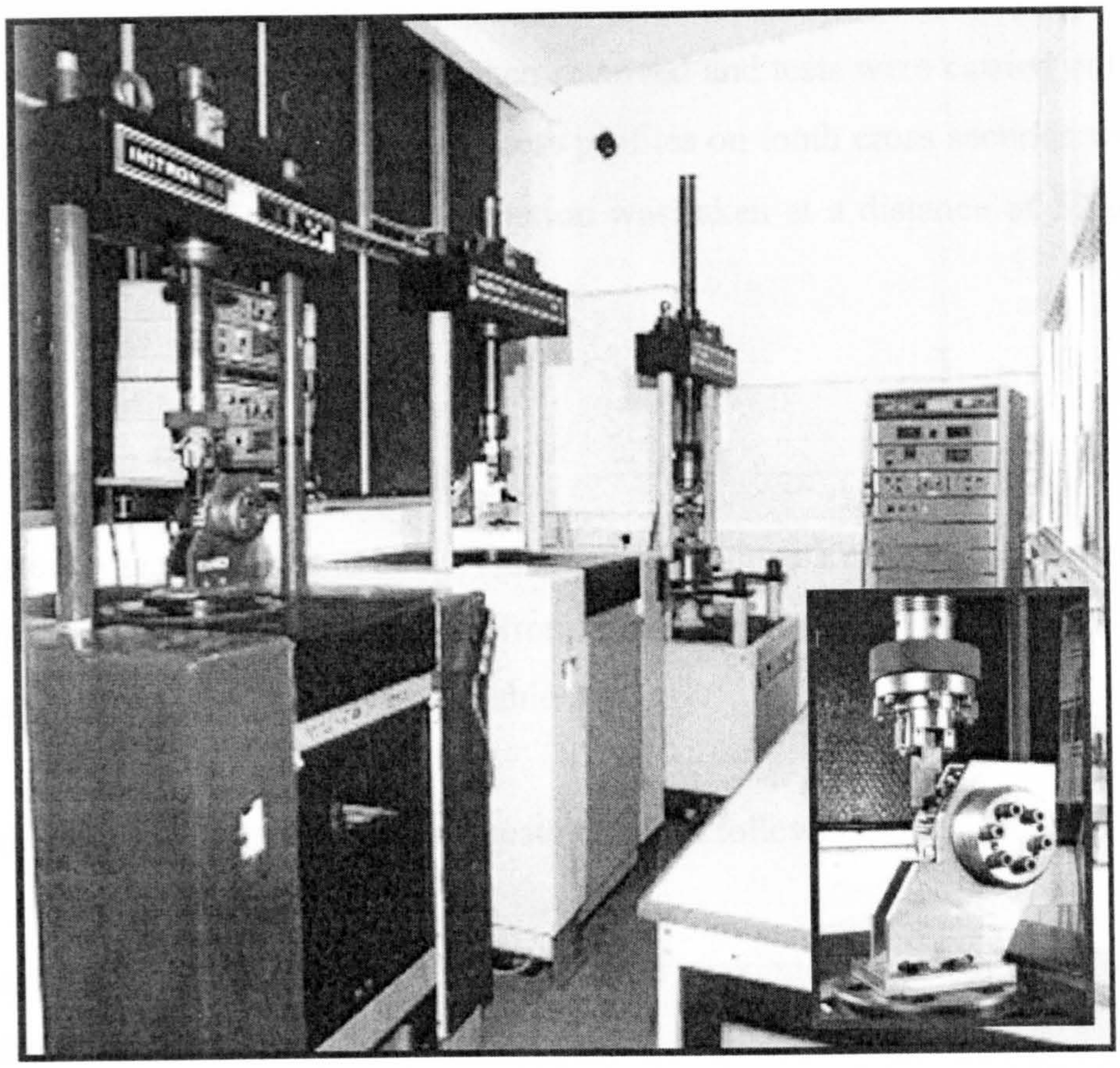

Fig.2.3 Test rig for root bending fatigue for spur gears

tested; measurements were made near to the tip of the teeth, the zone, which only could be accessed.

Teeth from the selected gear were then removed and tests were carried out on both the run and the un-run flank. Microhardness profiles on tooth cross sections were obtained with a 300 gm load. The first indentation was taken at a distance of 50 μm from the surface.

2.1.2 Ovako Steel 677

This steel was developed to be air hardened to produce a martensitic structure and high hardness by relatively slow cooling from the austenite field. The chemical composition of the Ovako steel 677 is given in Table 2.4.

The recommended hardening heat treatment is as follow.

(i) Austenitise at temperature 860-880°C with soaking for enough time to homogenise the structure.
(ii) Harden by air-cooling. After reaching room temperature, post quench by rinsing parts in cooled water.
(iii) Temper at 160°C for one hour.

It should be noted that prior to hardening the steel is treated by very slow cooling to be soft enough for gear hobbing operations.
The material was supplied as bars, 190 mm diameter, and as rods with 30 mm in diameter and 40 mm in length.

The austenitization temperature of the Ovako steel is less critical than it is for with other high carbon steels. Austenitization can be achieved over a wider range of temperatures.

The hardenability of high carbon Ovako steel is much greater than most other engineering steels. For instance a section with 30-mm thickness can be air hardened. If

Table (2.4) Chemical composition of Ovako steel 677 (wt %)

C	Si	Mn	Cr	Mo
0.67	1.50	1.45	1.10	0.25

oil quenching is used, sections in excess of 100 mm in thickness can be through hardened. Obviously the cooling rate must be faster than a critical minimum in the temperature range from 900°C to 200°C.

2.2 Metallographic Examination and Hardness Tests

Microstructural observations were made on sectioned specimens mounted in Bakelite using a BUEHLER SIMPLIMET 2000 automatic mounting press. A metallographic finish was obtained using the following procedure. The BUEHLER MOTOPOL 2000 grinder/polisher was used to prepare the specimens. Specimens were first ground using 240 silicon carbide paper for 3 to 6 minutes lubricated with running water. Specimens were then cleaned in an ultrasonic bath for 2 minutes. The polishing stage started with the 9-micron ultra pad cloth and finished using the 3-micron Texmet cloth. Each polishing step was carried out with the appropriate diamond suspension. The final polishing stage was completed with 1-micron Alumina cloth.

A nital etch was used to reveal the microstructure. Specimens were then examined in an OLYMPUS-BX60M optical microscope. A stereo zoom microscope type OLYMPUS SZ-CTV was also used to examine surface features such as surface fatigue test pits and micropits. Micrographs from either microscope were obtained with a JVC camera type KY F55B to a computer loaded with a digital image processor (MARS).

Microindentation hardness measurements were made using a BUHLER hardness tester with a load of 300g. Vickers Macrohardness testing was carried out using a range of loads. A portable hardness tester was also used for parts inaccessible by stationary testing machines.

2.3 Chemical Analysis

Chemical analyses for materials used in this investigation were carried out using LECO Glow Discharge Spectroscopy. Test specimens for the analysis were cut and placed inside a chamber. A selected spot at the specimen surface is excited under controlled voltage current and argon pressure. The excited atoms emit light of a characteristic wavelength when it returns to the ground state. The emitted light separated by wavelength and passed to detectors for accurate measurements. In addition to surface

analysis, depth profile chemical analysis can be obtained by removing material by ion sputtering.

2.4.1 Residual Stress Determination by X-ray Diffraction

X-ray diffraction was used to determine residual stresses and retained austenite. The XSTRESS 3000 X-ray analyser was used for these measurements. The basic geometry of this instrument is illustrated in Fig.2.4(a).

A miniature X-ray tube is used to generate the X-ray beam. In the present work on steel, monochromatic X-rays from a Cr target was used.

X-ray diffraction can be used to measure surface residual stresses in metals by measuring the interplanar distance. In a polycrystalline metal variants of a given crystallographic plane are oriented in all directions within the sample volume. Consider a general crystal plane with Miller indices $\{hkl\}$. When a tensile stress is acting in the longitudinal direction of a rod, the interplanar spacing d_{hkl} of the variants of $\{hkl\}$ that are oriented parallel to the longitudinal axis becomes smaller, while the interplanar distance is increased in the $\{hkl\}$ variants perpendicular to the stress. Thus the crystallographic planes are used as a sort of strain gauge in the X-ray diffraction method.

The interplanar spacing is measured in X-ray diffraction using the Bragg diffraction law. This relates the critical Bragg θ angle to d_{hkl} and the wavelength of the radiation λ by the well-known equation

$$\lambda = 2d_{hkl} \sin\theta \,. \qquad (2.1)$$

Since λ is constant, any change in the value of d_{hkl} can be measured by measuring the change in θ. The parameter varied is the angle of inclination of the main beam (and the detectors) to the specimen surface ψ Fig.2.4 (b). This is called the angle of rotation. The main beam is rotated to predetermined angles between –45 and +45 degrees. At each position, the solid-state detectors record the diffracted beam intensity over the

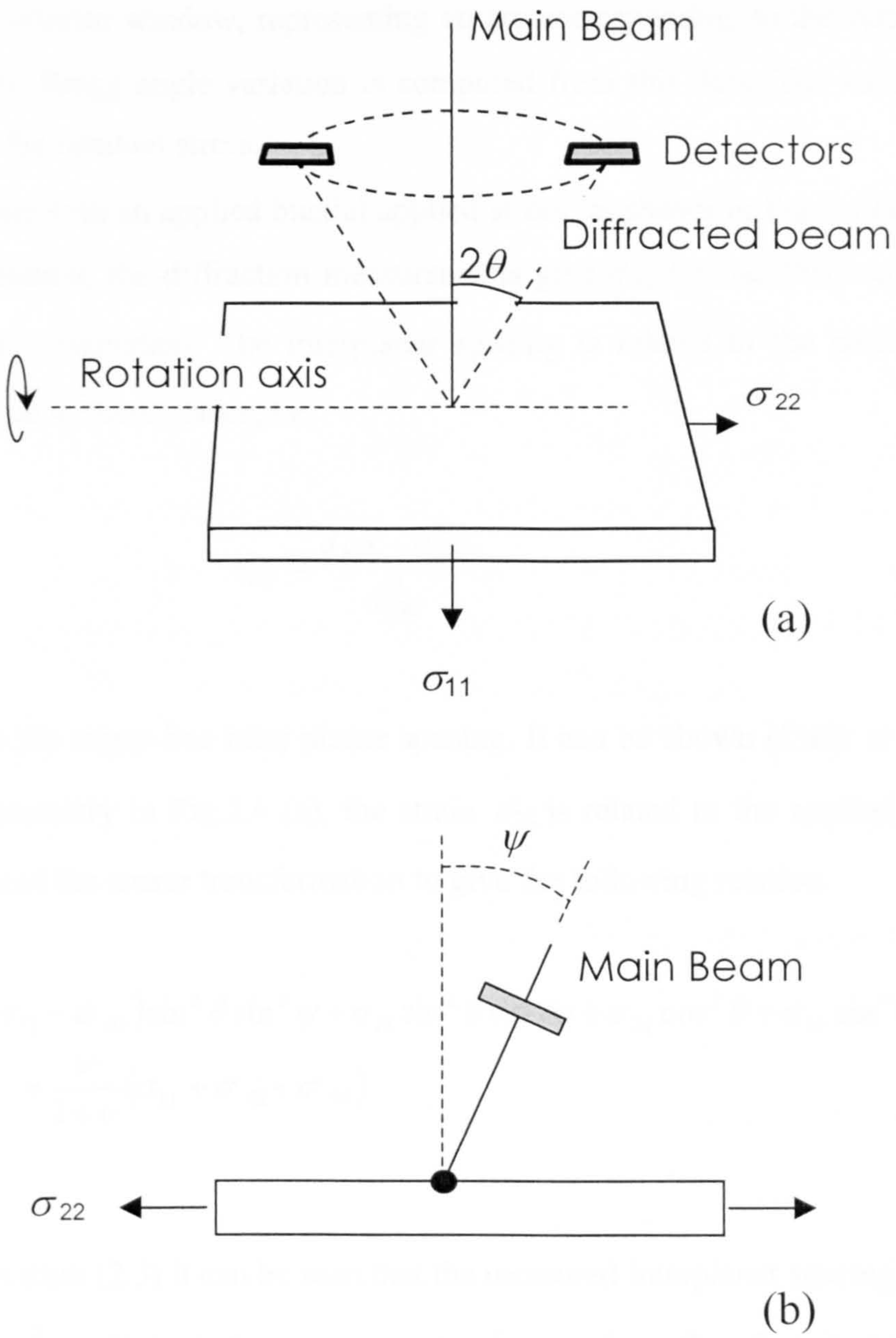

Fig. 2.4 (a). Basic geometry of the x-ray analyser. (b).Angle of inclination of the main beam relative to the test specimen.

length of the detector window, representing an arc corresponding to the variable θ. In due course, the Bragg angle variation is computed from this data. The variation of θ with ψ gives the residual stress.

Consider a plate with an applied biaxial applied stress, as shown in Fig.2.4 (a). At each angle of inclination, the diffraction measurements give d_{hkl} for the $\{hkl\}$variants with the appropriate orientation. The interplanar spacing is related to the strain e'_{33} in a direction normal to these planes, i.e.

$$e'_{33} = \frac{d_{kkl} - d^0_{hkl}}{d^0_{hkl}}, \tag{2.2}$$

Where d^0_{hkl} is the strain-free inter planer spacing. It can be shown (Calik *et al.*, 1996) that for the geometry in Fig.2.4 (a), the strain e'_{33} is related to the applied stress via Hooke's law and the tensor transformation to give the following relation

$$e'_{33} = \frac{1+\nu}{E}\left[\begin{array}{l}(\sigma_{11} - \sigma_{33})\sin^2\theta\sin^2\psi + \sigma_{13}\sin^2\theta\sin 2\psi + \sigma_{22}\cos^2\theta + \sigma_{33}\sin^2\theta \\ \quad + \dfrac{\nu}{1+\nu}(\sigma_{11} + \sigma_{22} + \sigma_{33})\end{array}\right] \tag{2.3}$$

Thus from equation (2.3) it can be seen that the measured interplanar spacing is a linear function of $\sin^2\psi$. Note that σ_{33} is zero at a free surface, therefore it must be very small in the surface layers. In most cases σ_{13} is zero (Calik *et al.*, 1996). Thus, a plot of d_{hkl} versus $\sin^2\psi$ should give a straight line that is the same for positive and negative rotations. Further, the slope of the line is directly proportional to the stress component σ_{11}. Note that if a stress component σ_{13} did exist it would show up in non linearity in the d_{hkl} vs. $\sin^2\psi$ plot and also in the non-coincident of the $0 \langle \Psi$ and $0 \rangle \Psi$ rotations. However, non-linearity can also occur through miss-alignment of the instrument. Special procedures are used to check for miss-alignments and rotation centre, involving measurements taken on stress free metal powders. The other stress

component σ_{22} can be obtained by repeating the determination with the specimen rotated through 90 deg.

The above operations and measurements are all carried out under computer control in the XSTRESS 3000. One residual stress determination gives an average value for a layer about 5 μm deep. Residual stress profiles were obtained by chemically etching masked areas of the specimen surface to remove layers in a controlled fashion. Of course, layer removal disturbs the residual stresses that are present. However, the proportion of the total section removed was small in the present work and it can be shown that the effect on the residual stress is minimal. Residual stress determinations in martensite were made using diffraction from the {211} planes. Residual stresses in the austenite phase were made using diffraction from the {220} planes.

2.4.2 Measurement of Retained Austenite Content

Hardened steels usually contain some retained austenite. Retained austenite is a soft phase and affects the mechanical properties and performance of the steel. Determination of retained austenite content by using X-ray diffraction is more precise than metallographic estimation especially when the amount of retained austenite is low.

The quantitative analysis by X-ray diffraction of phases in steel is based on the relative integrated intensities of the present phases in the mixture which reflects the concentration of each phase in the steel. The diffracted intensity per unit length of diffraction line I is given by

$$I = \frac{KR}{2\mu} \tag{2.4}$$

Where μ is the linear absorption coefficient and K and R are crystallographic factors.

If c_γ and c_α are the concentrations of the austenite and the martensite phases in the mixture, then

$$I_\gamma = \frac{KR_\gamma c_\gamma}{2\mu_m}, \tag{2.5}$$

And

$$I_\alpha = \frac{KR_\alpha c_\alpha}{2\mu_m} \tag{2.6}$$

The relative intensities are

$$\frac{I_\gamma}{I_\alpha} = \frac{R_\gamma c_\gamma}{R_\alpha c_\alpha} \tag{2.7}$$

Calculation of R_γ and R_α (by knowledge of crystal structures and lattice parameters of both phases) enable the relative concentration to be found. If the steel contains only austenite and martensite phases, then since $c_\gamma + c_\alpha = 1$, the value of c_γ can be found. (Cullity, 1978).

Measurements of retained austenite by the XSTRESS 3000 was made by comparing integrated intensities for two diffraction lines from each phase (austenite and martensite) using the Cr K_α radiation. Table 2.5 shows the 2θ values for the selected diffraction plane and the corresponding calculated R values. The retained austenite content is taken as the average of the four compared values between the ferrite and the austenite intensities.

2.5 Mechanical Testing

2.5.1 Plane Strain Fracture Toughness Testing (K_{Ic})

Since the Ovako steel is a new formulation, it was decided to characterise its fracture toughness as a function of heat treatment.

Fracture toughness (K_{Ic}) values were estimated using the chevron notch specimen test. This method of testing (Shih, 1981) was developed for measuring toughness of brittle materials. It is assumed that crack growth resistance curves for the test material are flat, (i.e. the fracture energy remains constant with crack length during crack extension) as

Table (2.5) Diffraction planes in ferrite and austenite phases

Phase	*hkl*	2θ	*R*
Ferrite (martensite)	200	106.1	20.73
	211	156.4	190.8
Austenite	200	79.0	34.78
	220	128.3	47.88

is usually the case for lower toughness metals. Cracking initiates at the apex of the chevron and continues under an increasing load because the effective width of the crack increases as the crack grows into the chevron. The point at which the effect of the increasing crack width is off-set by the increasing crack length can be calculated. At this point the applied load achieves a maximum value P_{max} and the fracture toughness can be computed from this value of load and knowledge of the specimen geometry.

Specimens for this test were machined from 190-mm diameter bar. The positions where the specimens were cut is shown in Fig.2.5 where it can be seen that the core material with a diameter of 70 mm was avoided because of possible segregation in the core. It also shows that the chevron notches in all specimens were machined perpendicular to the longitudinal rod axis. The specimen dimensions are shown in Fig.2.6. Specimens were austenitized and air cooled to harden the material. Ten specimens were then tempered at 160, 200, 300, 400 and 500°C respectively for one hour. Two replicate specimens were treated at each tempering temperature. A further two specimens were also tested for fracture toughness in the hardened condition (without tempering).

Specimens were tested in three point bending. Specimens were placed in the loading rig with the notch facing down. The load was applied manually in the testing machine. The K_{Ic} value was then calculated from the maximum load P_{max} using to the following formula.

$$K_{Ic} = \frac{P_{max}}{BW^{1/2}} Y_{min} \qquad (2.8)$$

Where

$$Y_{min} = 5.63 + 27.44(a_o/W) + 18.93(a_o/W)^2 - 43.42(a_o/W)^3 + 338.9(a_o/W)^4$$

Here, a_o and W are indicated in Fig.2.6 and B is the thickness. The relevant dimensions of the specimen are $a_o = 4$ mm, $W = 12.5$ mm and $B = 8.3$ mm. Because the span distance in the testing rig was 51 mm instead of 50 mm as specified in the

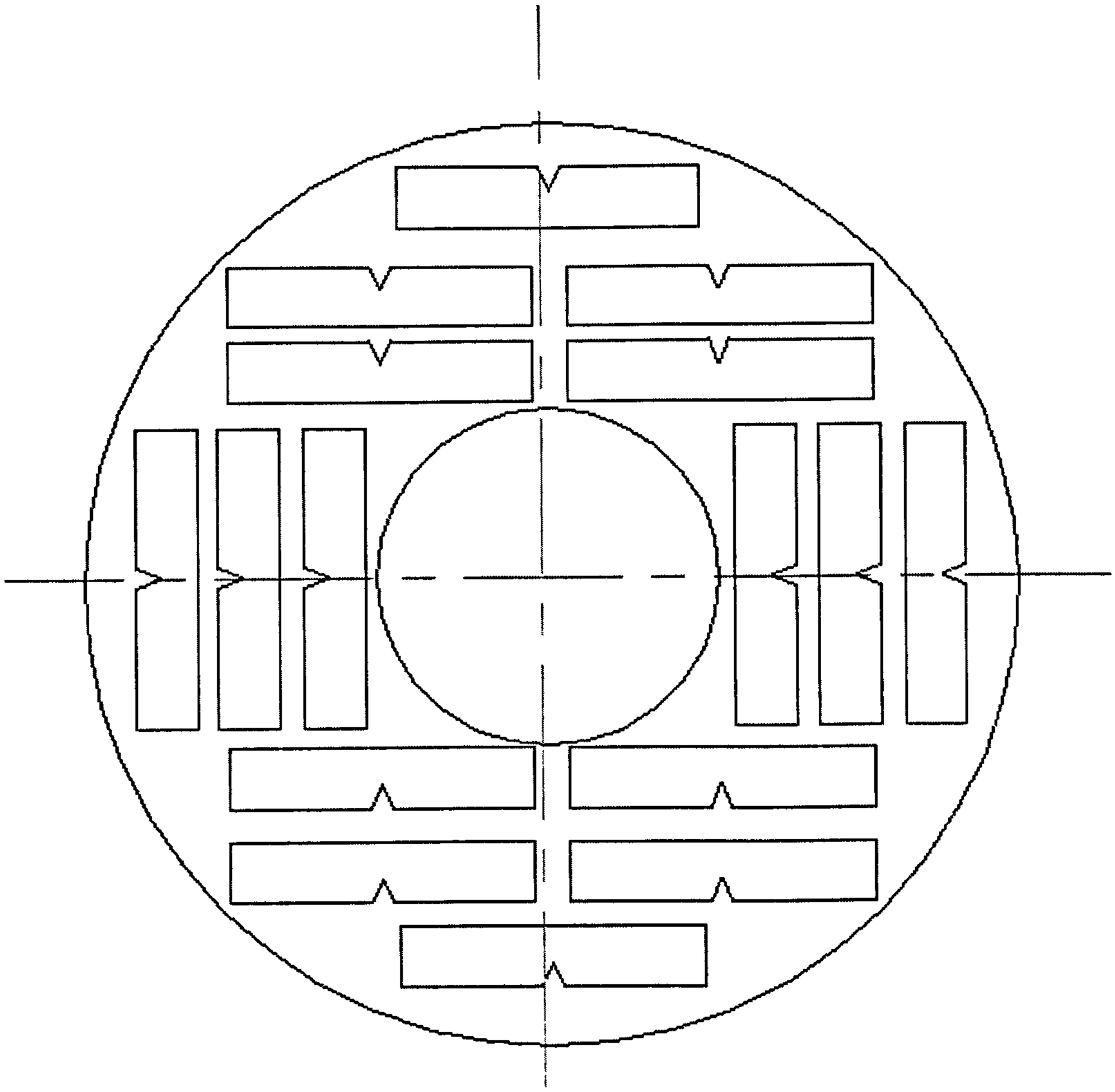

Fig. 2.5 Orientations and positions where the fracture toughness test specimens were cut from the bar

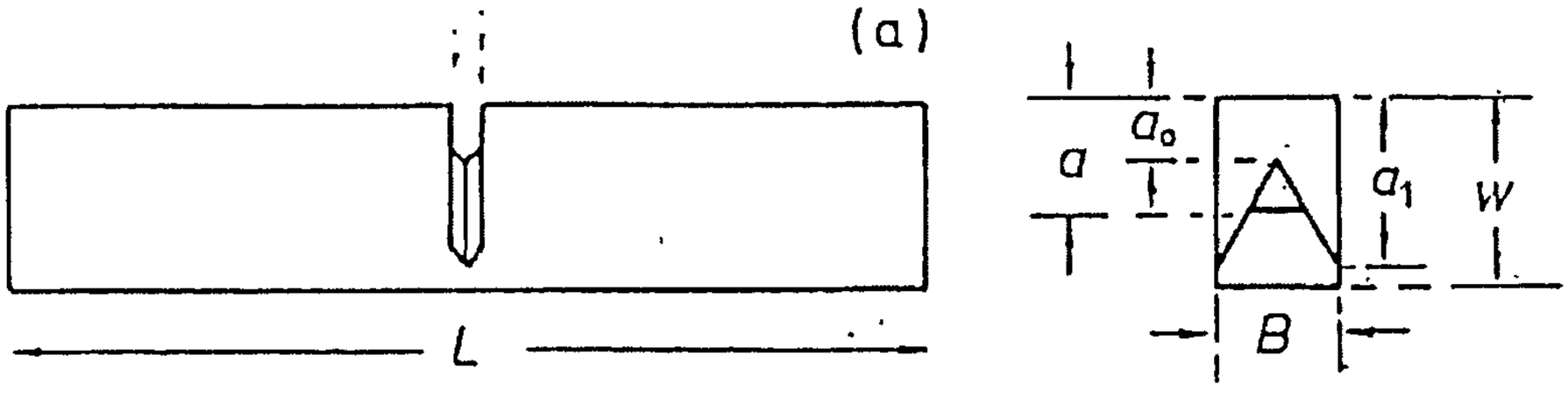

Fig.2.6 Cheveron notch specimen with dimensions in mm
$a_0 = 4,\ a_1 = 11.2,\ w = 12.5,\ B = 8.3,\ L = 62$

original test procedure a correction factor of 1.02 was used to allow for the increased moment.

2.5.2 Compression Test

Compression tests were carried out in order to evaluate stress-strain relation for Ovako steel. The results were used in the Finite Element analysis of indentation in the standing contact fatigue analyses.

Three solid cylindrical specimens from the Ovako steel stock were machined for the compression test. The specimens were 21mm long and 7 mm in diameter .The specimens were hardened and tempered at 160°C for one hour. The surface of the specimens were polished and cleaned. Hardness measurements on specimen's ends showed that the hardness was in the range of 735 to 745 Hv for each of the three specimens another set of specimens with dimensions 12 mm long and 6 mm in diameter were also treated and tested in the same procedure.

In order to measure the axial strain in compression; strain gages of type CEA-06-240UZ-120 were bonded to the specimens with the grid parallel to the axis of the specimens. A dummy strain gage on a specimen made from the same material was used as a comparior and connected to a half bridge circuit.

To carry out the test a compression test rig was used. The test rig is a steel box where the specimen can align vertically. Two hardened and un-tempered Ovako steel plates were put on both specimen ends to prevent damaging the platens. The applied load was increased in steps of 250 kg. At each load increment the corresponding measurement of strain was recorded. Engineering stress was calculated from load to plot the engineering stress-strain curve.

2.5.3 Standing Contact Fatigue Test

Standing contact fatigue tests were carried out on hardened and tempered through-hardened (Ovako) steel specimens. In this test a hardened steel ball was repeatedly

pressed against a test specimen. The test was developed by Alfredsson and Olsson (1999) to simulate on a large scale what might occur on a micro scale at contacting asperities. Although the relevance of the standing contact fatigue test to surface contact fatigue is open to question, it was felt to be of sufficient interest to explore the test in this research project. Fatigue crack initiation and growth is particularly difficult to study by conventional means in hard steels of the type used for high performance gears. The low level of fracture toughness ($K_{1c} \approx 20MNm^{-3/2}$) means that there is only a small window of load range available in which fatigue crack growth may be observed. The standing contact fatigue test allows the possibility of observing stable fatigue crack growth because the cracks produced grow in to a sharply reducing stress field.

To perform the test a specially designed jig was manufactured. The jig as shown in Fig.2.7 comprises two circular steel plates at the bottom and the top of the jig. The bottom plate was the specimen holder. The centre of the top plate holds a removable steel cone which housed the indenter ball at its end and faces the test specimen. Four steel rod pillars connected the lower and the upper plates. These pillars were connected to the lower plate and pass through four copper bush lined holes perforated in the upper plate. This arrangement secures the vertical alignment movement of the indenter ball against the stationary test specimen. On the top of the cone a steel ball with 22-mm diameter was placed to transfer the applied load from the fatigue-testing machine to the test specimen through the indentation ball.

Specimens used for this test were 30 mm in diameter and 100 mm thick. The indenter ball was hardened Cr bearing steel with 5-mm diameter and the hardness of which is about 850 Hv.

A servohydrolic testing machine was used to carry out the contact fatigue test. Testing parameters such as load and number of cycles were computer controlled. The maximum loads were 2, 4, 6, 8, 10 and 12 kN. In these tests the load ratio (P_{max}/P_{min}) was kept equal to 0.1 through all the range of the testing load, for example when the maximum compression load was 10 KN the minimum compression load was 1 KN.

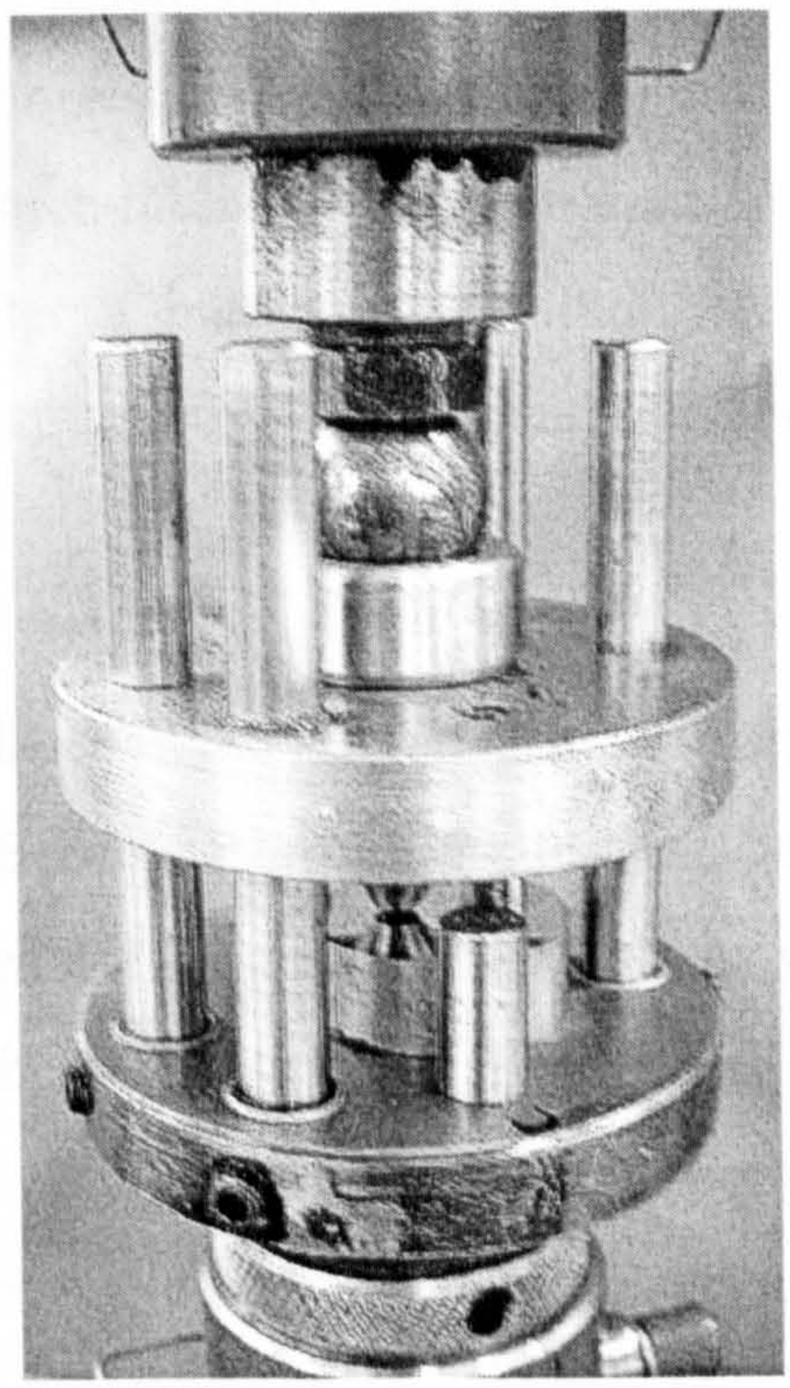

Fig 2.7 The test rig for standing contact fatigue

The test specimens were cut to the required thickness and then one side was ground and polished. Fatigue cracks are much more visible on a polished surface. The specimen then placed in the jig to be tested for a predetermined number of cycles. Testing parameters were selected which includes the mean load, load amplitude, frequency and the number of cycles. After a predetermined number of cycles, specimens were examined under the optical microscope. The indentation and any cracks that might have formed were photographed.

The specimen was then replaced in the jig to be tested in another position for a different load or number of cycles. Before restarting the test the ball was rotated or changed if any deformation was noticed. At least five different tests were conducted before using another test specimen. In the early stages of testing with the standing contact fatigue test, attempts were made to remove the specimens for periodic examination throughout the test. However it was found to be very difficult to replace the ball indenter at exactly the previous position after an examination. For this reason, the above procedure was adopted.

CHAPTER 3

Results

In this chapter the results of experiments on two steels are presented. The case carburised gear steel 17CrNiMo6 contains an abnormally high level of retained austenite. Material damage and characterisation in gears run in back-to-back tests was undertaken in specimens taken from these gear specimens. The second steel examined was a recently developed through hardening steel (Ovako 677). In this case, a more basic characterisation of the material was carried out. In addition, because the Ovako 677 is through-hardening and homogeneous in relatively large sections it is ideal for some investigations that can not easily be carried out on case carburised material. This includes the standing contact fatigue tests and experiments on the characteristics of the martensitic transformation in retained austenite.

3.1 Steel with High Retained Austenite (17CrNiMo6)

3.1.1 Effect of Retained Austenite on Contact Fatigue

Carburized helical gears Fig.3.1 made with 17CrNiMo6 steel were tested for surface contact fatigue. The gears were tested as part of a large programme sponsored by the British Gear Association. During the testing programme it was found that a whole batch of 17CrNiMo6 gears had been incorrectly heat treated with the consequence that the carburized case contained much more retained austenite than the 15% that was specified for the heat treated material. Retained austenite is softer than tempered martensite and therefore the gears containing the high level of retained austenite might be expected to be inferior in surface contact fatigue. The opportunity was taken to investigate the performance and microstructure of these specimens. The gears, tested by contact on one flank on each tooth in a back-to-back test, showed good pitting resistance, with fatigue strength greater than 1380 MPa. The SN curve in Fig.3.2 shows contact fatigue strength for steel with high and normal retained austenite contents. Spur gears made with the same steel and contain similar amount of retained austenite also showed good bending fatigue resistance with bending fatigue strength greater than 650

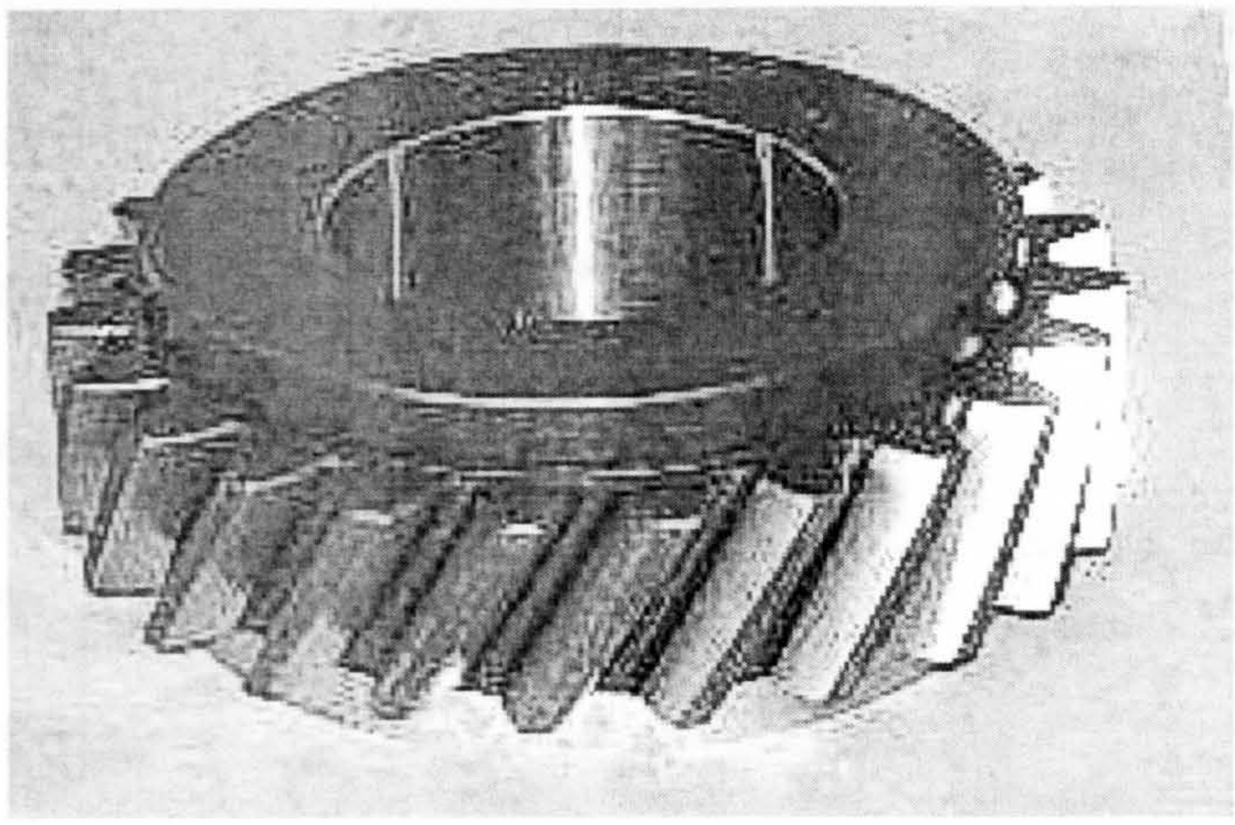

Fig.3.1 Helical gear used in back-to-back tests

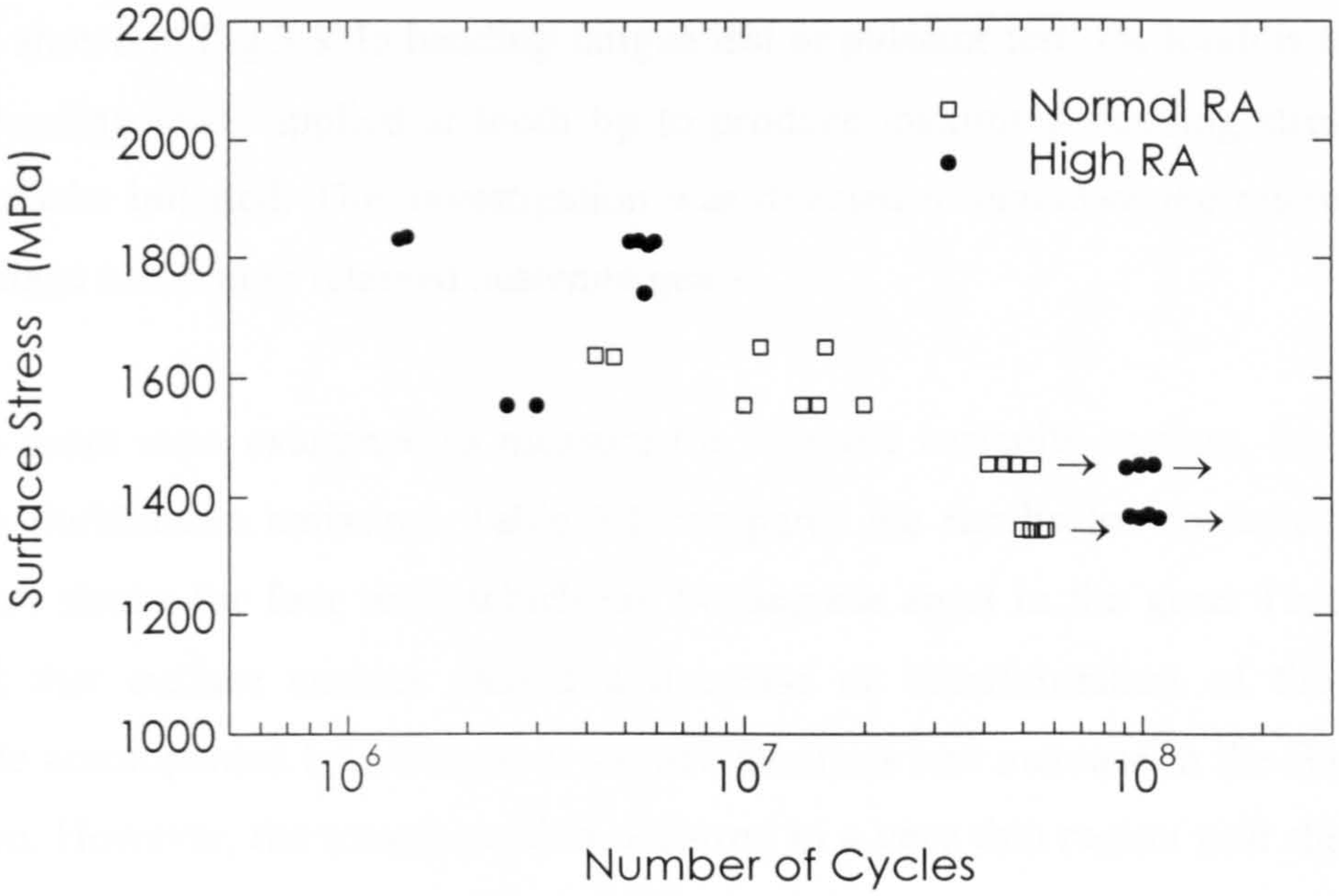

Fig.3.2 Surface contact fatigue in 17CrNiMo6 helical gears showing the effect of retained austenite (RA) content. The contact stress is the peak Hertzian pressure in the contacting flanks. The normal level of retained austenite is 15%. The retained austenite level in the high retained austenite gears varied from 40 to 60%. The arrows indicate run out.

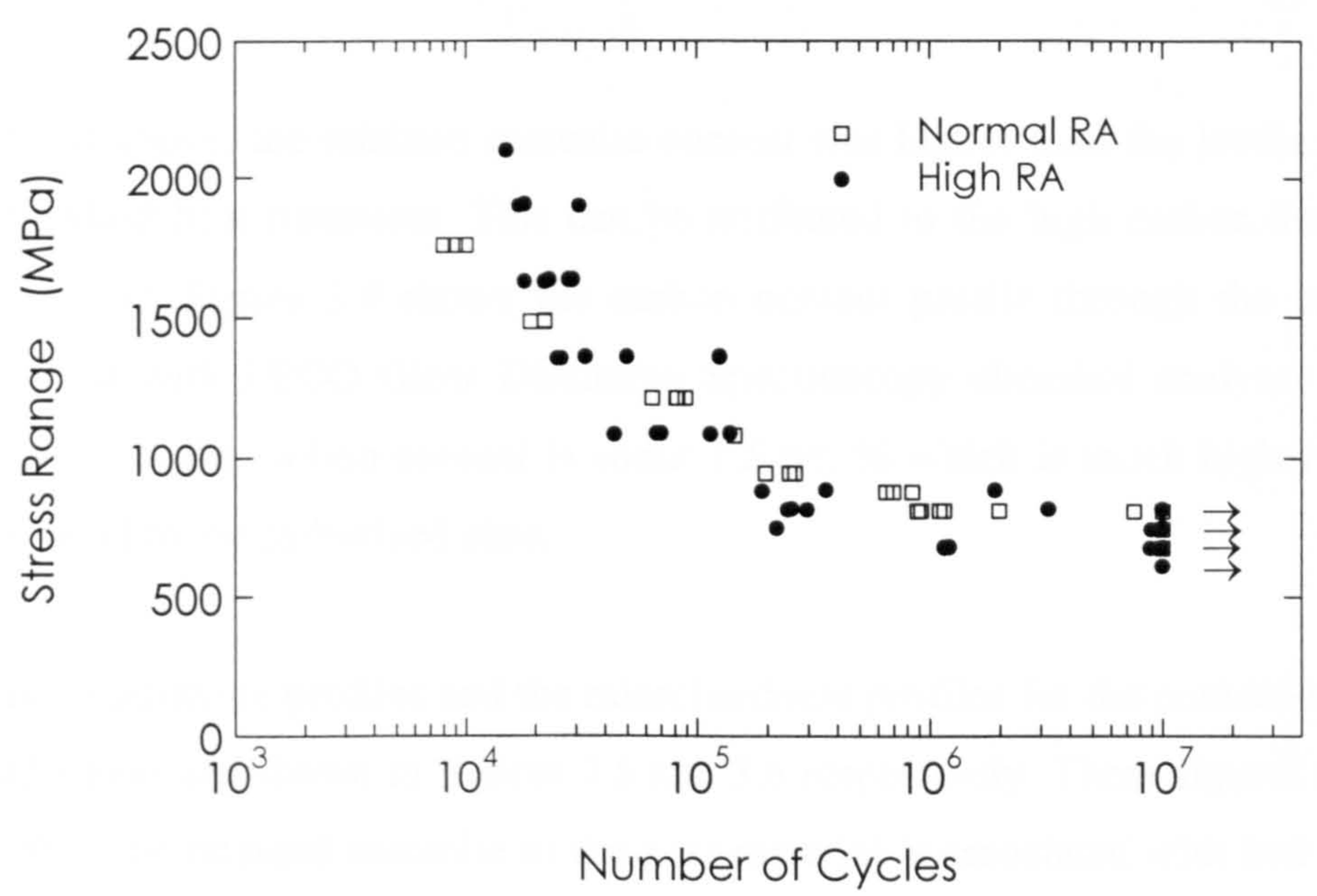

Fig.3.3 Bending fatigue in 17CrNiMo6 spur gears showing the effect of retained austenite (RA) content. Bending loads applied at tooth tip. Maximum bending stress act at the root where cracks initiate under cycle loading. The normal level of retained austenite is 15%. The retained austenite level in the high retained austenite gears varied from 40 to 60%. The arrows indicate run out.

MPa as shown in Fig.3.3. In bending fatigue test or pulsator test one tooth is tested at a time. Bending loads applied at tooth tip to produce maximum bending stress at root where cracks initiated. This investigation was directed to elucidate the microstructure and damage in the high retained austenite gears.

Sample gears were examined to measure the retained austenite content, the hardness and the Barkhausen emission. Table 3.1 compares the results for contacted and un-contacted flanks for four teeth which are 90 degrees apart in the gear. These results showed that surface contact caused a decrease or transformation of the retained austenite accompanied by increase in surface hardness and increase in the Barkhausen emission. However, the transformation occurred in a very thin region near the surface, in the region that may be affected by asperity contact.

For detailed examinations and to carry out profile measurements, teeth were cut from a gear. Retained austenite and residual stress profiles were made for contacted and un-contacted flanks. Microhardness profiles and metallographic examinations were made on a cross sectioned tooth.

As indicated above, the retained austenite content was higher than the levels specified in this standard heat treatment. This can be attributed to the high carbon level in the carburised case. Figure 3.4 shows the carbon content profile through the carburised case obtained with LECO Glow Discharge Spectroscopy chemical analyser where it can be seen that the carbon content is about 1.5 wt. % which is much higher than the specified level in the carburised case.

The retained austenite profiles and the microhardness profiles for the contacted and un-contacted flanks are shown in figures 3.5 and 3.6 respectively. These figures show the high level of the retained austenite in the gear material is associated with low hardness values at a depth down to 0.8 mm below the surface.

The retained austenite profile in a contacted flank is shown in Fig.3.5. The level of the retained austenite was substantially decreased at and near to the surface compared with the un-contacted flank. The change from 60% in the un-contacted flank to 34% in the contacted flank was limited to a shallow depth less than 20 μm below the surface.

Table 3.1 Surface characteristics of high austenite content gear comparing the run and un-run flanks.

Tooth	Retained Austenite (%)		Residual Stress* MPa		HV ($kgf\,mm^{-2}$)		Barkhausen Index	
	un-run	run	Un-run	run	Un-run	run	Un-run	run
1	68	41	-500 ± 38	-423± 8	650 ± 20	702± 7	28	30
2	68	45	-456 ± 32	-372 ± 29	600 ± 20	702 ± 7	30	35
3	70	42	-350± 29	-351 ± 38	657 ± 3	665 ± 75	29	32
4	68	36	-464 ± 9	-439 ± 13	677 ± 77	700 ± 25	31	34

* in martensite phase

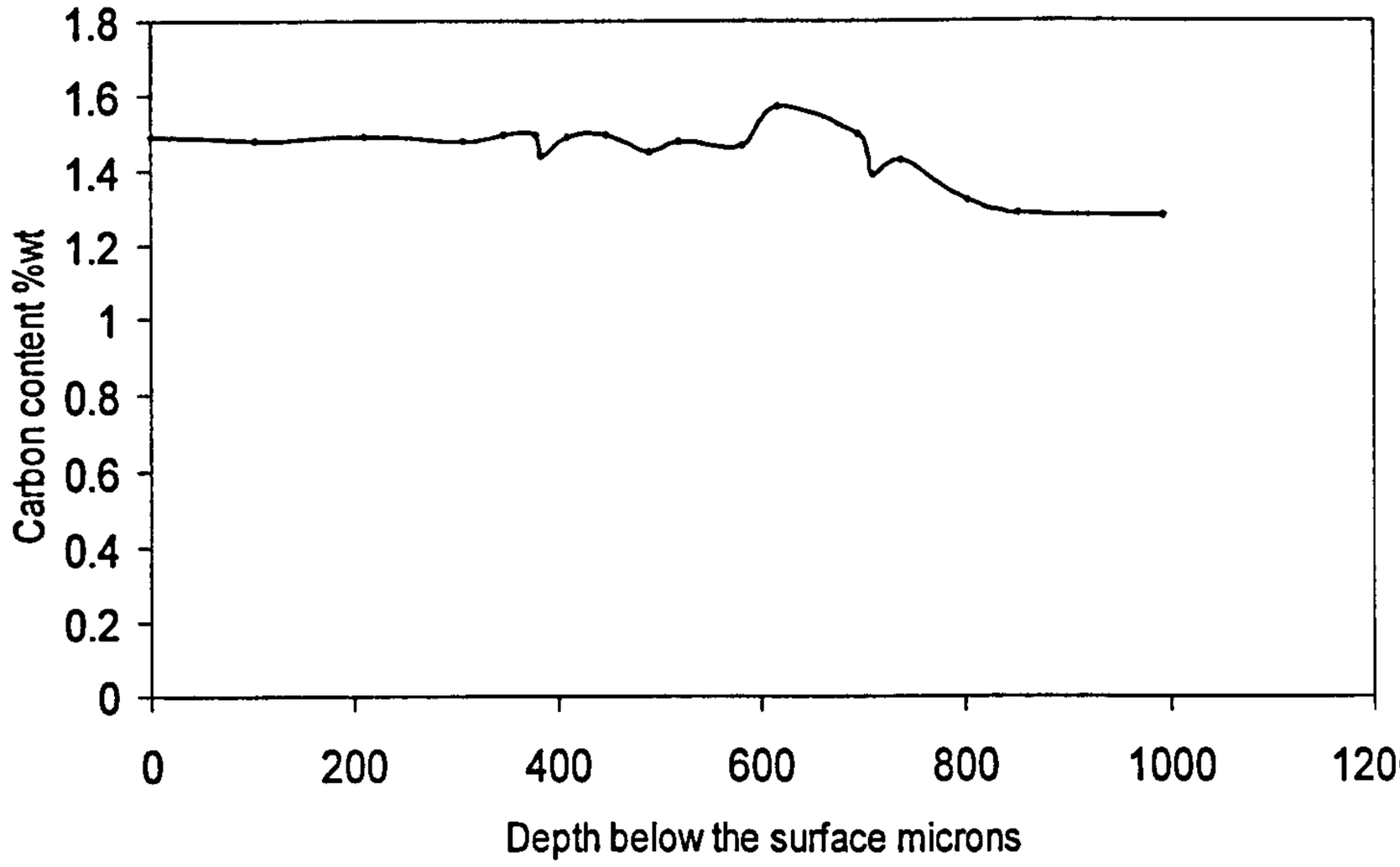

Fig.3.4 shows the carbon content in the carburised case for the helical investigated gears

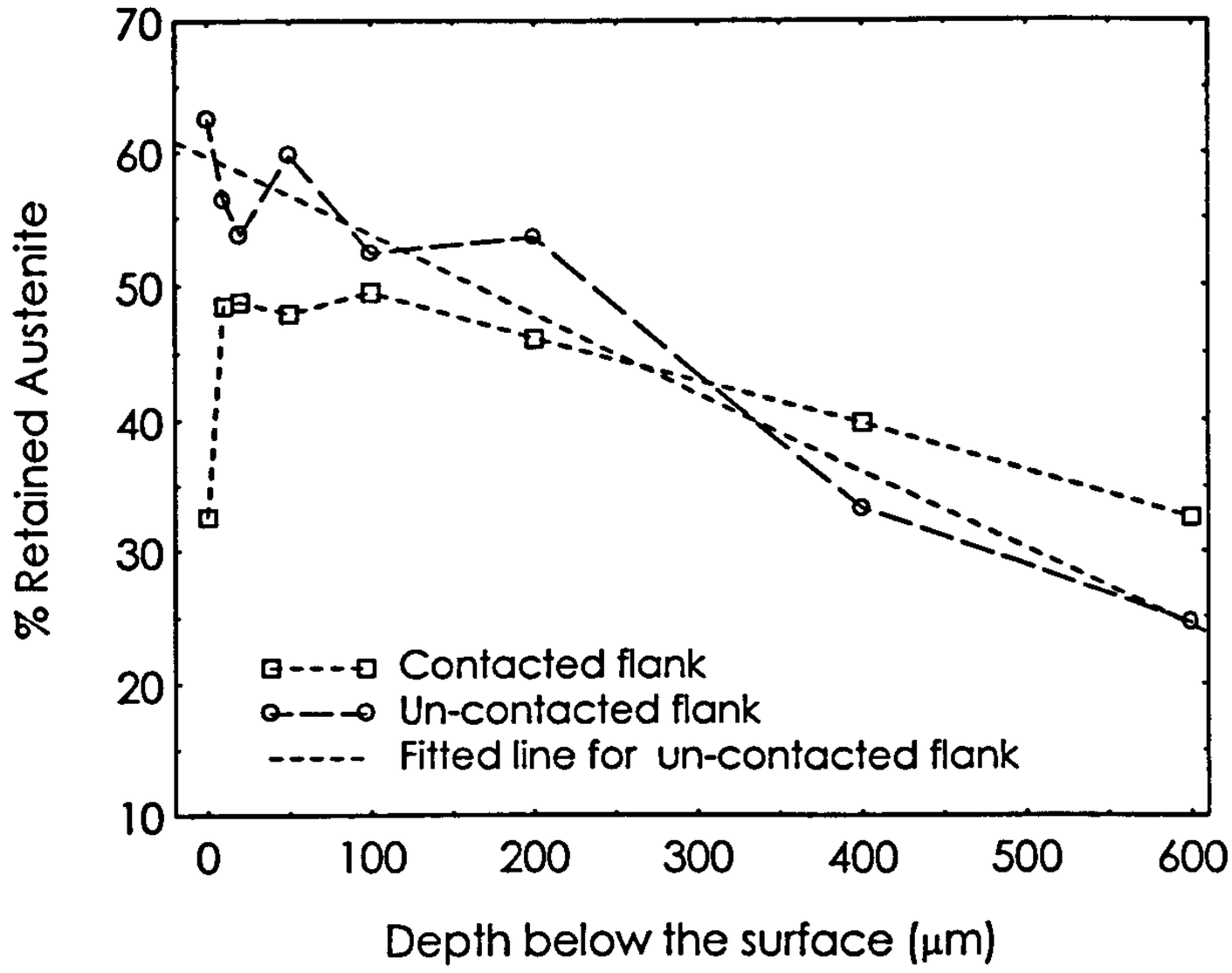

Fig.3.5 Retained austenite in contacted and un-contacted flanks. Substantial transformation occurs at shallow depth beneath the surface due to gear running

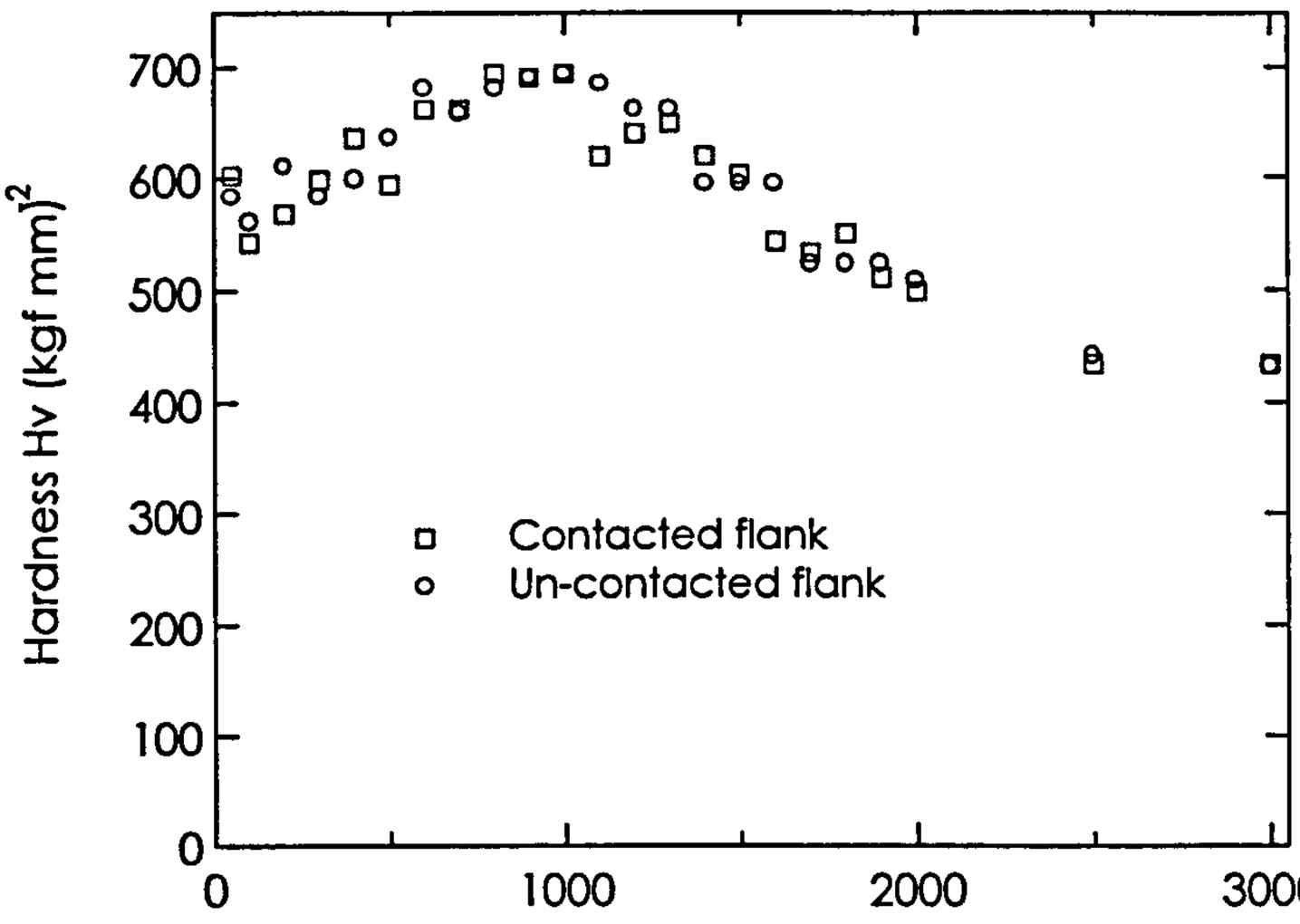

Fig.3.6 Microhardness profiles in contacted and un-contacted flanks. Lower hardness near the surface could be attributed to the high level of retained austenite. Running has no effect on hardness profile. The first hardness measurement was taken at a distance of 50 μm from the surface.

Because of the difficulty of measuring hardness profiles very close to the edge of a section, it was decided to measure surface hardness for a range of applied loads. This has the effect of sampling hardness at different depths below the surface. Because the pyramidal diamond indenter geometry is constant the depth of indentation can be calculated from the measurements of the width of the pyramidal indentation. Further more this method allows hardness to be sampled over a small range of depth below the surface. Figures 3.7 (a and b) shows surface macrohardness measurements versus depth of indentations. The depth of indentation was controlled by adjusting the applied load between 1 and 10 kg. The hardness of the contacted flank was higher than the un-contacted flank. However, when a surface layer of 10 μm was removed by chemical etching the hardness values of the run and un-run flanks were sensibly the same as shown in Fig.3.7 (b). These results suggest that the hardness difference between the contacted and un-contacted flanks is confined to a layer smaller than 10 μm below the surface.

Variations in residual stress at shallow depths were also noted. Figures 3.8 (a and b) compares the residual stress profiles in the martensite phase for the contacted and un-contacted flanks on two orthogonal directions, the longitudinal direction of the tooth (0° direction) which is parallel to the grinding direction and the transverse direction (90° direction) parallel to the direction of rolling and sliding.

Residual stresses in the austenite phase on both flanks and directions are shown in figures 3.8 (c and d). Surface contact appears to produce additional residual compressive stress at the surface that is greater in the 0° direction.

Microstructures near the surfaces on the contacted and un- contacted sides of the same tooth are shown in figures 3.9 (a and b) respectively. The microstructure is typical of material with large austenite grain size and with high retained austenite. Plates of martensite are clearly visible within the austenite matrix. A higher density of martensite plates was evident near the surface of the contacted flank compared with the un-contacted flank. This could be attributed to the stress-assisted or strain assisted martensite transformation that occurred during surface contact.

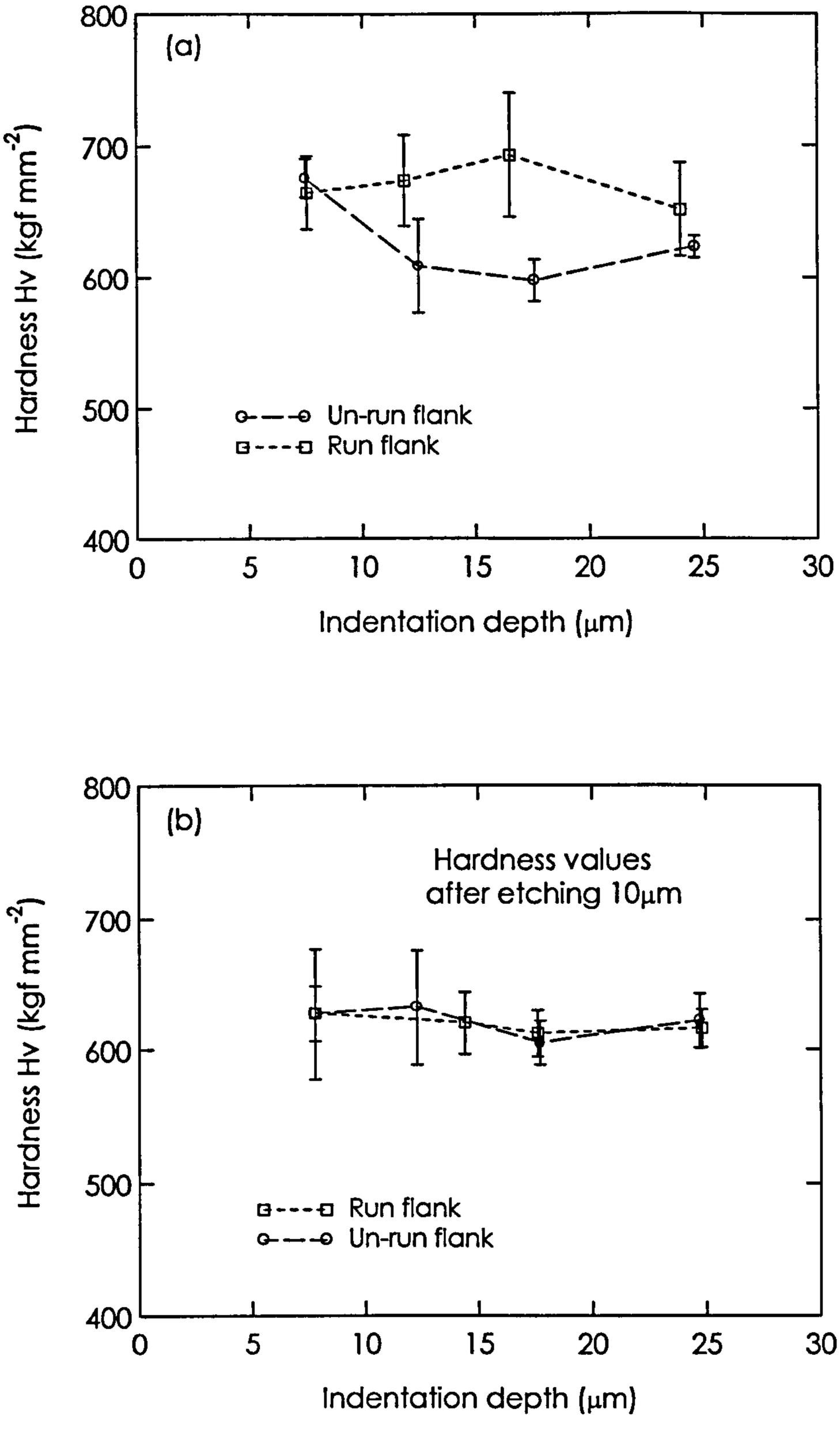

Fig.3.7(a-b) surface hardness as a function of depth of indentation showing the effect on surface layer removal. Indentation depth before layer removal (a) and after chemical etching of 10 μm surface layer(b).

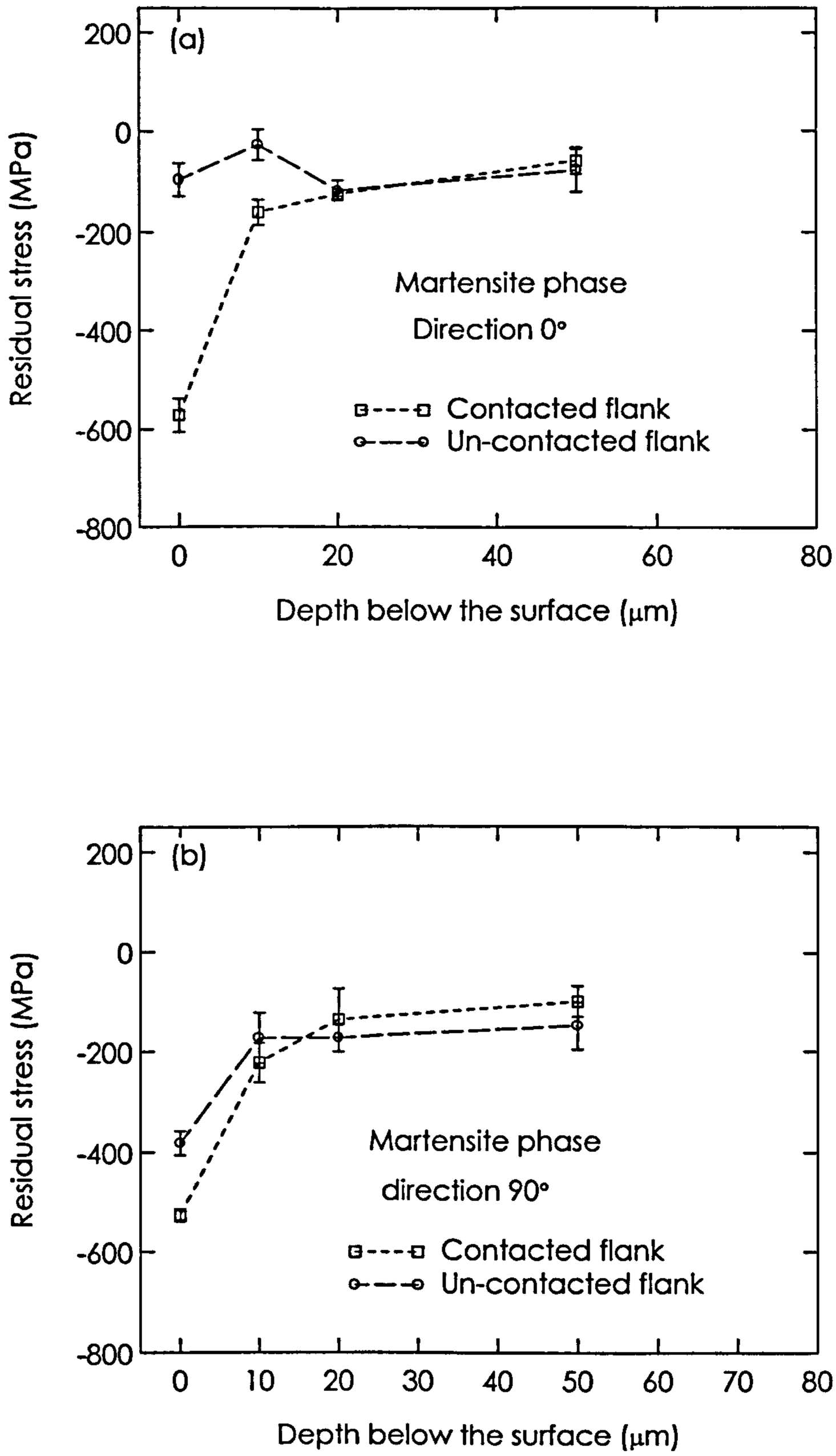

Fig.3.8(a-b) Residual stress distribution in the martensite phase. The 0° direction refers to stress in the transverse direction. The 90° direction refers to stress in the direction along the flank parallel to the direction of motion of the contacting teeth

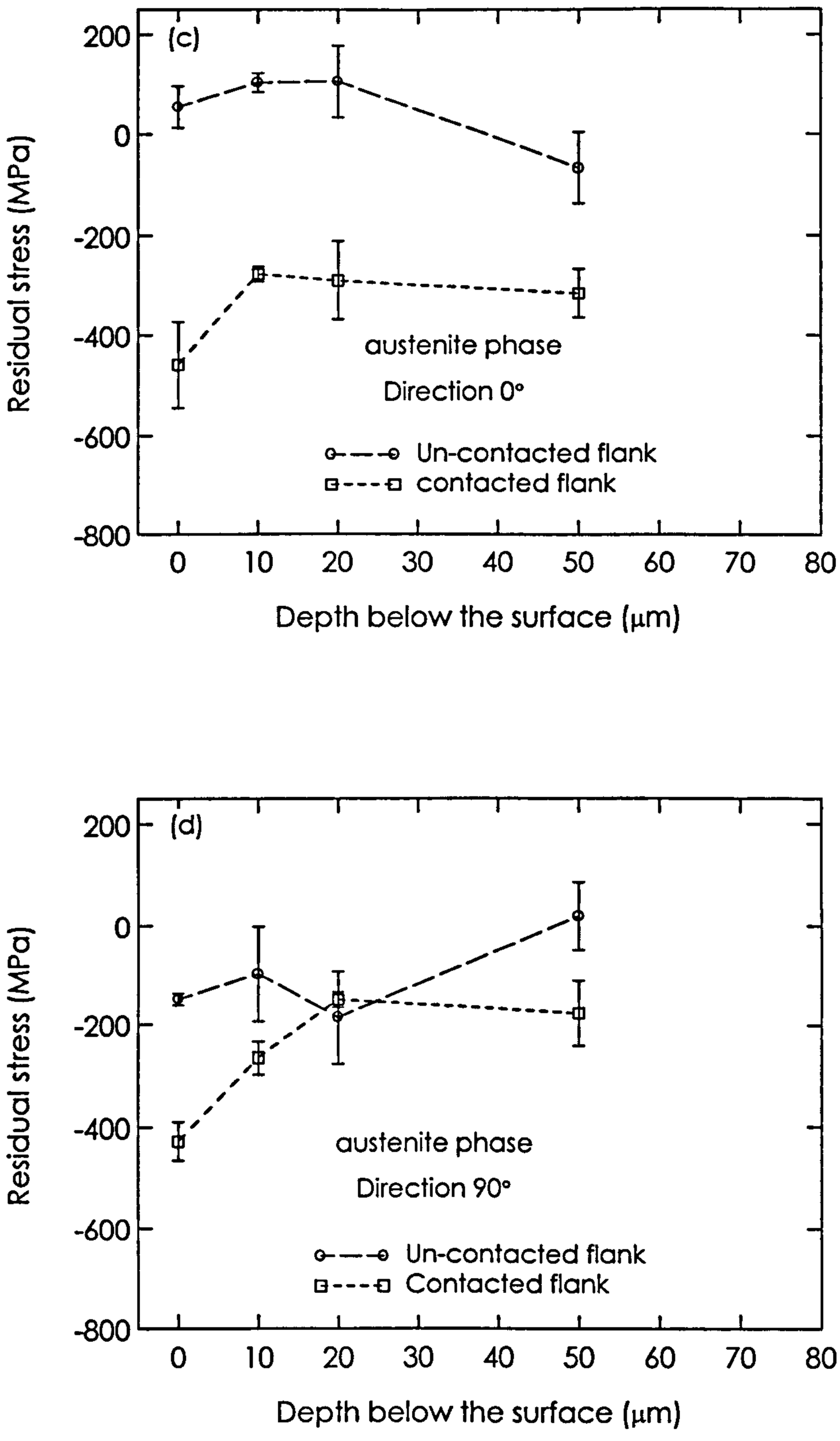

Fig.3.8(c-d) Residual stress distribution in the austenite phase. The 0° direction refers to stress in the transverse direction. The 90° direction refers to stress in the direction along the flank parallel to the direction of motion of the contacting teeth

Retained austenite

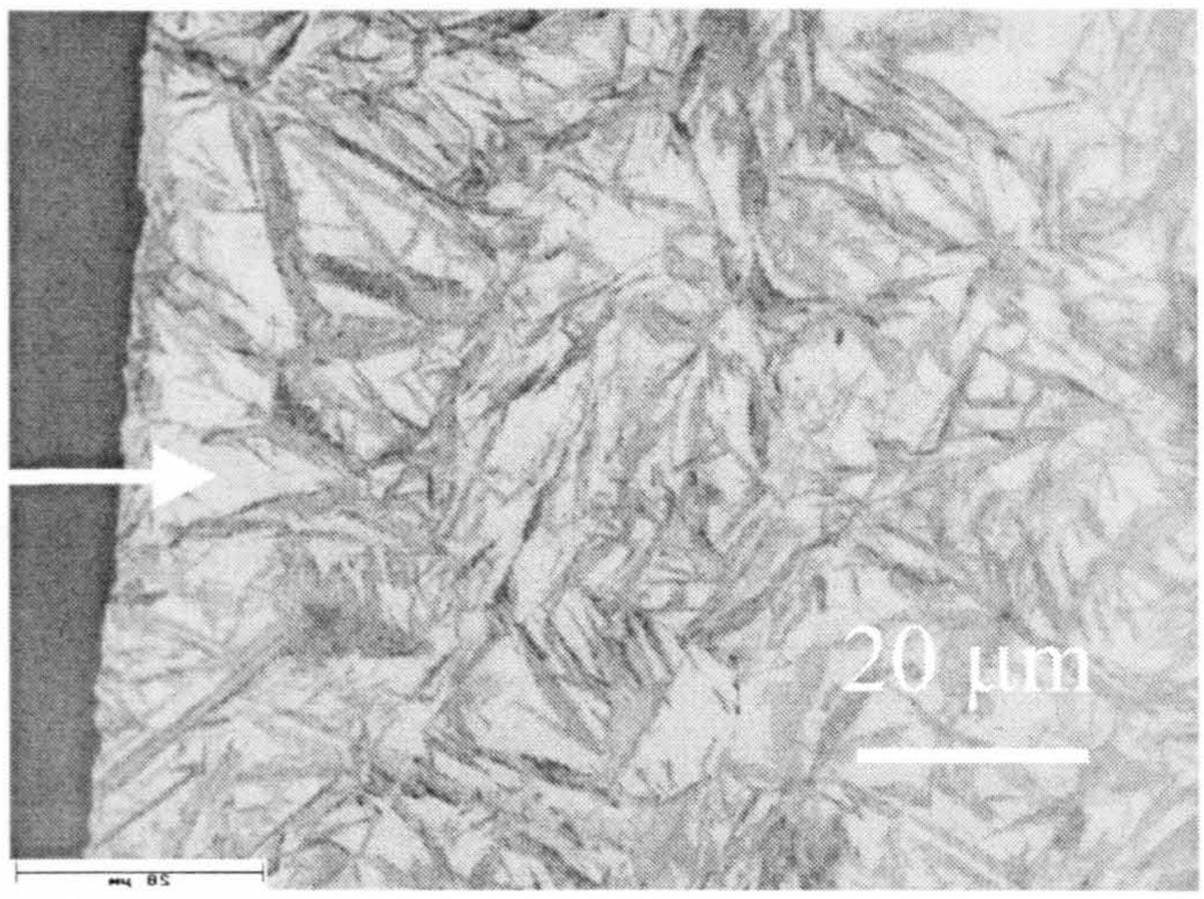

Fig.3.9(a) Microstructure near surface on un-contacted flank

Stress or strain assisted
transformed martensite

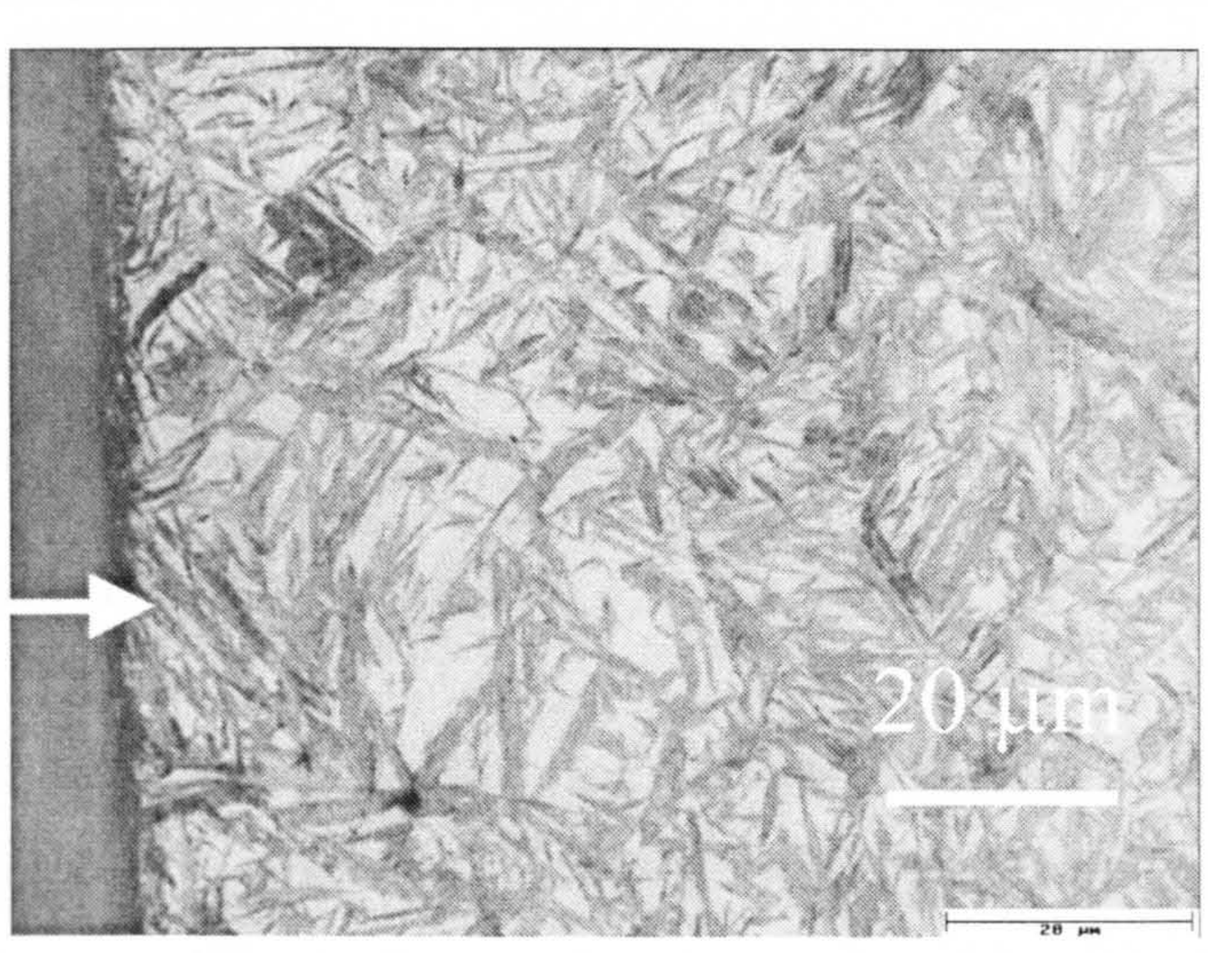

Fig.3.9(b) Microstructure near surface of contacted flank.

Micropitting on the gear teeth surfaces develops when microcracks initiate at the surface and grow at inclined angle to some depth before they change their direction or branched towards the surface to form a micropit. Figures 3.10 (a-c) shows stage in micropitting formation. The micropit can act as a nucleation site for other cracks to form larger pits as shown in figures 3.11 and 3.12. The angle of inclination of microcracks at initiation varies along the flank as shown in Fig 3.13. These data indicate a relation between (acute) angle between microcracks and the surface that is a minimum close to the pitch line. However, there is substantial scatter so the relation is not clear-cut.

The fact that the surface contact fatigue performance of the high retained austenite gears is relatively good figures 3.2 and 3.3 suggest that a strong hardening mechanism operates at the surface during running. The evidence is that strain assisted martensite transformation occurs, sufficient to impart good fatigue resistance. However, the present study shows that transformation is confined to a small depth below the surface of the gear flank. This is consistent with the idea that deformation in asperity contact is most affected by strain-induced transformation. The details of this are discussed in more detail in (Chapter 6).

3.2 Through Hardened Steel Characterisation

3.2.1 Characterisation of the Ovako Steel 677

To reiterate the points made in (Chapter 1), that the Ovako 677 steel is through-hardening steel. High hardness can be achieved without the need for carburizing, yet the material can be supplied in a condition soft enough to be machined by conventional shaping processes. Potential advantages for manufacturing gears, bearings and other machine elements have been outlined in (Chapter 1).

The as-received material was examined for hardness and microstructure. Vickers hardness testing with 20 kg applied load showed a mean hardness number of 270 $kgfmm^{-2}$. The nital etched specimens revealed a fully perlitic structure as shown in Fig. 3.14. Carbon content in the Ovako steel was determined using LECO Glow Discharge

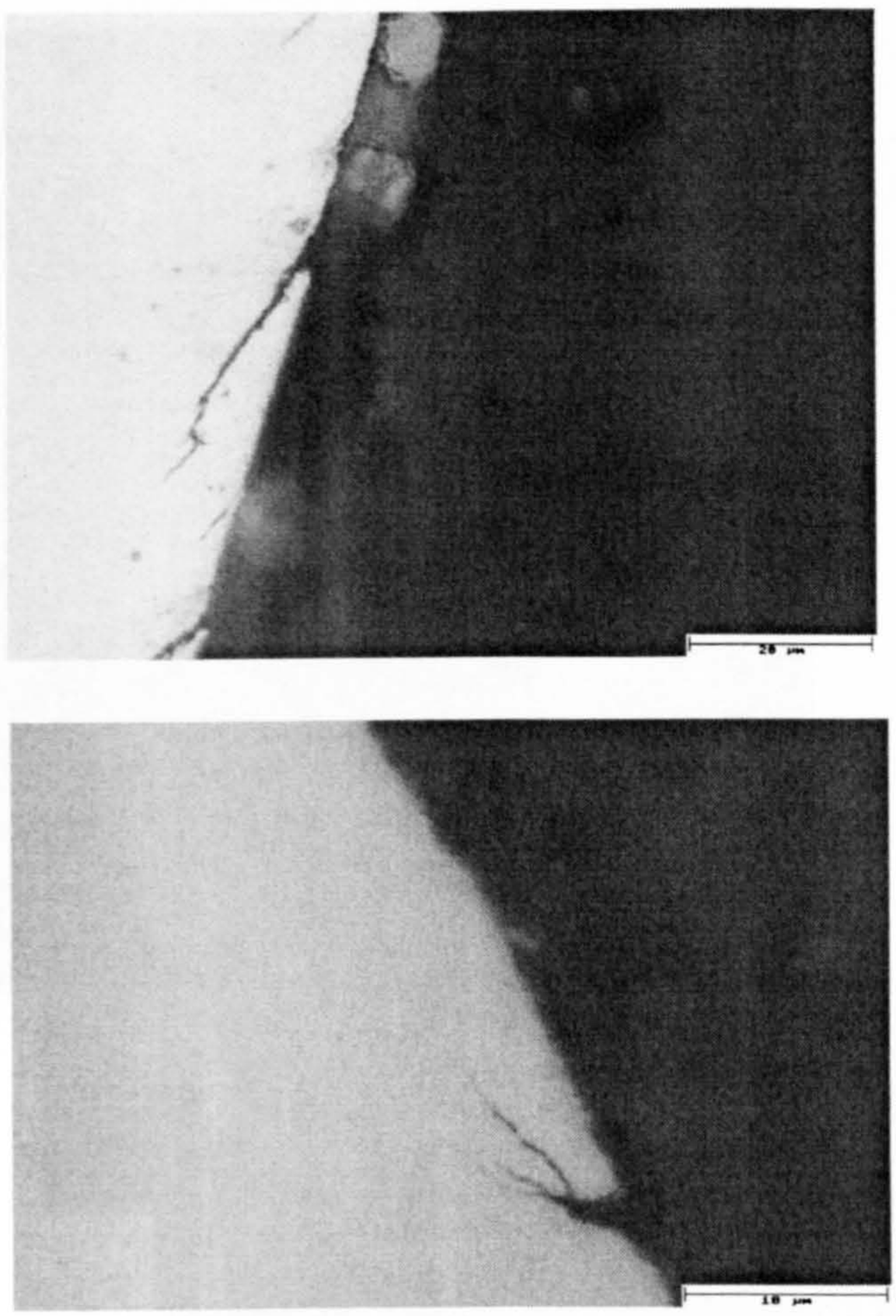

Fig.3.10 (a)to(c) Stages in micropitting formation.
Sections taken through contacted flank

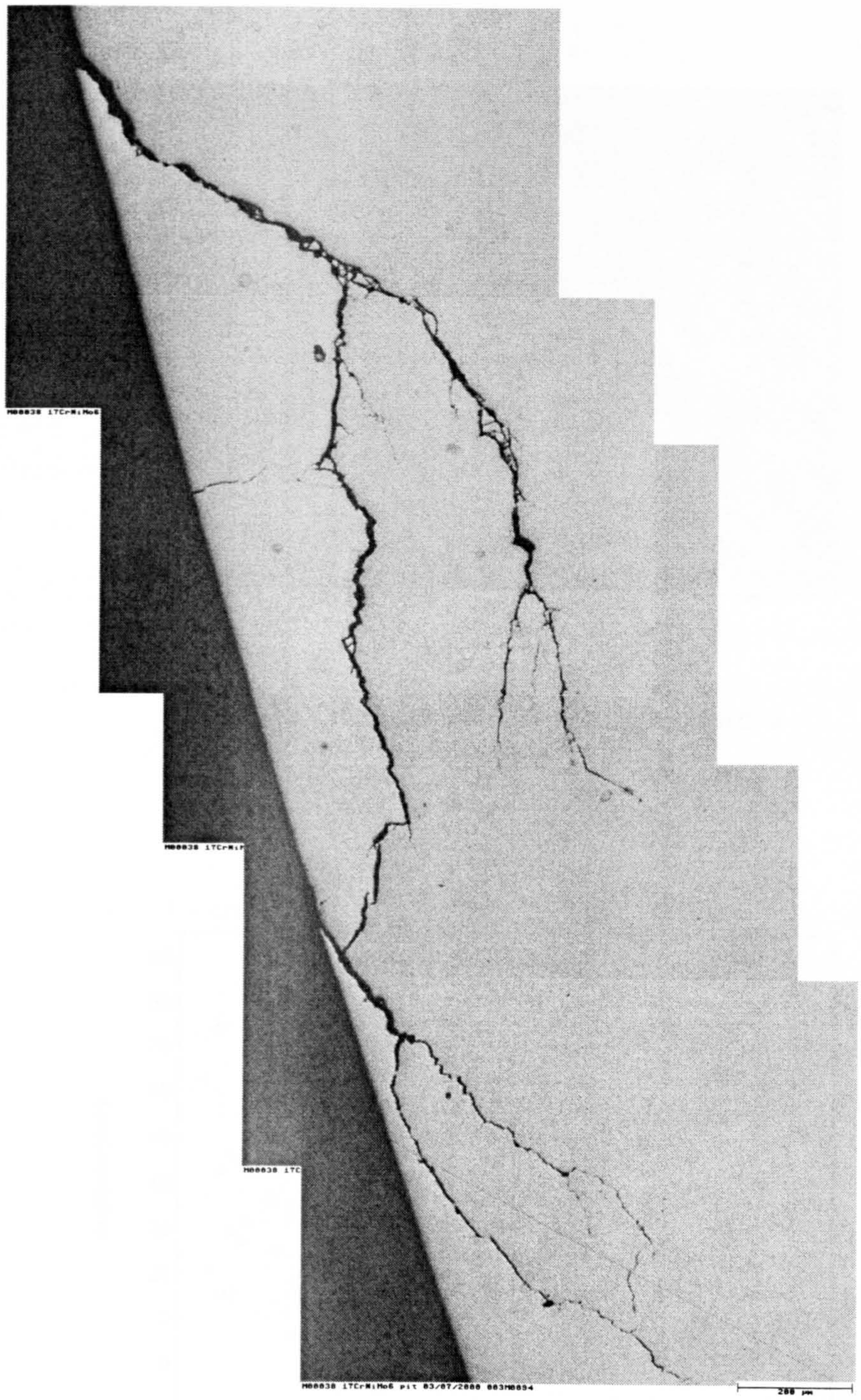

Fig.3.11 Microcrack branching to form surface micropit

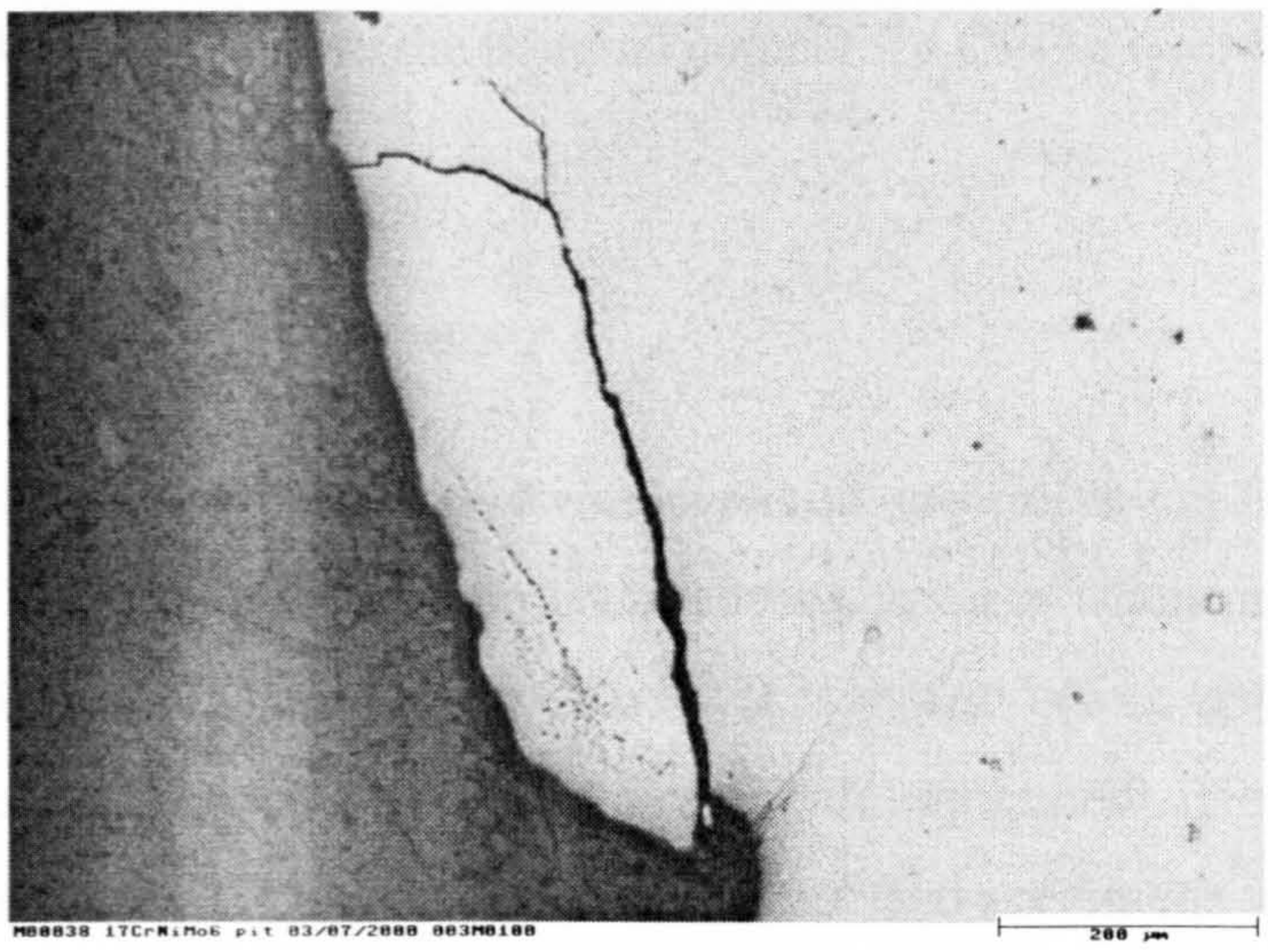

Fig.3.12 Crack nucleated a micropit to form a larger pit

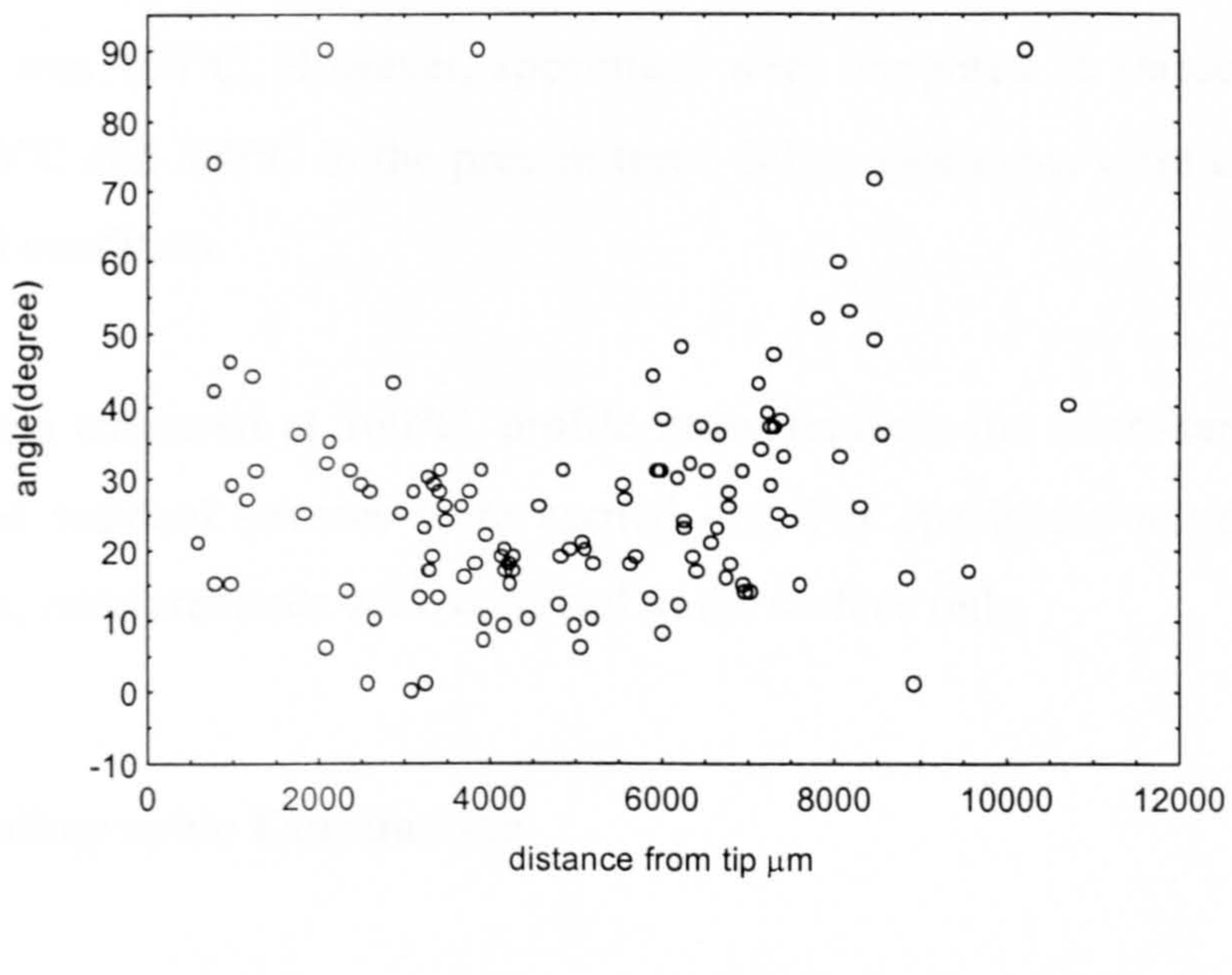

Fig.3.13 Variation of crack inclination along the flank surface (acute angle)

Spectroscopy instrument. The chemical analysis profile is shown in Fig.3.15. The mean carbon content was very close to the nominal content for Ovako steel 677.

3.2.1.1 Heat Treatment

Tests to characterise the material were conducted on specimens cut from both bar and the rod stock. To avoid any effect from the cutting process when measuring retained austenite content or residual stresses, rods were heat treated before testing.
Specimens were heat-treated using laboratory scale equipment. Heat treatment was conducted in a furnace with an argon gas atmosphere and specimens were encapsulated in shim steel foil. The purpose of encapsulation was to minimise surface decarburization which might occur during heat treatment (residual water and oxygen is present in the argon) and during air cooling after the specimens were removed from the furnace.

Specimens were heat treated as indicated in (Chapter 2). The recommended tempering temperature was 160°C. However, specimens were tempered at various temperatures between 160°C and 500°C in the present tests. Other specimens were examined in the un-tempered condition.

For specimens tempered at 160°C, profile measurements for microhardness, retained austenite and residual stresses were carried out. For specimens tempered at higher temperatures, measurements were confined to the surface only.

3.2.1.2 Metallographic Examination

The microstructure in the as-received material was pearlitic as shown in Fig.3.14. In hardened specimens, martensitic structure was produced. Fig.3.16 (a-d) shows microstructure in the as-hardened condition and at various tempering temperatures. Structures consist of plate martensite with retained austenite. At high tempering temperature of 500°C spherodization of carbides can be observed as shown in Fig.3.16 (d). Specimens tempered at lower temperatures revealed structure of tempered

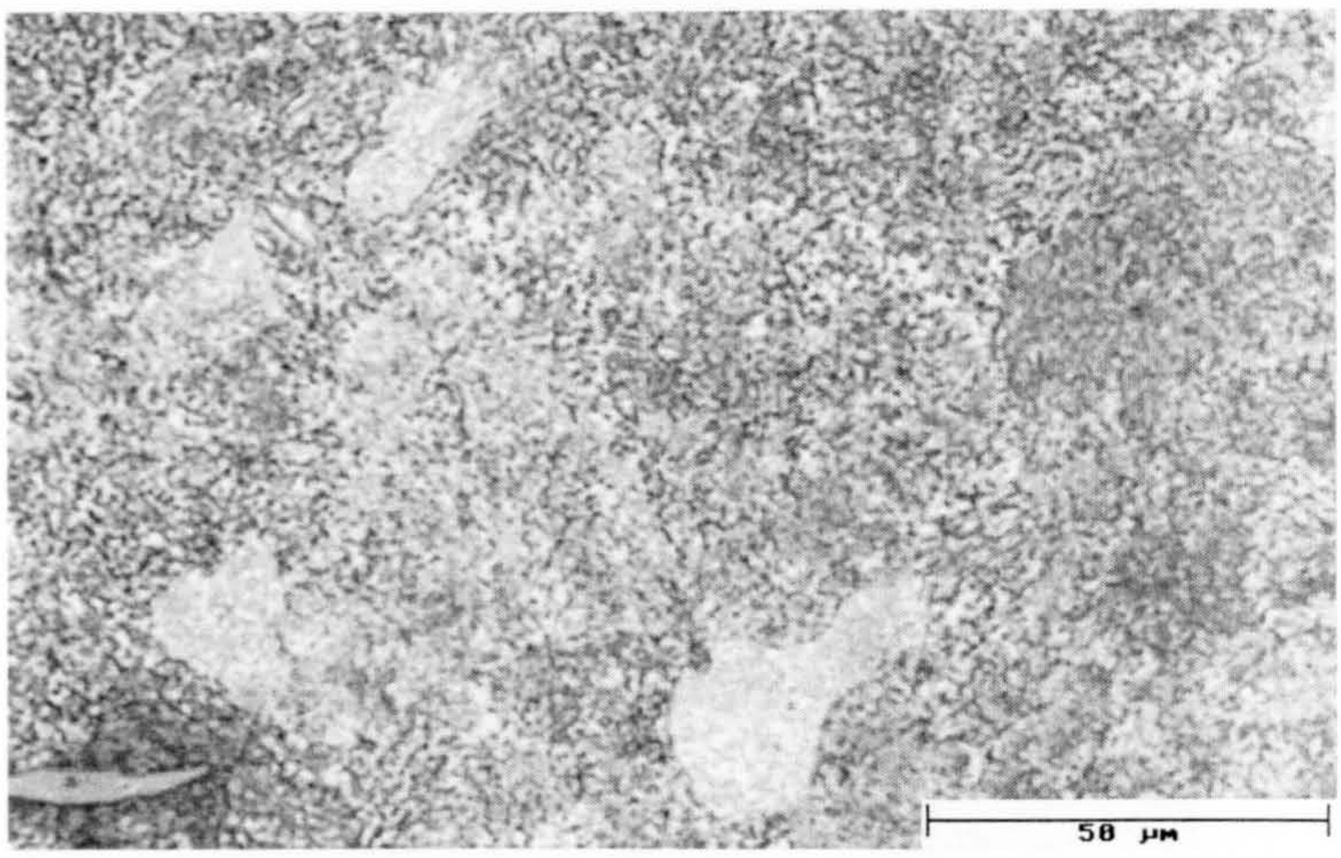

Fig.3.14 Microstructure of as-received Ovako steel 677.
Showing pearlitic structure

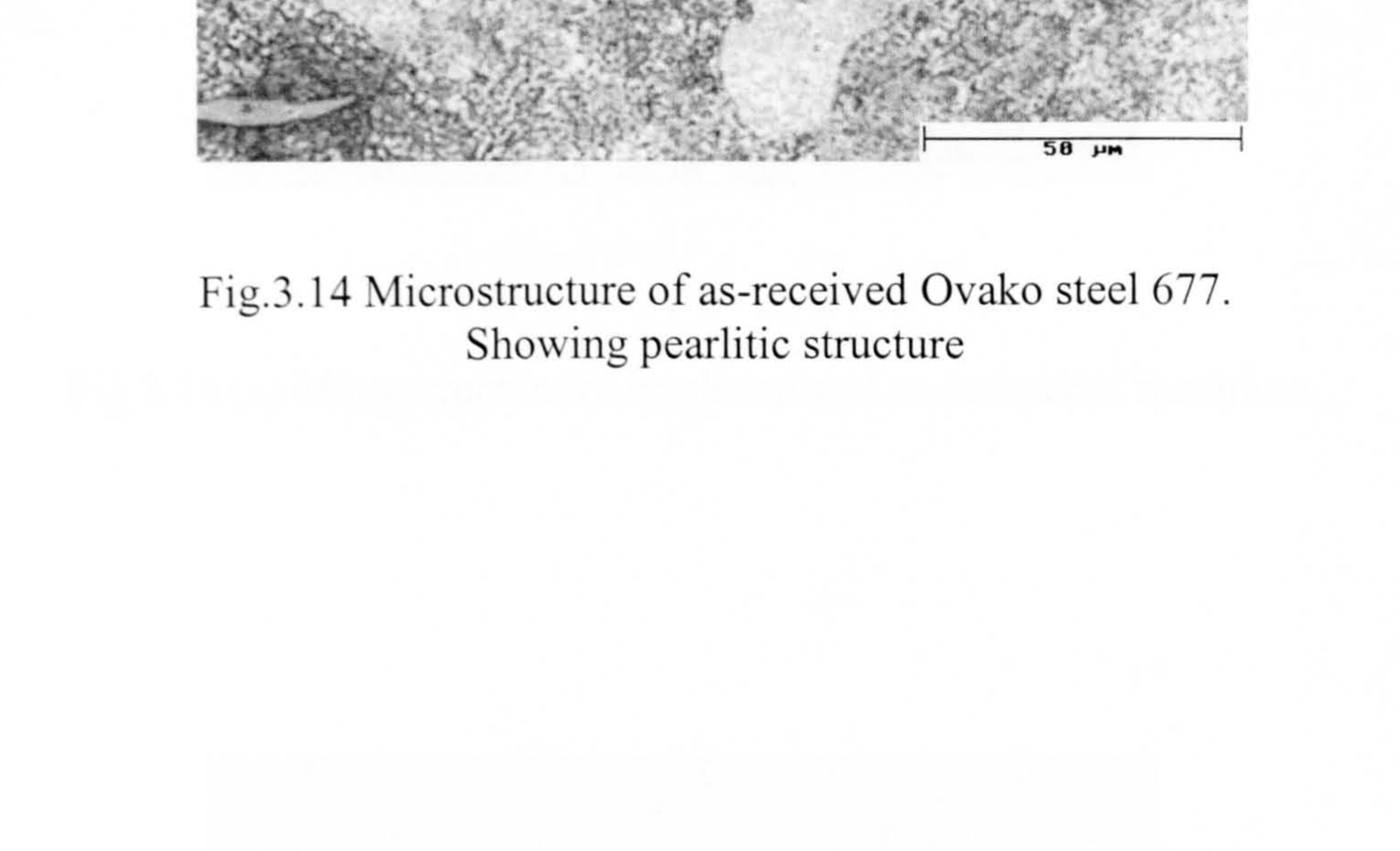

Fig.3.15 Carbon content in Ovako steel 677 measured by Glow disharge spectroscopy

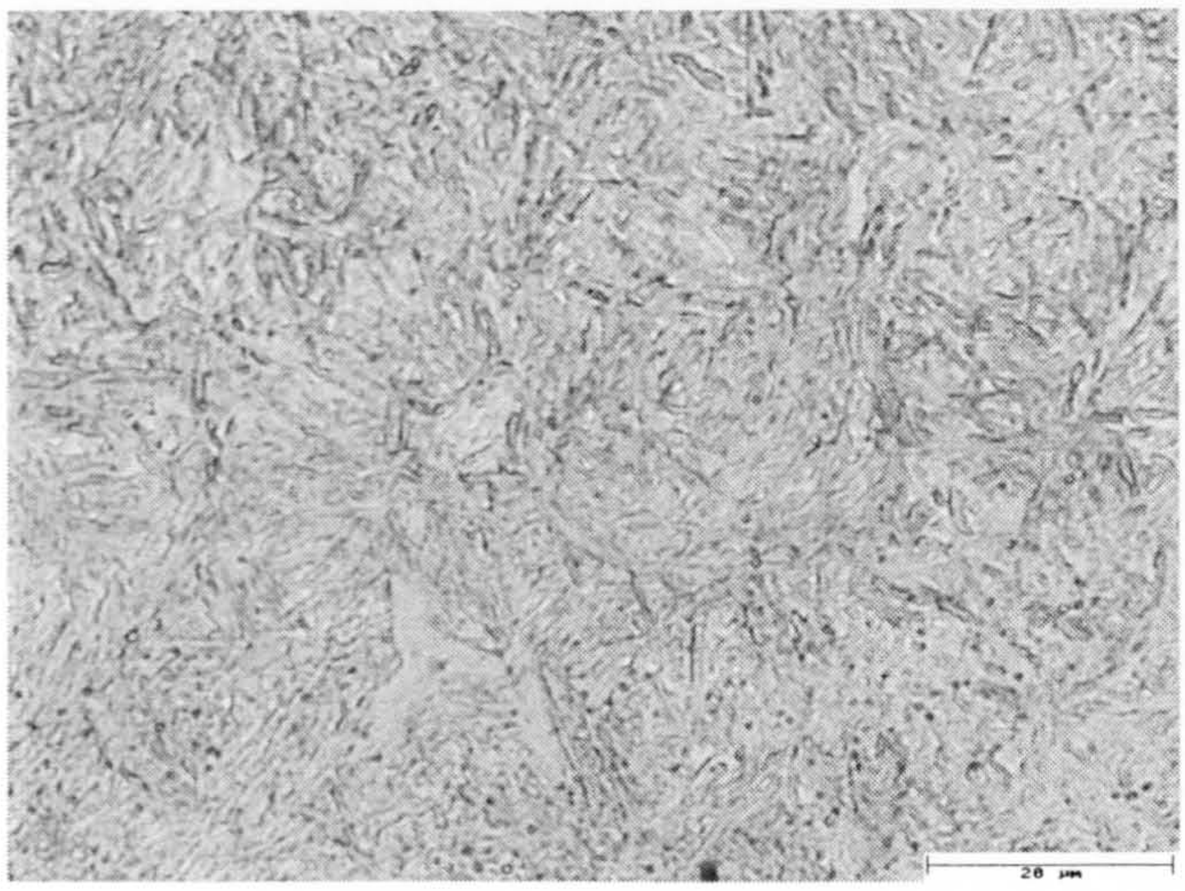

Fig 3.16 (a) Microstructure of hardened and un-tempered specimen

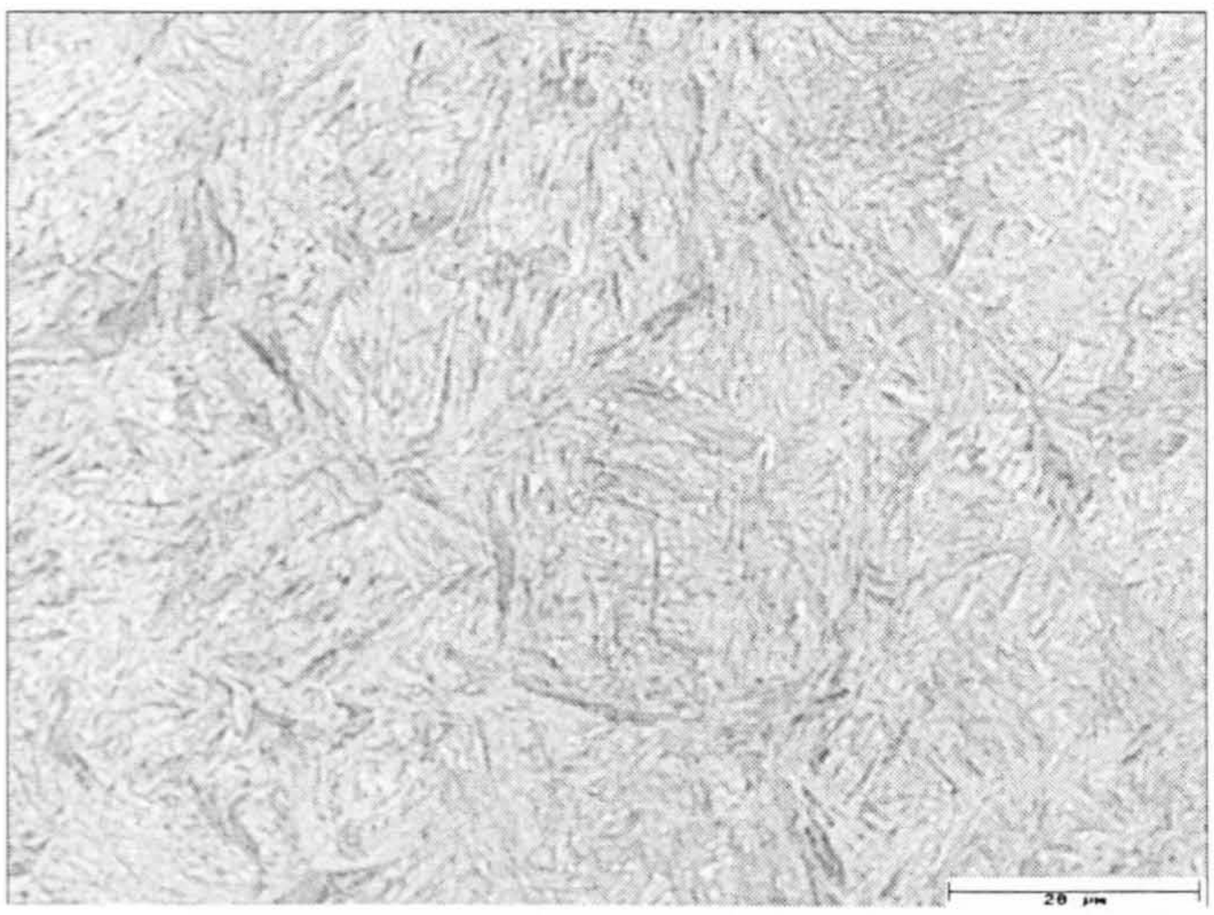

Fig.3.16 (b) Microstructure of a specimen tempered at 160°C for 1 hour

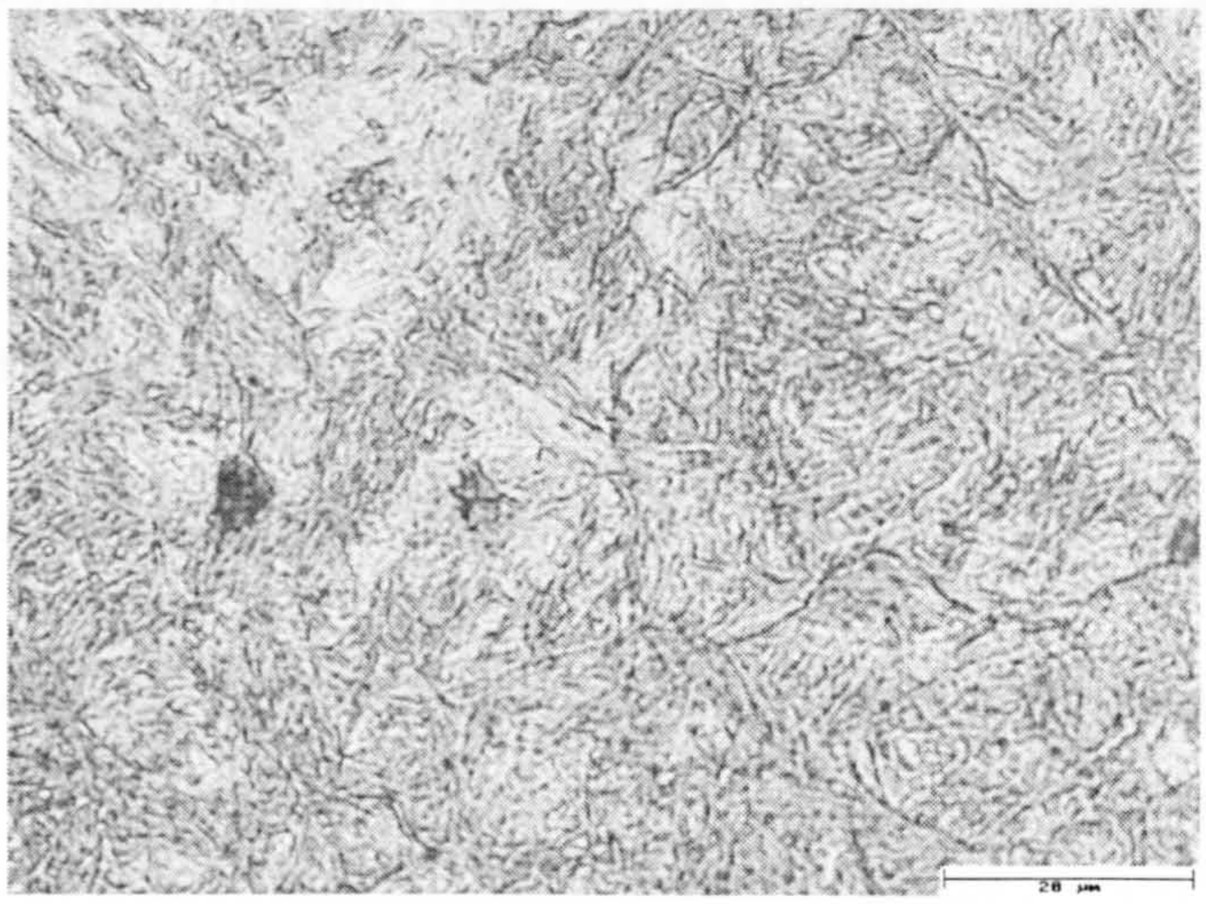

Fig.3.16 (c) Microstructure of a specimen tempered at 300°C for 1 hour

Fig.3.16 (d) Microstructure of a specimen tempered at 500°C for 1 hour

martensite with retained austenite as shown in Fig.3.16 (b-c). Metallographic examinations confirmed that this steel can be hardened merely by air cooling after austenitization.

3.2.1.3 Hardness Test

3.2.1.3.a Effect of Tempering on Hardness

One specimen was tested in the hardened condition (no tempering) Five specimens were tempered for 1 hour at temperatures of 160, 200, 300, 400 and 500°C respectively.

The specimens then sectioned using the cut-off machine to prepare polished cross sections for the microindentation hardness test using a 300 gm load. The hardness values reported were the average of four hardness readings on each specimen. Fig.3.17 shows the microhardness vs. the tempering temperature. It can be seen that the hardness decreases with increasing tempering temperature, i.e. there appears to be no secondary hardening. The decrease in hardness after tempering at 160°C is small. Larger falls in hardness were recorded as the tempering temperature was increased above 160°C.

3.2.1.3.b Hardness Profile

A microhardness profile was obtained on a complete rod section after hardening and tempering at 160°C. A disc shaped specimen with thickness of 10mm was cut and the surface was prepared for microhardness test using 300 gm load. The profile was made from the outer surface down to the centre. The microhardness profile is shown in Fig.3.18. Since the steel is through-hardening with high hardenability, The hardness is expected to be constant through the depth of the specimen. This is observed to be the case within a range of ± 20 kgfmm^{-2}.

3.2.1.4 Retained Austenite

3.2.1.4.a Effect of Tempering on Retained Austenite

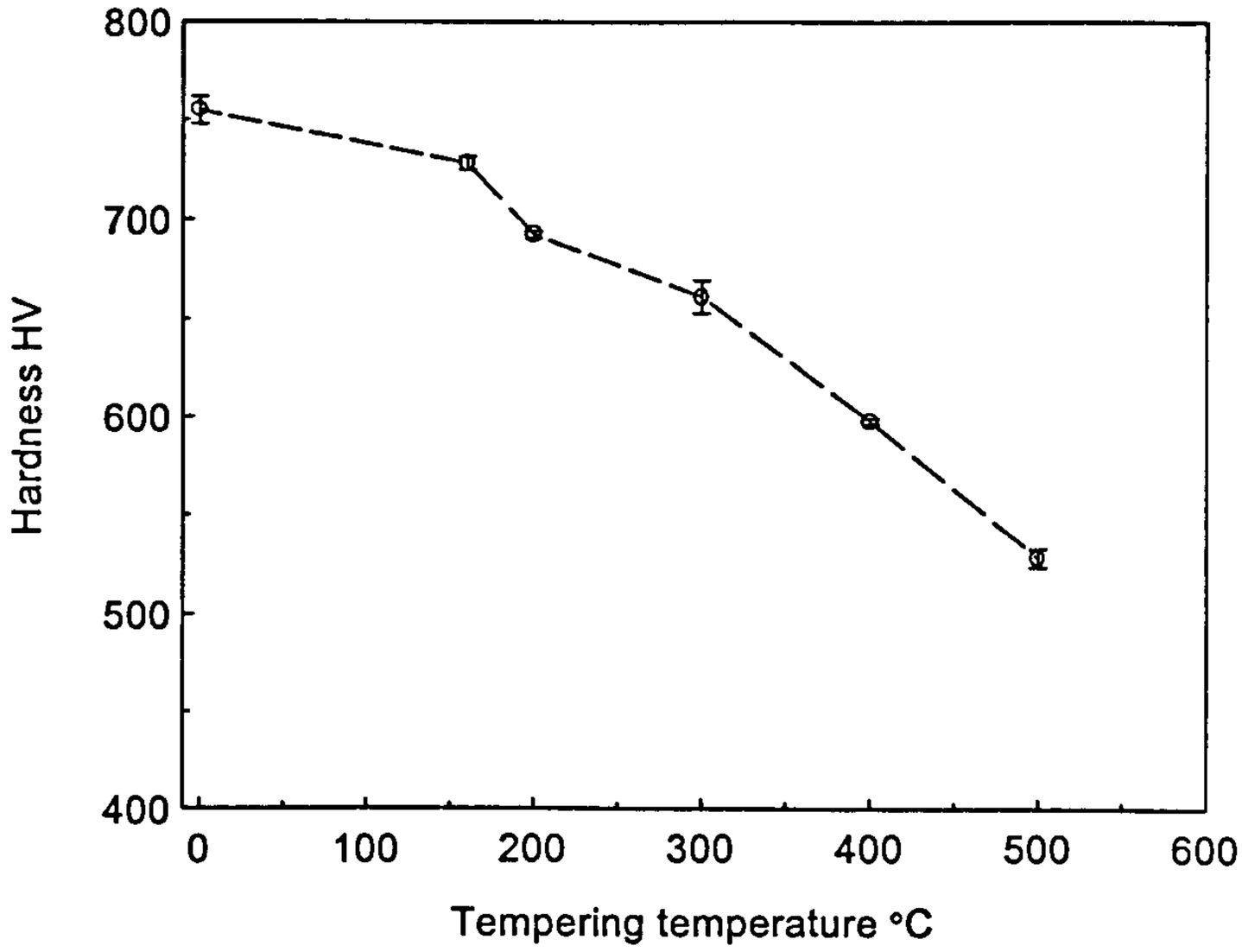

Fig.3.17 Surface hardness of Ovako steel 677 versus tempering temperature

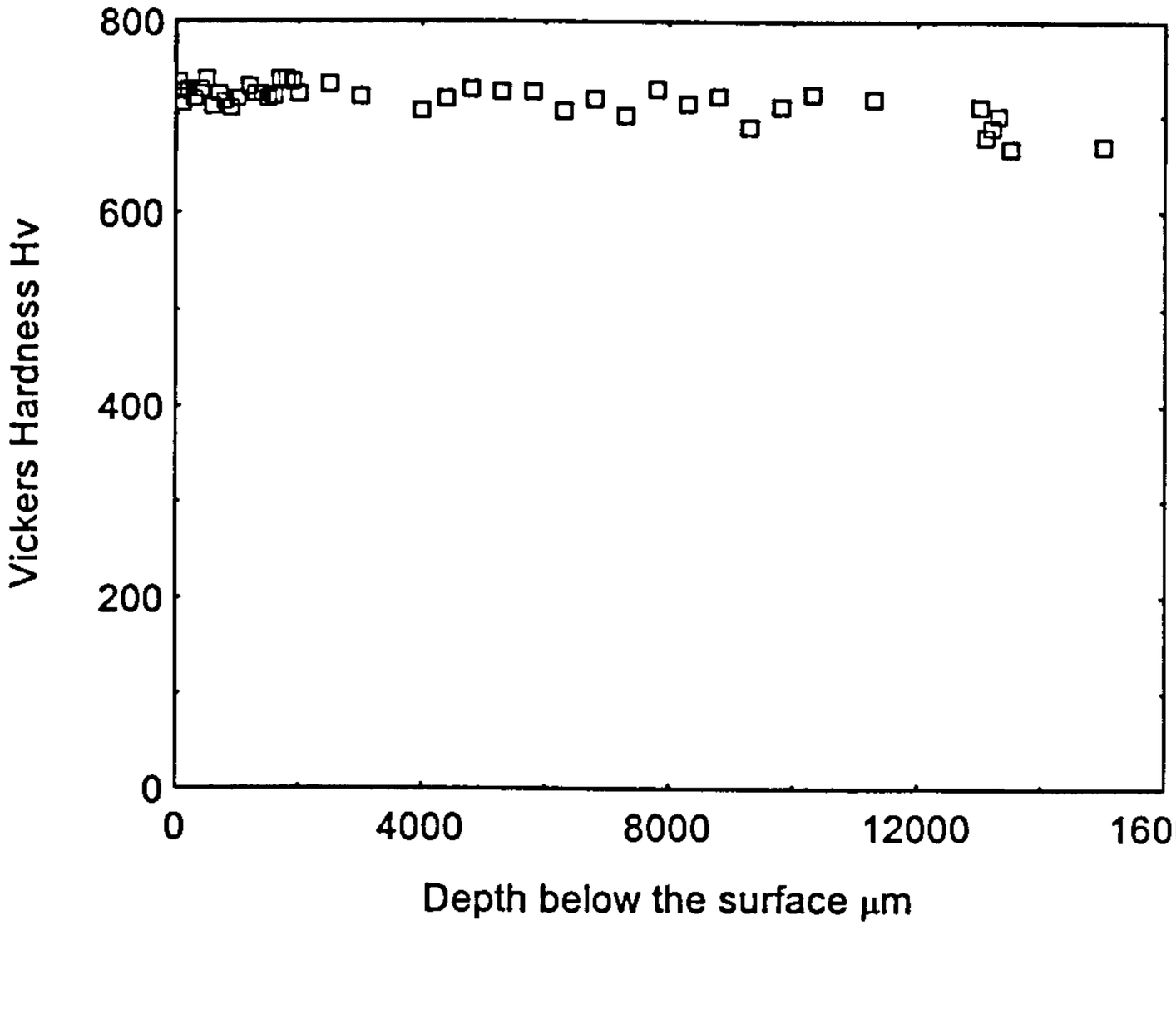

Fig.3.18 Hardness profile For Ovako steel 677

Retained austenite content at the various tempering temperatures and in the un-tempered condition is shown in Fig.3.19. The retained austenite content immediately after air cooling was about 23 %. After tempering at 160°C the retained austenite was below 20 %. The retained austenite appears to be relatively stable up to 400°C. At higher tempering temperatures the retained austenite decomposes.

3.2.1.4.b Retained Austenite Profile

A retained austenite profile was obtained for the rod specimen tempered at 160°C for 1 hr. Fig.3.20 shows the retained austenite profile up to depth of 100 μm below the surface. The amount of retained austenite was about 20 % through out the measured depth. Austenite is retained in the hardened condition because of the high carbon content in this steel which stabilises austenite phase and reduces the M_s temperature. The results in Fig.3.20 are consistent with the fact that Ovako steel 677 is homogeneous and through-hardening.

3.2.1.5 Residual Stress

A residual stress profile was obtained for a rod specimen tempered at 160°C for 1 hr. The result is shown in Fig.3.21. Tensile residual stresses were found at and beneath the surface. Residual stress was positive at the outer surface. This state of residual stress is quite different to that is observed in conventional case carburised steel. The positive surface stress is considered harmful from the fatigue strength point of view. Because fatigue cracks usually initiate at the surface and propagate inwards, any surface tensile residual stresses will help fatigue crack initiation.

3.2.1.6 Fracture Toughness Testing (K_{Ic} determination)

The K_{Ic} values obtained from tests on chevron notch specimens are shown in Fig 3.22. Each point on the curve represents the average value from two specimens. The toughness of the material is low but consistent with previous estimates of the toughness of case- carburised steels (eg. Hyde *et al.*, 1998). There is a gradual increase in toughness (corresponding with a reduction in hardness) with increasing tempering

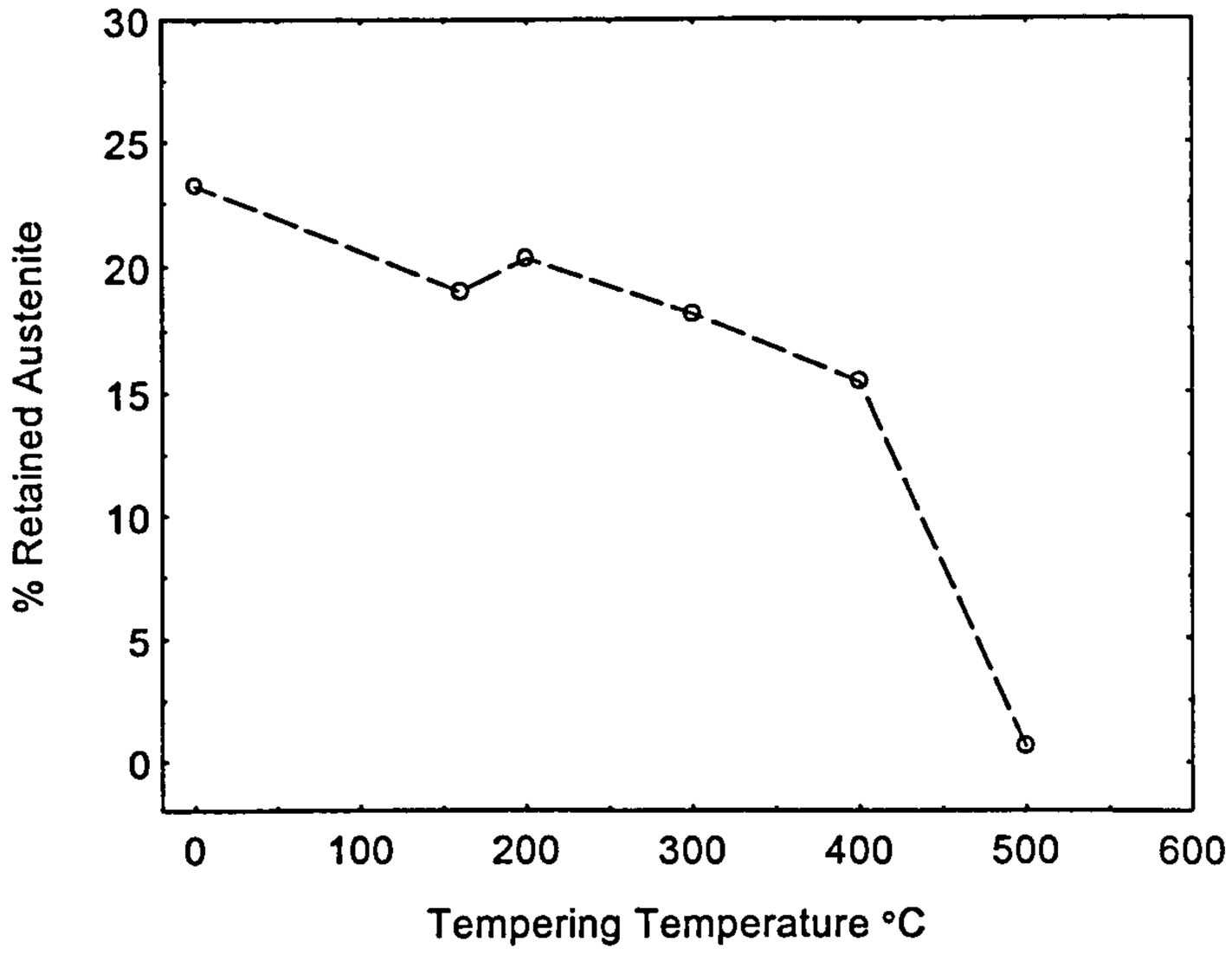

Fig.3.19 Effect of tempering temperature on retained austenite content

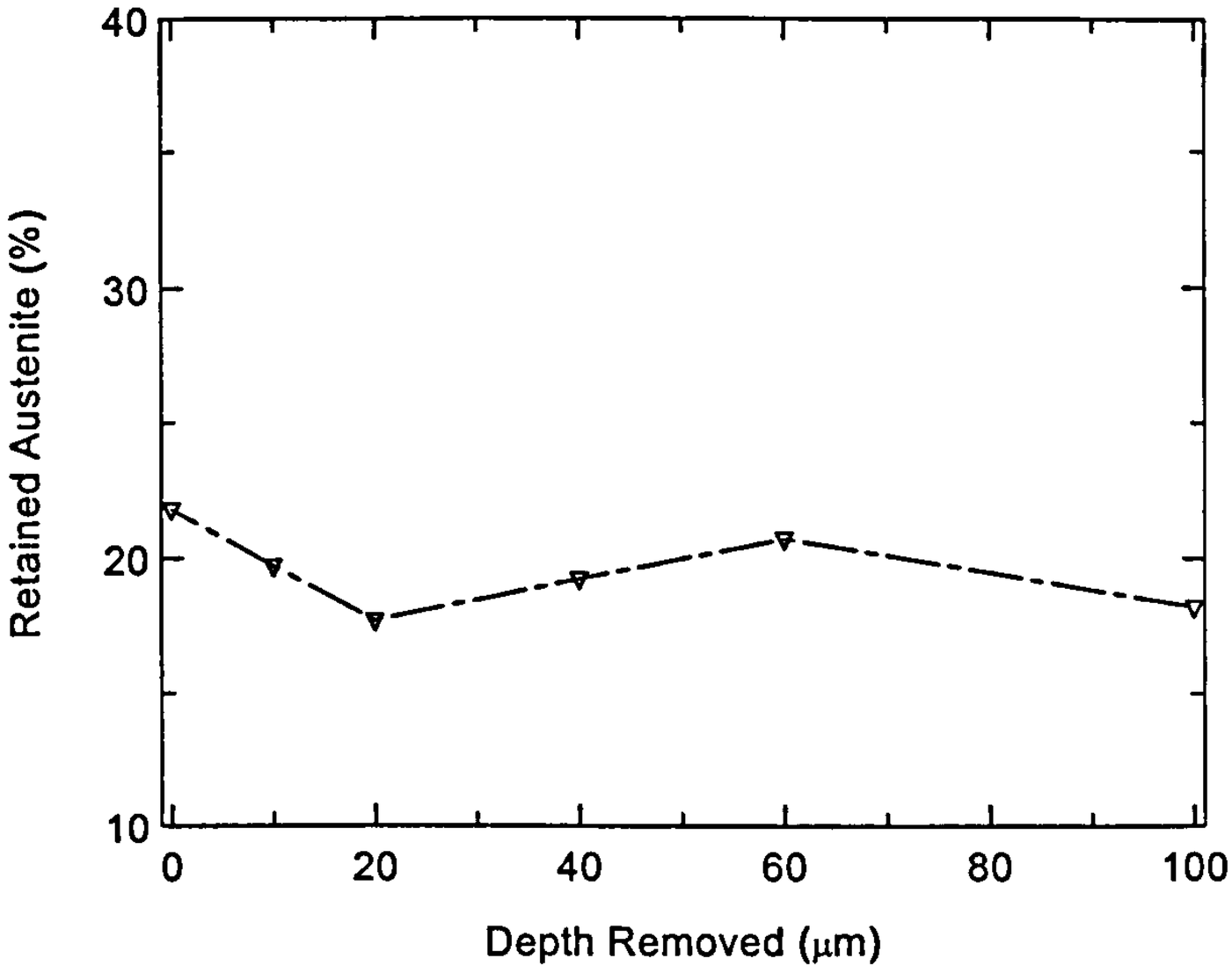

Fig.3.20 Retained austenite profile in Ovako steel 677. Showing homogenous content of retained austenite in the region examined

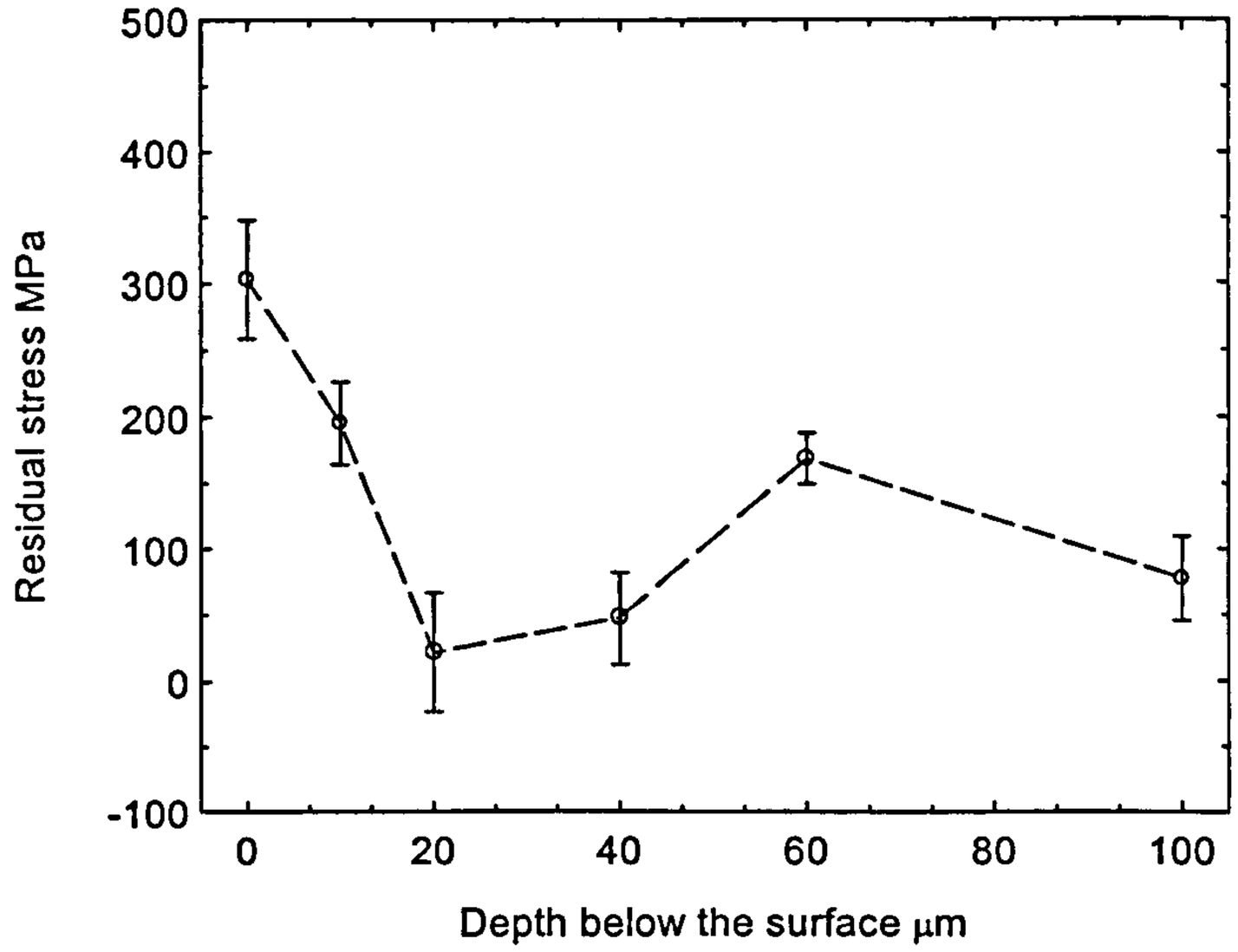

Fig 3.21 Residual stress profile in Ovako steel 677 after heat treatment and tempering.

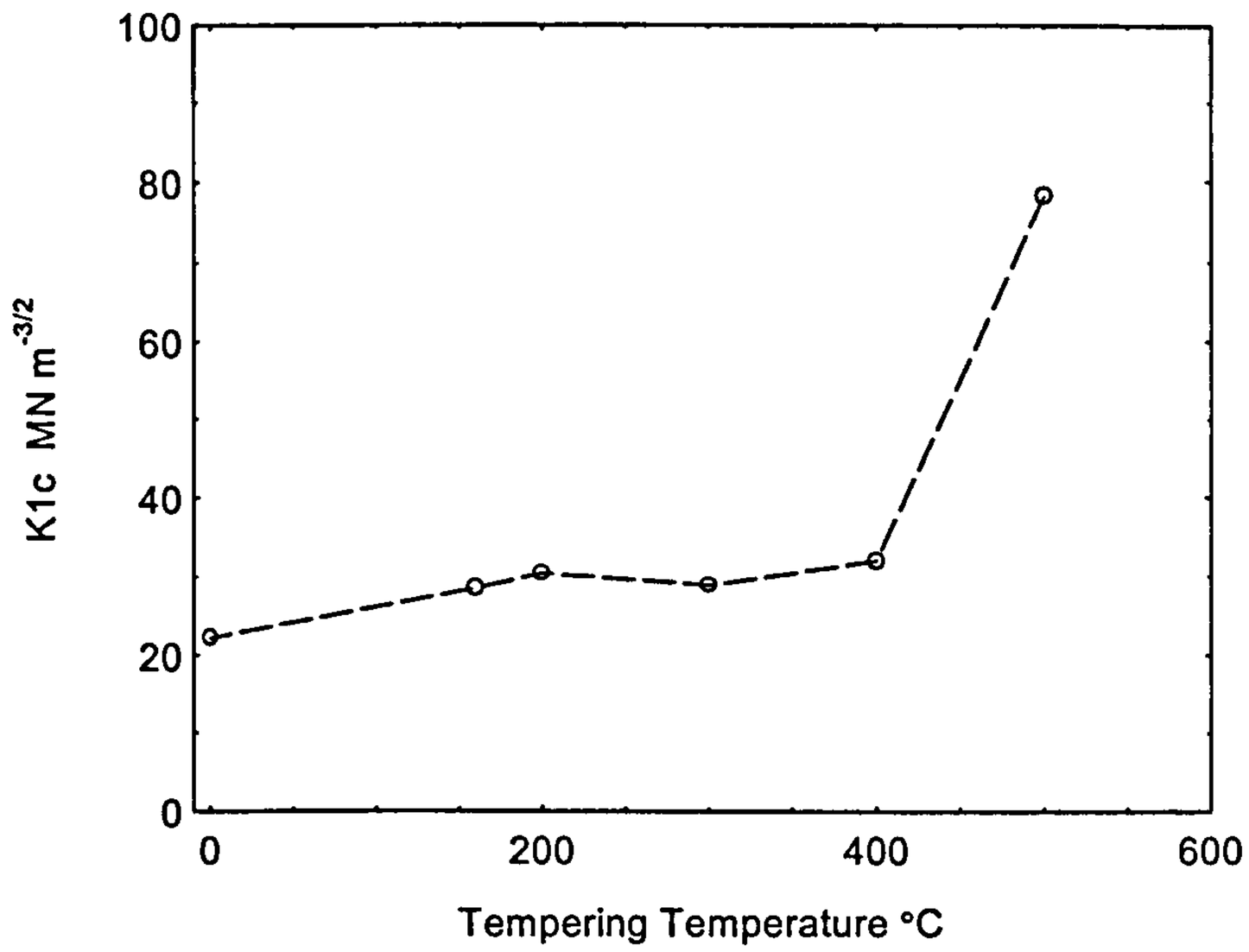

Fig.3.22 Effect of tempering temperature on fracture toughness K_{1C}.A large increase occurs at temperatures above 400 °C.

temperature up to 400°C. At higher tempering temperature there is a large upward jump in toughness.

The fracture surfaces of some of these specimens were examined by SEM. Figs.3.23 (a-d) shows the fracture surfaces for the un-tempered specimen and specimens tempered at 160°C and 500°C. In the un-tempered specimen and the specimen tempered at 160 °C fracture was intergranular. The fracture of the specimen tempered at 500°C was transgranular with microvoid growth coalescence. These changes in the fracture type and the amount of the plastic deformation accompanied the fracture causes the fracture toughness K_{Ic} values to be increased at the high tempering temperature. It is believed that the low toughness values at high hardness is due to the intergranular fracture caused by segregation of phosphorous to the prior austenite grain boundaries (eg. Hyde *et al.*, 1998).

3.2.1.7 Compression Test

Stress-strain data is essential for finite element analysis (see Chapter 4). These can only be obtained in compression tests for material with low ductility such as the Ovako 677. These data and the FE analyses were used to interpret the results of the standing contact fatigue tests.

Four specimens were tested to obtain the engineering stress-strain curve. In this test load was increased gradually and the corresponding strain was recorded using strain gauges adhesively bonded to the specimen surface. Two specimens were tested up to the fracture load. Fig. 3.24 shows the stress-strain curves for all specimens tested. The stress-strain curve showed a linear relation at the beginning of the elastic deformation as expected. The material then showed strain hardening as stress exceeded the elastic limit (or yield point). Fracture finally occurred at strain beyond 4 % reduction in length. Figure 3.25 showed a fitted tri-linear relations for this steel. The fitted curve consisted of three straight lines in three strain ranges. The first strain range lies in the linear, elastic deformation regime, the other two in the non-linear part of the relationship. In the first range, up to a strain of 0.0119 the slope in the stress-strain curve represents the modulus of elasticity. The elastic modulus in compression was 190 GPa. Table 3.2

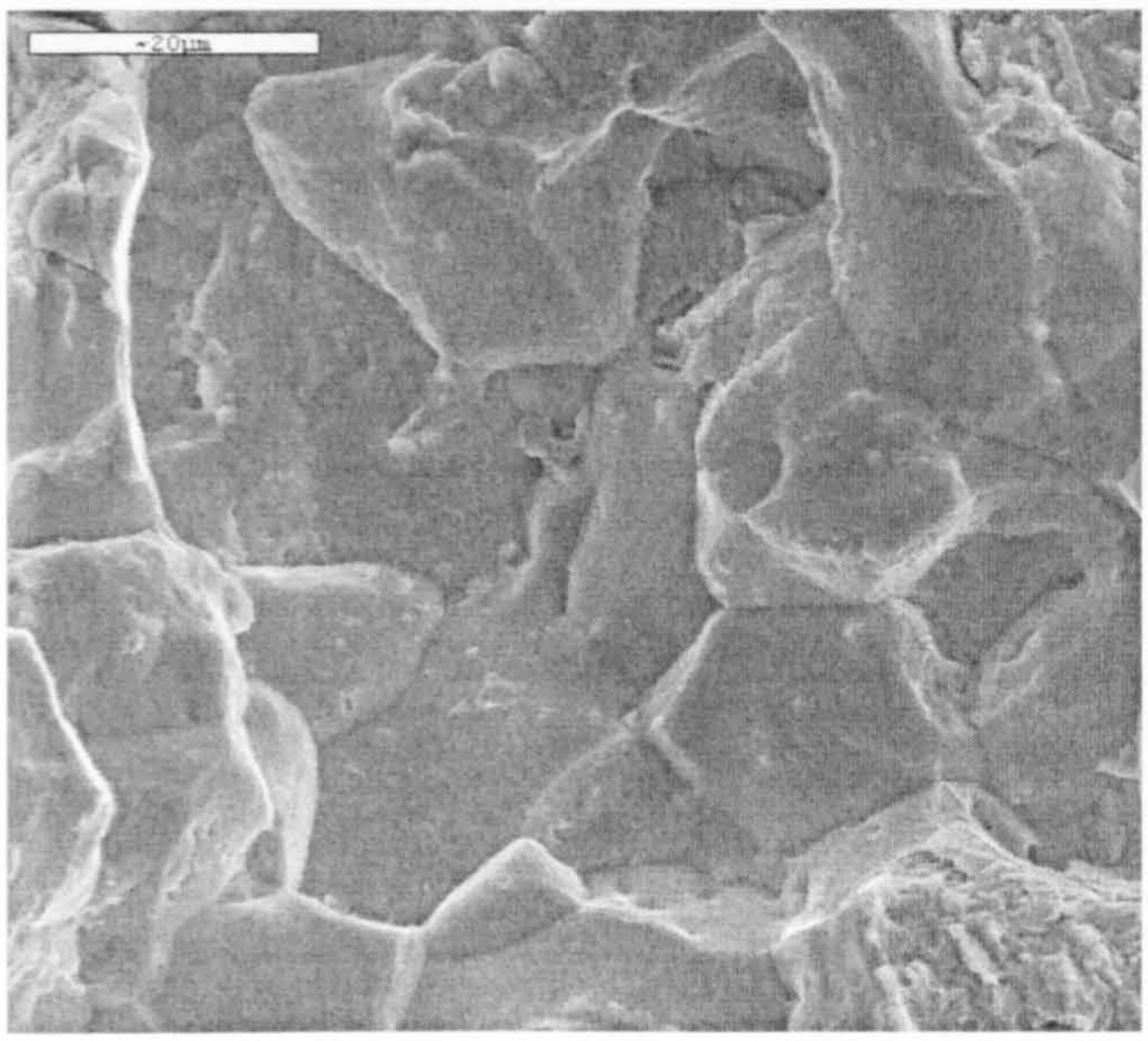

Fig.3.23 (a) SEM fracture surface of air hardened specimen (un-tempered)

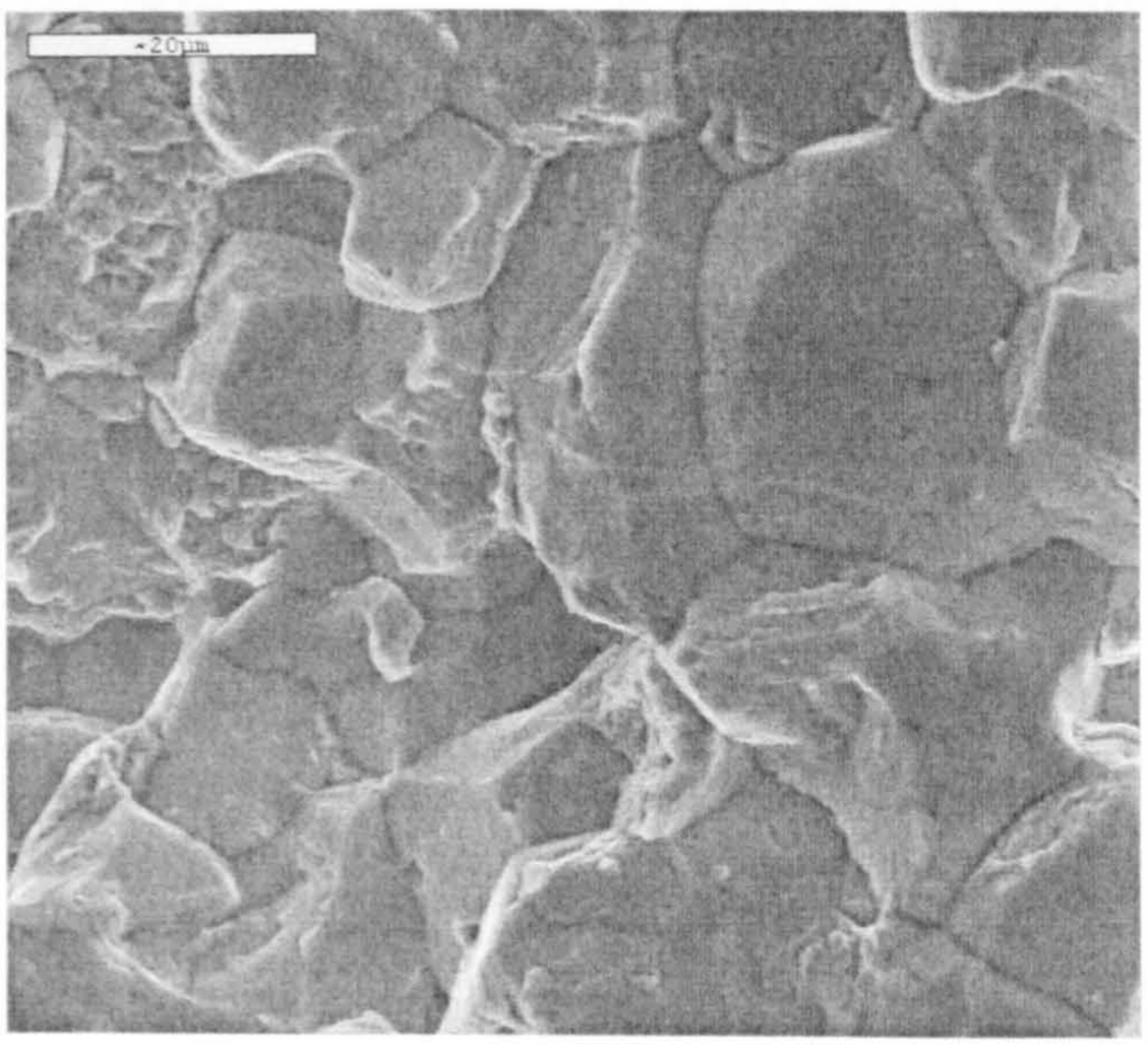

Fig.3.23(b) SEM fracture surface of a specimen tempered at 160°C for 1 hr

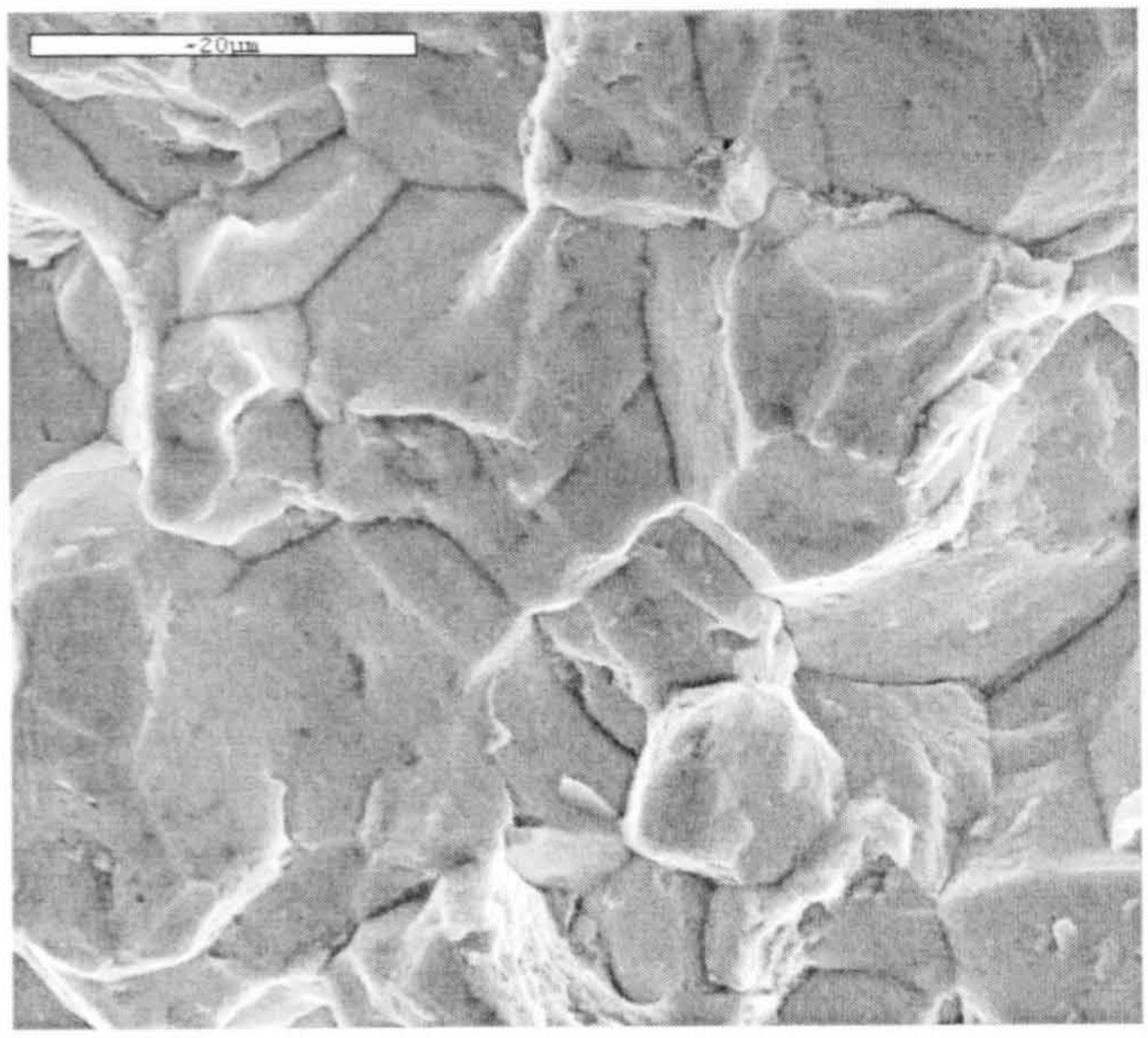

Fig.3.23(c) SEM fracture surface of a specimen tempered at 160°C for 1 hr. Similar to previous figure but different location on fracture surface

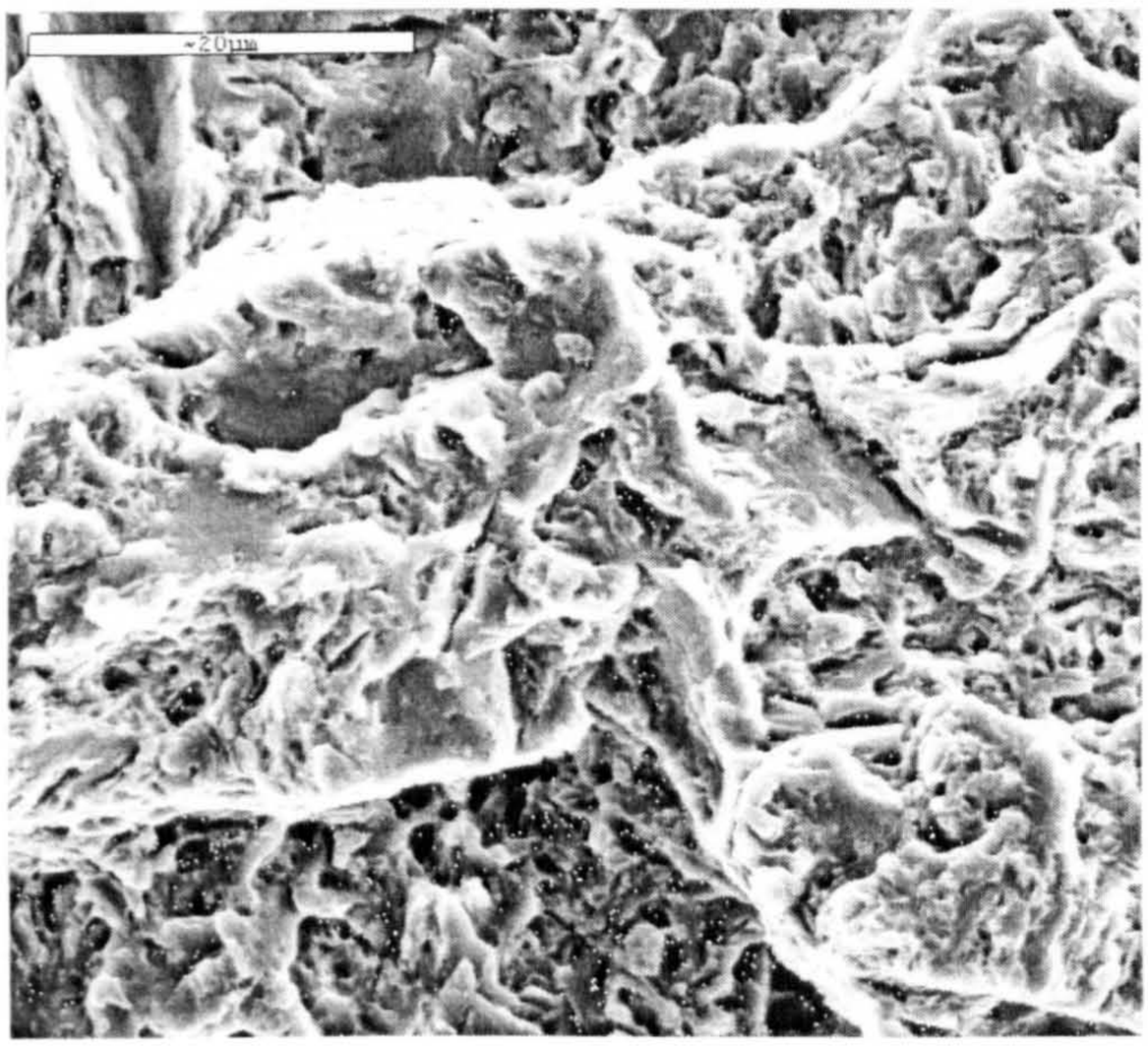

Fig.3.23-d SEM fracture surface of a specimen tempered at 500°C for 1 hr

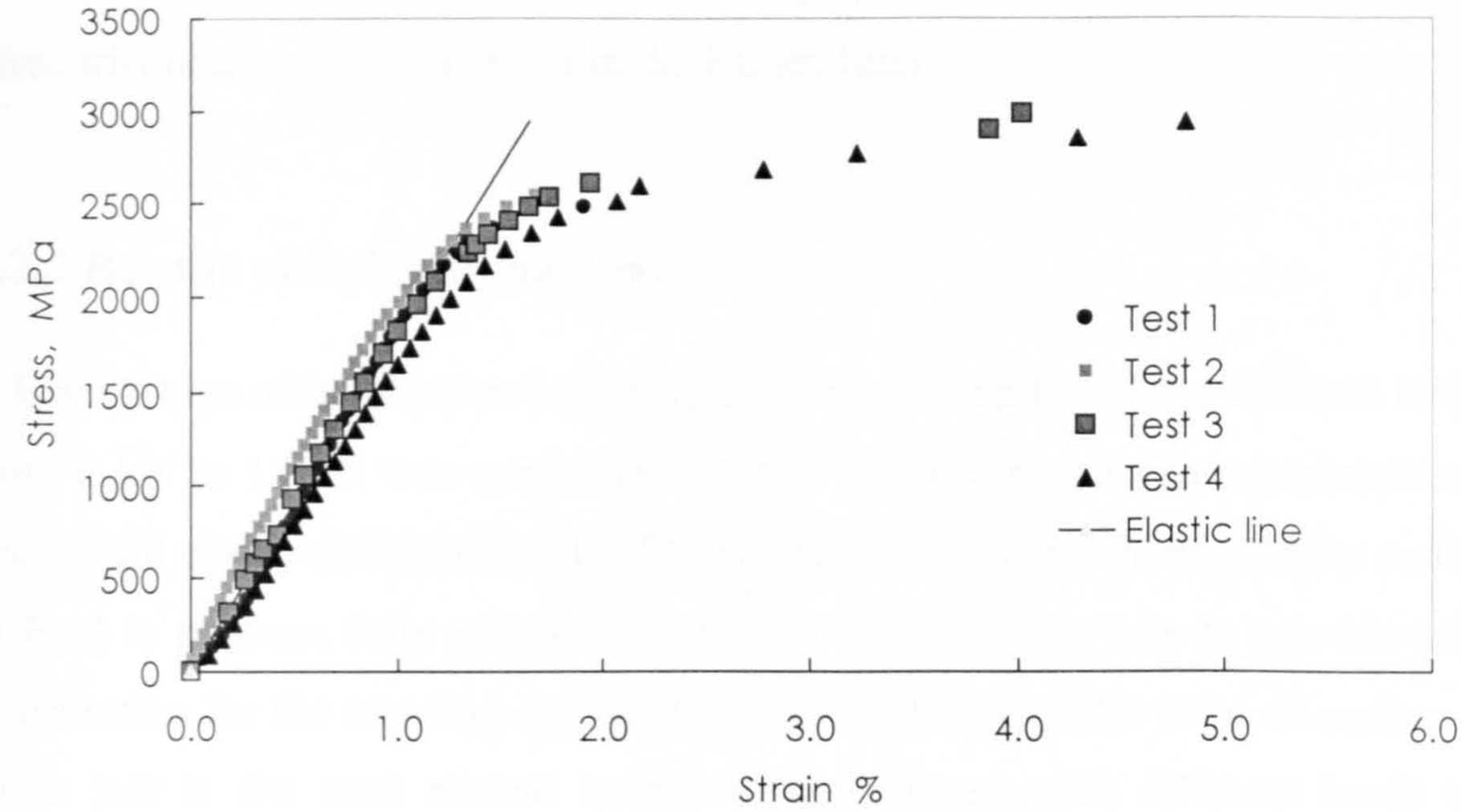

Fig.3.24 Stress strain curves for four specimens of Ovako steel tested in compression test specimens. Two specimens were tested to fracture.(compression)

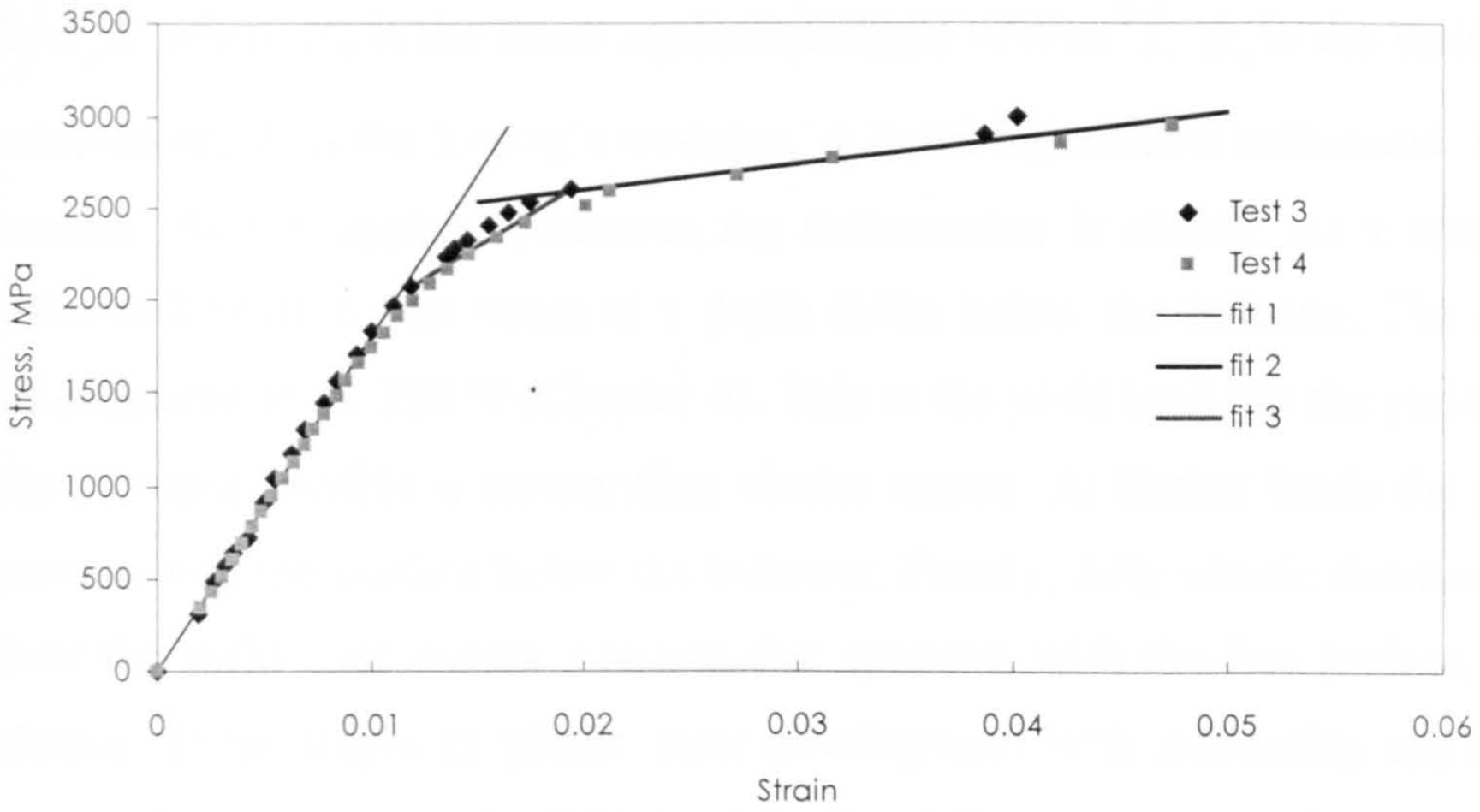

Fig.3.25 Tri-linear fit stress-strain curve based on experimental results

Table 3.2 Stress strain relationships adopted in the tri-linear fit simulation.

Tri-linear fit strain range	Stress in units of Pa
$e < 0.0119$	$\sigma = Ee$
$0.0119 \le e < 0.0194$	$\sigma = 1225 \times 10^6 + 71.433 \times 10^6 e$
$0.0194 \ge e$	$\sigma = 2331 \times 10^6 + 13.89 \times 10^6 e$

$E = 190 \times 10^9 \, Pa$

indicates the strain ranges and the modelling equation corresponding to each range. The fitted tri-linear curves were used in the FE analysis.

3.2.2 Results of Indentation Test

A Brinell-type of indentation test using a 5-mm steel ball with applied load in the range from 2 kN to 15 kN was performed. It was aimed through this experiment to assess elastic and plastic deformations for Ovako steel 677 under contact stresses and the level of load to produce fully plastic deformation. The purpose was to provide supporting information for the standing contact fatigue test (below). The level of surface residual stress left in the steel around indentations produced with different loads was also measured.

Indentation radii were measured with the aid of stereo scan microscope. The normalised mean pressure P_m/σ_y was then plotted versus the non-dimensional strain $Ea/\sigma_y R$ where P_m is the mean applied pressure $=P/(\pi a^2)$, σ_y is the yield strength in compression, E is the Young's modulus, a is the indentation radius and R is the ball diameter. At low applied pressures the deformation is elastic. At a critical load P_y plastic deformation first occur at a depth 0.48a below the indenter. The critical load was estimated to be 350 N (Chapter 4). This is the yield load but the yielded region is fully contained within a surrounding elastic region. At higher loads the plastic zone connects with the surface below the indenter. Finally, fully plastic deformation occurs where the yield zone covers a region that connects with the free surface, beyond the indenter. These stages of plastic zone development with increasing applied load are shown schematically in Fig.3.26 (a-c) In the fully plastic state the mean pressure is expected to be $P/(\pi a^2) = 3\sigma_y$ for an elastic-perfectly plastic material (Johnson, 1985).

From this test it was aimed to produce an indication of the extent and type of deformation produced at various levels of applied loads. The standing contact fatigue was performed under a range of load. The resultant deformations are elastic at low loads. At very high loads deformations are fully plastic. When the applied load is capable of producing plastic deformation, the pressure underneath the indenter has exceeded the yield strength of the material. The first zone to be plastically deformed

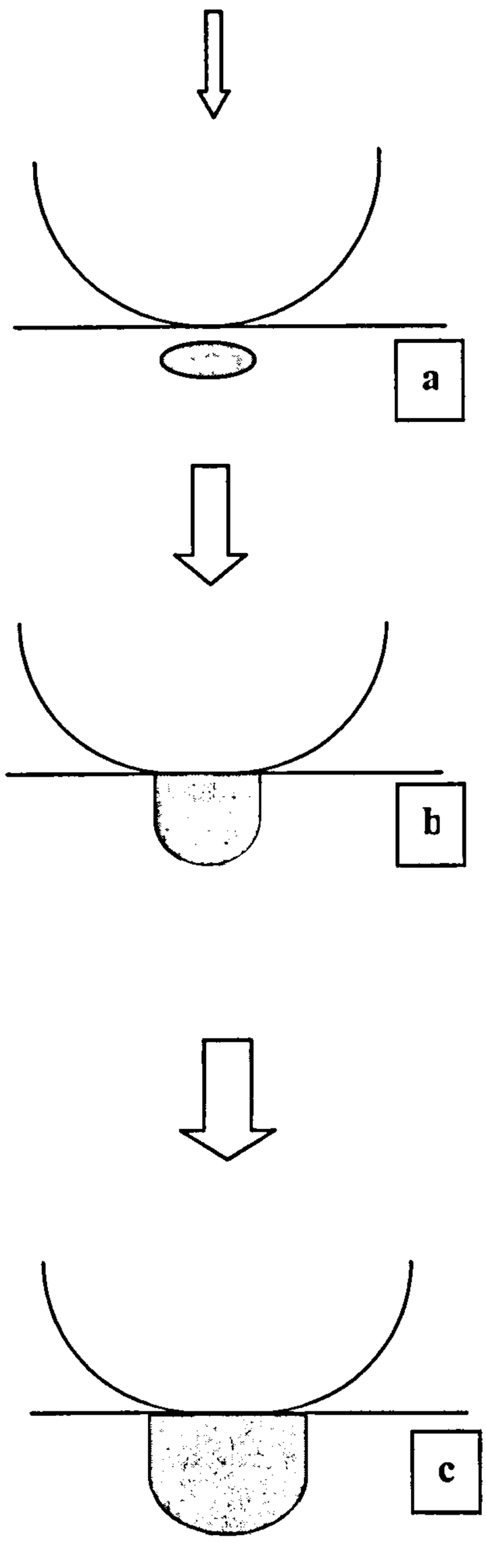

Fig.3.26(a-c) Shows stages in development of plastic zone (grey area) with increasing applied load on spherical indenter. Yielding commences below the surface (a). Elastic-plastic stage developed when plastic zone connects with the surface below the indenter (b). Fully plastic deformation occurs when plastic zone grew to connect with the free surface (c).

resides beneath the surface and completely contained within elastically deformed material. This transition stage between purely elastic and fully plastic is known as elastic-plastic deformation. As the applied loads increases the size of plastic zone increase and eventually breaks to the free surface when the fully plastic regime is reached. It is not intended through this test to analyse stresses in the elastic plastic deformation. However it was merely desired to know whether deformations produced under the range of applied load in the standing contact fatigue test lays within the elastic-plastic regime or it may exceed it to fully plastic deformation. Stress analysis in contact problems depends on deformation regime produced by the applied load. For purely elastic deformation the solution is given by Hertzian theory (Chapter 4). Theories such as slip line field or theory of rigid-plastic solids give the solution for the fully plastic regime. Summaries of some works for the elastic-plastic regime solutions are reviewed in (Chapter 4).

Johnson, 1985, deduced an upper limit for mean pressure (for non-work hardening material) as $(P_m/\sigma_y)\approx 3$. Fully plastic regime is attained at this level of mean pressure and a corresponding non-dimensional strain $Ea/\sigma_y R \approx 40$. Figure 3.27 shows the result of indentation test. It can be seen that the criterion for fully plastic deformation was not reached at highest applied load although the applied load was 15 kN the mean pressure approach the upper limit for fully plastic deformation. However for the applied load of 11 kN which is very close to the highest load used in the standing contact fatigue performed in this work, both mean pressure and the resultant non-dimensional strain indicate that at this level of applied load the resultant deformation is within the elastic-plastic regime. Thus, fully plastic deformation was not achieved in the tests using the hardened Ovako steel. Residual stress produced by elastic-plastic indentation could be important in standing contact fatigue. It is not possible to measure residual stress accurately using X-ray diffraction because the diameter of the X-ray beam is large compared with the distance over which stress changes significantly. However it is possible to make an approximate assessment of residual stress near an indentation, accepting that the values are average over space. Figure 3.28 shows residual stress measure near an indent as a function of applied load. It should be noted that the hoop stress is tensile and the radial stress is compressive in the region just outside the contact circle. This is consistent with the FE calculations as discussed below.

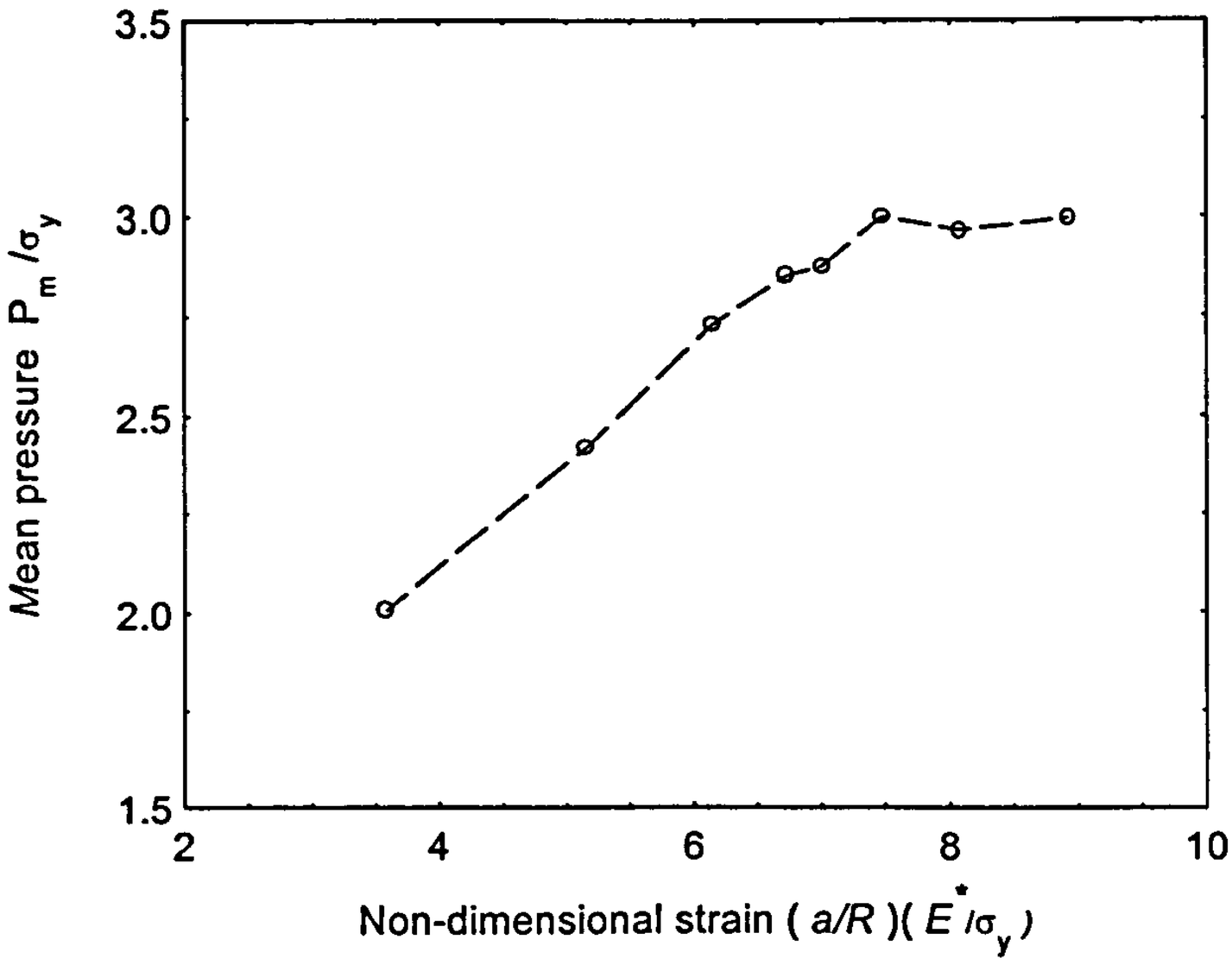

Fig.3.27 Mean pressure versus non-dimensional strain for indentation test

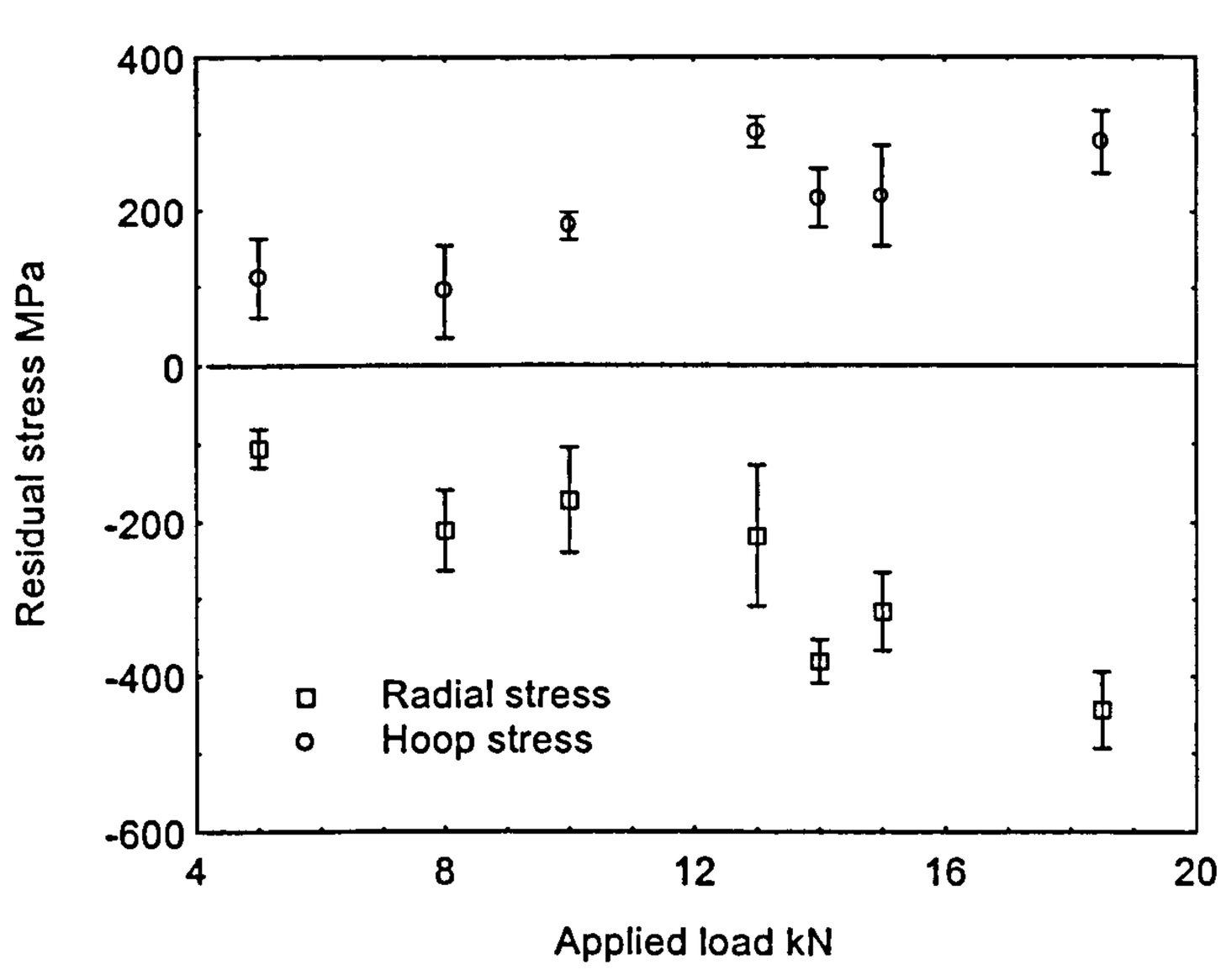

Fig.3.28 Magnitude of surface residual stresses in hoop and radial directions left around indentaion made by a 5 mm steel indenter at various applied loads in the indentation test. Measurements were taken on two orthogonal directions very close to the outer indentation periphery on a circle of 0.8 mm diameter. Values represent average stress within the area of measurements.

3.2.3 Standing Contact Fatigue Test (SCF test)

3.2.3.a Test Specimens

The standing contact fatigue test was carried out on discs of 10 mm thickness and diameter of 30 mm. For each specimen one side was prepared for the test by grinding and polishing. The preparation enabled the fatigue cracks to be observed easily when the indents were inspected. Specimens were then heat treated and tempered as explained above. Specimens were then divided into three groups. The first one was tested directly after tempering; the second one was given another surface polish to remove few microns from the surface while the third group of specimens were shot peened on the repolished side before testing for standing contact fatigue test.

3.2.3.b Shot Peening

Shot peening process was carried out by Metal Improvements Ltd. Specimens were peened to the intensity in the range of 14-16A according to The Almen test using 230H steel shots and 200% coverage. The intensity is measured on standardised test specimens which are shot peened to 100% coverage. Test specimens are steel strips with length of 3.0 inch and 0.75 inch width. There are three types of test specimens classified according to their thickness, the most thin specimen or N strip has a thickness of 0.001 inch, the other two have thickness of 0.051 inch and 0.0938 inch for A strip and C strip respectively. The selected test specimen is then peened on one side. After testing the specimen is bent due to stretching of the peened surface. The intensity is taken as the arc height measured in inches at the middle of the test specimen. A letter in the shot peening specification such as 14A refers to strip type used in the test and the number for the intensity which is 0.014 inch. Shots are classified for size and hardness. Size is designated with numbers in the range from 110 for smallest shots and 330 for largest. Letters H or S. refers to hard shots which have hardness in the range 55-62 RC and S for soft shots in the range 45-55.

3.2.3.c Residual Stress in Test Specimens

Figures 3.29 and 3.30 show the residual stress and retained austenite profiles in the shot peened specimen. For the un-peened specimens measurements of residual stress were carried out before specimens cutting to avoid any effect of the cutting and grinding processes. Measurements were made on the outer surfaces in hardened rod specimens. In addition to results shown previously in Fig.3.21, (Sections 3.2) for residual stress, measurements were made on two other specimens. In each specimen two opposite sites on the cylindrical surface were selected for residual stress measurements. The results show that in hardened un-peened specimens the residual stress is tensile which considered harmful from the fatigue resistance point of view. However shot peening induces a very high compressive residual stress in a shallow layer beneath the surface. The maximum compressive residual stress of about 1400MPa was attained at a depth of about 40-50 μm below the surface. The shot peening process also caused transformation of the retained austenite at and beneath the surface as can be seen in Fig.3.30.

3.2.3.d Observations of Cracks

Indentations from the SCF test were examined under the optical microscope. Photography and cracks length measurements were carried out through the digital camera. Estimation of cracks depth was made either by measuring the depth directly on sections cut through or near the indentations or by grinding and polishing the surface until cracks disappears and noting the depth of material removed. In the later method estimation of the depth was made by measuring a Vickers hardness indentation made in the vicinity of the indentation and using this as a reference for the thickness of the material removed.

3.2.3.e Contact Fatigue Cracks

Standing contact fatigue tests were carried out firstly for material in the hardened and tempered condition without further treatment. It was found that many tiny cracks were initiated around the indentation as a shown in Fig.3.31. Figures 3.32 and 3.33 show these cracks after etching and at higher magnifications, respectively. Surface

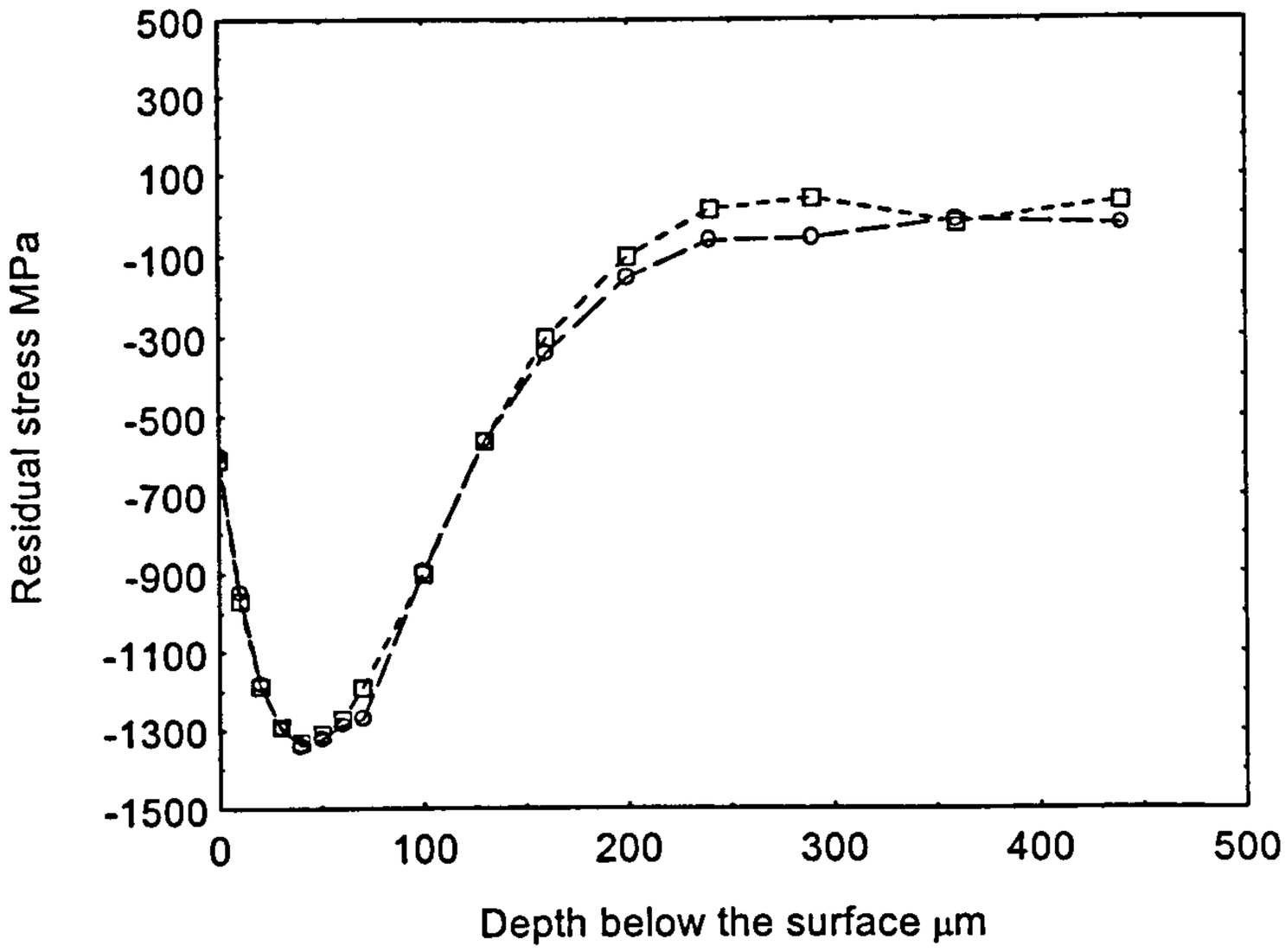

Fig.3.29 Residual stress profile in Ovako steel specimen after shot peening. High compressive residual stress induced at and beneath the surface

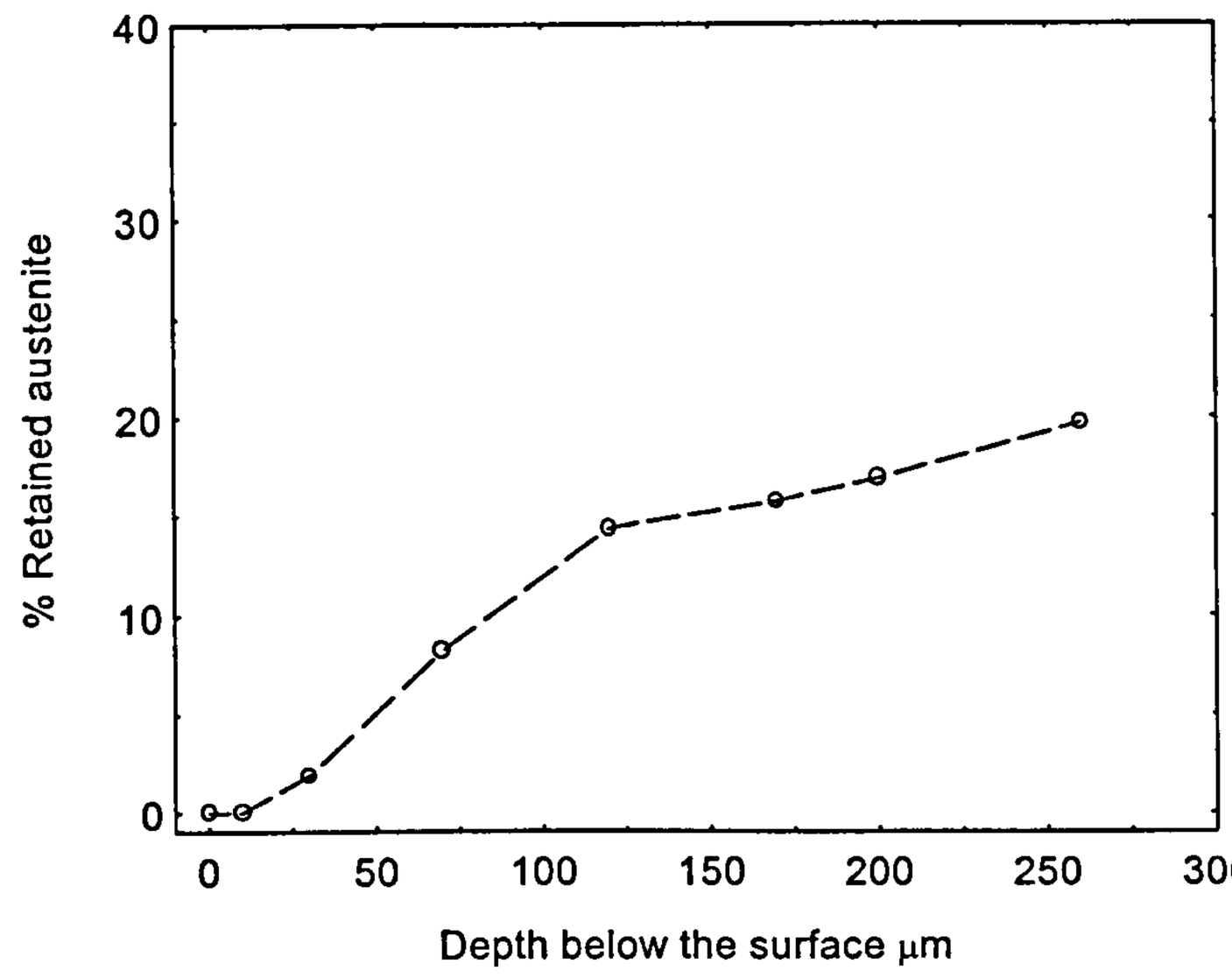

Fig.3.30 Retained austenite profile at the shot peened side. Complete austenite transformation due to the peening process occurs at the surface

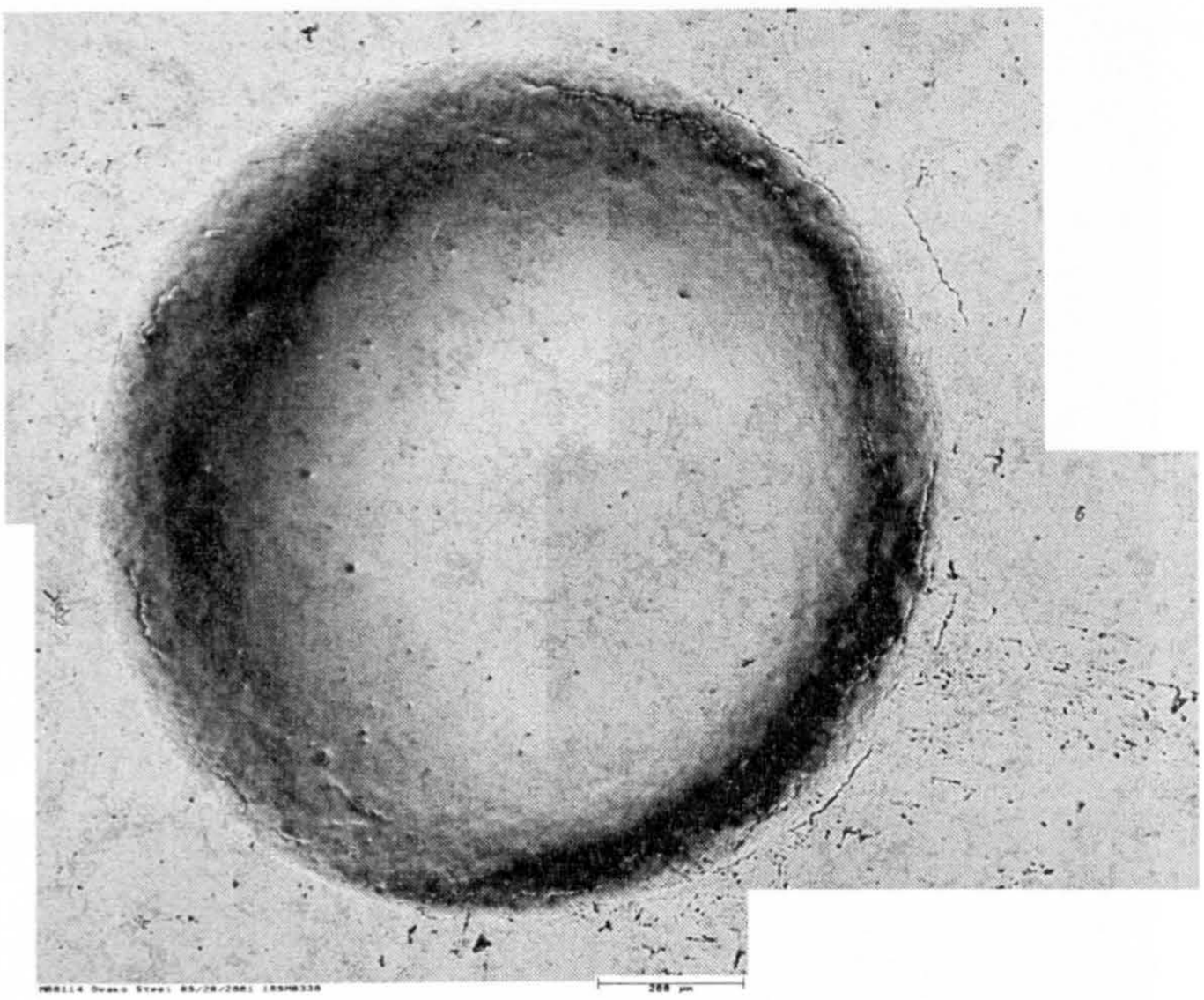

Fig.3 31 Specimen tested without surface repolishing. Test carried out for 3000 cycles at applied load of 6kN. Note the incomplete ring cracks near the periphery of the indentor

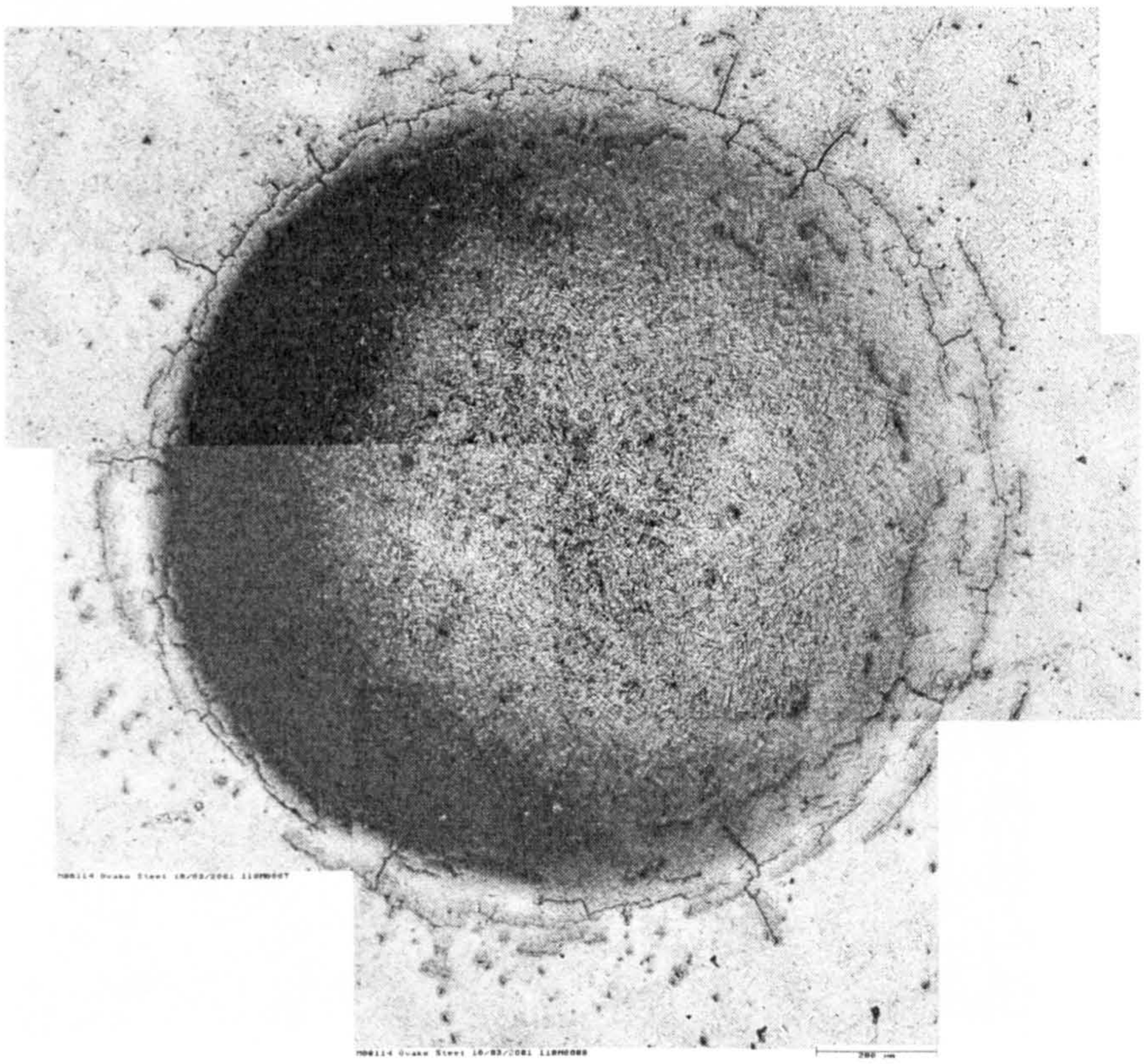

Fig.3.32 Specimen tested without surface repolishing. Test carried out for 5000 cycles at applied load of 8kN. Surface etched with 2% nital etch after test to reveal small cracks believed to be associated with oxidation of boundaries during heat treatment

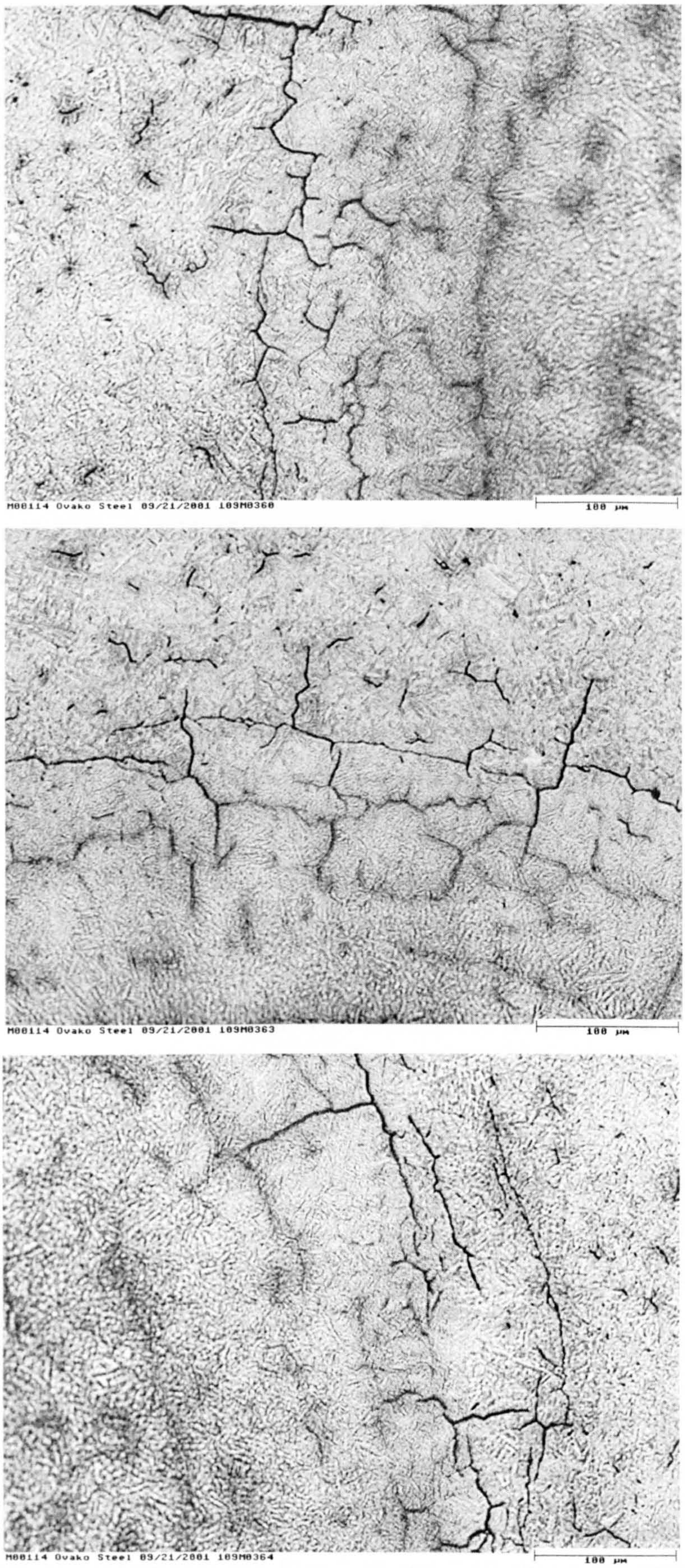

Fig. 3.33 Higher magnification for cracks shown in the previous figure.

repolishing after heat treatment was found to be effective in eliminating these tiny cracks around the indentation, which could be associated with oxidation of the prior austenite grain boundaries during heat treatment. Repolishing remove the internally oxidised layer.

Repolished specimens were tested in the load range from 2kN to 12kN for various numbers of cycles at a stress ratio of 0.1. Each indentation was examined to characterise any cracking that had occurred. For specimens tested at maximum load of 2 kN no cracks of any type were observed around the indentation as indicated in Fig 3.34 When the applied load was 4kN or higher both radial and tangential or ring cracks were produced. Figures 3.35-45 show samples for specimens tested at 4, 6, 10 and 12 kN. Both radial and tangential cracks are apparent around indentations in these tests. Radial cracks were found to be much deeper than ring cracks. Cuts made through radial cracks in some samples to reveal depth of radial cracks are shown in Figs.3.39, 3.40 (b) and 3.44 (b). these results contrast with those of Alfredsson and Olsson (1999; 2000) who found that ring cracks were predominant with only small numbers of radial cracks.

Successive surface polishing was made for other samples to determine the depth of ring cracks. Figs.3.42 shows a series of photographs represent successive stages in surface polishing until disappearance of ring cracks. Radial cracks were in the order of a millimetre in depth while ring cracks were less than 70 μ m in depth.

Cross sections made through indentations revealed the presence of cracks within the indentations, which could be initiated by fretting mechanism or could have resulted from growth of radial cracks initiated outside the indentations. These cracks have comparable depth to radial cracks and may branch to produce lateral cracks underneath indentations as shown in Figs.3.36 and 3.45.

The total lengths of radial and tangential cracks were measured for each test. Total length of radial cracks and tangential cracks are plotted versus number of test cycles. Figures 3.46 and 3.47 show the results for the 12 kN applied load for radial and tangential cracks respectively and Figs.3.48 and 3.49 shows the results for the entire range of applied loads. Cracks were found to initiate at early stages of the test namely

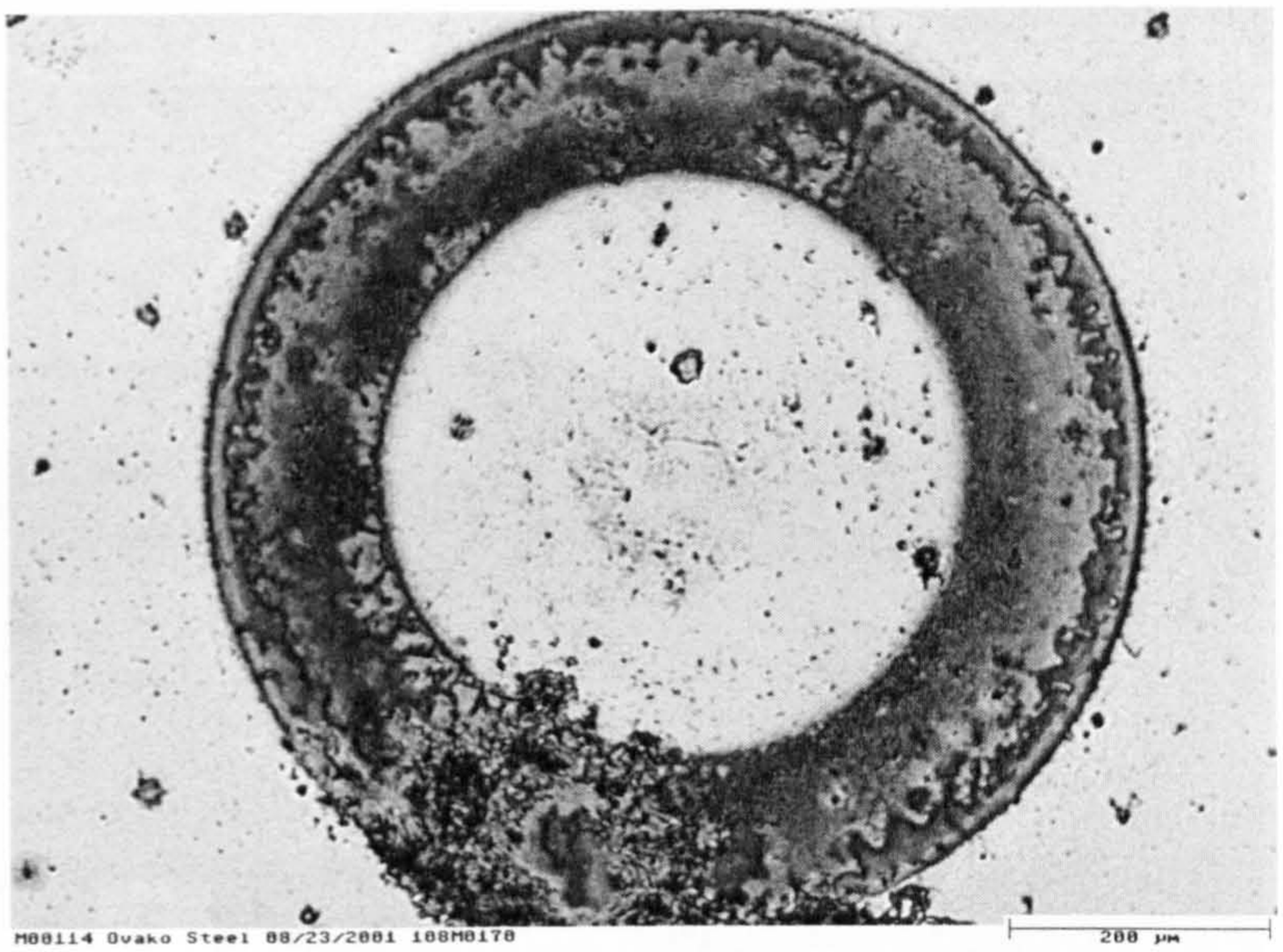

Fig.3.34 Specimen cycled between 2 and 0.2 KN for 5 million cycles. No cracks were observed at this level of applied load

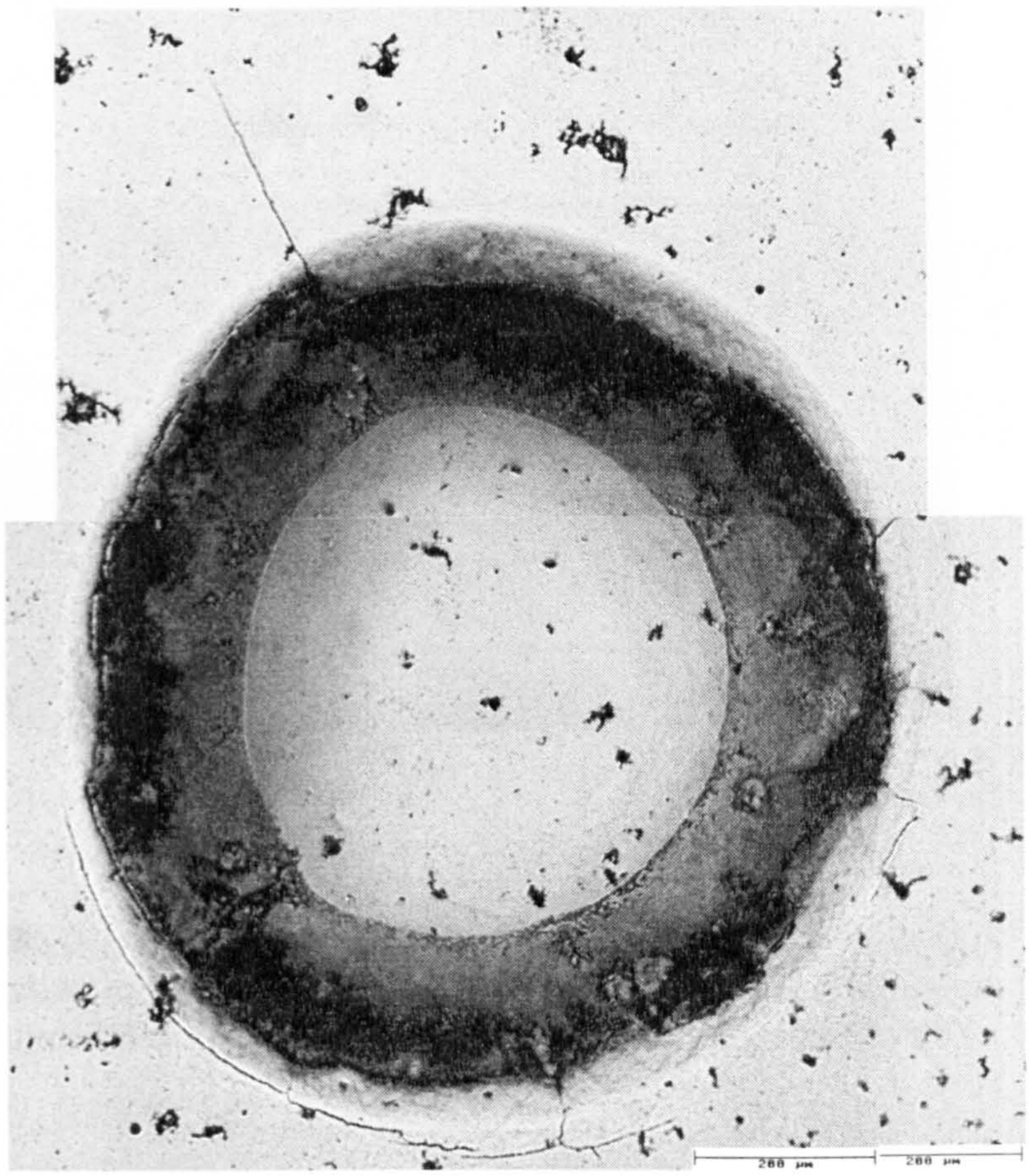

Fig 3.35 Indentation produced during cyclc loading between 4 kN and 0.4 kN for 2 million cycles. Radial and ring cracks can be seen

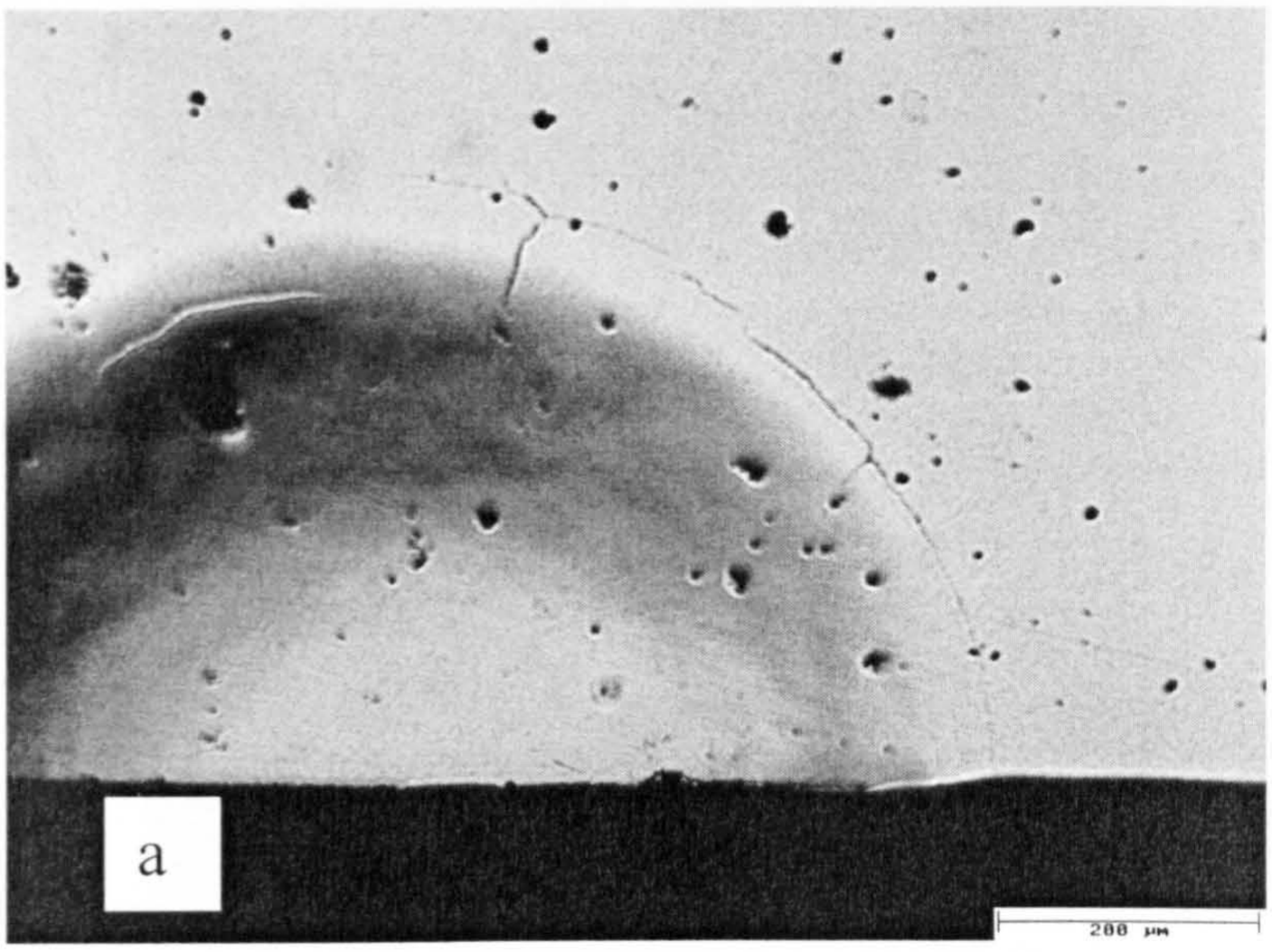

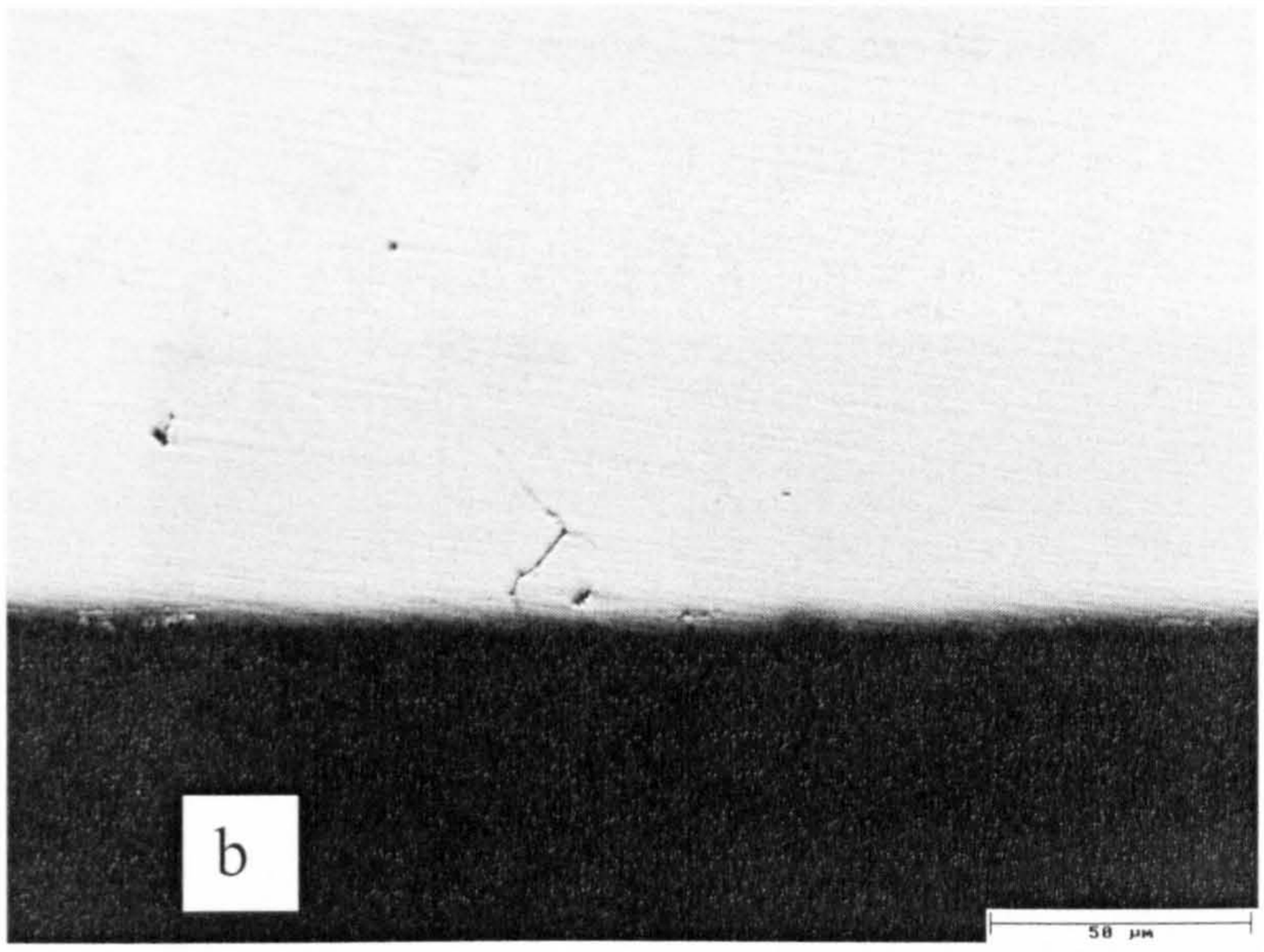

Fig.3.36 (a-b) Cross section through indentation made with 4kN. Note fretting crack inside indentation (a). Depth of the fretting crack produced during the test. Ring cracks were very shallow (b).

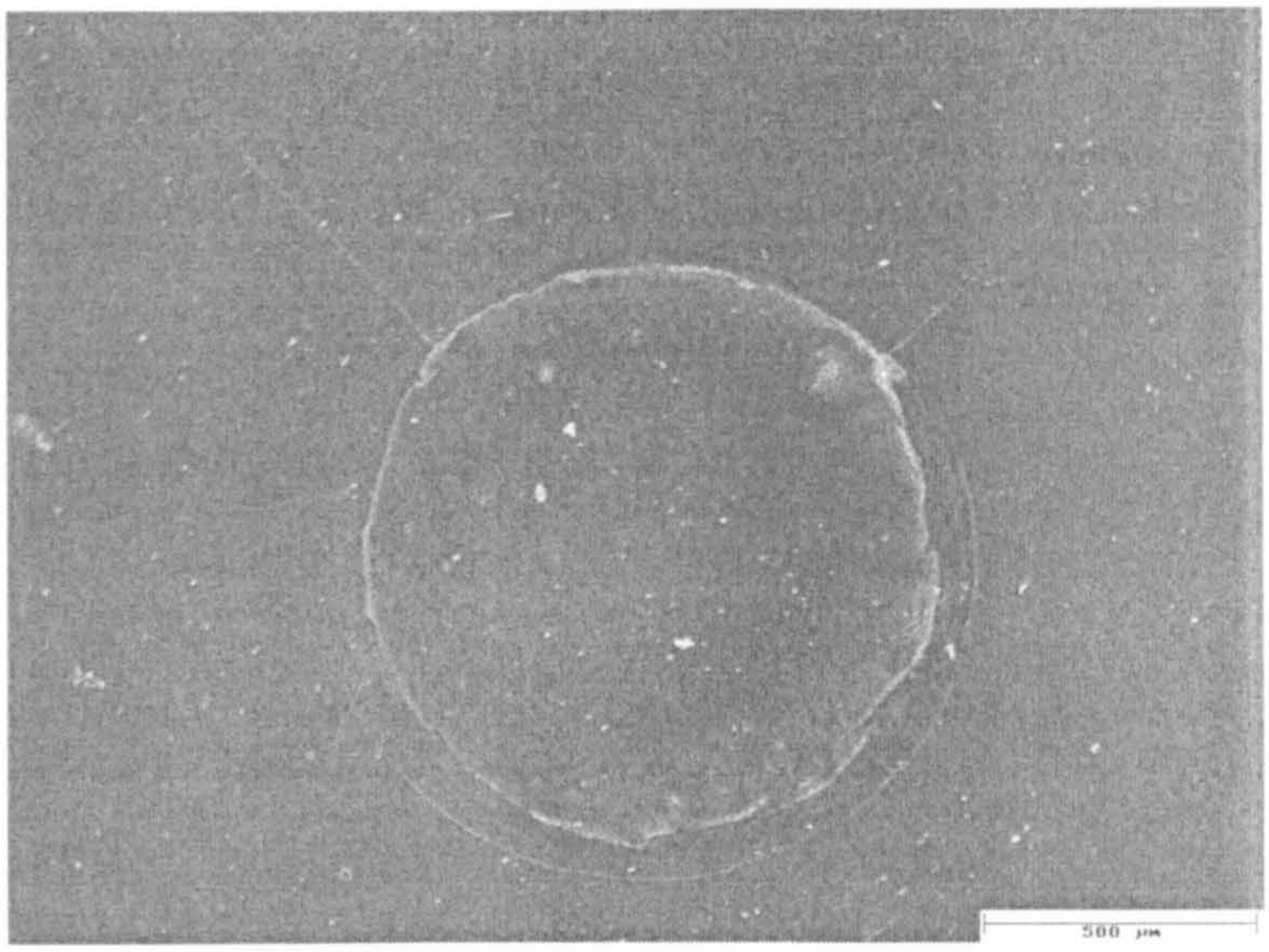

Fig.3.37 Indentation produced during cyclc loading between 6 KN and 0.6 KN for 1500000 cycles. Radial, ring and fretting cracks can be seen

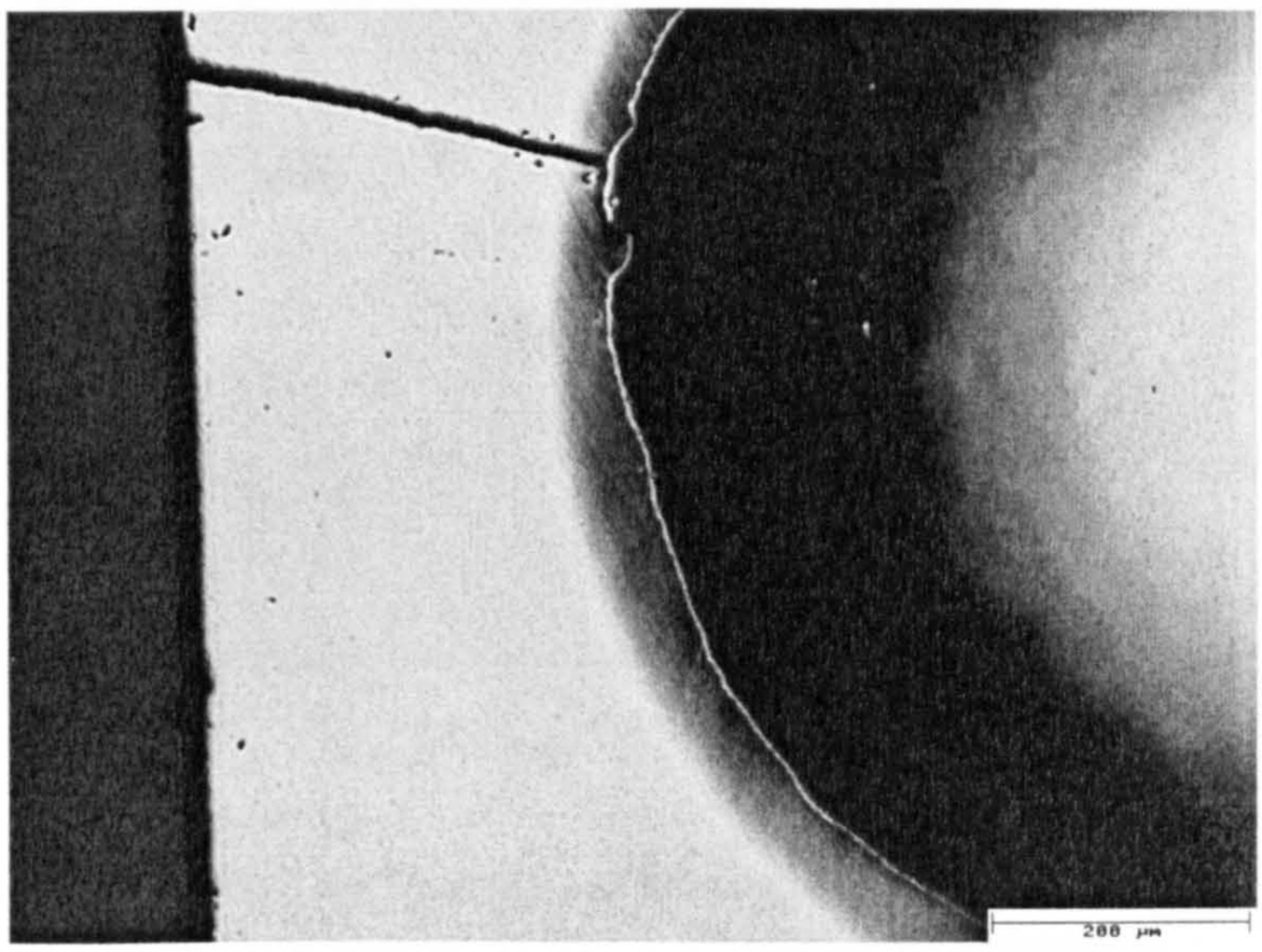

Fig.3.38 A section made across one of the radial cracks shown in previous figure

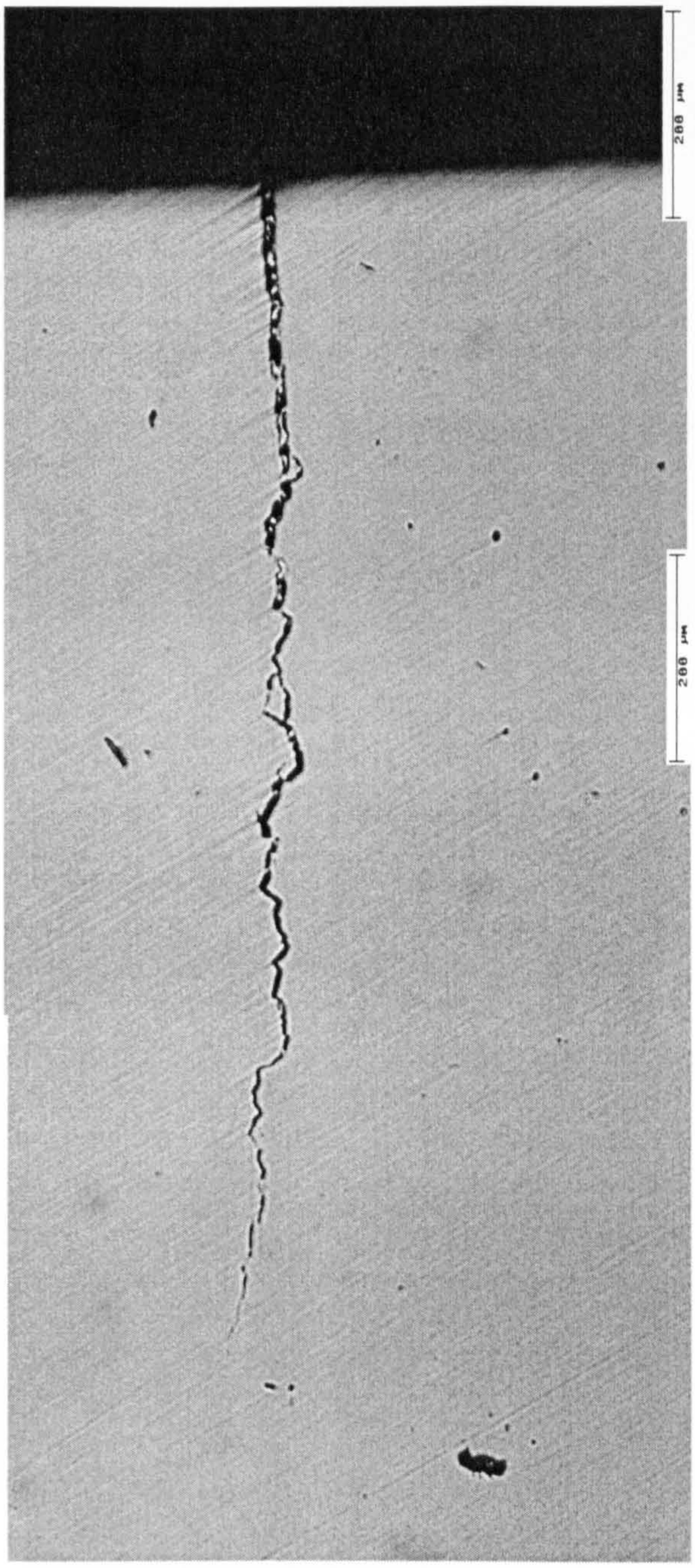

Fig.3.39 Polished surface reveal the depth of the radial crack of indentation shown in Fig.3.37-6kN-150000cycles

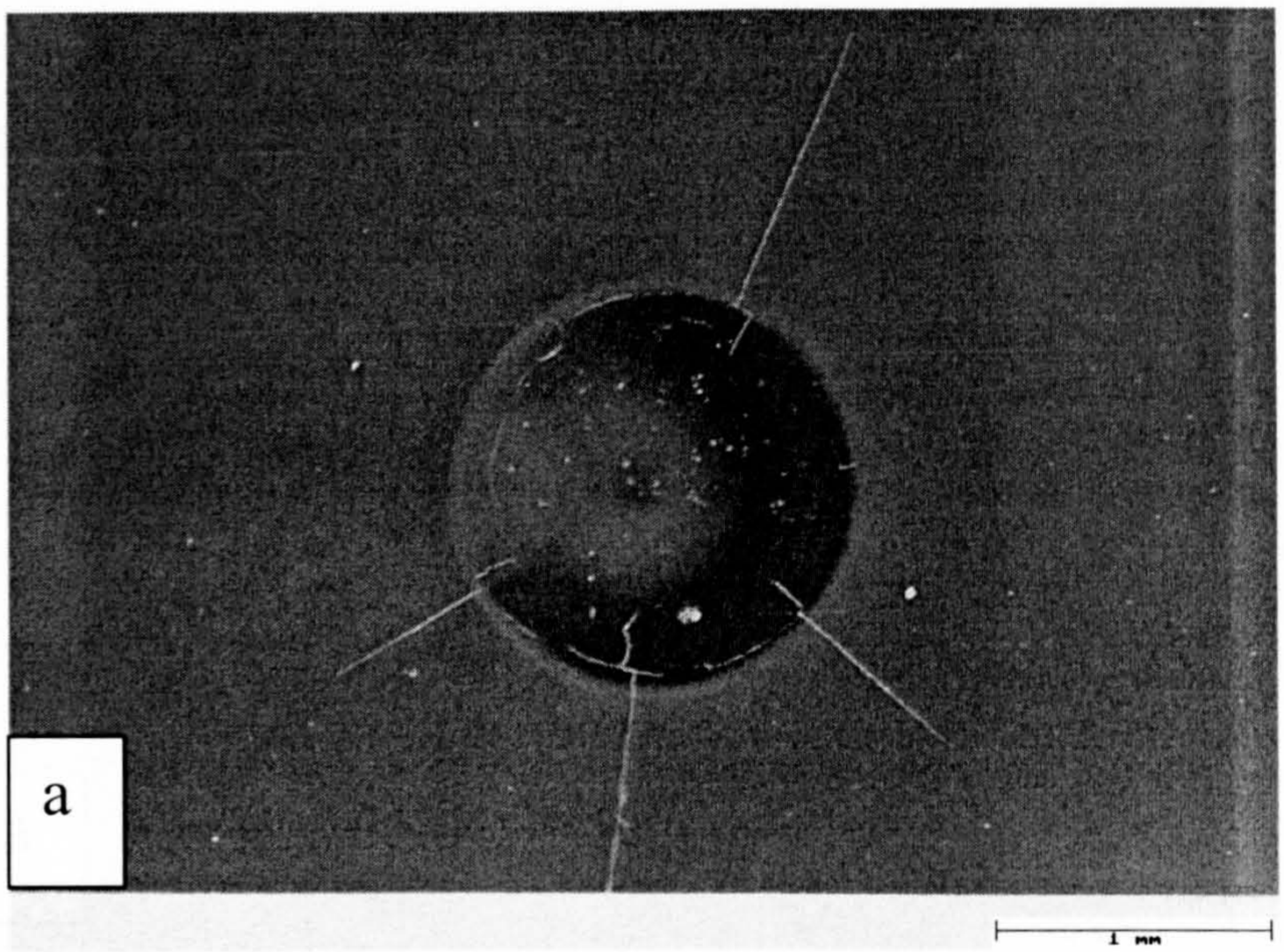

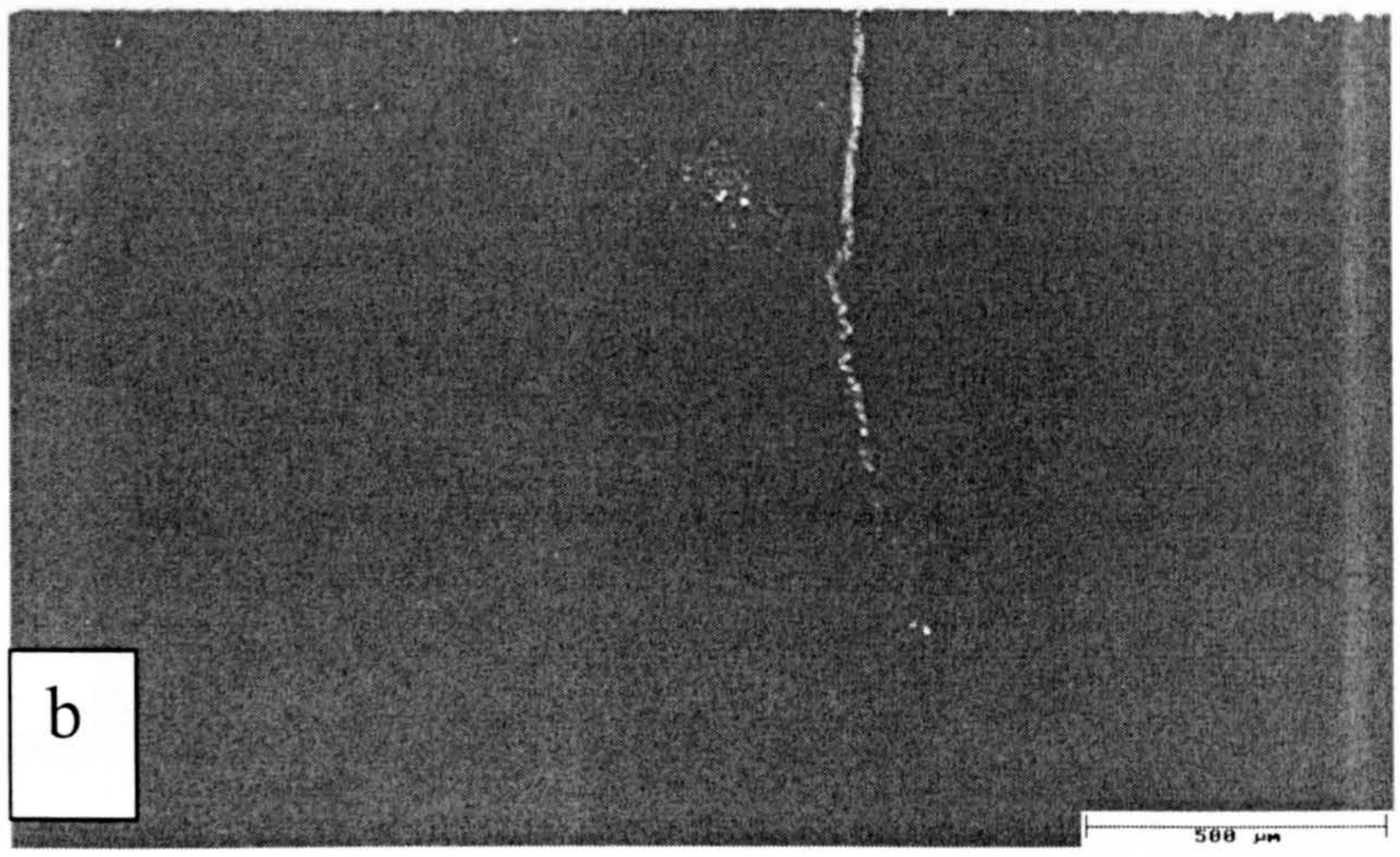

Fig.3.40 (a&b) Specimen loaded at 10 kN for 150000 cycles. A section was made across a radial crack in (a). Depth of the radial crack (b)

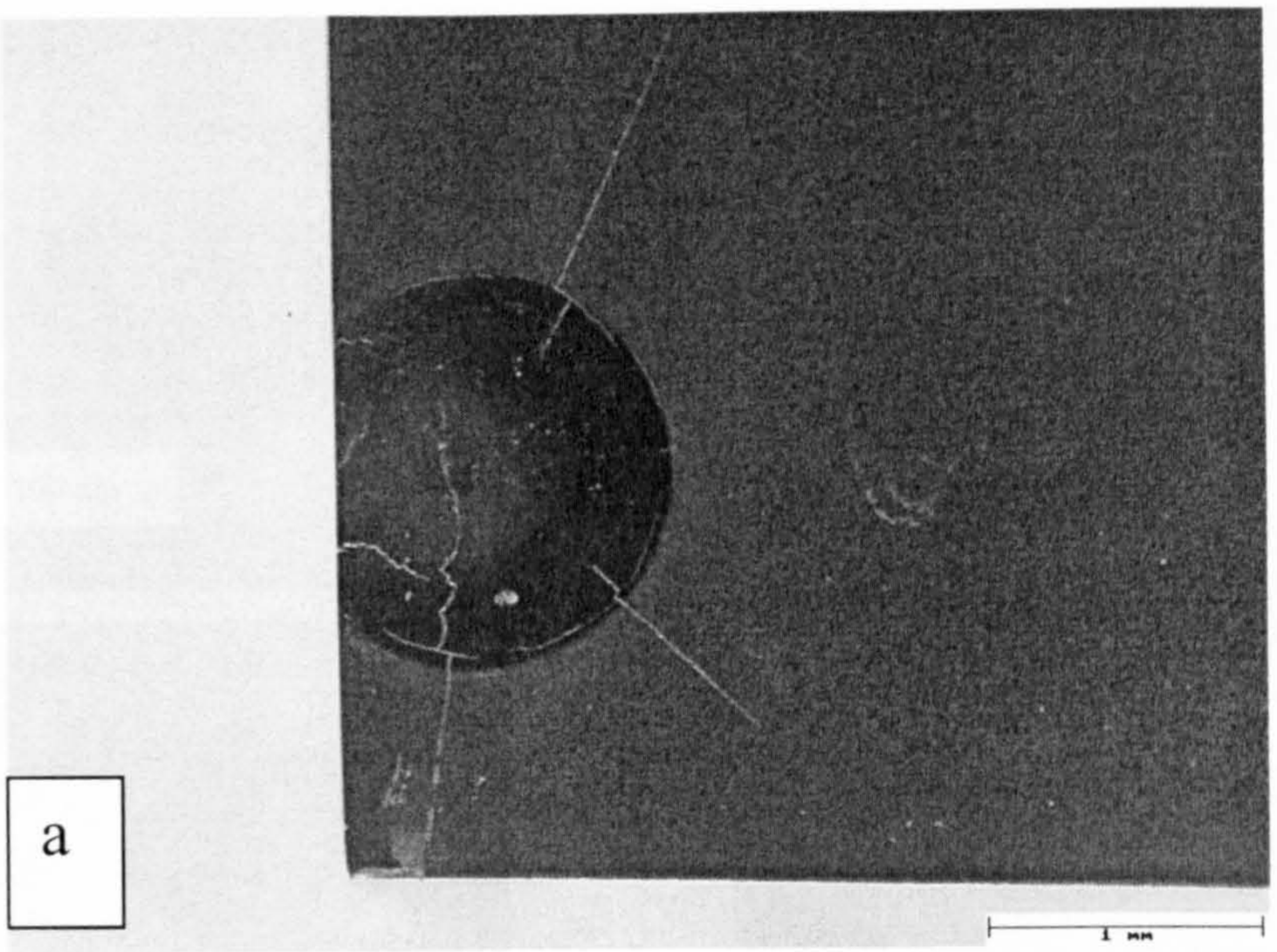

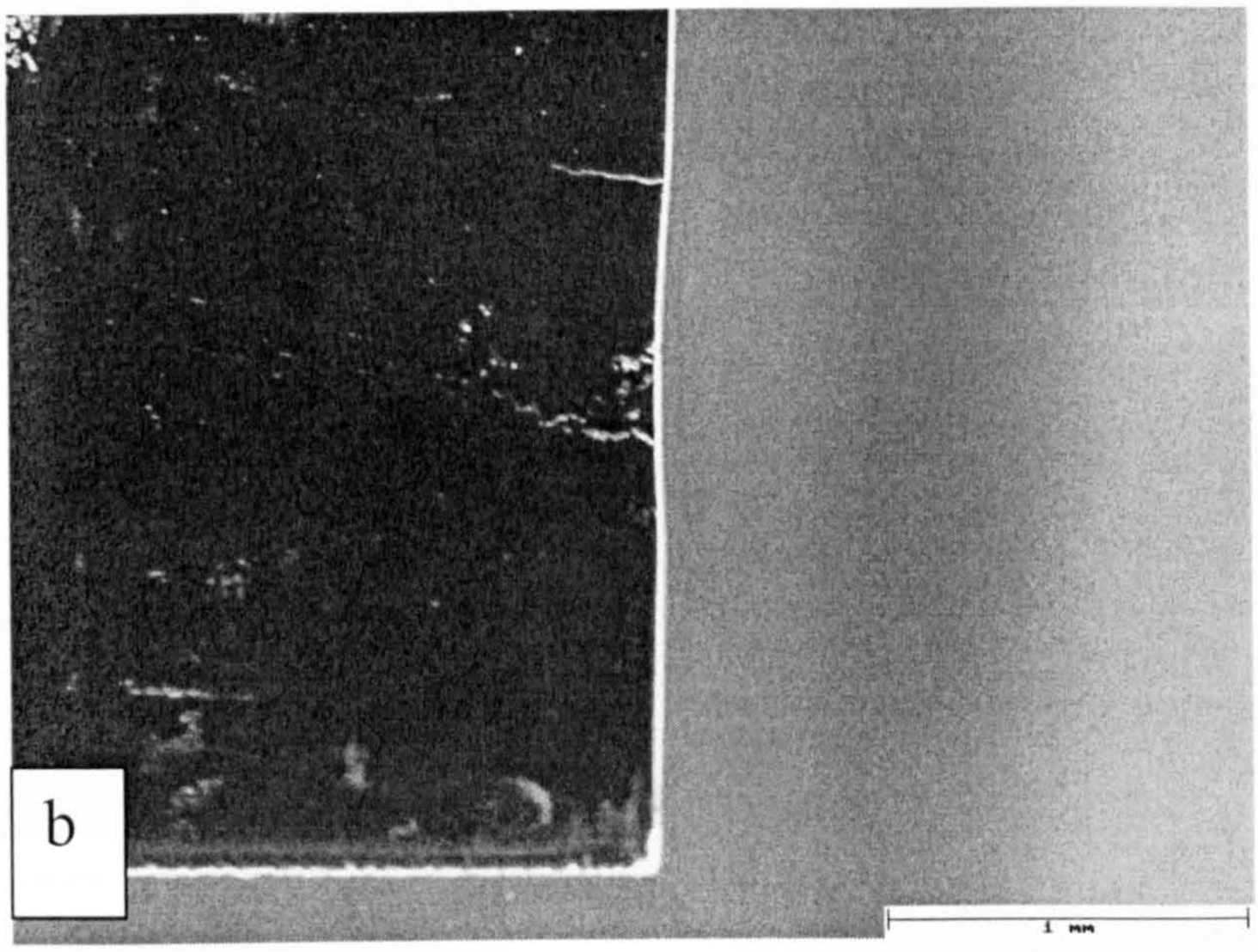

Fig.3.41 (a&b) Specimen loaded at 10 kN for 150000 cycles. Note the cut made cross fretting crack in (a). Depth of the fretting crack (b)

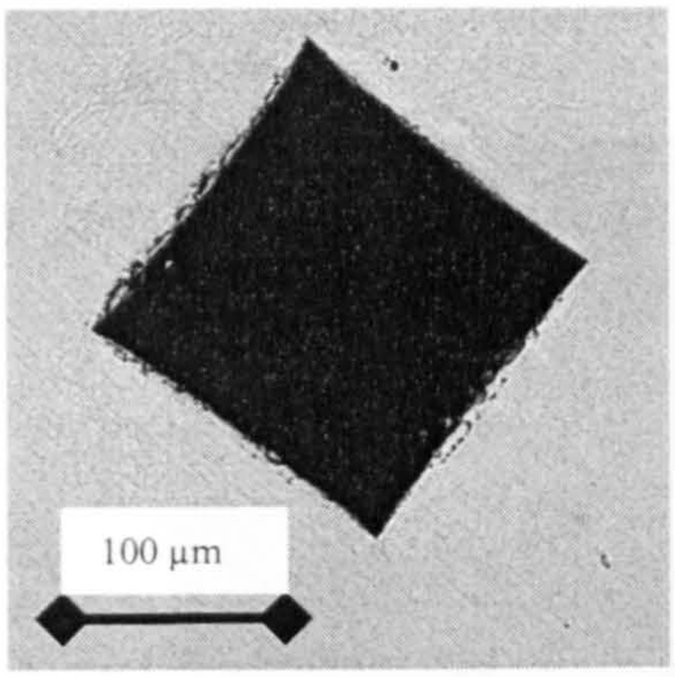

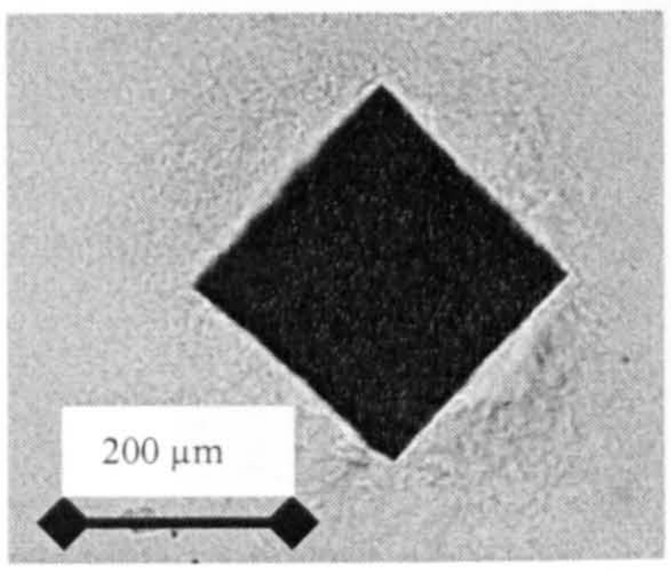

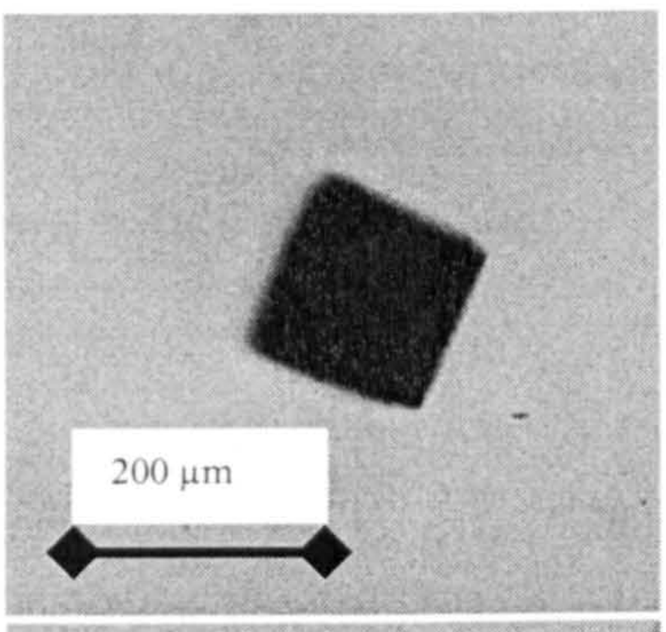

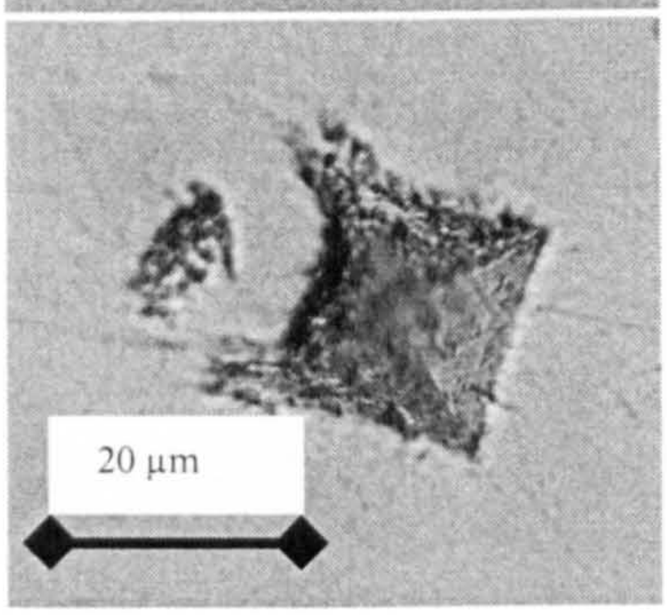

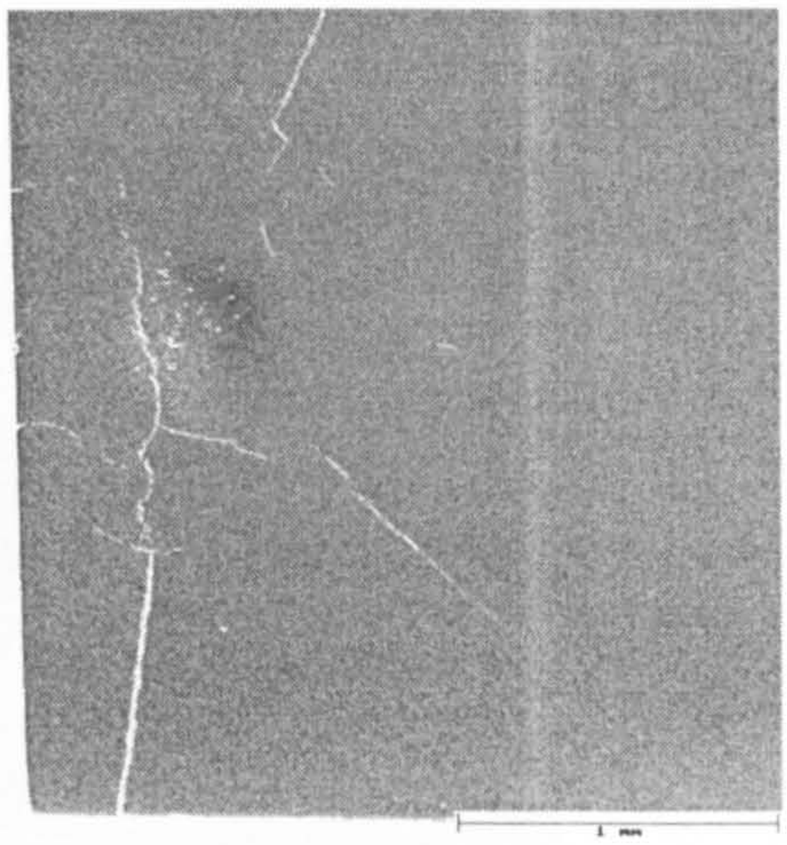

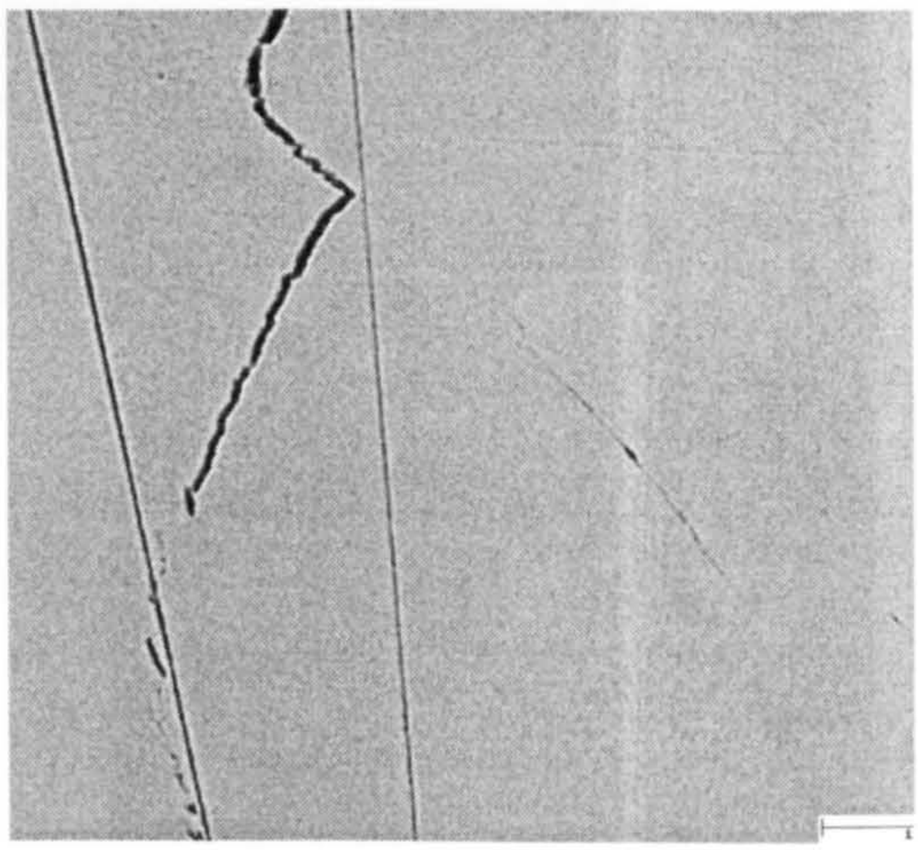

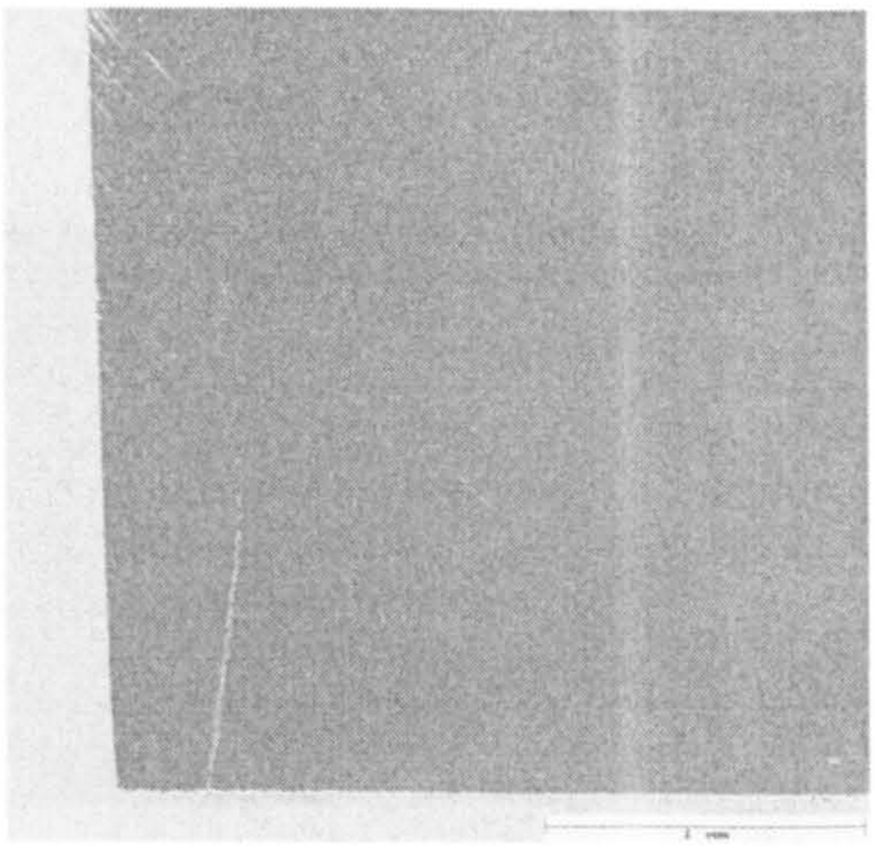

Fig.3.42 measuring the depth of the ring crack for indentation in Fig 4.40 by surface polishing. Depth of layer removed was measured via the shrinkage of indentation size and knowing the diameter to depth ratio for Vickers indentation.
Left column shows size of indentations through out the grinding and polishing process. The upper most indentation was completely removed in the process. Other indentations represent successive stages in the second indentation during surface removal.
Right column shows the indentation before polishing, during surface removal and after ring cracks had disappeared. Crack depth estimated to be about 70 μm

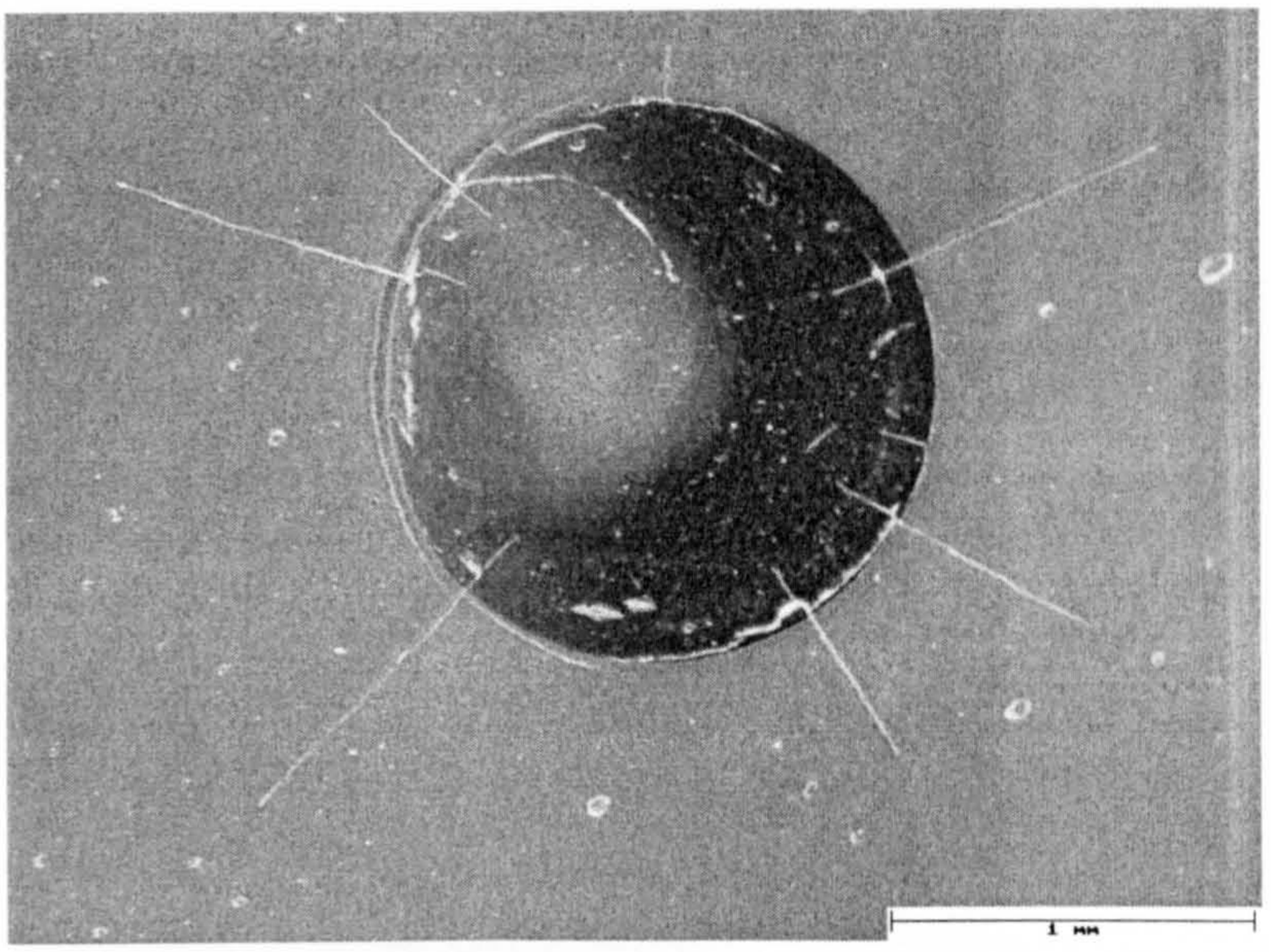

Fig.3.43 Indentation due to applied load of 12 kN and 50000 cycles resulted in radial and ring cracks

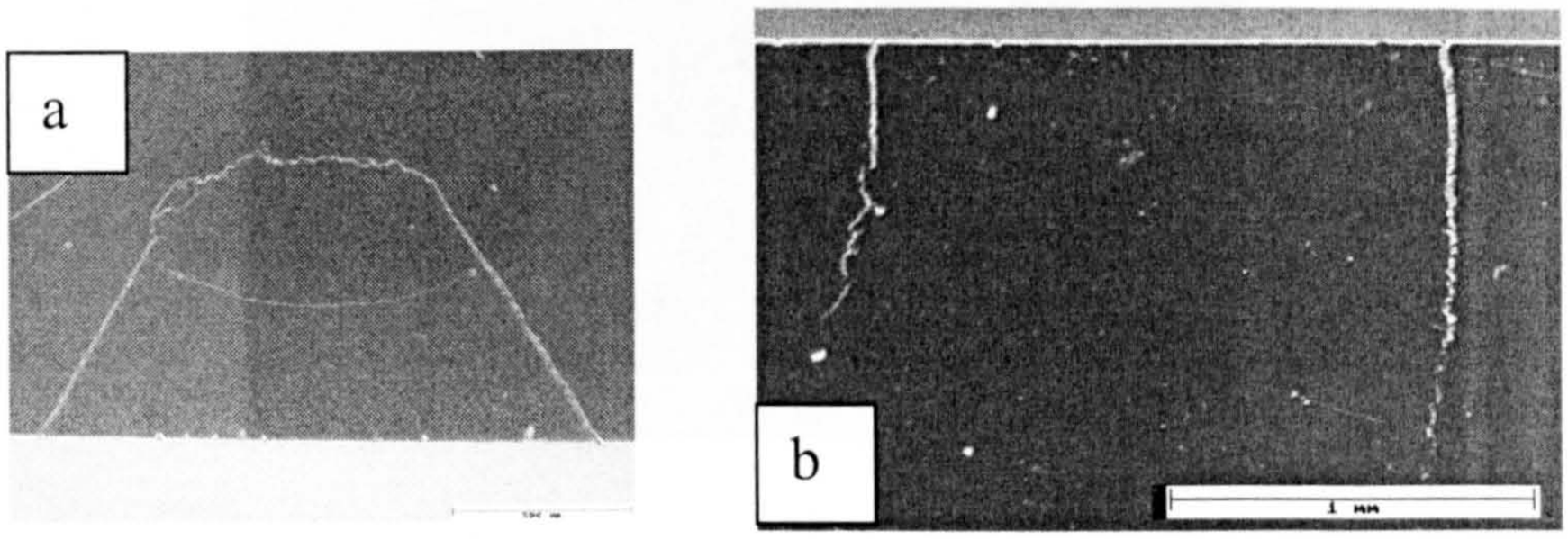

Fig.3.44. Depth of radial cracks. Cut cross two radial cracks shown in previous figure (a). Depth of the two radial cracks (b)

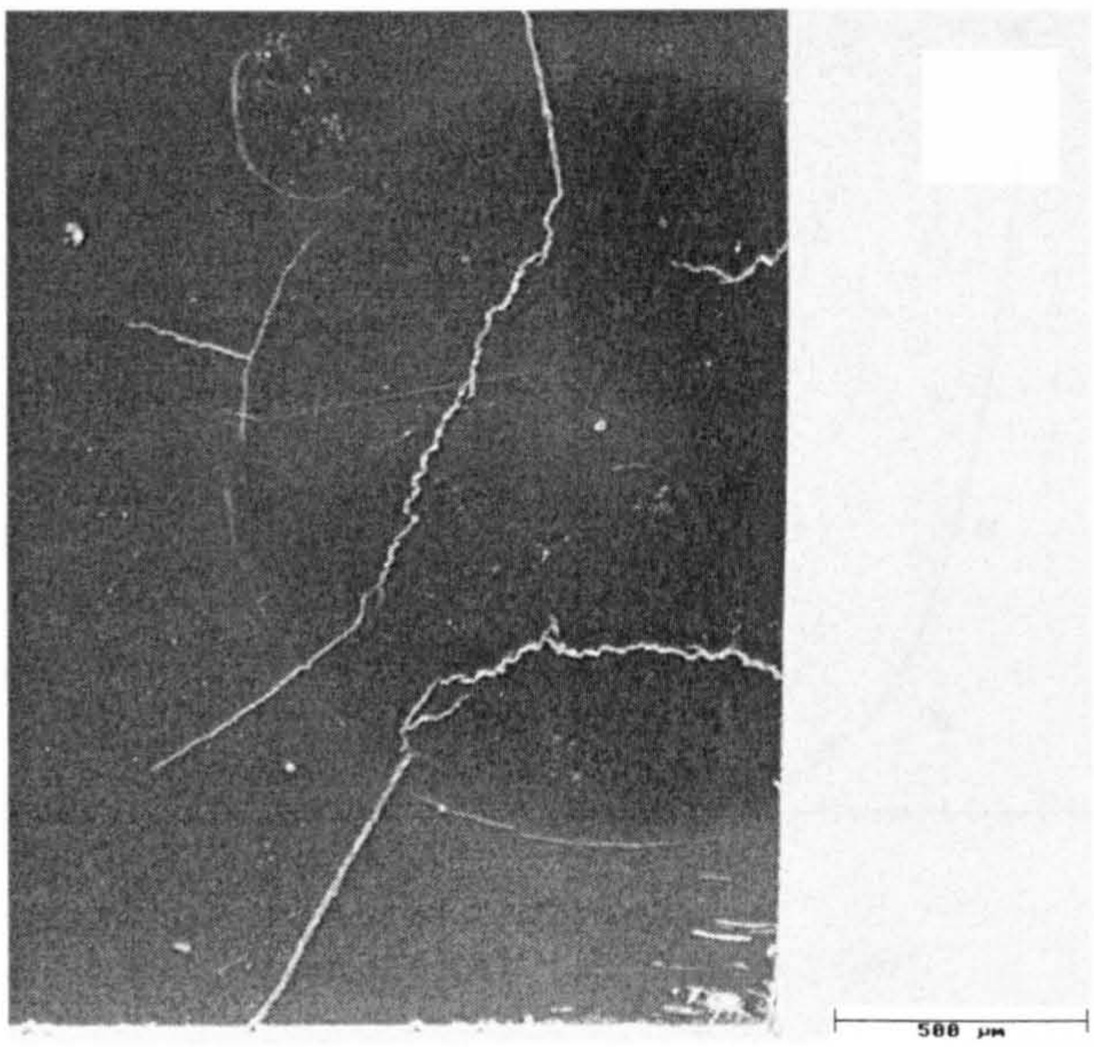

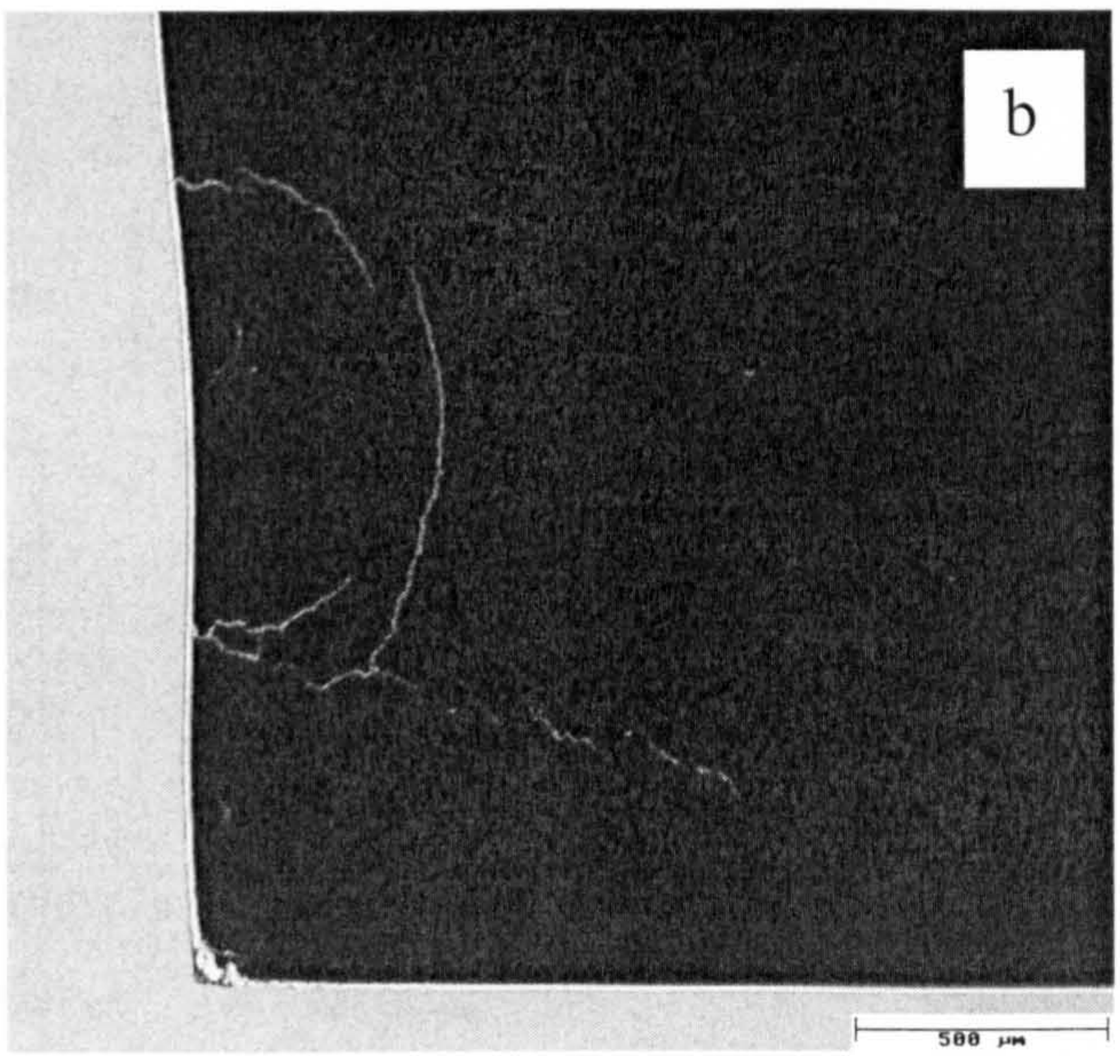

Fig.3.45. Another cut made at right angle to the first one shown in Fig.4.42 cutting through ring and fretting cracks(a). Fretting cracks could penetrate deep beneath the surface and branch to lateral cracks. Ring cracks are much shallower (b)

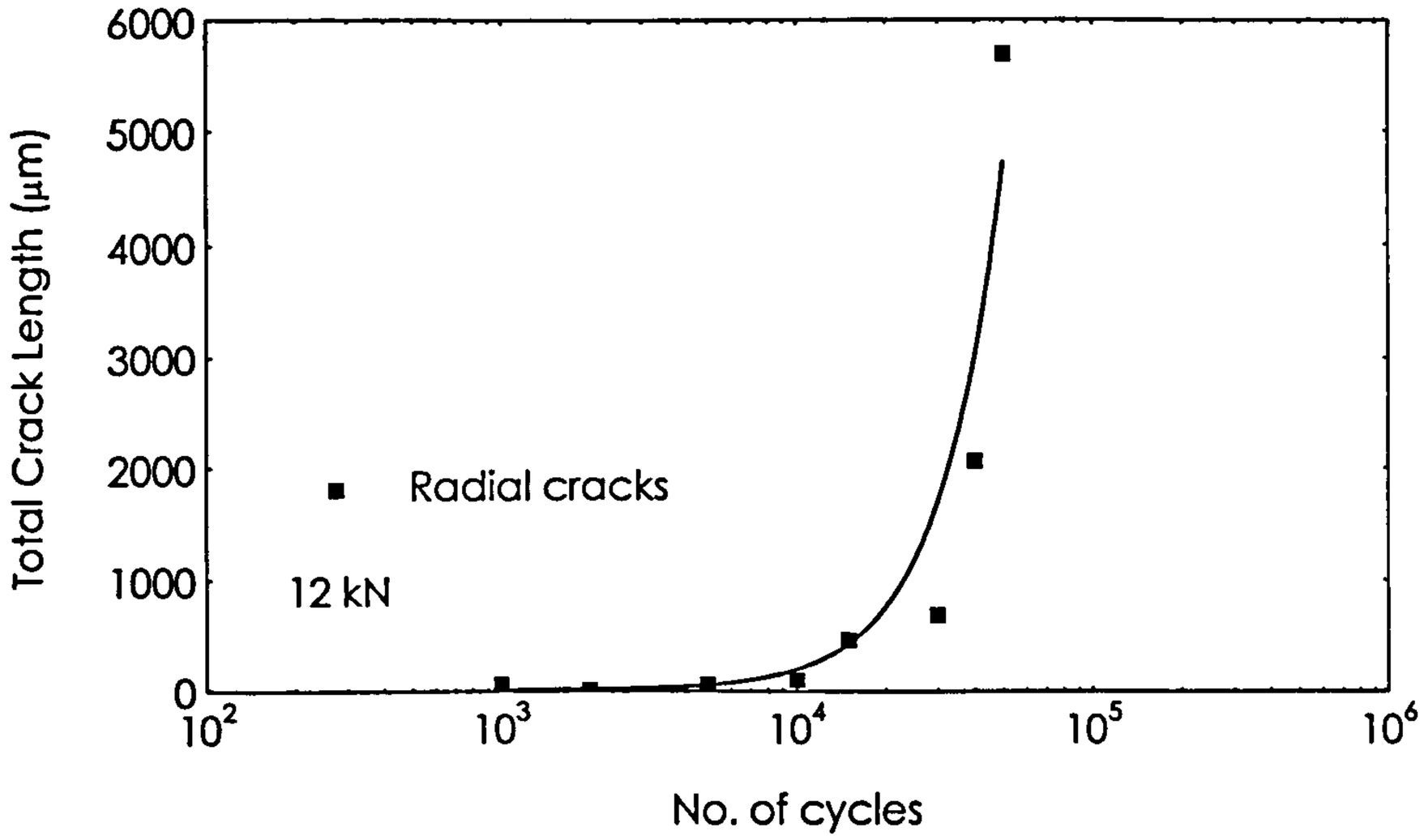

Fig.3.46 Total radial crack length versus number of cycles at applied load of 12 kN. The line represents a fitted curve

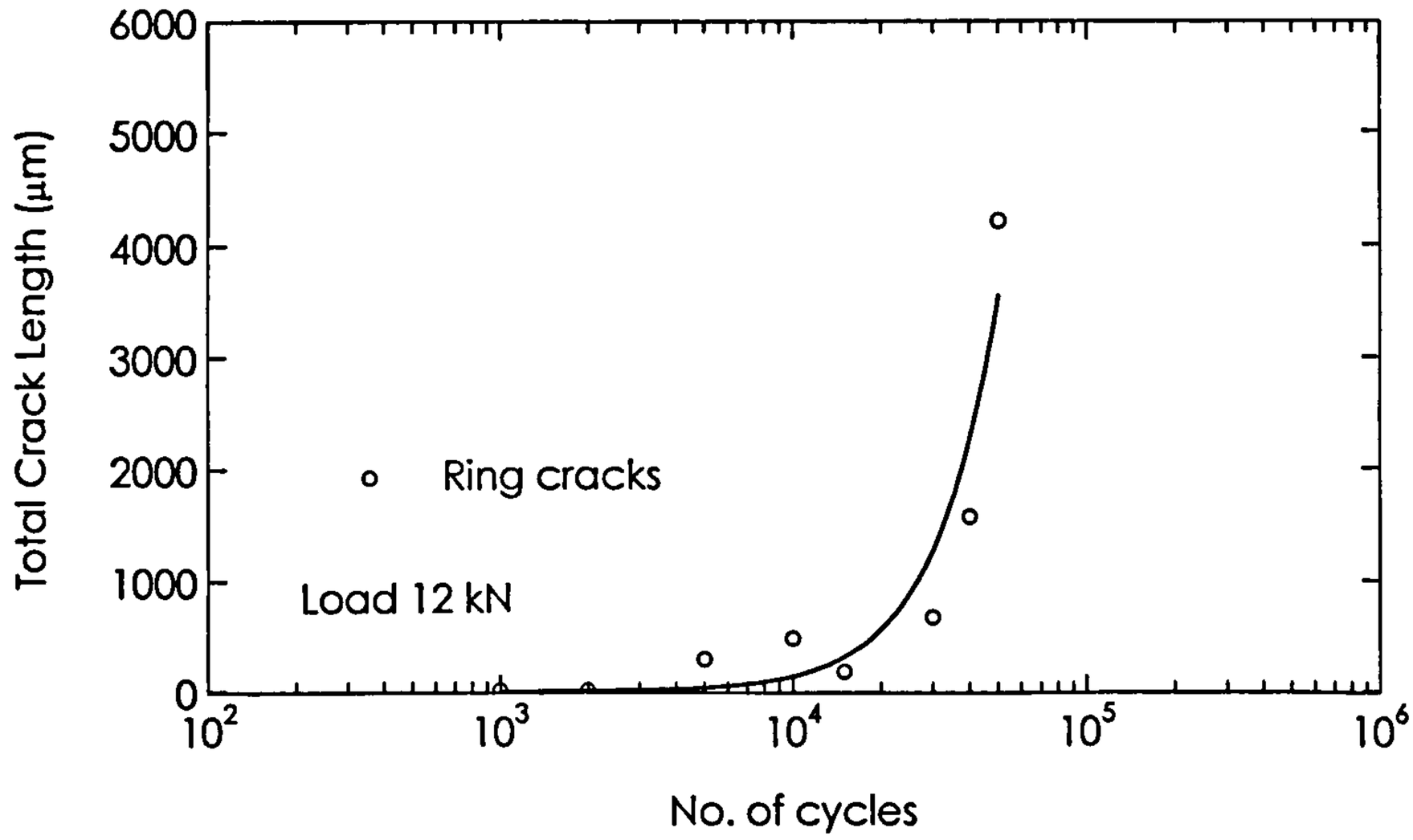

Fig.3.47 Total ring crack length versus number of cycles at applied load of 12 kN. The line represents a fitted curve

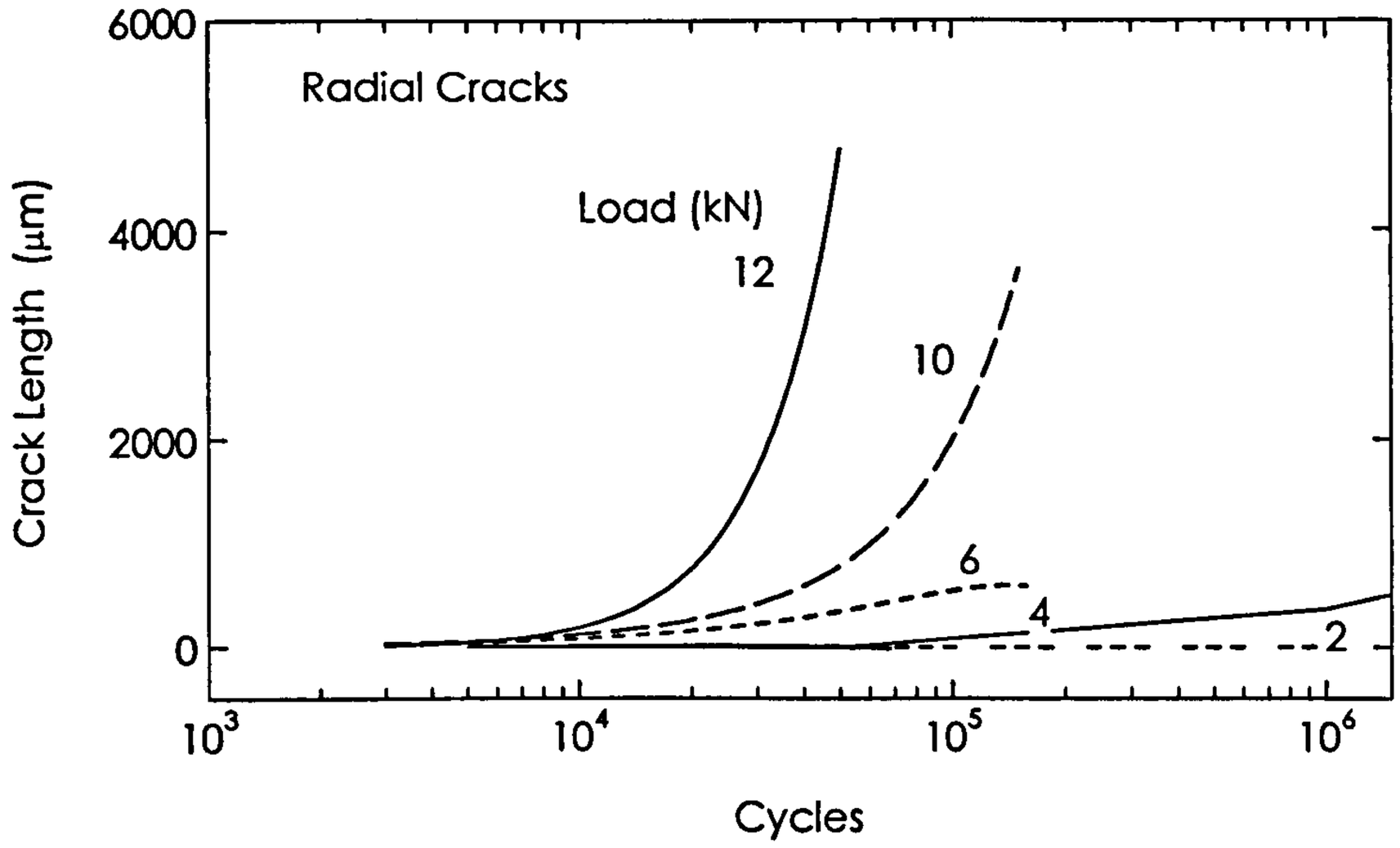

Fig.3.48. Total radial crack length versus number of cycles for the entire range of applied loads. Crack growth rate increases as the applied load increased. The effect is more pronounced above applied load of 6 kN. The curves fitted to discrete results

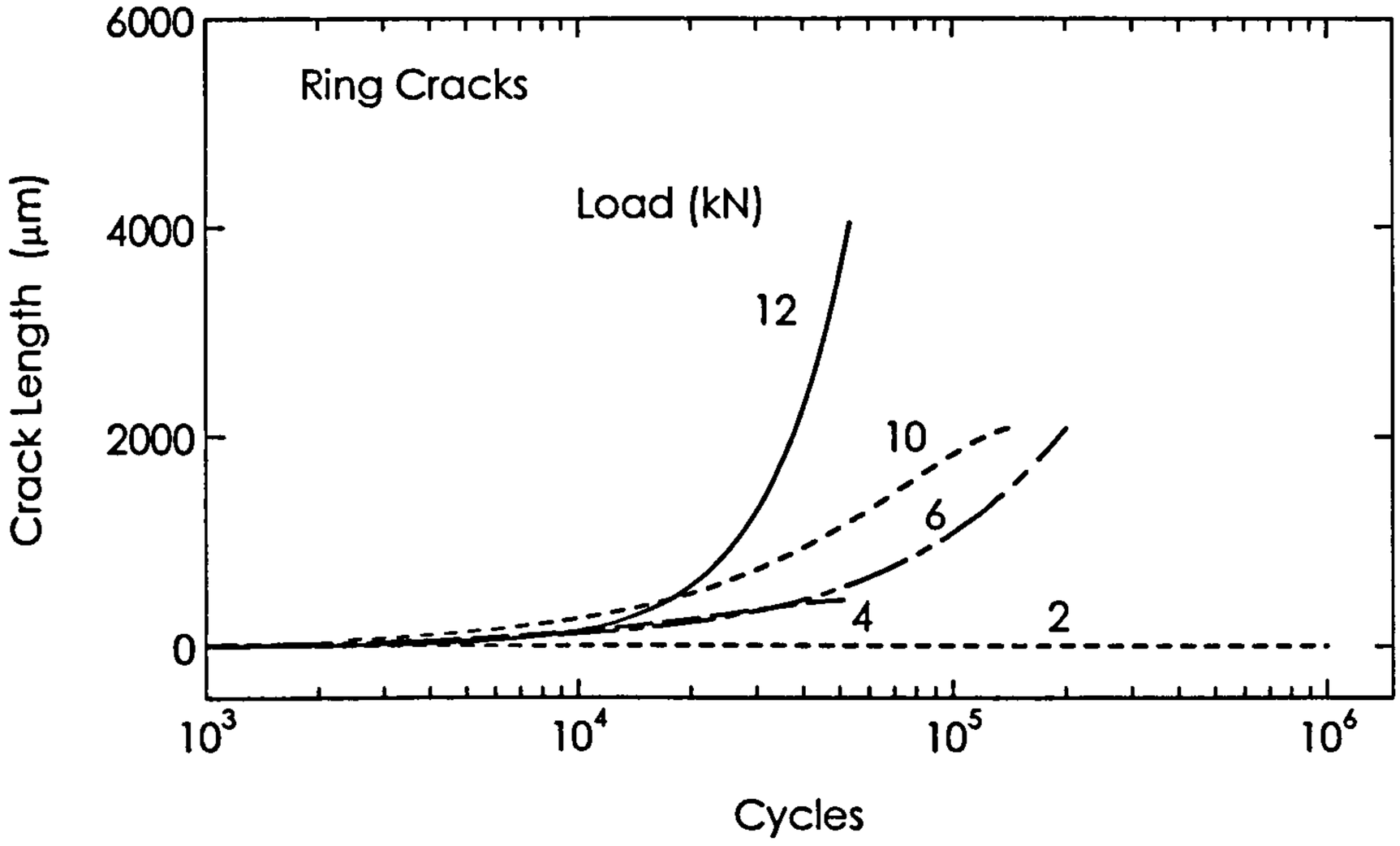

Fig.3.49. Total ring crack length versus number of cycles for the entire range of applied loads. Trend of growth is similar to radial cracks. The curves fitted to discrete results

at about1×10^3 to 10^4 cycles. Cracks then propagate at different rates depending on the applied load. As the applied load increases the growth rate increased. The effect of increasing applied load on crack growth rate propagation was as expected as the hoop residual stress induced by indentation was found to increase with increasing applied load (Fig.5.19 section 5.4.3). However, residual stresses in the radial direction after indentation were found to be compressive. This means that ring cracks should not be produced in these tests especially at higher loads where the resultant residual stresses become more compressive. It should be emphasised at this point that residual stress measurements shown in (Fig.5.19 section 5.4.3) represents the average stress on a circular area of 0.8mm diameter and not at a specific point.

Shot peened specimens were tested at the higher levels of the testing load range and for greater number of cycles compared with un-shot peened specimens. This is due to the improved resistance against surface fatigue cracks manifested by shot peened specimens. No radial cracks were formed in shot peened specimens. Figs.3.50 shows indentations and ring cracks produced under 12 kN tested for one million and ten millions cycles respectively. The high compressive residual stress induced by the shot peening process should oppose any crack formation around indentations. Examinations of cross sections made through indentations showed that there are no fretting or lateral cracks produced in shot peened specimens as can be seen from Fig.3.52. However ring cracks still appear around indentations. Cross sections cut through indentations showed that depth of ring cracks in both specimens were almost the same as shown in Figs.3.53. The depth of ring cracks was about 40 μm. Ring cracks seems to be arrested at this depth which corresponds to the depth of the maximum compressive residual stress induced by the shot peening process.

3.2.4 Analyses of Stresses in Standing Contact Fatigue

The results of the standing contact tests are difficult to interpret because of the uncertainty about the local stresses developed in loading and un-loading an elastic-plastic material. At first sight this appears surprising in view of the fact that indentation of a flat specimen by a hardened ball has been studied for many years. However, a reading of the literature demonstrate the uncertainty about the stresses developed near

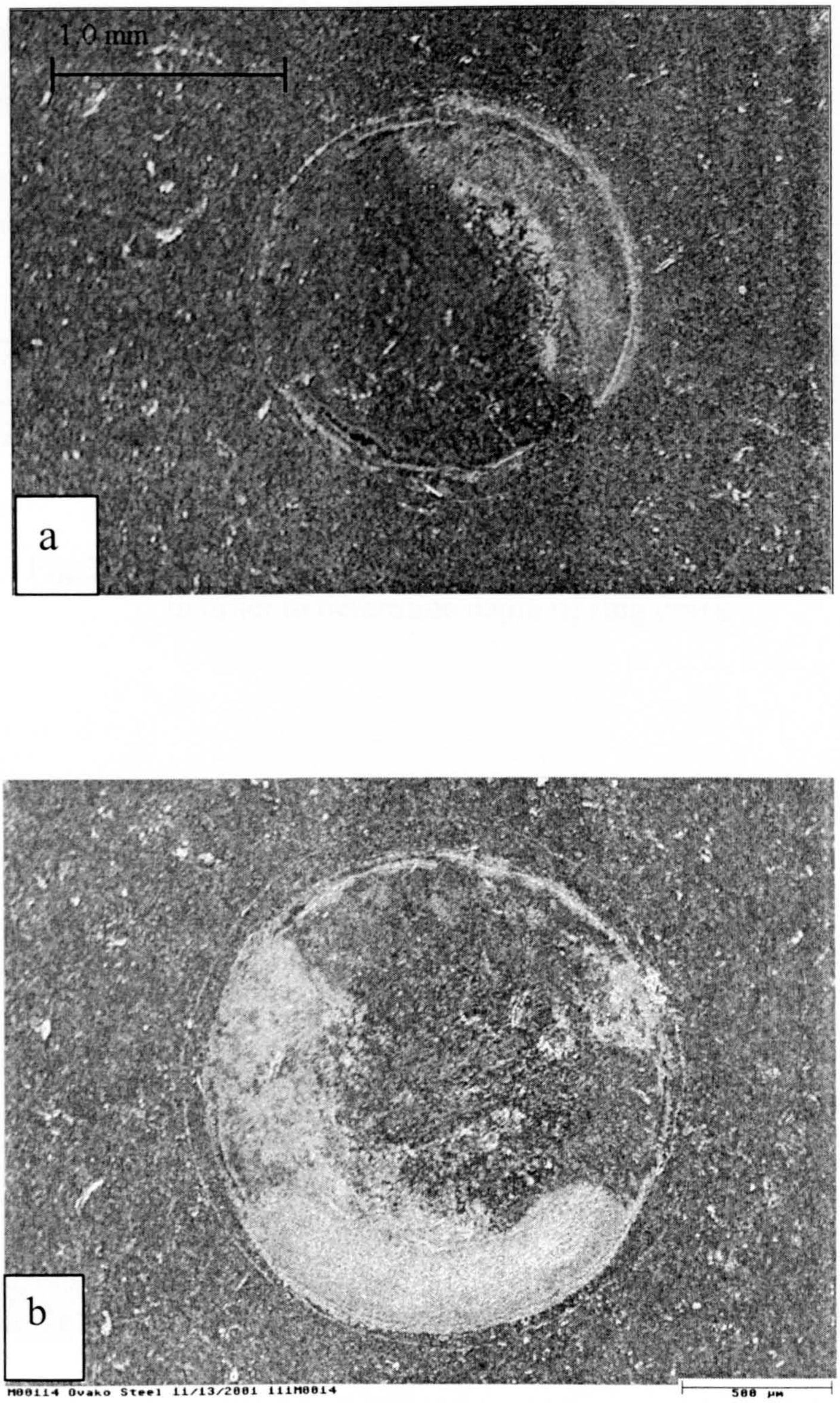

Fig.3.50 Indentations after applied load of 12kN on shot peened specimens. Tested for 1×10^6 cycled (a) and 10×10^6 cycles. No radial cracks produced in either test

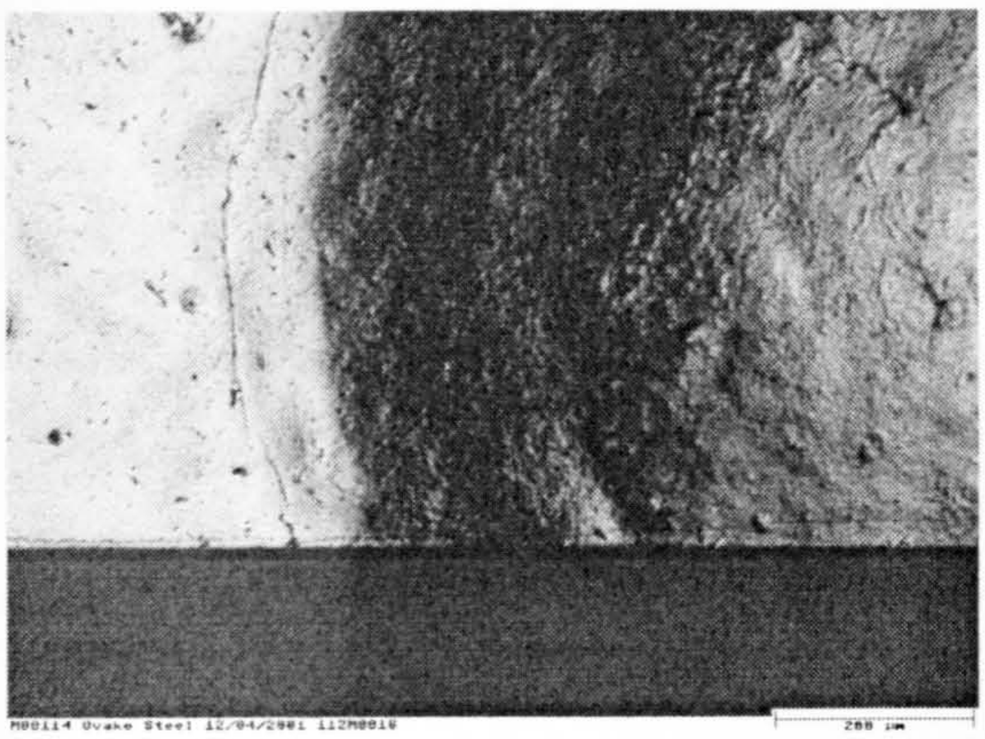

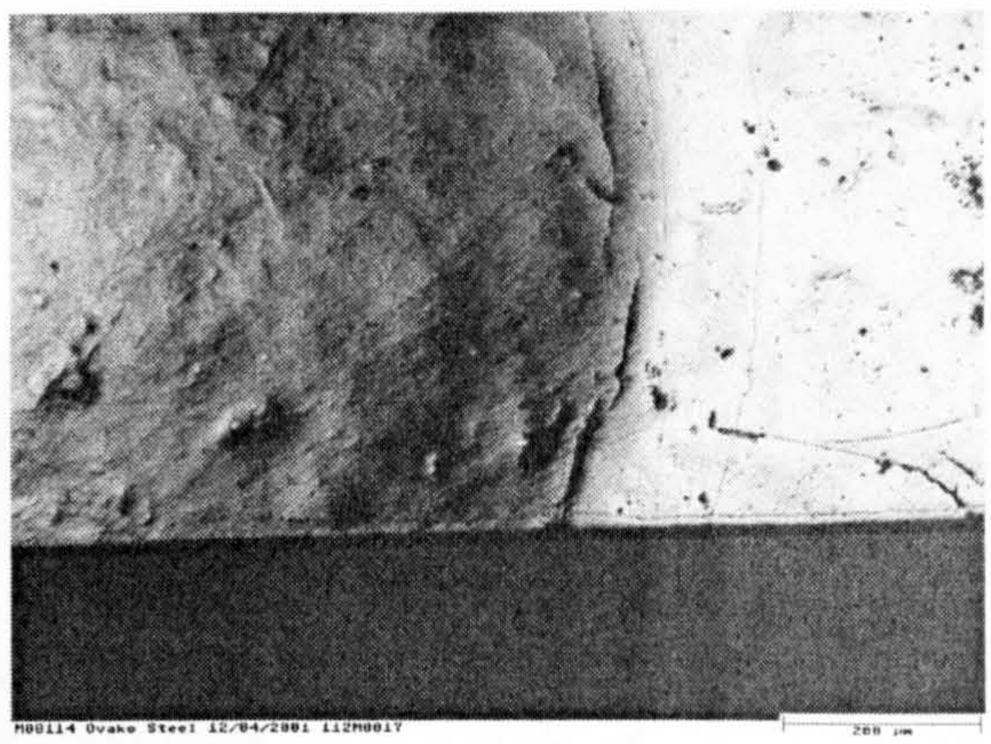

Fig.3.51 Cut made cross indentation shown in figure 3.50(b) in order to determine depth of ring crack

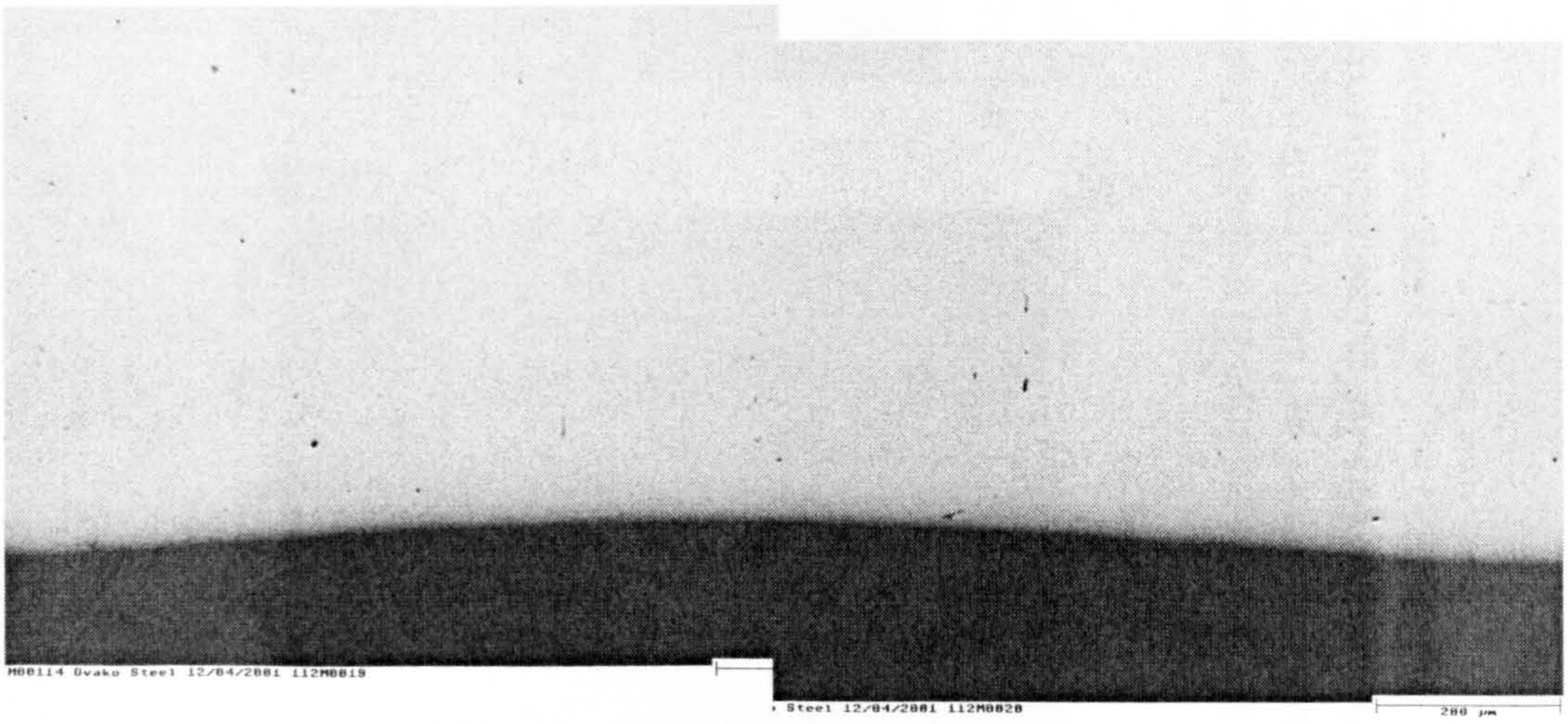

Fig.3.52. Polished cross section through the indentation shown in figure 3.50(b) revealed no cracks of any type at this magnification

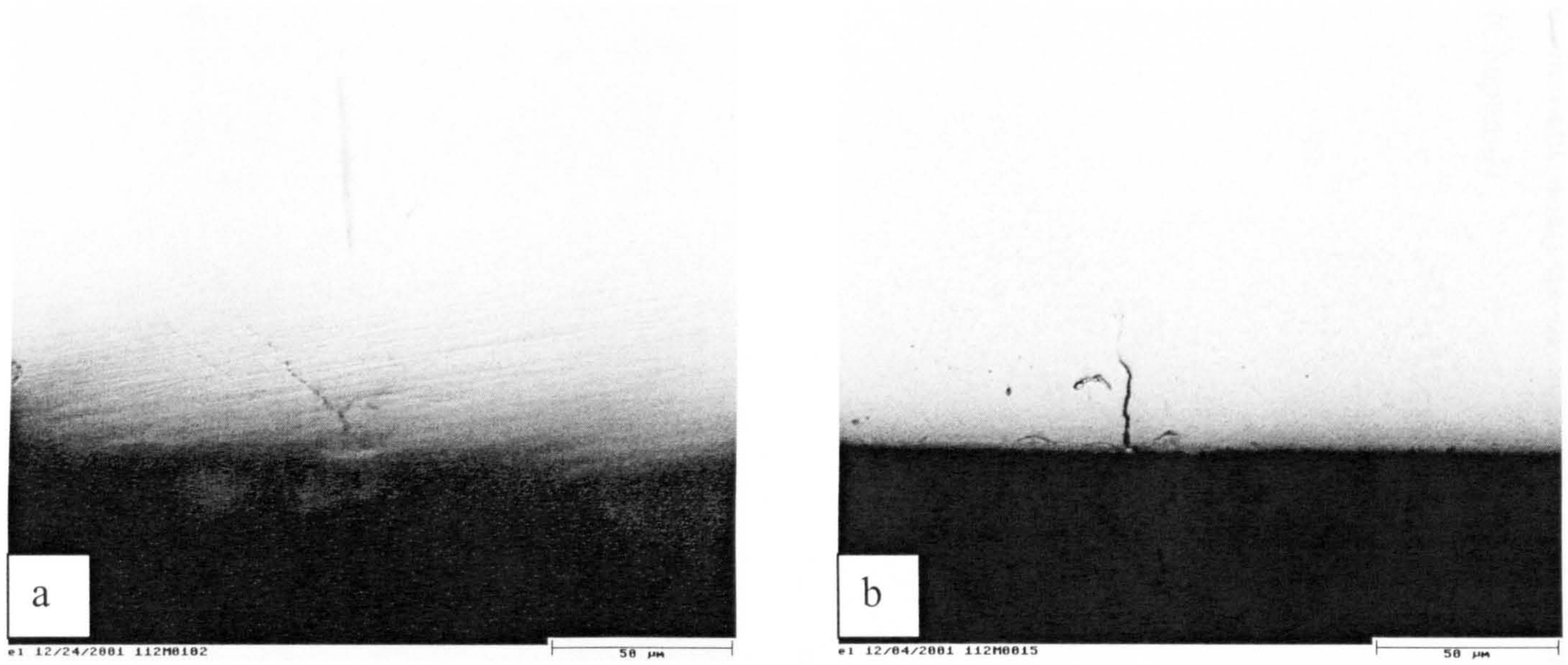

Fig.3.53. Higher magnification revealed shallow ring cracks around indentations in shot peened specimens tested at 12kN. Depth of ring cracks in (a) and (b) for specimens tested for 1×10^6 cycles and 10×10^6 cycles respectively were similar. Ring cracks seems to be stop growing beyond this depth

an indentation. The answer seems to lie in the sensitivity of the results to the assumptions made about elastic-plastic behaviour and to the loading regime that is used. In addition, we have considerable doubt about the analysis used by Alfredsson and Olsson (1999) to explain their observations on standing contact fatigue. For this reason, finite element analysis of standing contact indentation was undertaken as explained in (Chapter 4)

CHAPTER 4

Stresses Produced by Contact of a Sphere with a Flat Surface

(Finite Element Results)

4.1 Background

Micropitting and surface contact fatigue are difficult to analyse because the exact boundary conditions that produce nucleation and growth of small fatigue cracks are uncertain. For instance, there is case a for assuming some Mode I opening is required for fatigue crack growth. This requires a tensile stress component and one question is: how is tensile stress generated under contact, where stresses are predominantly compressive? The development of tensile stresses under these circumstances is a second order effect. One possibility is that lubricant pressure acting on the faces of a surface crack could provide Mode I opening. Another possibility is that localised surface shear tractions that might occur in asperity contact could provide the Mode I opening.

The standing contact fatigue test (SCFT) was developed to simulate on a macroscopic scale what might occur on the microscale at asperities in surface contact fatigue (Alfredsson and Olsson, 1999). It is argued that the tensile components of stress developed near the contact between a sphere and a flat specimen are the driving force for fatigue crack nucleation and growth. The test may or may not be a valid simulation of micropitting, but it turns out in practice that the tensile stresses near a spherical contact are not well defined. This is surprising in view of the fact that has a well-tested analytical solution that has been known for many years. The difficulty arises because of the effect of plastic deformation, as is explained below. First, though it is worth reviewing Hertzian contact between a sphere and a flat surface for elastic deformation only.

4.2 Hertzian Elastic Contact

The Hertzian solution for contact is well known. Consider a sphere with radius R, modulus E and Poisson's ratio ν pressed with a force P against a flat surface (figure

4.1). For simplicity we assume that the sphere and the flat plate have the same elastic constants. The radius of the circle of contact is a. The deformation is axially symmetric about the z-axis, $r = 0$.

The relation between a and P is

$$a = \left[\frac{3PR}{4E}\right]^{1/3} . \tag{4.1}$$

The pressure at the contact surface is parabolic in form with a maximum p_0 at $r = 0$ and zero at the periphery of the concact at $r = a$. The value of p_0 is

$$p_0 = \frac{3P}{2\pi a^2} = \left[\frac{6PE^2}{\pi^3 R^2}\right]^{1/3} . \tag{4.2}$$

The stresses at the surface, along the line $z = 0$ are defined by the relations

$$\sigma_z = p_0\left[1-(r/a)^2\right]^{1/2}; \qquad r < a$$

$$\sigma_z = 0 ; \qquad r \geq a$$

$$\sigma_r = p_0\left[\frac{(1-2\nu)}{3}\frac{\left|1-(1-(r/a)^2)^{3/2}\right|}{(r/a)^2}-\left(1-(r/a)^2\right)^{1/2}\right]; \qquad r < a$$

$$\sigma_r = p_0\left[\frac{(1-2\nu)}{3}\left(\frac{a}{r}\right)^2\right]; \qquad r \geq a \tag{4.3}$$

$$\sigma_\theta = -p_0\left[\frac{(1-2\nu)}{3}\frac{\left|1-(1-(r/a)^2)^{3/2}\right|}{(r/a)^2}-2\nu\left(1-(r/a)^2\right)^{1/2}\right] \qquad r < a$$

$$\sigma_\theta = -p_0\left[\frac{(1-2\nu)}{3}\left(\frac{a}{r}\right)^2\right] \qquad r \geq a$$

The maximum tensile stress occurs at the surface in the radial direction at $r = a$, i.e.

$$\sigma_r = \frac{1}{3}(1-2\nu)\, p_0 . \tag{4.4}$$

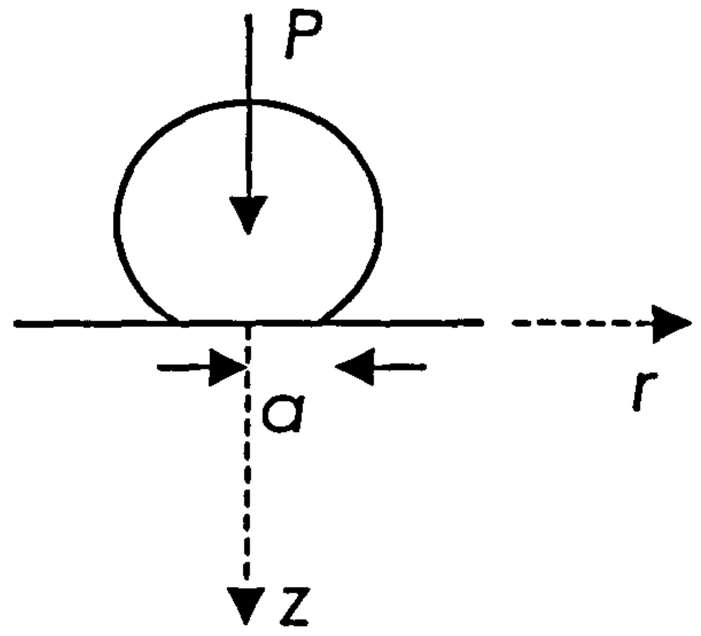

Fig. 4.1. Sphere against flat contact.

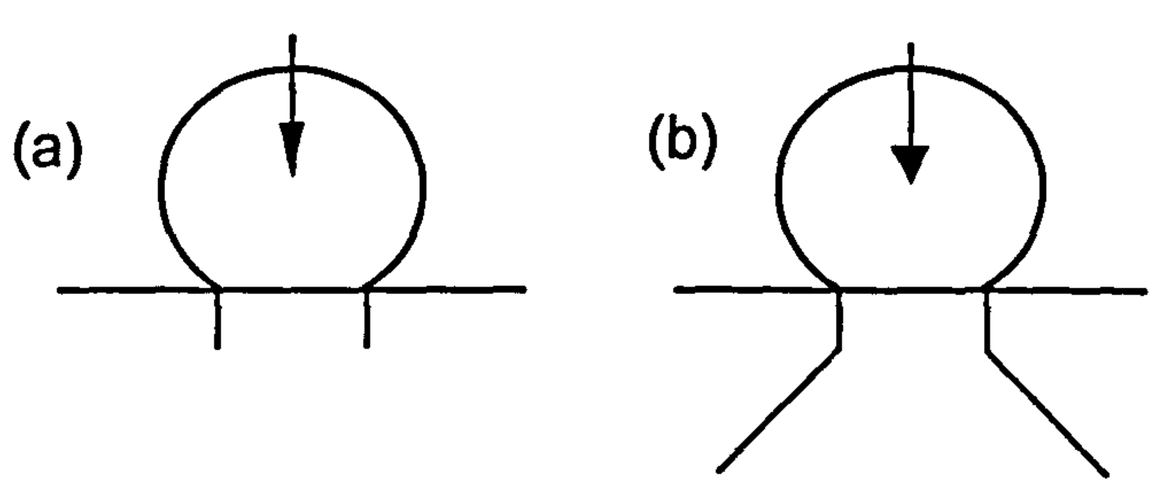

Fig. 4.2. Formation of ring(a) and cone cracks(b)

The hoop stress is equal in magnitude but compressive at this position

$$\sigma_\theta = -\frac{1}{3}(1-2\nu)\, p_0 \quad . \tag{4.5}$$

The combination of these two stress components represents a state of pure shear at this point.

The stresses along the central axis $r = 0$ are

$$\sigma_z = -p_0 \frac{1}{1+(z/a)^2}$$

$$\sigma_r = \sigma_\theta = p_0\left[\tfrac{1}{2}\frac{1}{1+(z/a)^2} - (1+\nu)\left(1-\frac{z}{a}\arctan\left(\frac{a}{z}\right)\right)\right] \tag{4.6}$$

The maximum shear stress at any point in the specimen is equal to $p_0|\sigma_z - \sigma_r|/2$. The maximum shear stress reaches a peak equal to $0.31p_0$ at a depth $z = 0.481a$ on the central axis. Thus yielding in an elastic-plastic material will first start at this position below the surface at a critical applied load $P_Y = 85R^2\sigma_Y^3/E^2$ For example, when indented by a 5 mm ball, yield first occurs in a steel with a yield strength of 2 GPa at a load of 350 N. However, yield is confined to a small region below the surface and the applied load can be increased very many times before any observable plastic deformation can be detected.

4.2.1 Implications of the Elastic Solution

The purely elastic Hertzian contact of a sphere produces a tensile stress in the radial direction at the surface. This does not occur in the contact of cylinders (neglecting the ends), where the stress field is purely compressive. It is noted that note also that the radial tensile stress depends on the property of the material through the appearance of Poisson's ratio (eqns. 4.3 and 4.4). Thus, the appearance of the tensile stress can be thought of as a second order effect, liable to modification by variations in the properties of the material. This is particularly significant when plastic deformation can occur, as discussed in more detail below.

The elastic solution has been used to deduce a number of characteristics of brittle or elastic solids. Consider first an elastic solid such as glass.

At a critical applied load, ring cracks are observed to form at the periphery of the contact circle. In glass clearly these cracks form under the influence of the radial tensile stresses that are a maximum at this point (eqn. 4.4). However, the ring crack is stable because it is growing into a diminishing tensile stress field. When the load is increased, the ring cracks extend along a path to form a cone crack (figure 4.2). The stable growth of ring and cone cracks was analysed in detail by Frank and Lawn (1967) on the basis of the Griffith theory of fracture. In this case the crack grows along the path determined by the local maximum principal stress near the crack tip.

It is argued that the same principles apply to fatigue crack growth in metals, i.e. that the fatigue crack follows the path of the maximum tensile stress. Hence, Alfredsson and Olsson (2000) produced ring and cone cracks in steel specimens in standing contact fatigue tests. However, in contrast to their results, work by the present author, using the same method, produced extensive radial cracks as well as ring cracks. The nature of the observations suggests that the tensile stresses developed at the surface are not as clearly predictable as implied by Alfredsson and Olsson. Evidently the effect of plasticity must be taken into account but an indication of the difficulty is given by a consideration of the Hertzian elastic solution. In fact, the simple elastic solution shows that the surface stress is sensitive to the materials properties through Poission's ratio, Figure 4.3 demonstrates how a change in ν changes the surface stress. When $\nu = 0.5$, the surface stresses are zero outside the contact area. Poisson's ratio approaching a value of 0.5 is tyipcal of rubber, which changes shape easily but is resistant to volume change. The ability to change shape whilst resisting volume change is also characteristic of elastic-plastic materials. Thus, it is not surprising to find that plastic deformation also has a significant effect on the surface stresses outside the contact area.

4.3 Spherical Indentation of an Elastic-Plastic Material

Solutions for the stresses developed by indentation of an elastic-plastic material have to be obtained either by approximate treatments or numerically, by finite element analysis.

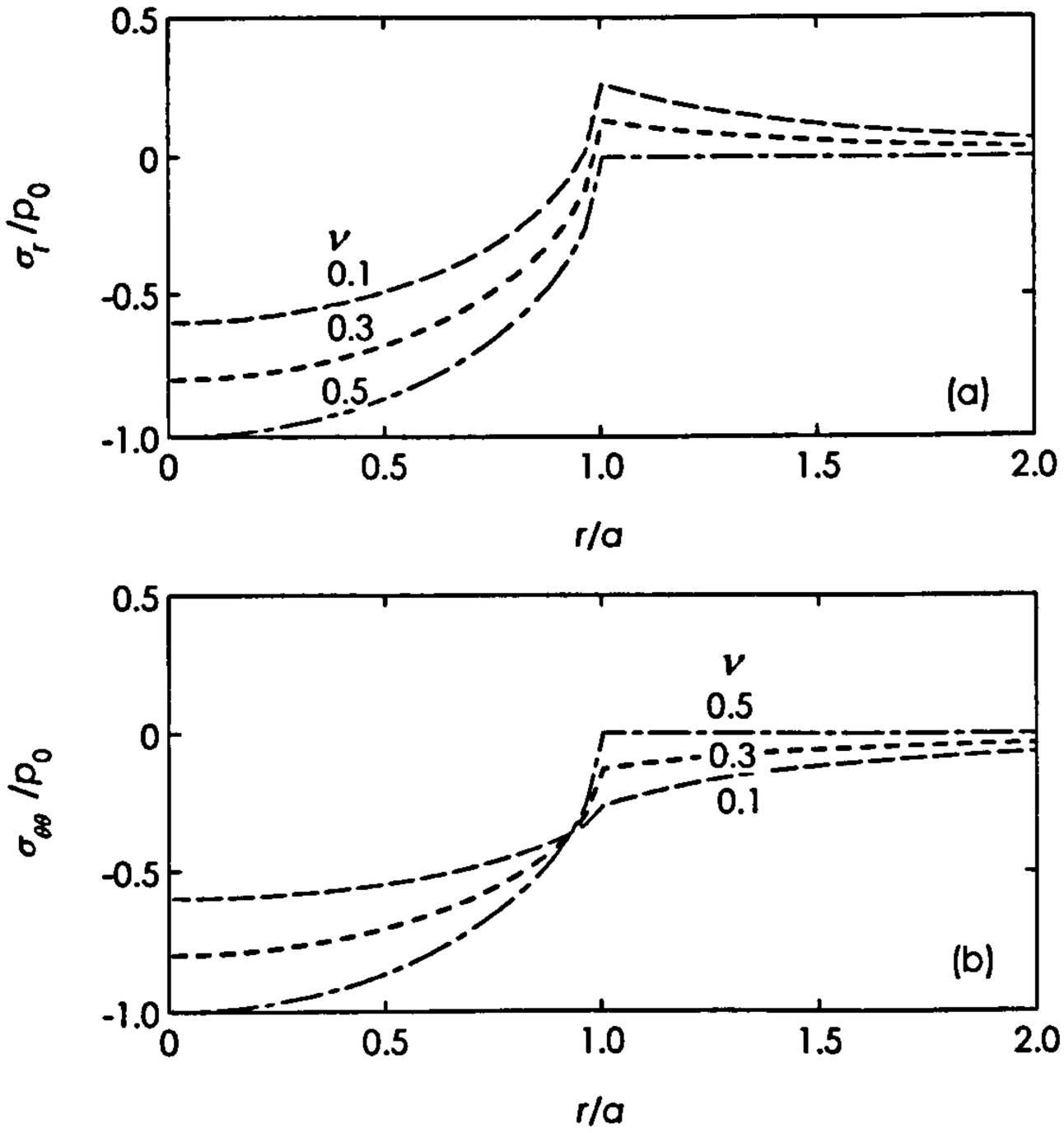

Fig. 4.3. Effect of Poisson's ratio on the radial and circumferential stress components at the surface of purely elastic materail

Before considering some proposed solutions, we note that the predicted stresses are likely to be sensitive to the assumptions made about yield stress and work hardening.

4.3.1 Approximate Analyses

Johnson (1968) made an aproximate analysis of indentation of an elastic-plastic material by a hard sphere. The analysis was informed by experimental observations. It will be remembered that the pressure distribution in Hertzian contact is parabolic over the contact area. A major effect of plastic deformation is to flatten the pressure distribution. Thus an idealisation used in modelling plasticity is that $\sigma_z = p = 3\ \sigma_Y$ when $r < a$ and $\sigma_z = 0$ when $r \geq a$, where σ_Y is the yield strength. Johnson's model predicts that $\sigma_r = 0$ and $\sigma_\theta = \sigma_Y$ at $r = a$. This is in stark contrast to the Hertzian solution (eqns. 4.4 and 4.5). Johnson also estimated the residual stresses remaining after unloading. The model predicts a residual *tensile* stress $\sigma_r = \sigma_\theta \approx 0.6\sigma_Y$ at the surface in the contact area. Outside the contact area the model predicts that plastic flow will occur during unloading. Thus the residual stress was not calculated in this region. Studman and Field (1977) refered to Johnson's analysis to explain the radial cracks they observed in the indentation of hard steel. The elastic Hertz solution predicts only ring and cone cracks and it was necessary to include plastic deformation to account for the observed radial cracks.

Johnson revisited the identation problem in his book on contact mechanics (Johnson, 1985). The basis of the treatment was the assumption that plasticity in an elastic-perfectly plastic material occurs in a spherical zone under the indenter. The details depend on the size of the plastic zone relative to the contact radius a. At the elastic-plastic boundary, the followings stresses are predicted: $\sigma_r = -2/3\sigma_Y$, $\sigma_\theta = 1/3\sigma_Y$. Within the plastic zone both σ_r and σ_θ are compressive at the surface at $r = a$. Johnson (1985) also estimated the residual stress after indentation using the same model. Again, residual *tensile* stresses were predicted in the centre of the contact zone at the surface equal to $\sigma_r = \sigma_\theta = 0.4\sigma_Y$ after fully plastic indentation. Below the surface at $z = 0.64a$, the residual stresses are compressive and of the order $\sigma_r = \sigma_\theta \approx -0.9\sigma_Y$ Outside the contact zone some plastic deformation is predicted to occur on unloading. Note that

fully plastic indentation means that the boundary of the plastic zone has grown to include the contact area within it.

These models do not give a consistent picture of the stresses near an indetation. The difficulty of reaching a clear conclusion may arise because several regimes exist in the course of indentation of an elastic plastic material by a sphere. These have been classified by Mesarovic and Fleck (1999): elastic, elastic-plastic, similarity solution and finite deformation. Further, the results are likely to be sensitive to the yield strength and work hardening rate. In other words the stresses developed at a contact may depend on which of these regimes apply. Thus finite elenent analyses are required to resolve these points.

4.3.2 Review of Finite Element Analysis from other Authors

The following results from other authers are reviewed here because they differ significantly from the FE results obtained in the present work.

Hardy *et al.* (1977) performed a finite element analysis of spherical indentation of an elastic-plastic solid. However, they experienced difficulty in obtaining convergence in the fully plastic regime. Sinclair *et al.* (1985) overcame these difficulties and produced results with contact radii ranging from $a/R = 0.01$ up to $a/R = 0.32$ for a material modelled on the plastic deformation of austenitic stainless steel with $\sigma_Y/E = 1.3\times10^{-3}$. The indentation was modelled using a rigid sphere and the contact was frictionless. Note that austenitic stainless steels are considerably softer than the gear materials of interest in the present work.

The plastic zone as a function of a/R is shown in Fig.4.4. The near surface stresses are shown in Fig.4.5

It is evident that the stress field outside the contact region is mainly *compressive*. The σ_θ component is slightly tensile ($\sigma_\theta/\sigma_Y = 0.1$) at larger distances from the periphery of the contact region. This is completely at odds with the analysis of Alfredsson and Olsson (2000) and out of line with the approximate analysis of Johnson (1985).

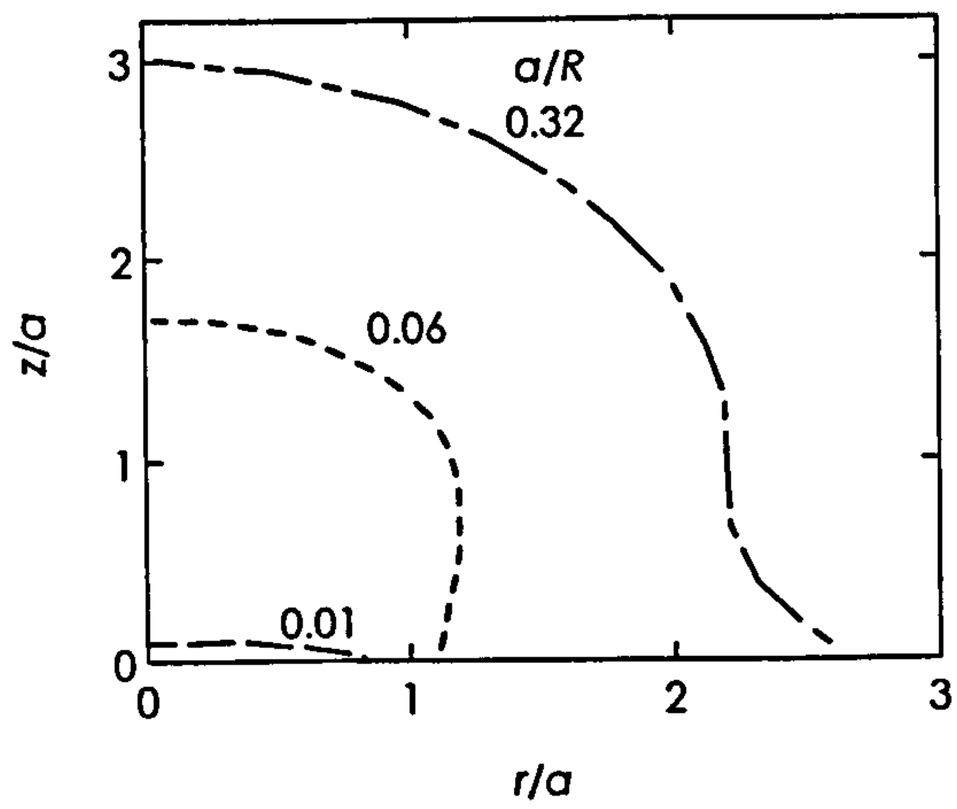

Fig. 4.4. Plastic zone as a function of *a/R*. After Sinclair *et al.* (1985)

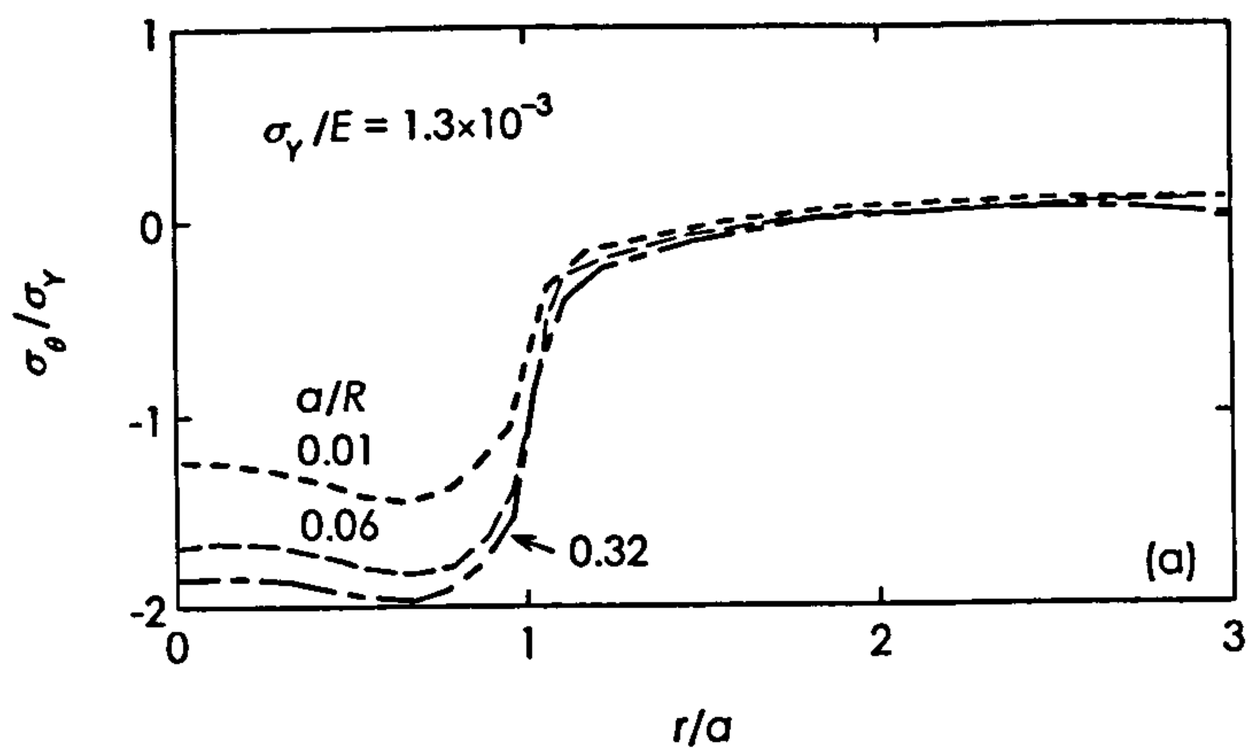

Fig. 4.5 Near-surface stresses after Sinclair *et al.* (1985). In hoop direction (a) and radial direction (b)

The residual stresses after unloading were obtained by Sinclair *et al.* (1985) These are shown in Fig.4.6. Note that the radial and hoop stress is *tensile* at the centre of the contact surface after unloading.

4.4 Finite Element Simulation for Standing Contact Fatigue Test

The results of the standing contact tests are difficult to interpret because of the uncertainty about the local stresses developed in loading and un-loading an elastic-plastic material. The results reviewed in the last section indicate the wide variation in the results previously reported. Further, we have considerable doubt about the analysis used by Alfredsson and Olsson 1999 to explain their observations on standing contact fatigue. For this reason, finite element analysis of standing contact indentation was undertaken.

Finite element simulation for the standing contact fatigue test was made using the Ansys package software. An axisymetric model was adopted to reduce the time and amount of mathematical calculations involved in the analysis. The work piece was meshed in such away that finer elements were placed in the vicinity of the contact zone. The mechanical behavior of the steel under compression load was modeled from the result of the compression test explained earlier. The indenter is considered as a steel ball with diameter of 5 mm. The applied load was increased in steps to the required level and then unloaded in the same manner. Contact was modeled using gap elements. The procedure was repeated for different maximum loads. Radial and hoop stresses were recorded. Contours of von Mises strain were also recorded. Note that the FE model was initially set up in Ansys by P.Dickinson, to whom grateful thanks are due. The author utilized this model to produce the results given below. Note that the data obtained in the compression tests reported in Chapter 3 was used for constitutive equation for the material.

4.4.1 Results of Simulations by Finite Element

It was intended to determine the stresses around indentations at various applied loads during the course of load application and after load removal. If plastic deformation is

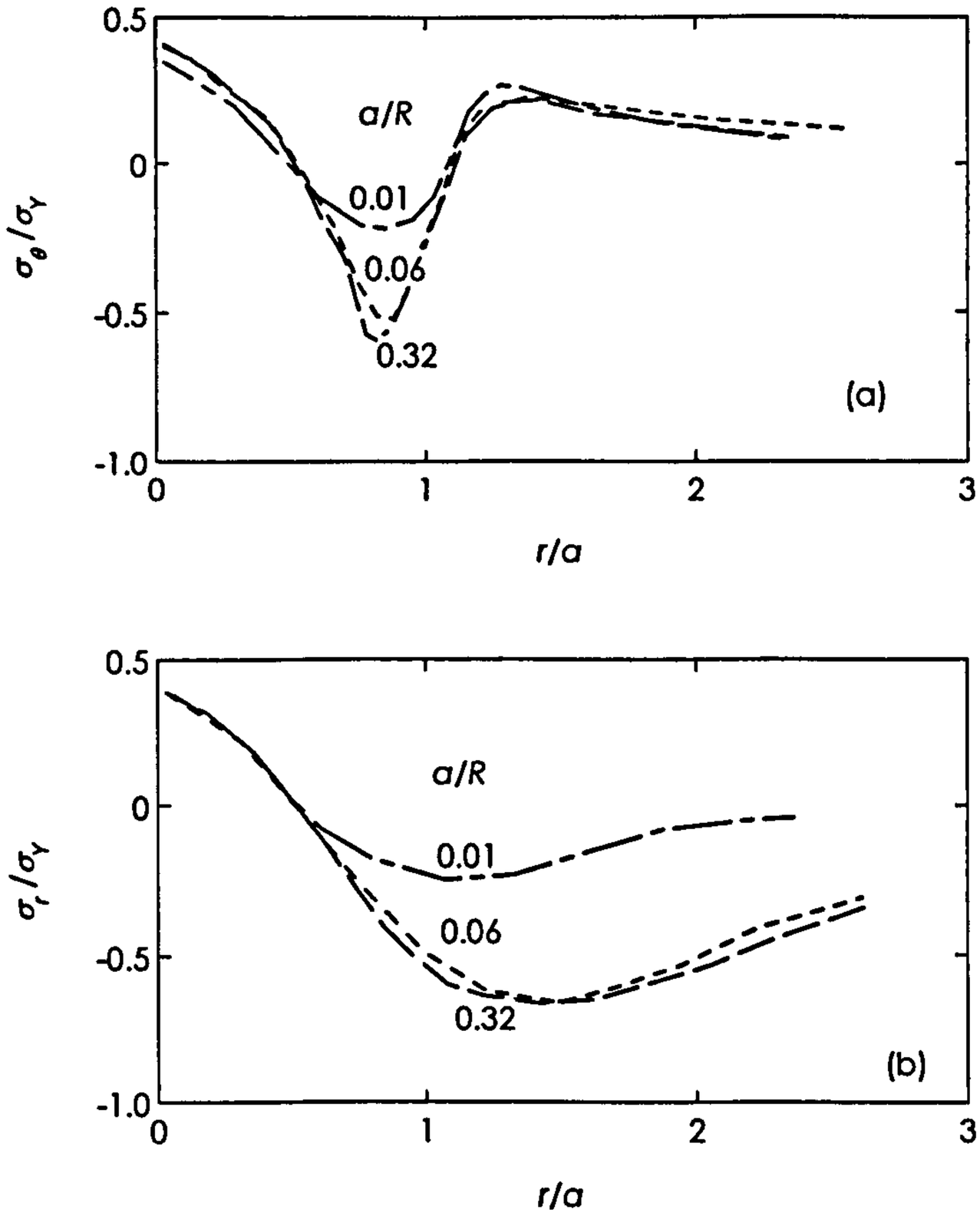

Fig. 4.6. Near-surface residual stresses after unloading (Sinclair *et al.* 1985).
In hoop direction (a) and radial direction (b)

induced during load application, then residual stresses will be left after load removal. The state of stress after load removal represents the residual stresses around indentations which affects the mean stress during fatigue test. Both stress range and mean stress affect the fatigue life of a component subjected to cycling loading. Fatigue cracks usually initiate at the surface. Any surface compressive stresses render the material more resistant to fatigue failure through opposing crack initiation. The role of tensile residual stresses is obviously detrimental from the fatigue point of view.

Figure 4.7 shows the indenter ball and the flat specimen in the simulated test. A closer view of the meshing is shown in Fig.4.8. The disc shaped specimen and the ball indenter assembly is symmetric about vertical axes. In axisymetric solutions shapes are generated by revolution about axis of symmetry. The shape indicated in Fig.4.7 will yield a specimen with radius of 30 mm and thickness of 10 mm and the ball radius is 5 mm. The total numbers of elements are 6240 of 8 nodded quadratic type with smaller elements allocated to the contact area as shown in Fig.4.8. The total number of nodes was 18442. The bottom side of the specimen was horizontally constrained from movement and no constrained was imposed in the vertical direction. Gap elements were used at the contact surfaces to allow contact to occur on mating elements from both sides in accordance with the applied load. The stiffness of the gap elements was adjusted to achieve convergence without interpenetration of material.

4.4.2 Stresses and Strain Contours under Load

Data obtained from the compression tests (Chapter 3) were used to represent the stress strain behaviour of the simulated test specimen. This data was utilised in the FE model.

4.4.2.a Strain Contours

Figures 4.9 (a-k) show von Mises plastic strain contours at various loads. Shear stress is responsible for plastic deformation. Planes of highest shear stresses lies below the surface where plastic deformation commenced first. It can be seen that at small loads (1kN) plastic deformation took place below the surface and is completely surrounded by elastically deformed material. The volume of plastically deformed zone grew in size

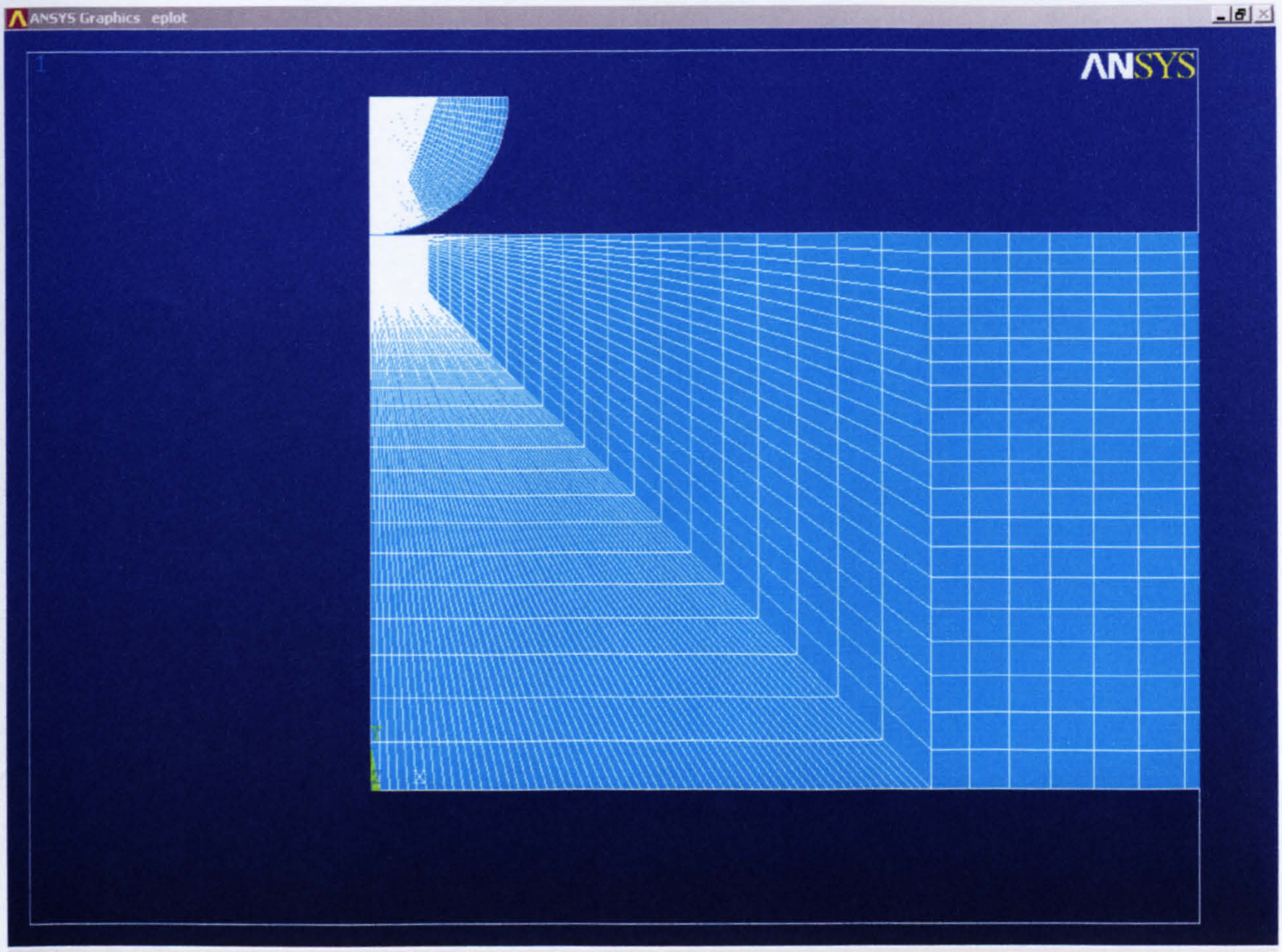

Fig.4.7 Shows arrangement of specimen and ball indenter in the FE simulation

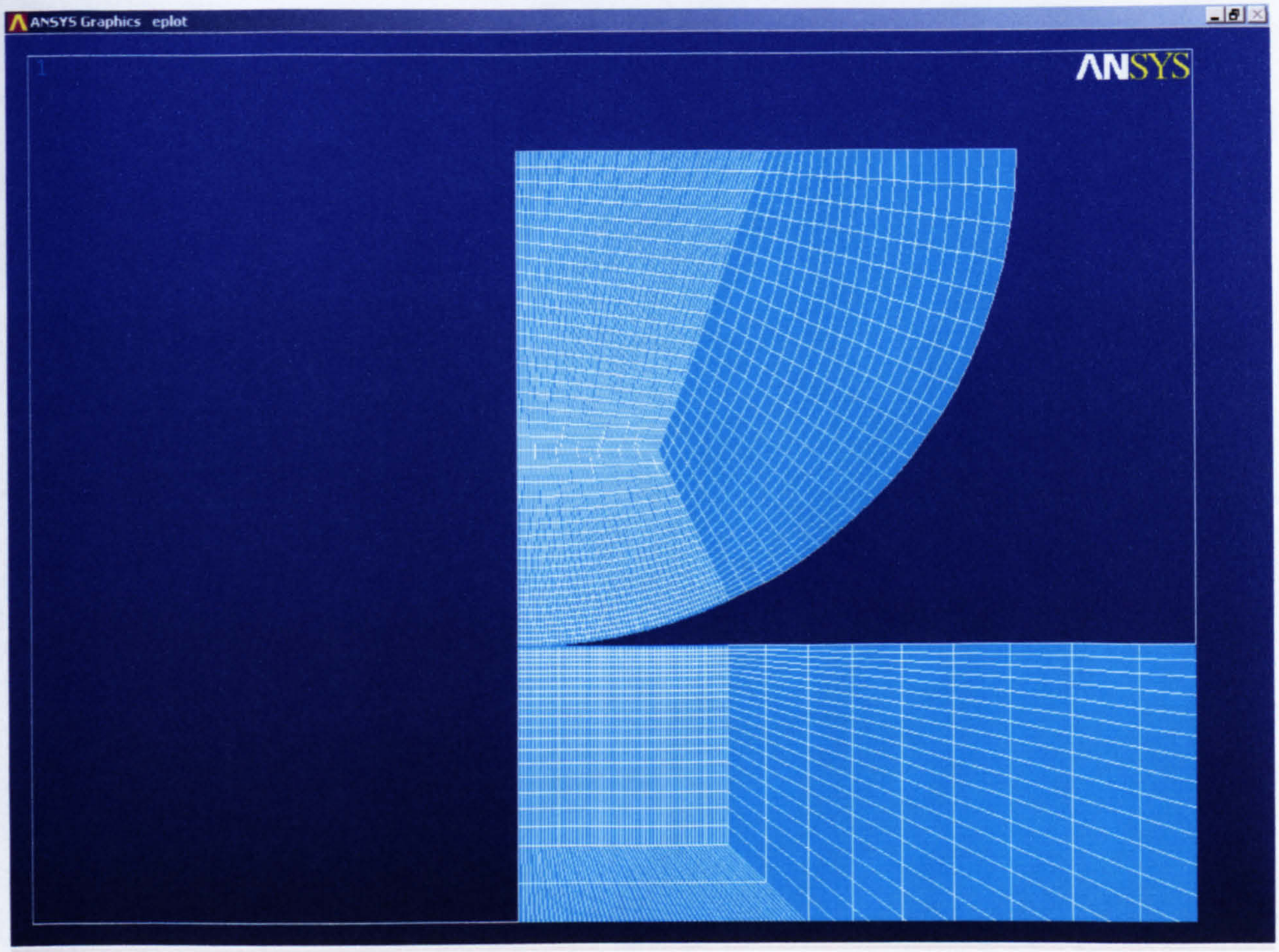

Fig. 4.8 A closer view for the previous figure shows meshing in specimen and indenter

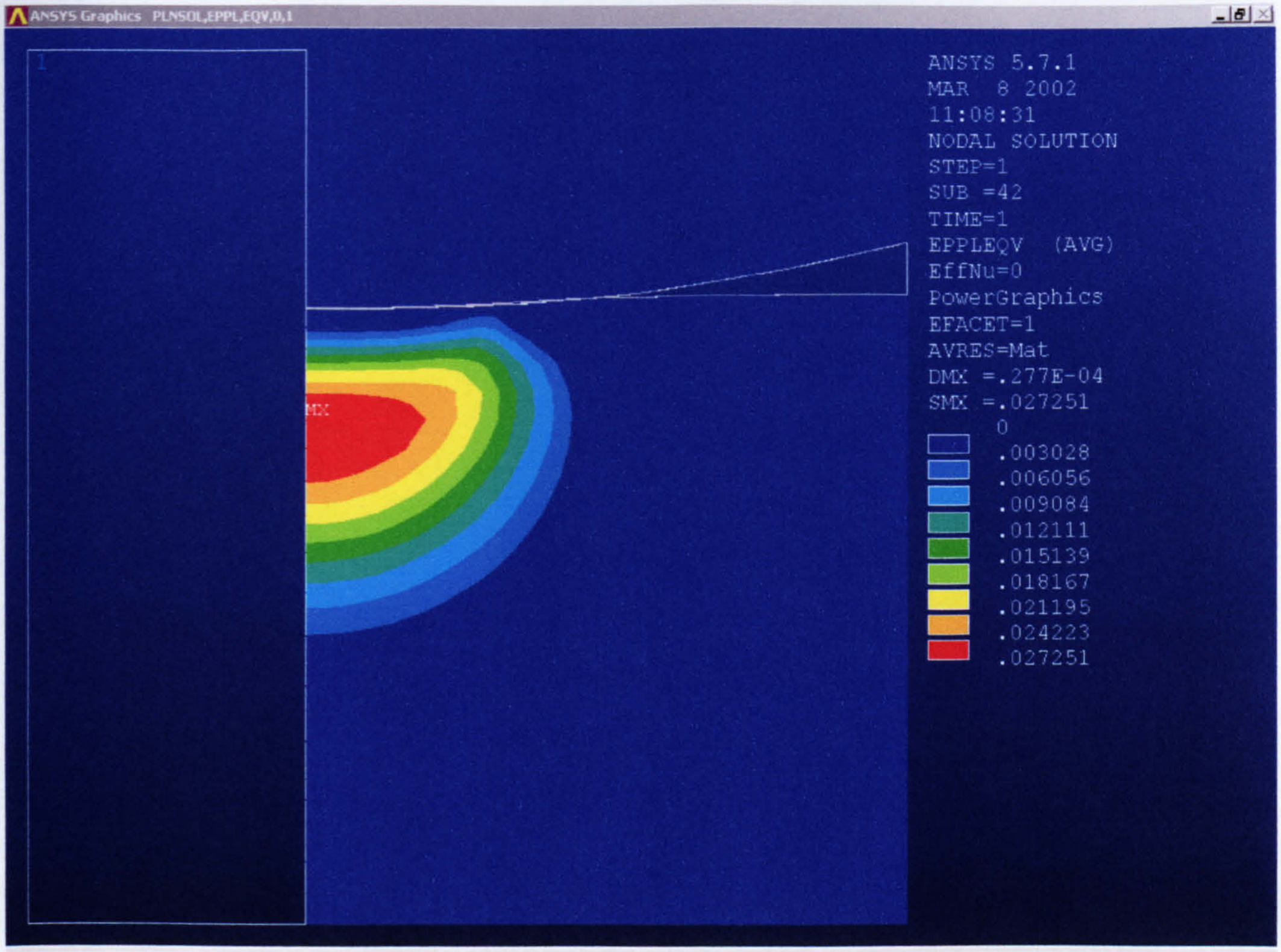

Fig.4.9 (a) von Mises plastic strain contour at applied load of 1 kN. Plastic zone is completely embedded below the contact surface.

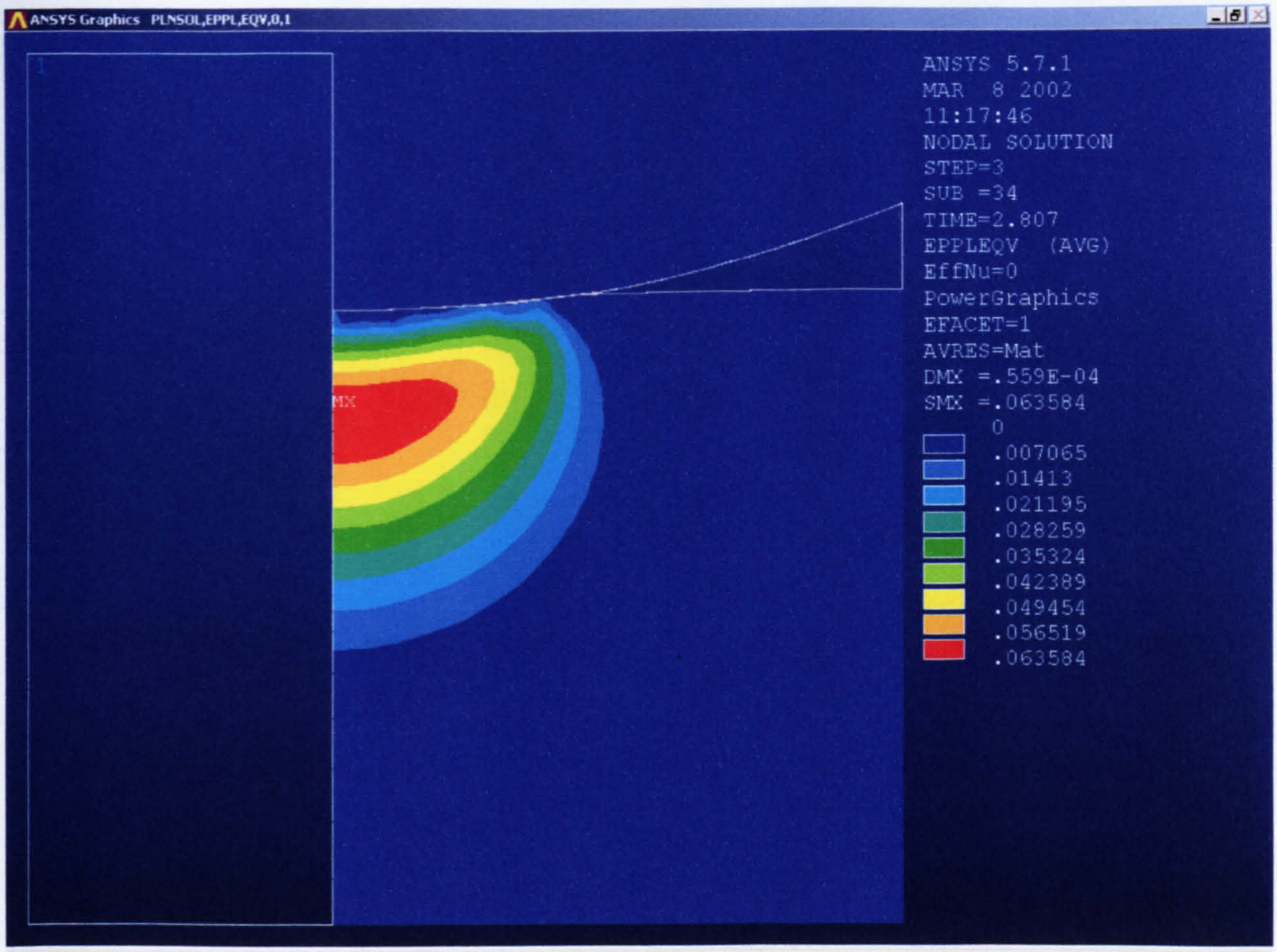

Fig.4.9 (b) von Mises plastic strain contour under applied load of 2807.5 N.
Plastic zone reached the contact surface.

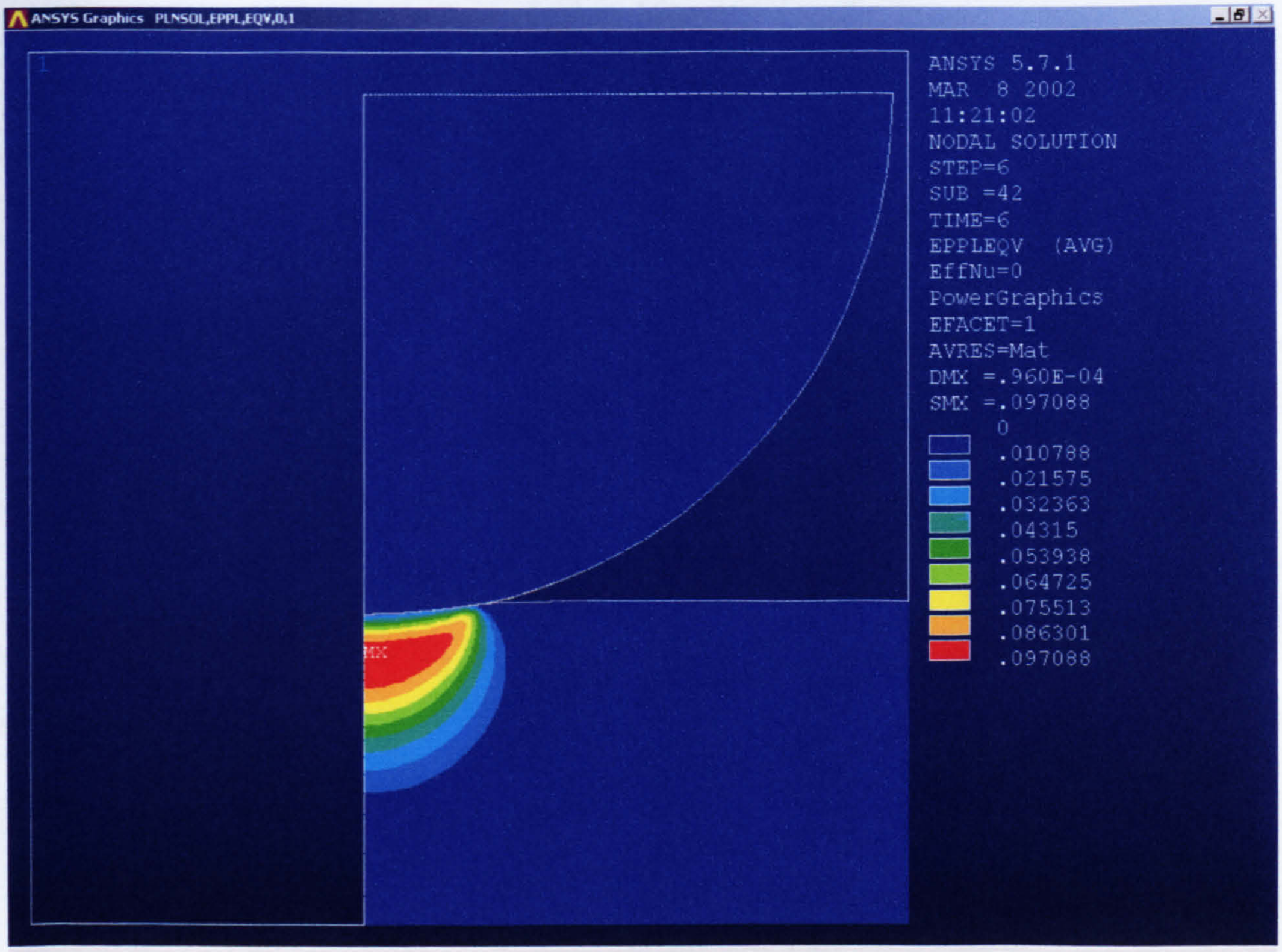

Fig.4.9 (c) von Mises plastic strain contour under applied load of 6 kN

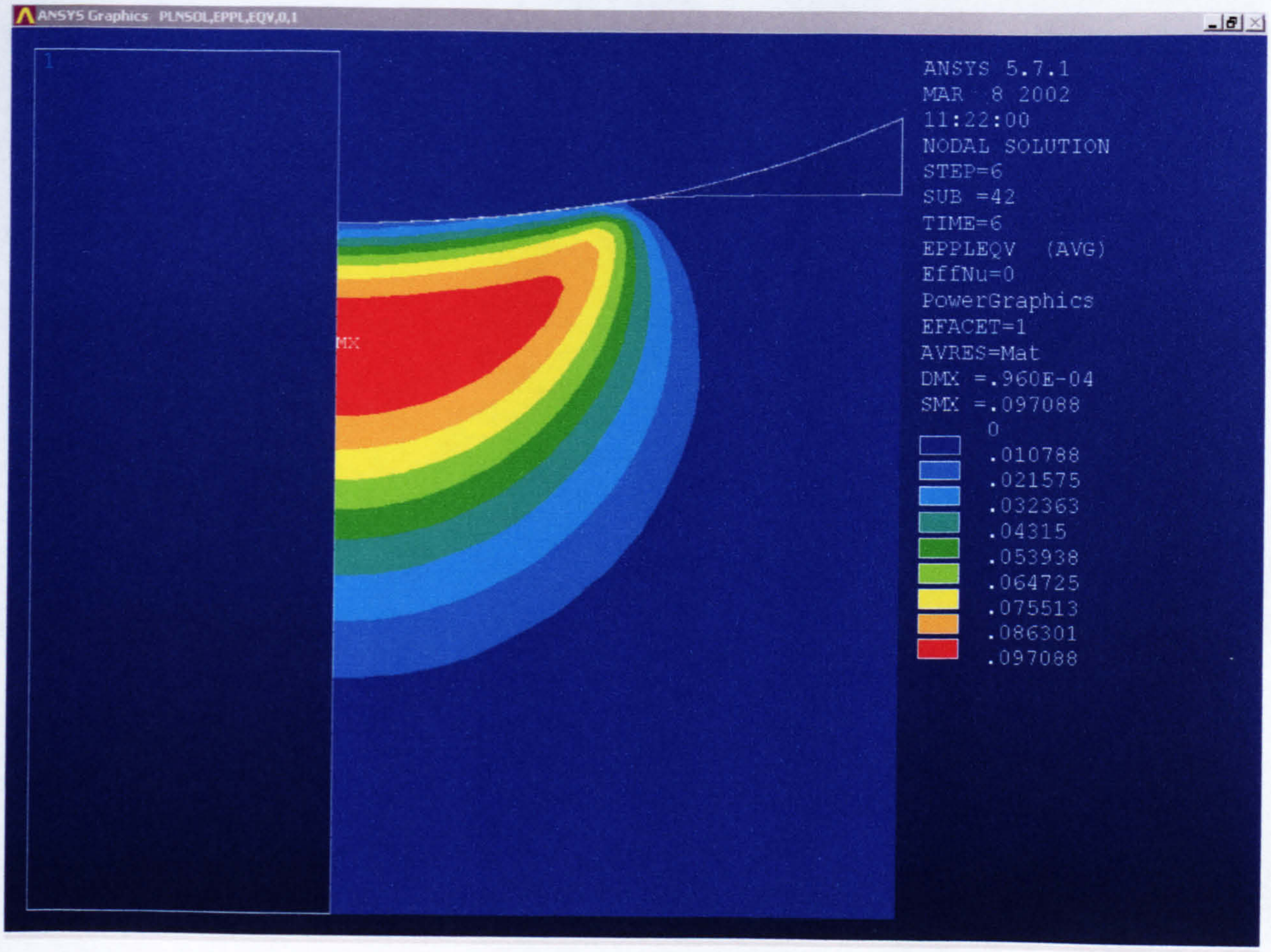

Fig. 4.9 (d) same as previous with closer view

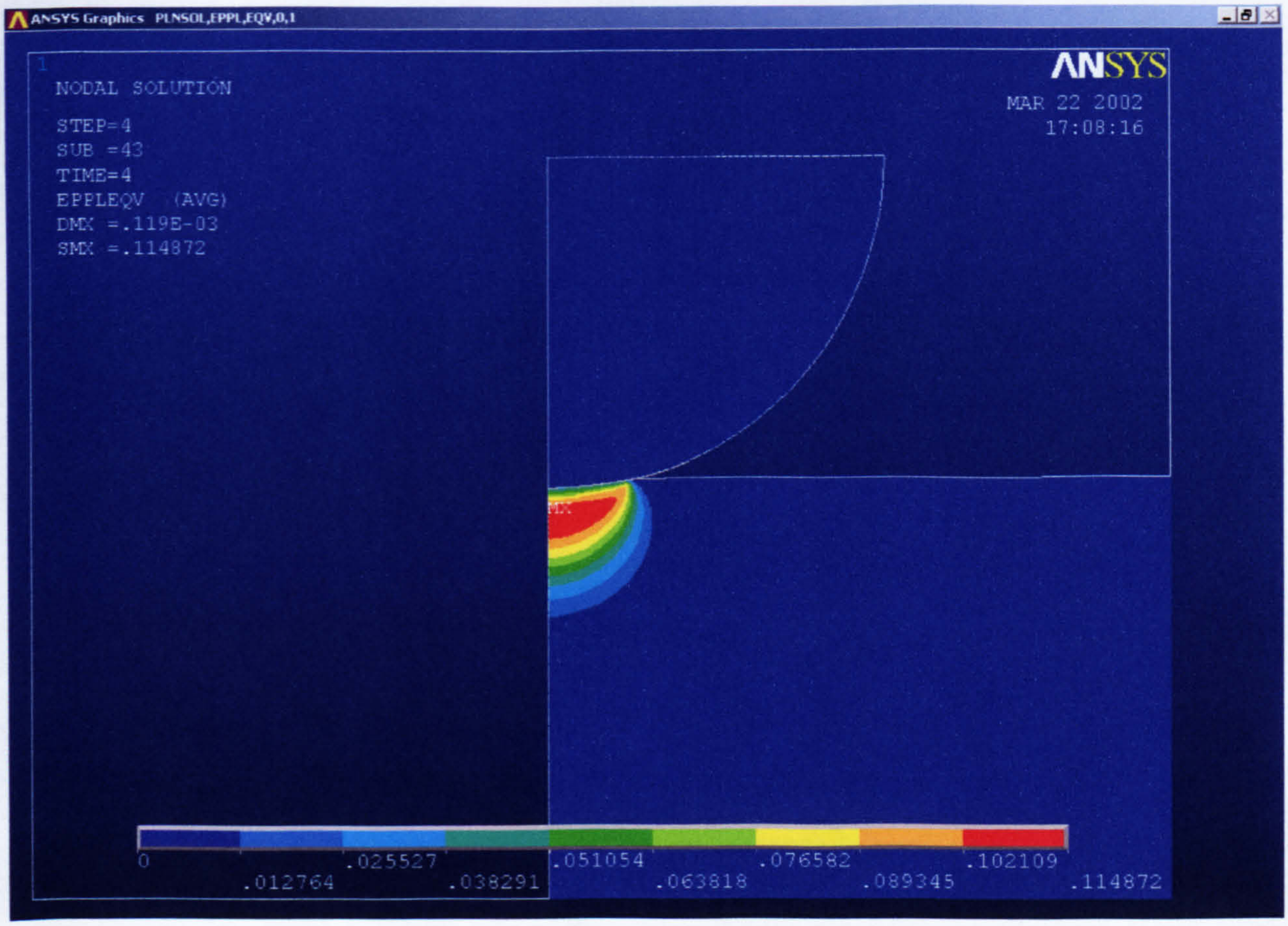

Fig.4.9 (e) von Mises plastic strain contour under applied load of 8 kN

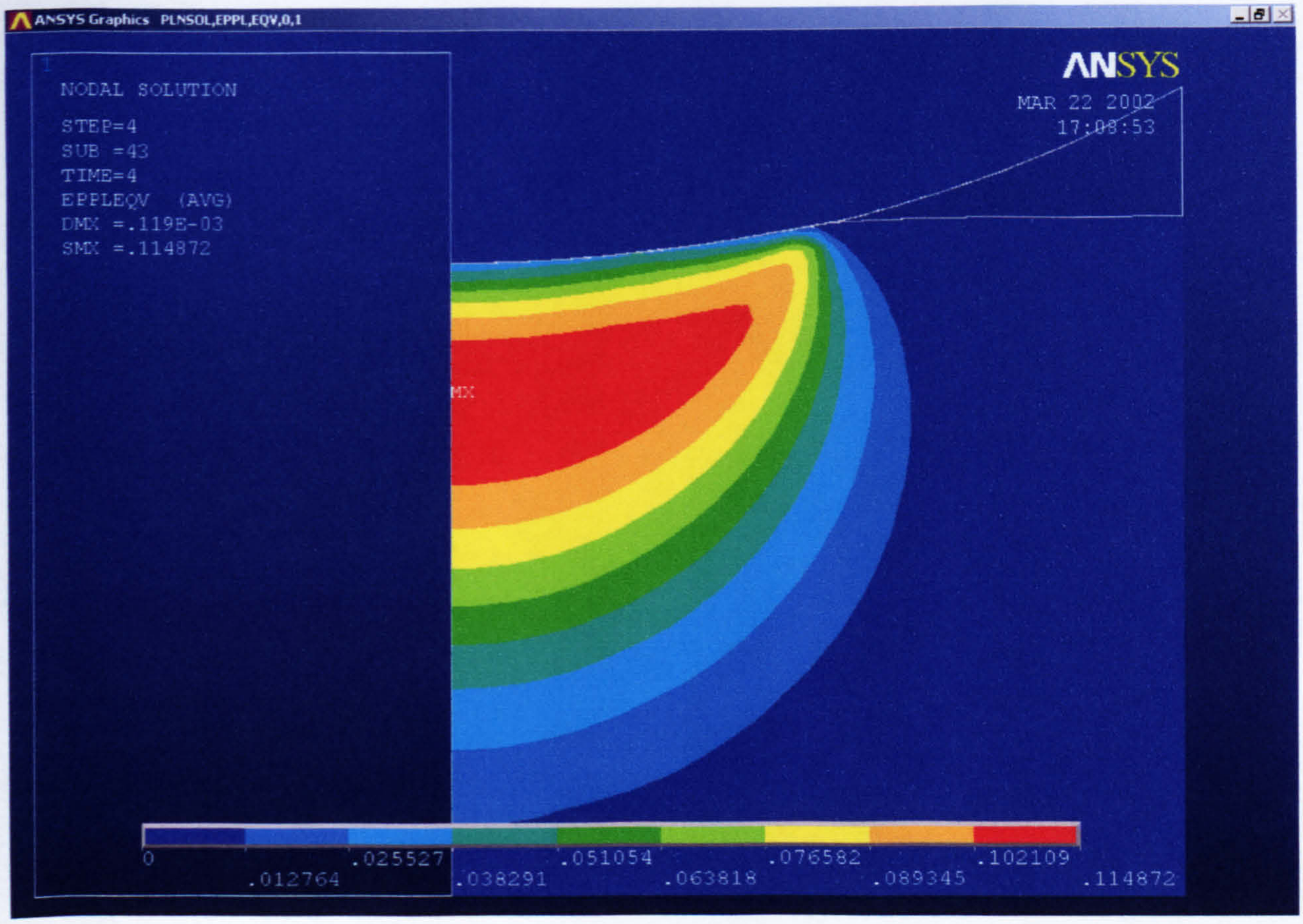

Fig.4.9 (f) same as previous with closer view

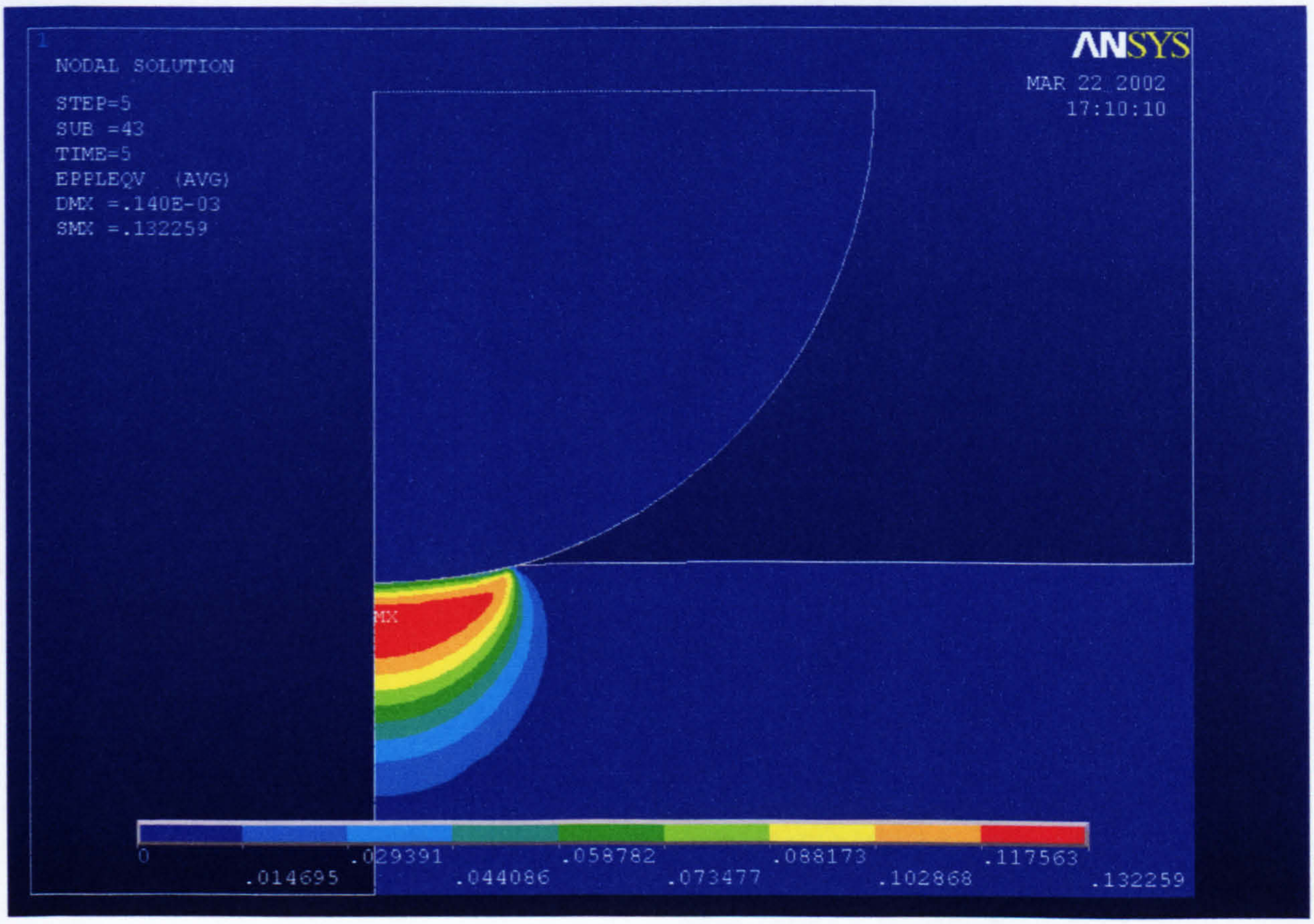

Fig.4.9 (g) von Mises plastic strain contour under applied load of 10kN

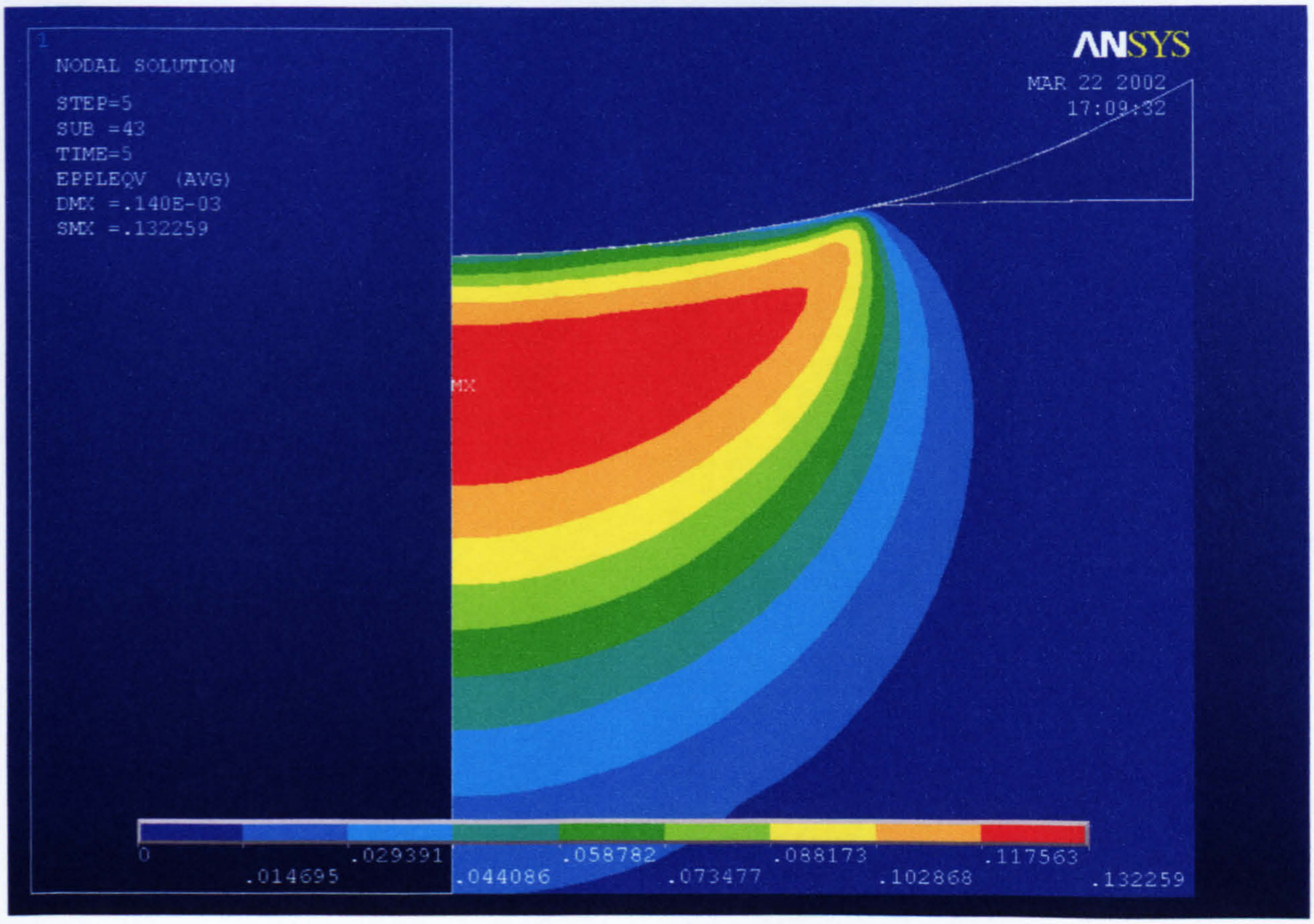

Fig.4.9 (h) same as previous with closer view

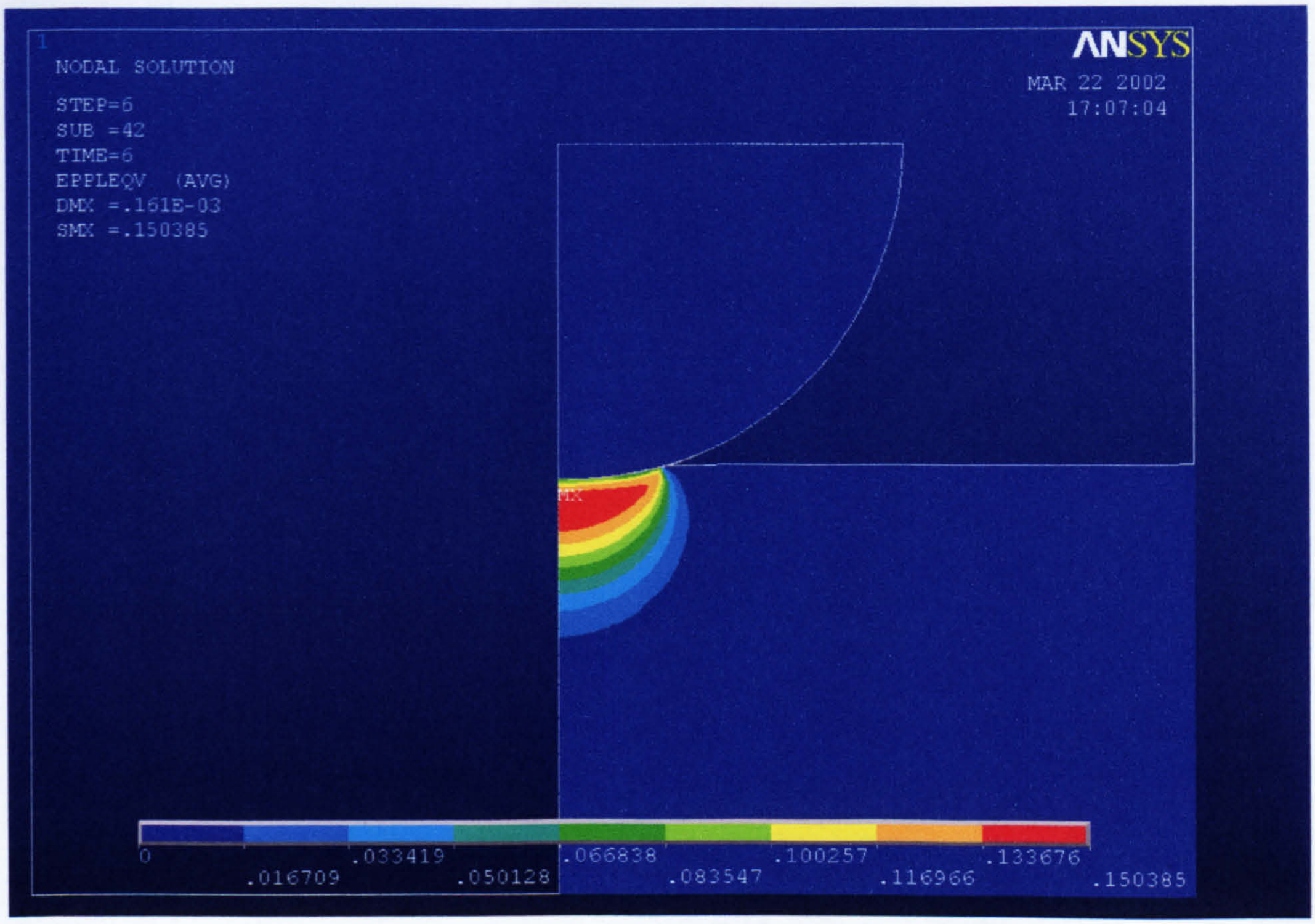

Fig.4.9 (i) von Mises plastic strain contour under applied load of 12 kN

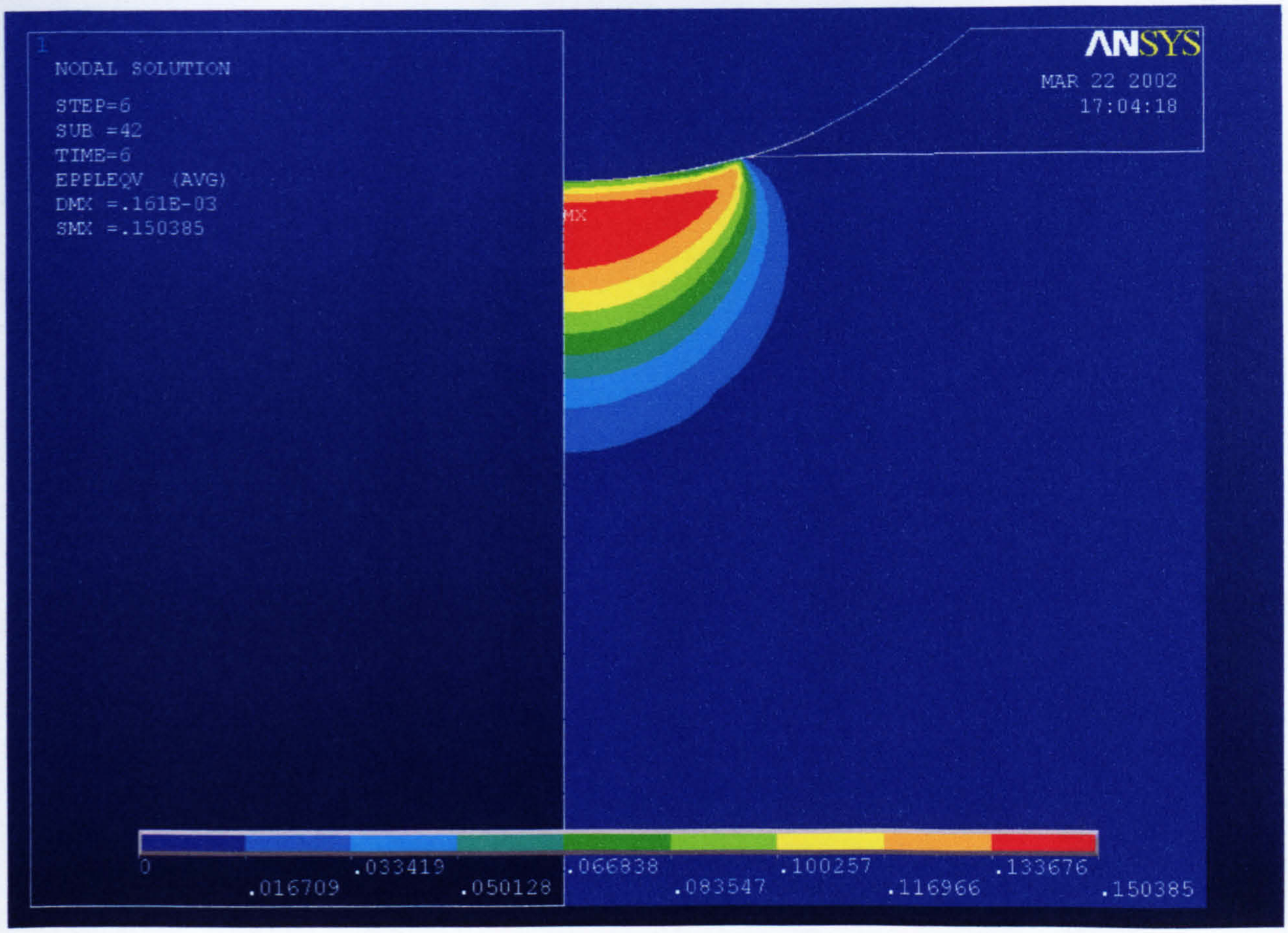

Fig.4.9 (j) same as previous with closer view

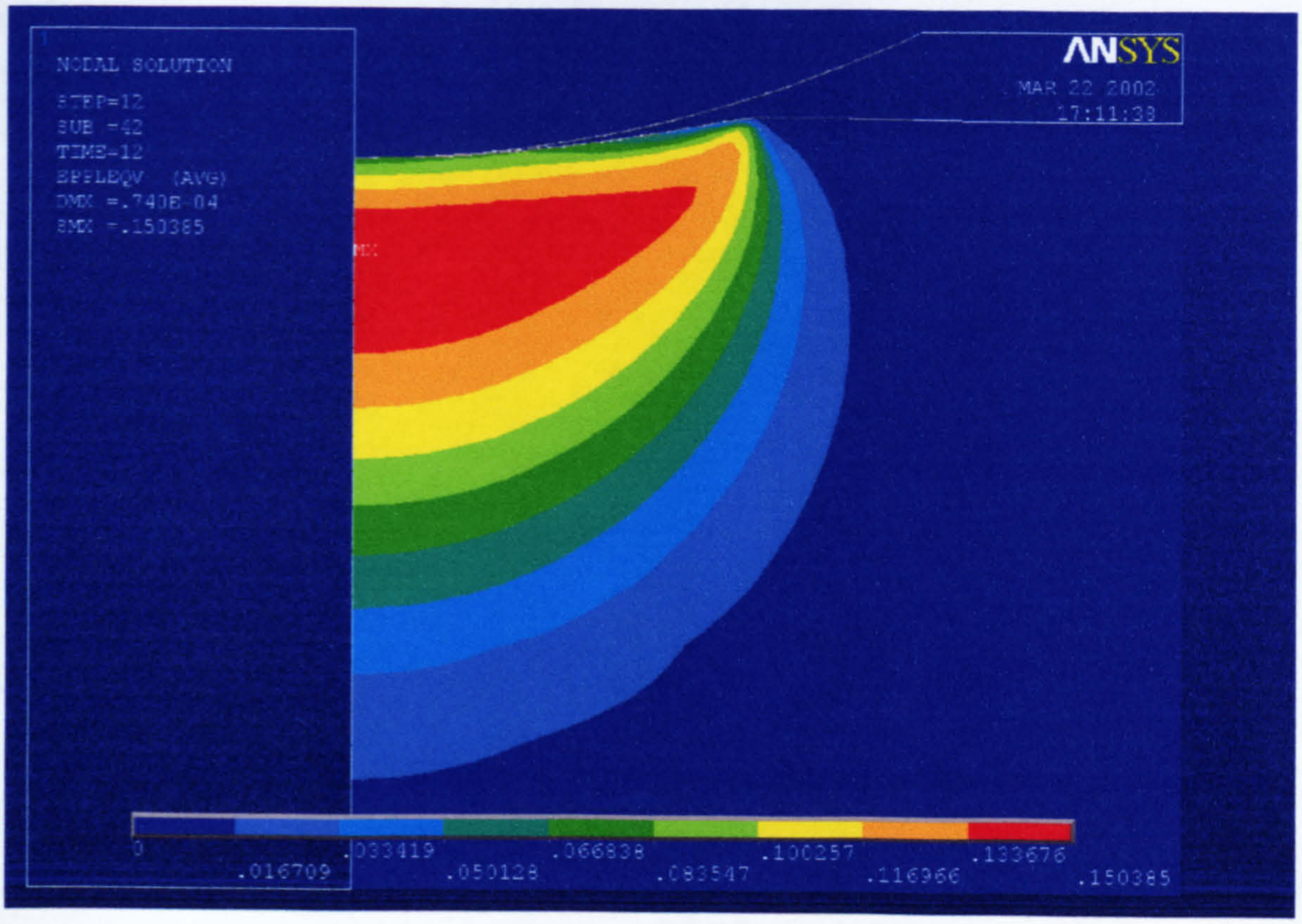

Fig. 4.9 (k) von Mises plastic strain contour at 12 kN after load removal

as the applied load increased. At applied load of 2708 N the specimen at the contact surface undergoes plastic deformation as shown in Fig.4.9 (b). The volume of plastically deformed zone continue to increase in volume with increasing load. However at the highest applied load of 12 kN the plastic deformation is still restricted to the contact area and did not spread beyond it. Thus, the indentation did not enter the fully plastic deformation regime. We believe that this is an important distinction between our analysis and some others. As a first approximation, the boundaries of the various deformation regimes are likely to depend on the yield strength to modulus ratio. This ratio is relatively large for hard steel.

4.4.2.b Induced Stresses under Loading

With an applied load of 2 kN, results from FE simulation showed that a high tensile radial stress was produced very close to the outer edge of indentation and a very small compression stresses developed in the hoop direction as shown in Fig.4.10 (a). The state of stress induced with applied load of 2 kN is not too dis-similar to what would be obtained when only elastic deformation occurs, (the tensile radial stress and compressive hoop stresses are equal in magnitude when deformation is purely elastic). Induced stresses for other applied loads are shown in figures 4.10 (b-f).

With an applied load of 4 kN the plastic zone reached the contact surface. Stresses in radial and hoop directions are tensile as shown in figures 4.11 and 4.12 respectively. The induced radial stress is large and approaches the yield strength of the steel. The induced hoop stress is much lower than the radial stress. As the applied load increased above 4 kN, the plastic zone increase in volume. The induced radial stress decreases after reaching the peak at the range of 4-6 kN applied load. The radial stress profile declines very rapidly outside the contact area. At higher applied loads radial stress change its sign from tensile to compressive and the peak moved away from the contact area in the radial direction. When the applied load is 12 kN the radial stress becomes compressive at all points along the radial path.

The induced hoop stress at all loads higher than 4 kN load are tensile outside the contact area. The induced hoop stress increases with increasing applied load. The

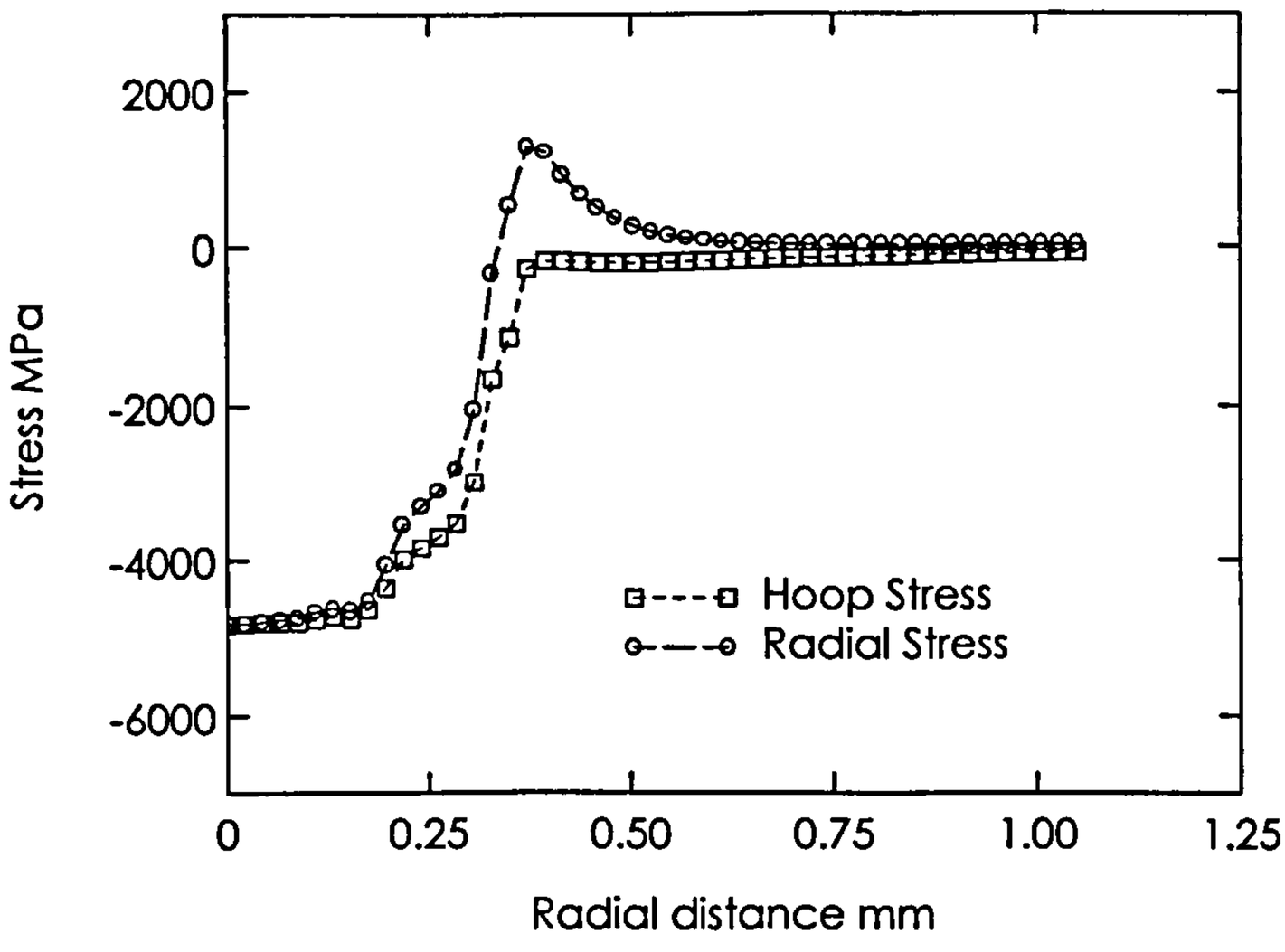

Fig.4.10(a) Surface radial and hoop stresses around indentation due to a load of 2 kN

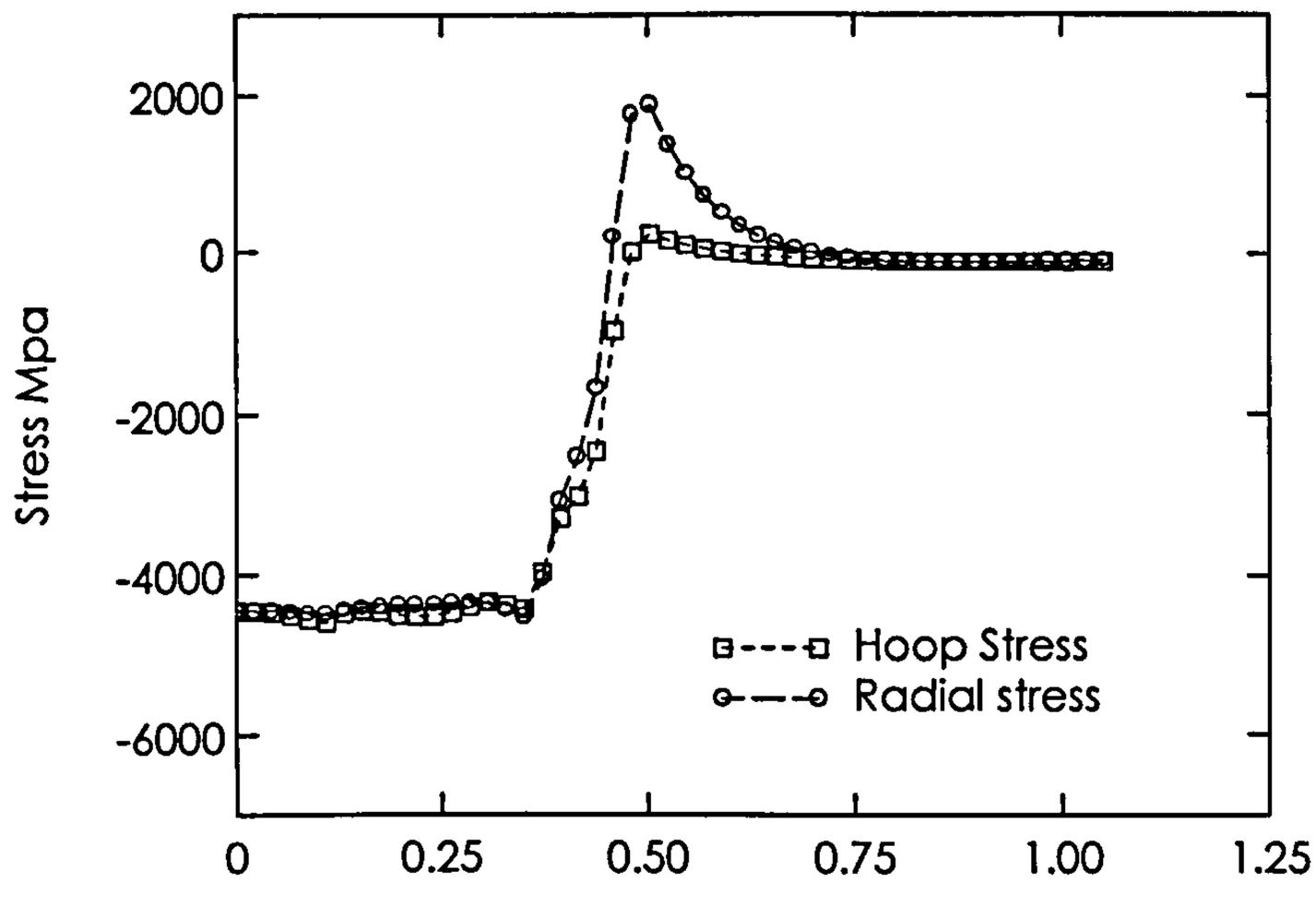

Fig.4.10(b) Surface radial and hoop stresses around indentation due to a load of 4 kN

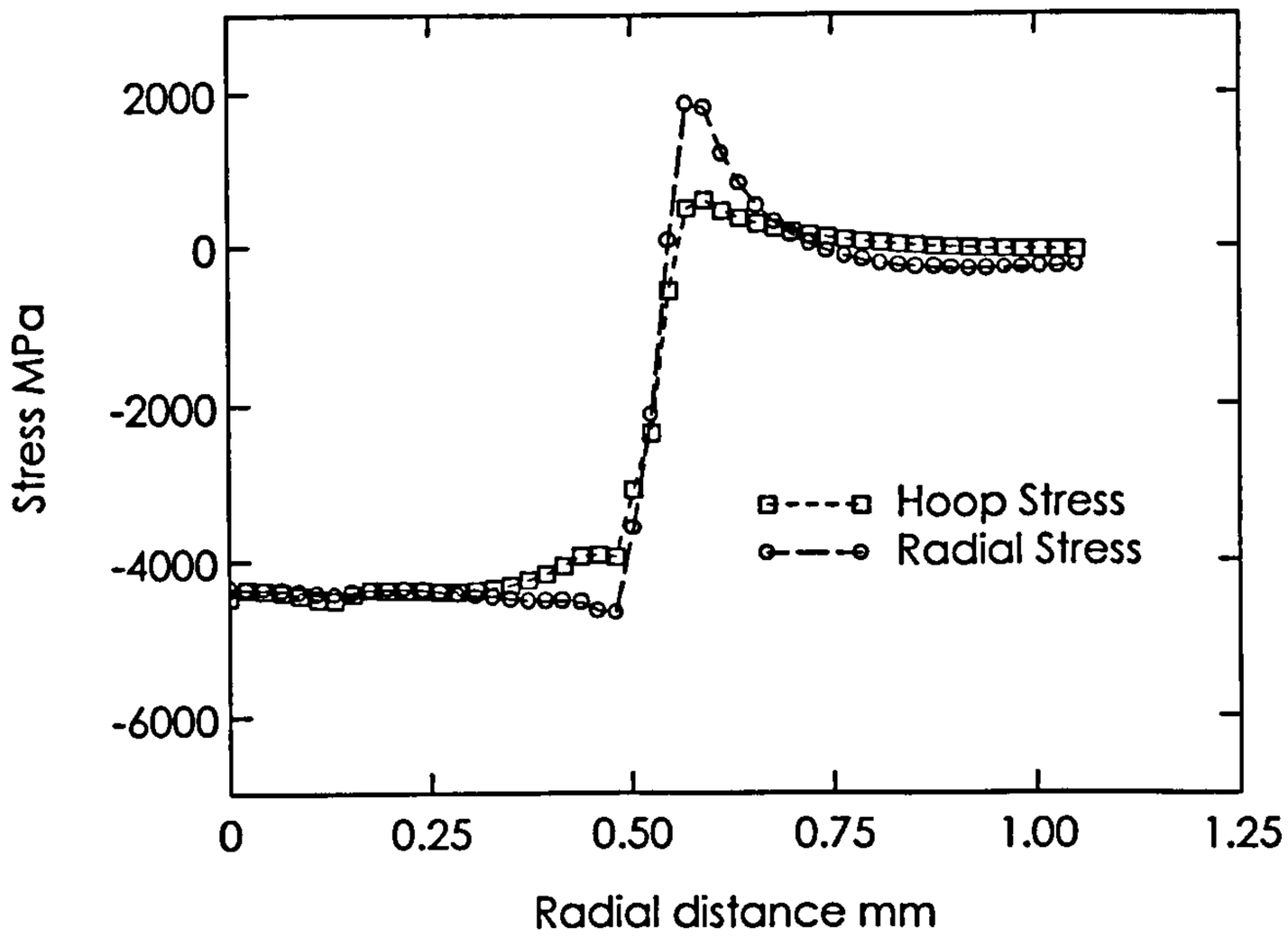

Fig.4.10(c) Surface radial and hoop stresses around indentation due to a load of 6 kN

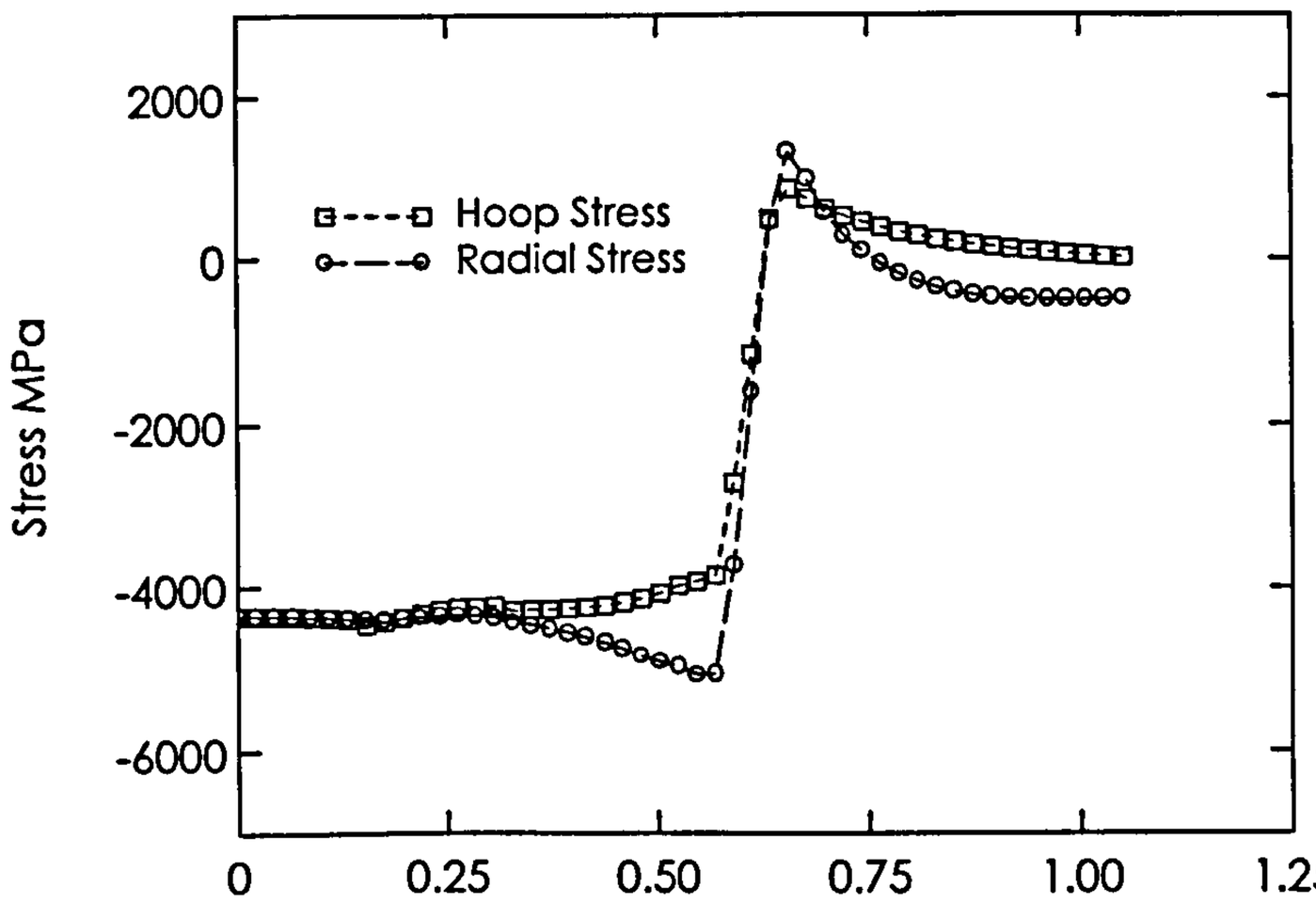

Fig.4.10 (d) Surface radial and hoop stresses around indentation due to a load of 8 kN

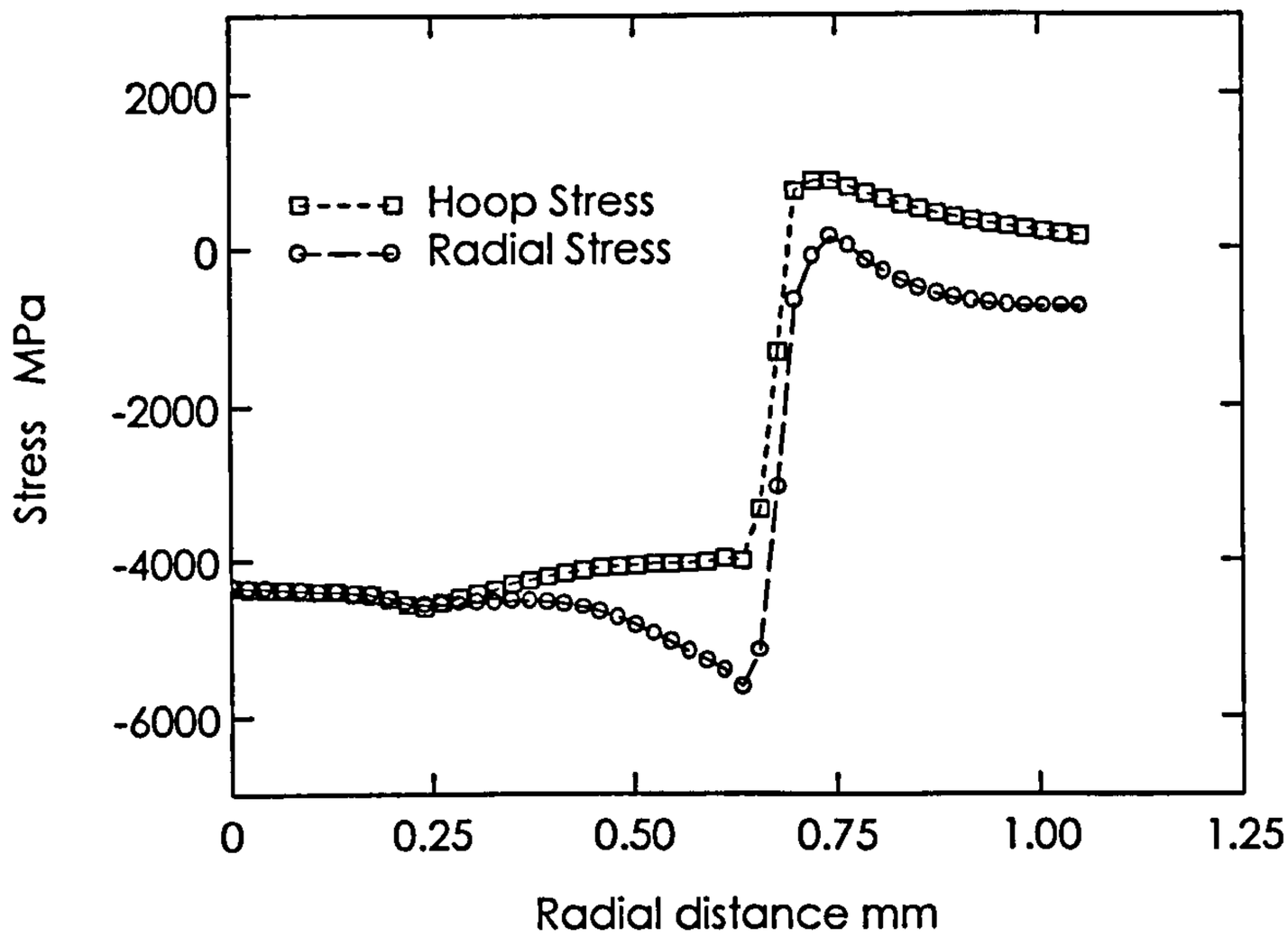

Fig.4.10 (e)Surface radial and hoop stresses around indentation due to a load of 10 kN

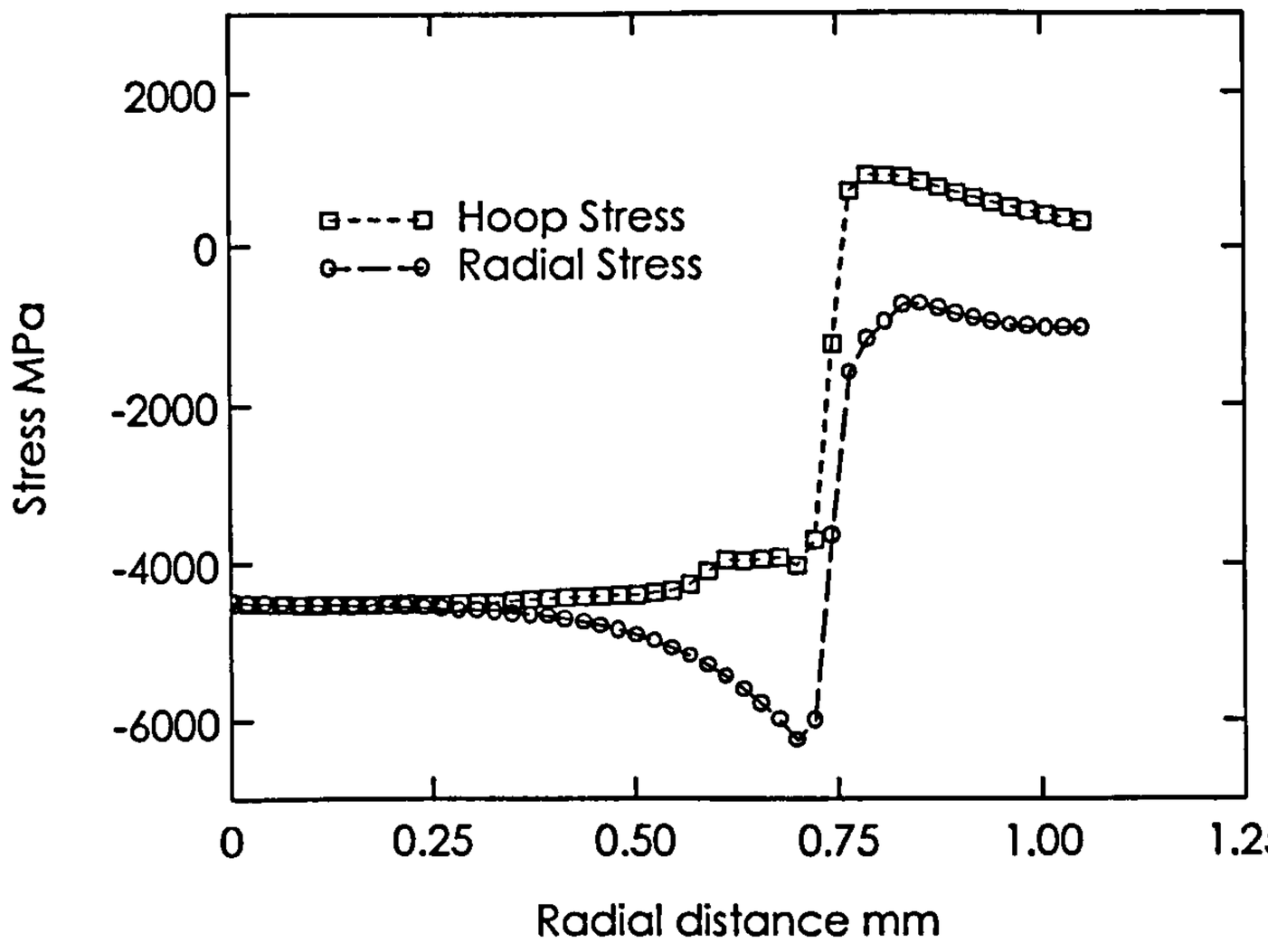

Fig.4.10 (f)Surface radial and hoop stresses around indentation due to a load of 12 kN

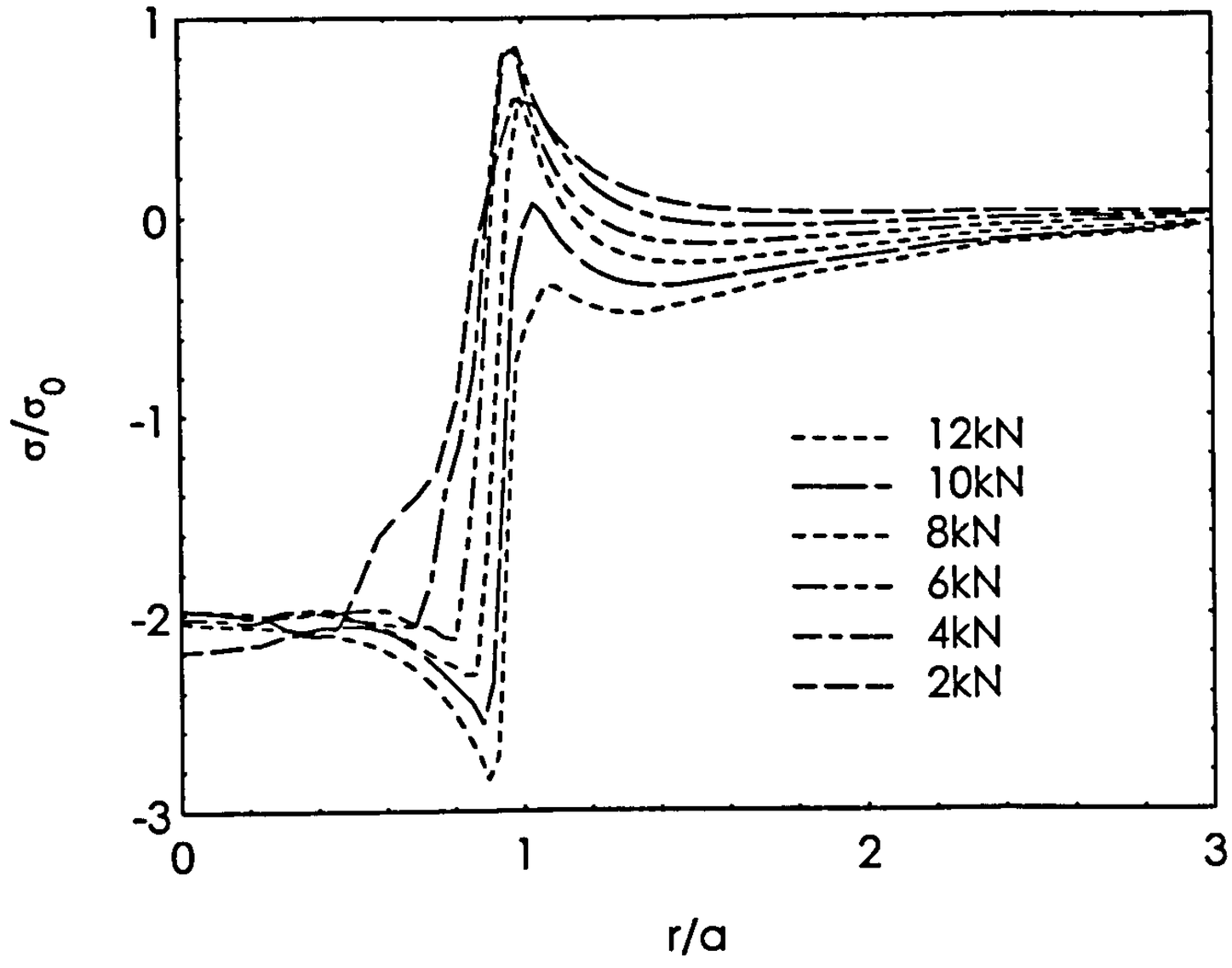

Fig.4.11 Stresses in radial direction during loading

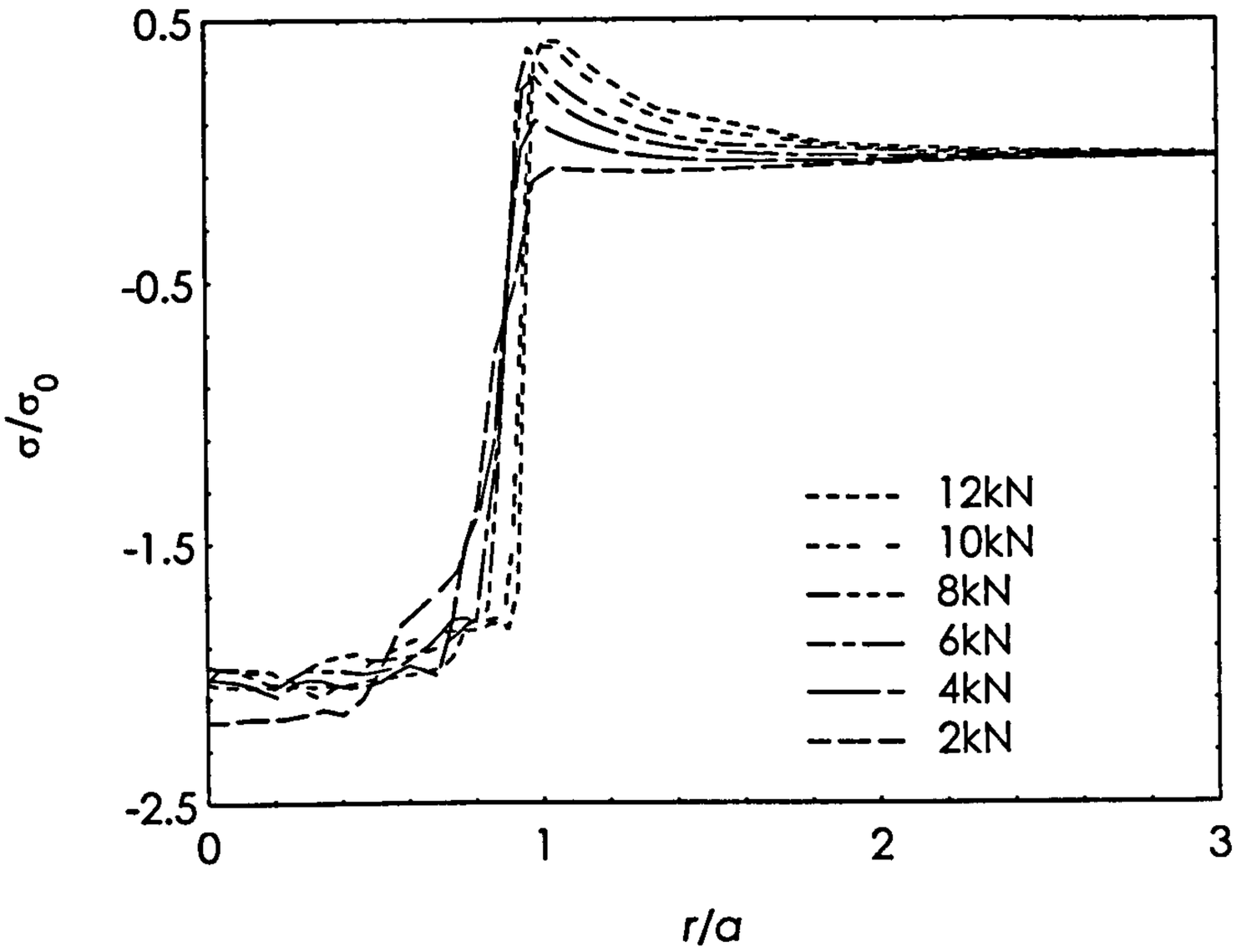

Fig.4.12 Stresses in hoop direction during loading

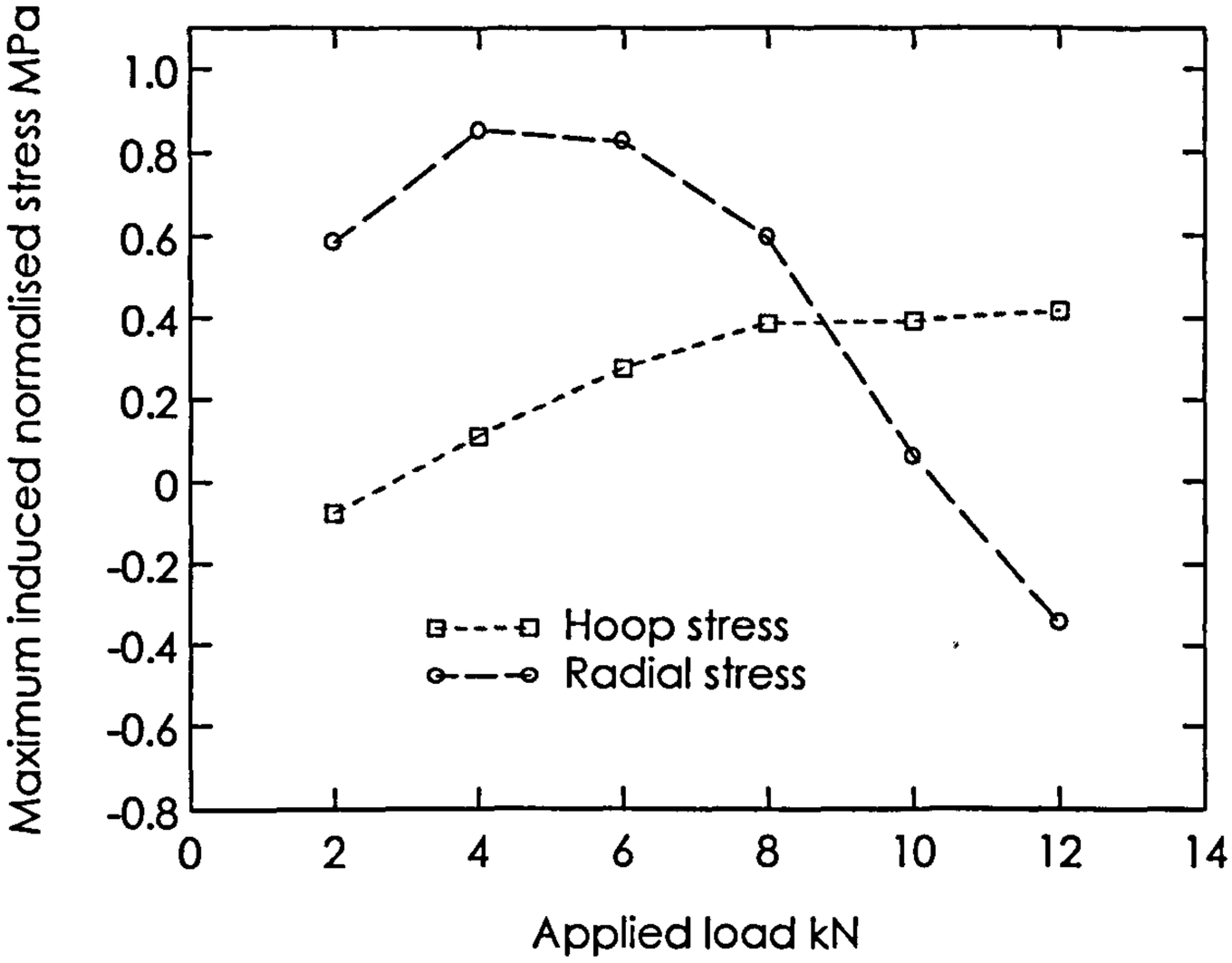

Fig.4.13 Highest stresses in radial and circumferential directions at the contact area boundary for various applied loads.

highest level of stress occurs at the contact area periphery. Figure 4.13 shows the maximum stresses attained in hoop and radial directions at various applied loads. The maximum induced hoop stress increases as the applied load increased while the induced radial stress decreases as the applied load increased beyond 4 kN and become compressive at applied load of 12 kN.

The results from the current work do not agree with results produced by Sinclair *et al.* (1985) (shown above). Both results predicted compressive stresses in radial and hoop directions within the indentation area which is expected. However outside the indentation results obtained by Sinclair *et al.* (1985) did not predict any tensile stresses near the surface in either the radial or hoop directions. In similar work, Hardy *et al.* (1977) obtained compressive stresses in radial and hoop directions. Only at low applied loads, tensile radial stress of small fraction of yield strength were obtained outside the contact area. These differences are ascribed to different stress-strain relations used in the different simulations. The stress-strain relation used in the present work are typical of hard steel, showing a large yield stress to modulus ratio and a modest degree of work hardening. Even at the maximum load used in the present work, the specimen did not enter the fully plastic regime.

4.4.2.c Contact Area

The radius of the contact area is not directly relevant to standing contact fatigue but results from the FE model can be compared with the experimental data.

Figures 4.14 and 4.15 compare results obtained with FE simulation with experimental standing contact fatigue test and indentation test for the size of the contact area. Figure 4.14 shows that the areas of contact obtained by FE simulation are very close to contact areas measured in experimental tests. Consequently plots for mean pressure versus the non-dimensional strain are in good agreements for results obtained with FE simulation compared with experimental tests as shown in Fig.4.15. In FE simulation as well as in the standing contact fatigue test the highest applied load was 12kN. Note that the limit for the ratio P_m/σ_Y is expected to be 3 for fully plastic indentation. The results in

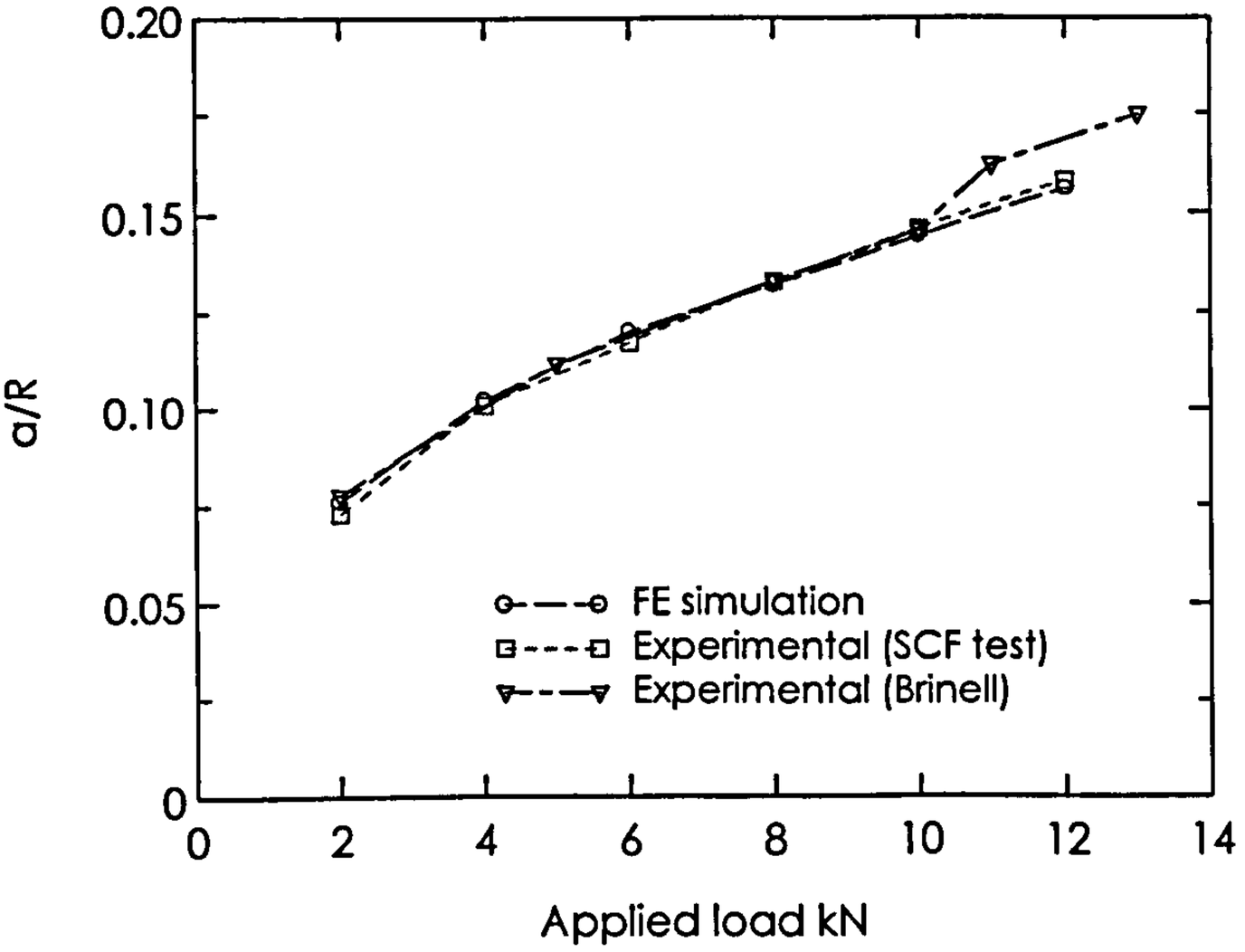

Fig.4.14 Comparison of contact area between FE simulated solution and experimental results

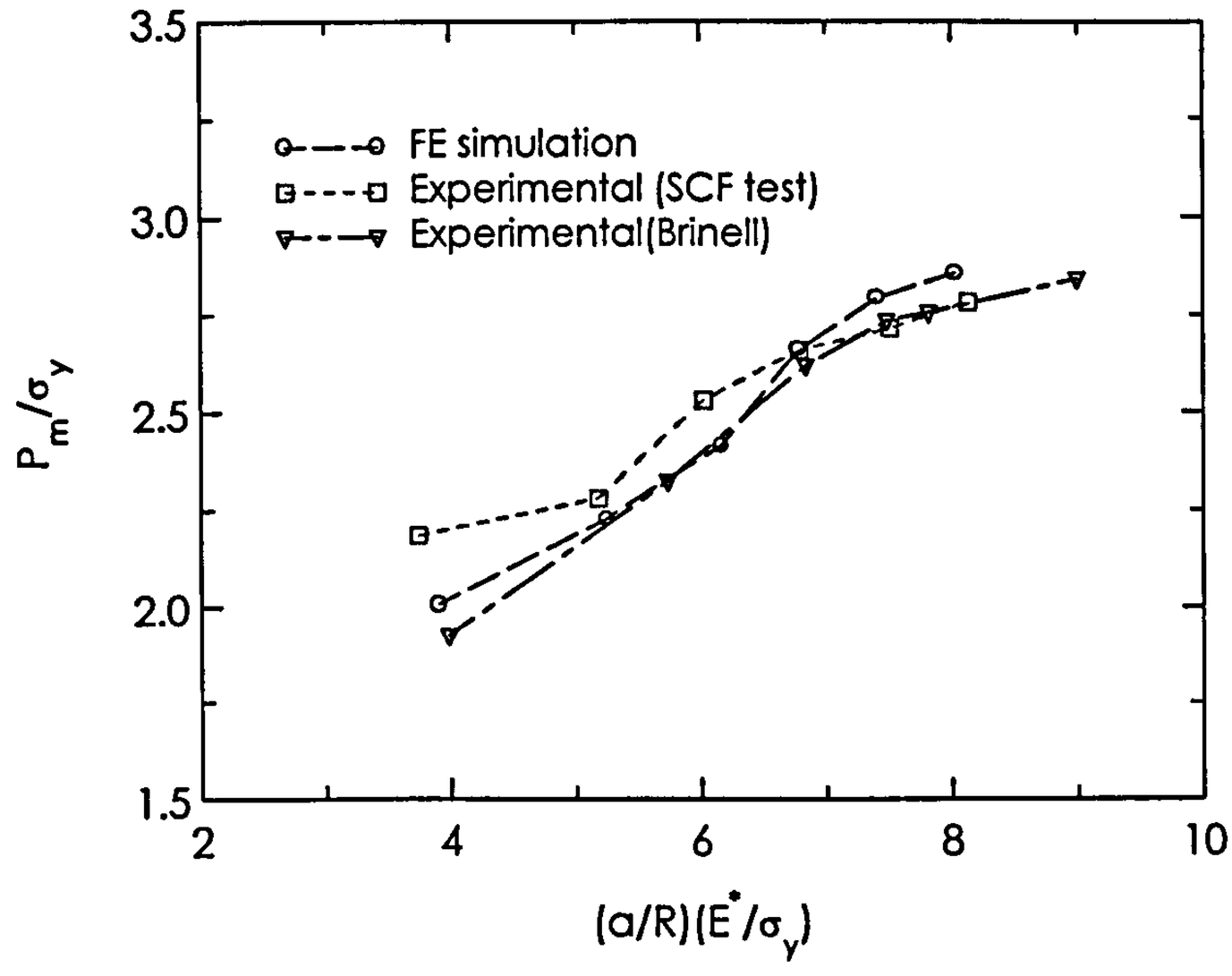

Fig.4.15 Relation between normalised applied pressure and corresponding non dimensional strain for FE simulation solution and experimental results

Fig.4.15 indicate that the fully plastic limit was not reached in our indentation test, as is consistent with other aspects of FE results.
It was found (Chapter 3) that the radial crack propagation rate increases with increasing applied load. This could be attributed to the higher hoop stress induced as a result of increasing applied load.

It is more difficult to explain presence of ring cracks based on FE results. As the applied load increased the induced radial stress decreased and become compressive at 12 kN applied load. However it was found in (Chapter 3) that ring cracks are very shallow. Ring cracks could result from deformed surface and plastic deformation induced by the indenter. When the applied load is 2 kN, plastic deformation did not approach specimen surface because the plastic zone was embedded within the material. At higher loads the plastic zone reach the contact surface as shown in figures 4.9 (c). This plastic deformation could be responsible for shallow ring cracks appeared in standing contact fatigue test although the exact mechanism is unclear. Further analysis of the FE results to calculate mean stress and stress variations are given below.

4.4.3 Measured and Estimated Residual Stresses

4.4.3.a Measured Residual Stress

The residual stress after indentation is important in calculating the mean stress and fluctuation stress in fatigue loading. This can be calculated using FE results and also measured in crude way on real indented specimens.

Surface residual stresses near indentations obtained in indentation test which were mentioned previously in (Chapter 3 Fig. 3.28) were measured using X-ray diffraction. Each value represents the average stress inside an area of a diameter of 0.8 mm adjacent to indentations peripheries. Measurements were taken in two orthogonal directions which correspond approximately to stresses in radial direction and very close to the hoop direction. Stress measurement at a single point is not possible by the X-ray technique, rather measurements taken over a small circle covered by the X-ray beam.

Therefore these results will be dealt with as comparative measurements and can not be considered suitable for detailed analyses.

Experimental results showed that tensile residual stresses and compressive residual stresses were induced in the hoop and radial directions, respectively. The magnitude of surface residual stresses around indentations in both directions increases as the applied load increased as shown in Fig 3.28.

4.4.3.b Estimated Residual Stress and Effect of Stress Range and Mean Stress on Fatigue Life

The radial cracks observed in standing contact fatigue must result from circumferential tensile stresses around indentations. FE results showed that at loads higher than 2 kN applied load, circumferential tensile stresses were developed around indentations. Circumferential residual tensile stresses should affect radial fatigue cracking. Tensile residual stresses raises the mean stress to higher level and promotes fatigue crack initiation.

The importance of assessing residual stresses after load removal is to estimate the applied stress range ($\Delta\sigma$) and mean applied stress ($\bar{\sigma}$). These two parameters are significant in determining fatigue strength. The stress range is the difference between the maximum applied stress and the minimum stress. Due to the presence of residual stress after load removal, the residual stress represents one of the extremes of stress. Residual stress affects also the mean stress. When residual stresses are compressive the level of mean stress is lowered. The contribution of these two parameters to fatigue life can be found in the following (Goodman) relation.

$$\Delta\sigma = \Delta\sigma_o\left[1-(\bar{\sigma}/\sigma_u)\right] \qquad (4.7)$$

where

$\Delta\sigma = \sigma_{max} - \sigma_{min}$ and $\bar{\sigma} = \left(\frac{\sigma_{max}+\sigma_{min}}{2}\right)$. $\Delta\sigma_o$ is the fatigue limit in completely reversed cyclic stress and σ_u is the tensile strength. Note that in the

Goodman relation $\Delta\sigma$ is taken to be the fatigue strength with a finite mean stress acting where as $\Delta\sigma_o$ is the fatigue strength with zero mean stress.

Estimation of residual stresses was based on an assumption suggested by Johnson (1989). He proposed that no plastic deformation accompanies unloading. In the loaded state the stress distribution in spherical contact will depend on the plastic deformation that has occurred. Denote the surface stress distribution at maximum load by the terms σ_r^L, σ_θ^L and σ_z^L. Outside the contact area ($r > a$) $\sigma_z^L = 0$. Within the contact area ($r < a$), the distribution of σ_z^L depends on the load and the plastic deformation. In purely elastic deformation, the distribution is parabolic, with $\sigma_z^L = p_0 (1 - (r/a)^2)^{1/2}$, where p_0 is the maximum pressure = $3P/(2\pi a^2)$. As the plastic zone increases in size, the distribution becomes increasingly flattened. However, in all cases the mean pressure $\overline{p}$ is equal to $P/(\pi a^2)$ where P is the applied force and a is the radius of the contact area. The stresses outside the plastic zone after unloading can be estimated by superimposing an elastic solution on the results obtained at the maximum load.

An important result to consider is that with elastic deformation, the stress distribution at all points outside the contact radius ($r > a$), depends only on the total applied force or the mean pressure $\overline{p}$ and is independent of the distribution of pressure within the contact area (Johnson, 1989). This allows an estimation of the residual stresses after unloading to be made.

Consider spherical contact with plastic deformation in the flat specimen. The response of the specimen is the same as if the appropriate pressure were applied over the surface of the contact area (Fig.4.16). Now consider unloading the ball. The response of the specimen is modelled by applying positive tractions to the contact area to exactly cancel the pressure distribution that occurred after the initial loading. Now assume that *no plastic deformation accompanies unloading* (Johnson, 1989). The residual stress can then be calculated by superimposing the stress distribution produced by the *elastic* deformation from the positive tractions (negative pressure).

The surface stress components produced by a mean pressure $\overline{p}$ in elastic deformation are

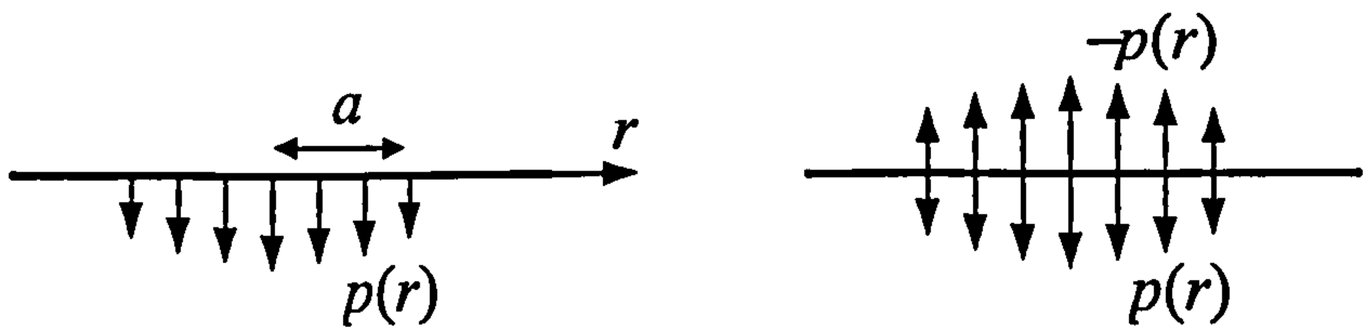

Fig.4.16 Equivalent contact pressure for spherical indenter (left) and opposite and equal pressure to resemble load removal (right)

$$\sigma_r = \frac{(1-2\nu)\overline{p}}{2}\frac{a^2}{r^2}, \qquad (r > a) \qquad (4.8)$$
$$\sigma_\theta = -\frac{(1-2\nu)\overline{p}}{2}\frac{a^2}{r^2},$$

The application of positive tractions (negative pressure) will produce stresses of equal magnitude but with opposite sign. It follows that the residual stresses are given by

$$\sigma_r^R = \sigma_r^L - \frac{(1-2\nu)\overline{p}}{2}\frac{a^2}{r^2}, \qquad (4.9)$$
$$\sigma_\theta^R = \sigma_\theta^L + \frac{(1-2\nu)\overline{p}}{2}\frac{a^2}{r^2}, \qquad (r > a).$$

Where the superscript R denotes residual stress after unloading and the superscript L denotes the stress at the maximum load.

In subsequent load cycles the stress variations are

$$\Delta\sigma_r = \Delta\sigma_\theta = \frac{(1-2\nu)\overline{p}}{2}\frac{a^2}{r^2}, \qquad (r > a). \qquad (4.10)$$

Finally, the mean stresses are

$$\overline{\sigma}_r = \sigma_r^L - \frac{(1-2\nu)\overline{p}}{4}\frac{a^2}{r^2}, \qquad (4.11)$$
$$\overline{\sigma}_\theta = \sigma_\theta^L + \frac{(1-2\nu)\overline{p}}{4}\frac{a^2}{r^2}, \qquad (r > a).$$

The stress distribution in the radial and hoop directions under loading was obtained from the FE stress profiles presented previously. Results for mean stress and stress range for all applied loads are shown in Fig.4.17 (a-f) for radial stresses and Fig.4.18 (a-f) for hoop stresses.

For both stress components the highest values for stress range and mean stress occurs at indentations edges and then decreases gradually with radial distance. Therefore the areas near indentations peripheries are the most potent sites for crack initiation.

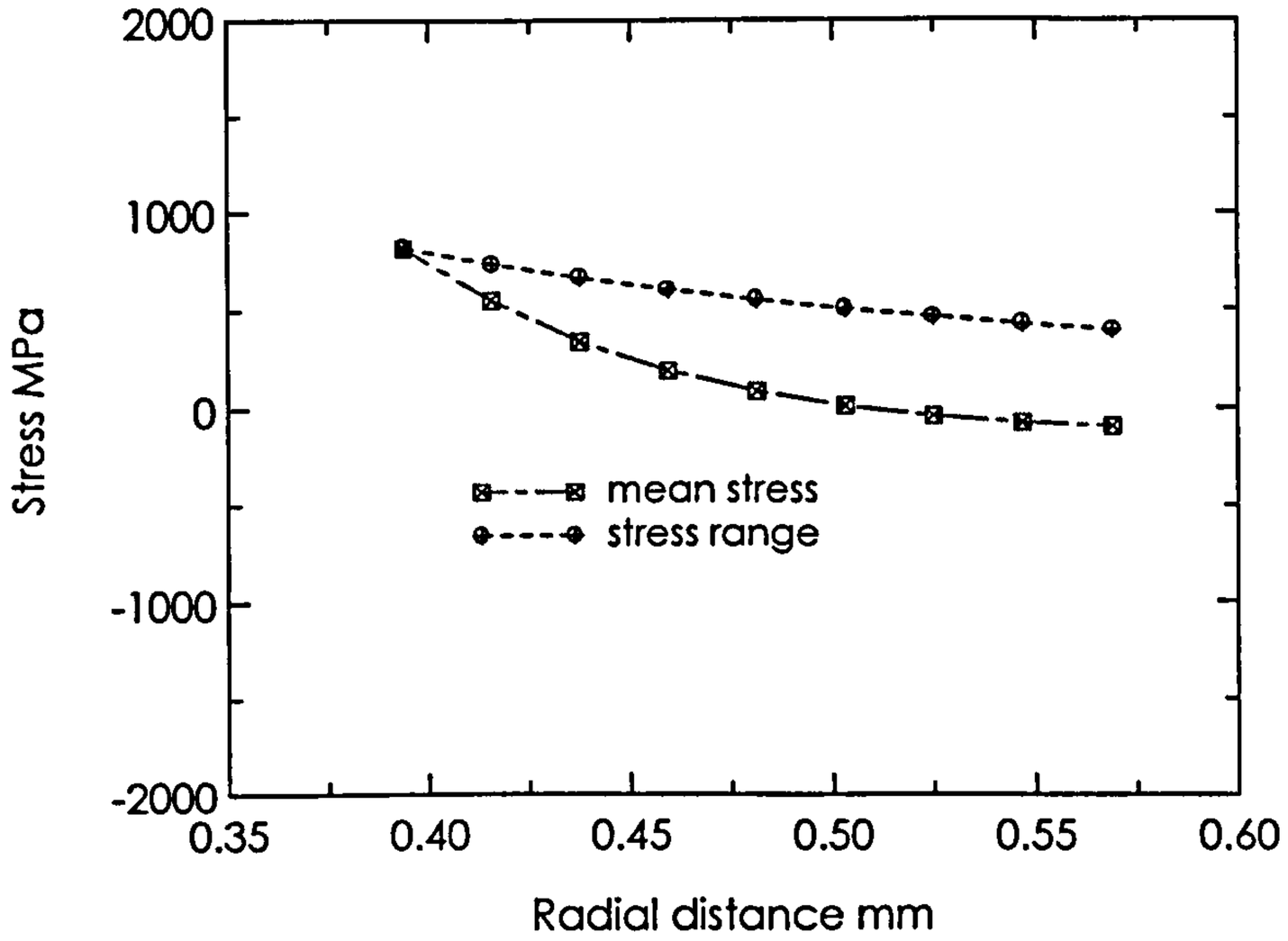

Fig 4.17(a) stress range and mean stress in radial direction with applied load of 2 kN. Radius of contact area is 0.38 mm

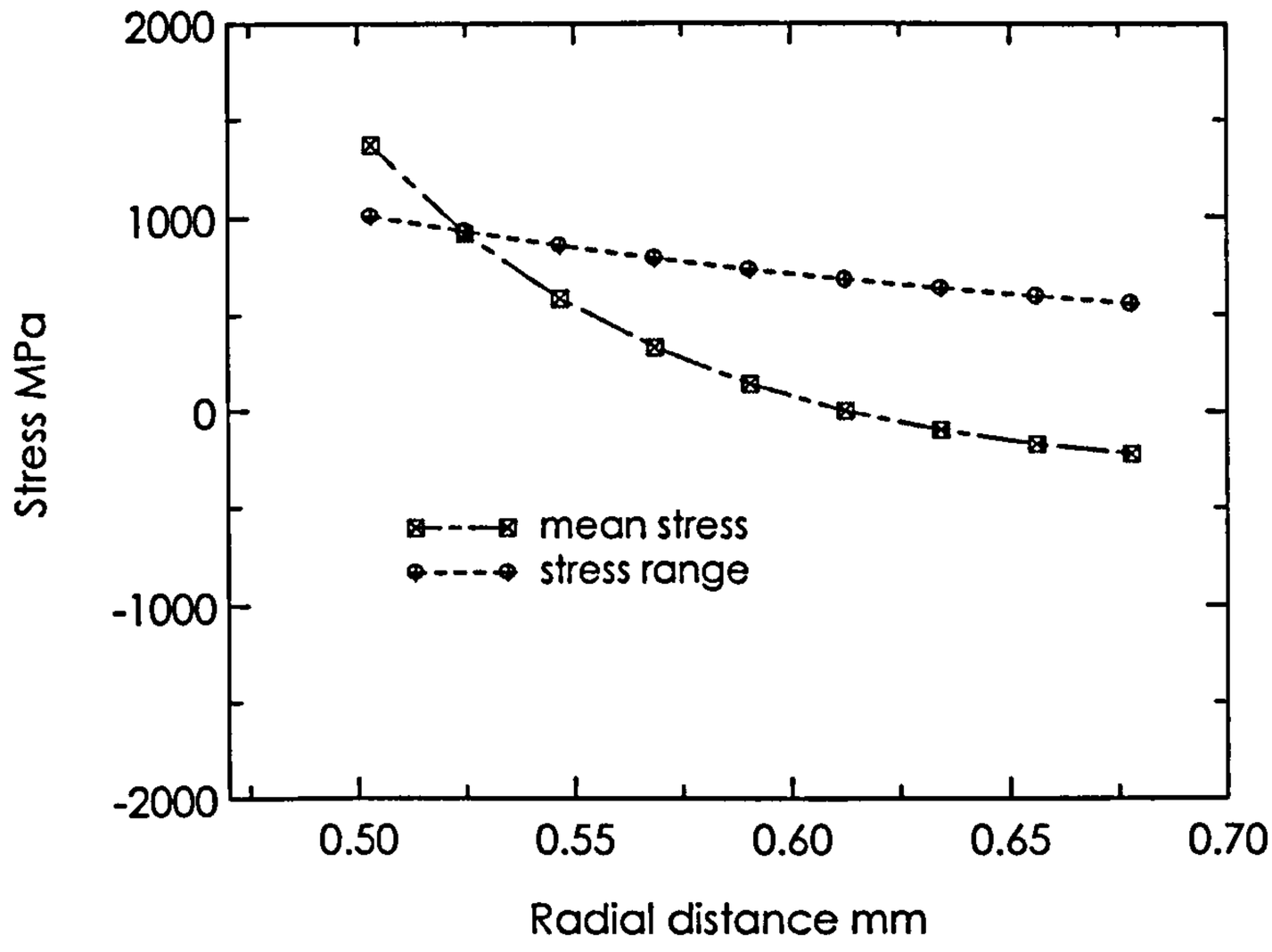

Fig 4.17(b) stress range and mean stress in radial direction with applied load of 4 kN. Radius of contact area is 0.51 mm

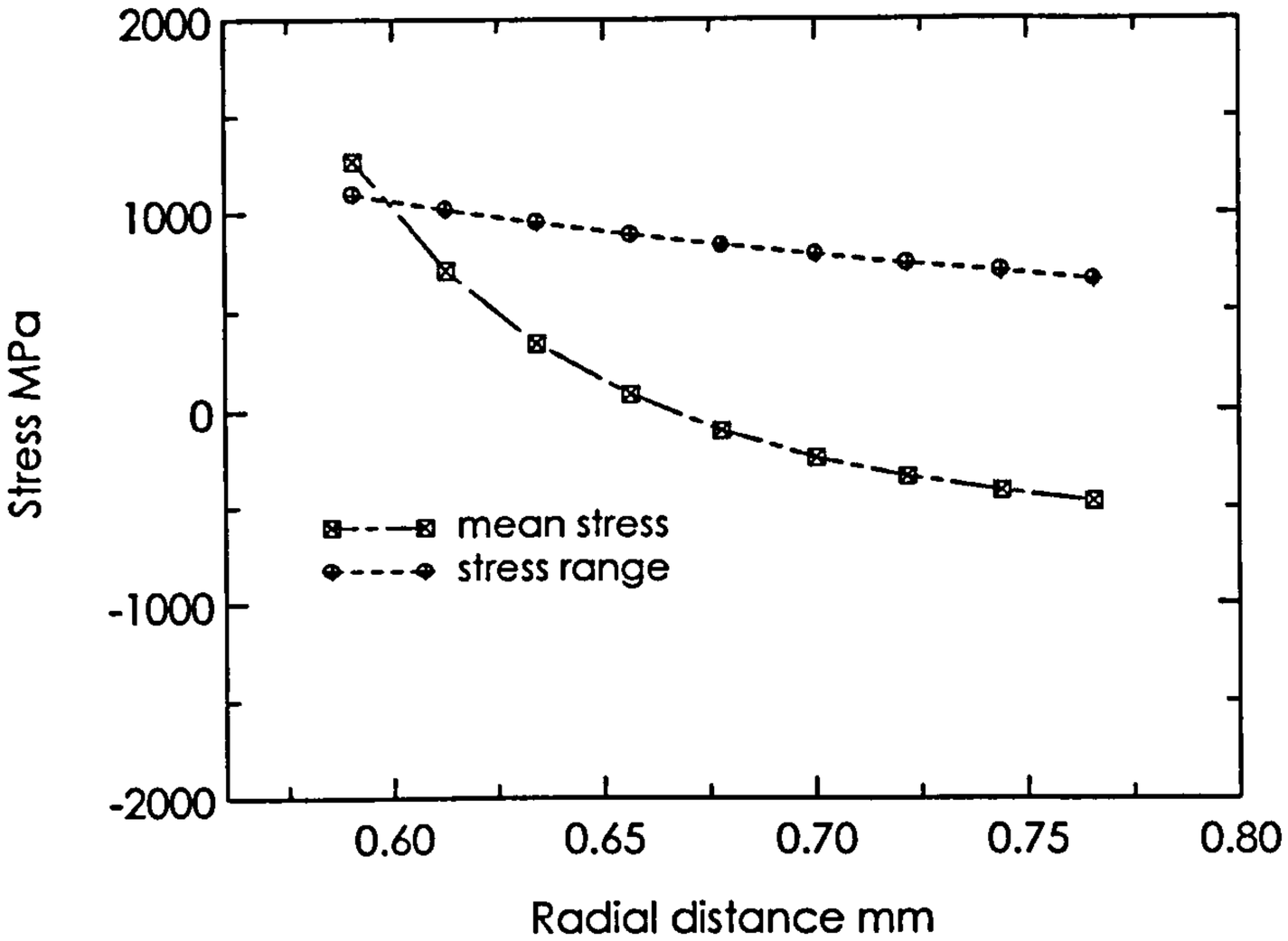

Fig 4.17(c) stress range and mean stress in radial direction with applied load of 6 kN. Radius of contact area is 0.6 mm

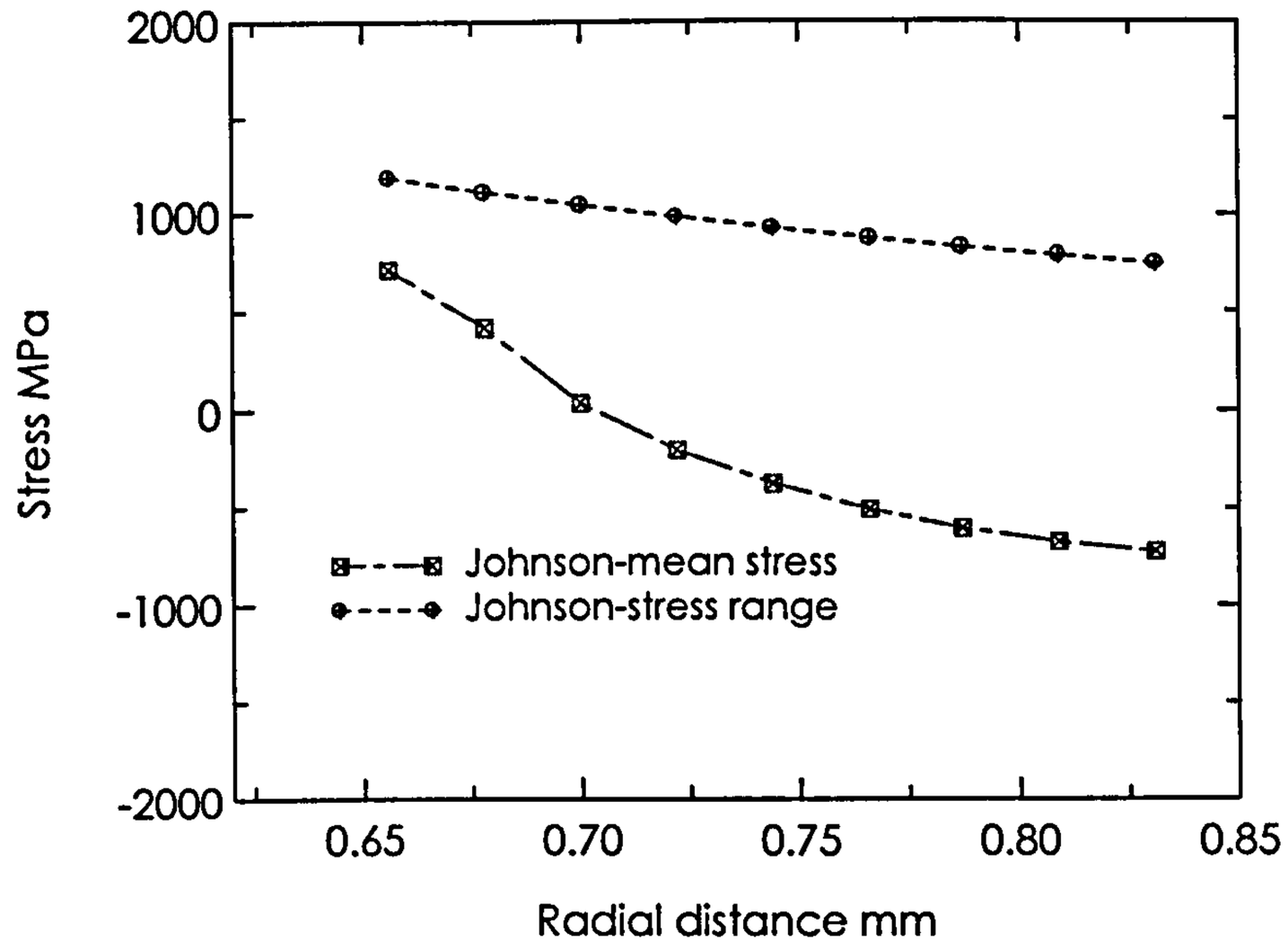

Fig 4.17(d) stress range and mean stress in radial direction with applied load of 8 kN. Radius of contact area is 0.66 mm

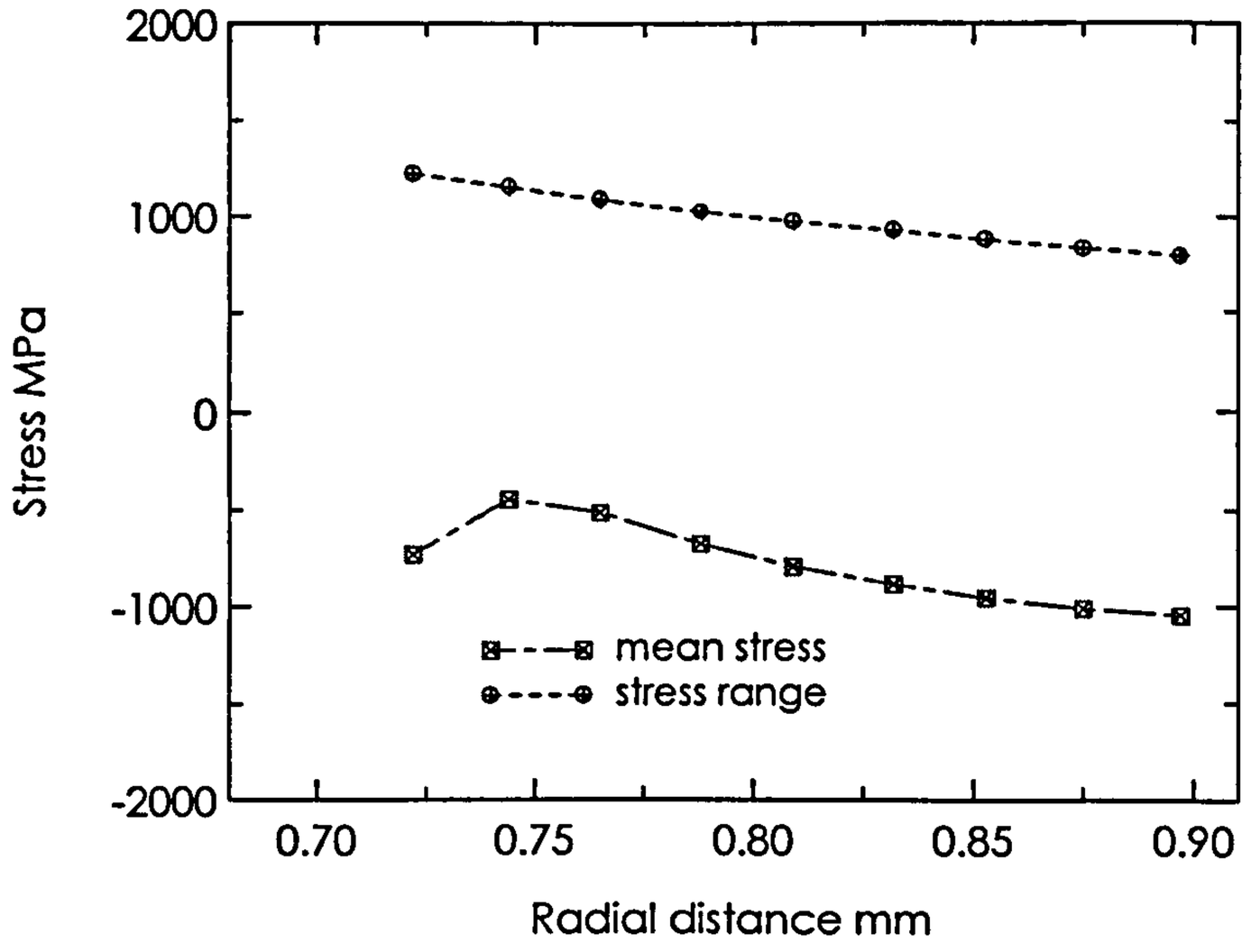

Fig 4.17(e) stress range and mean stress in radial direction with applied load of 10 kN. Radius of contact area is 0.72 mm

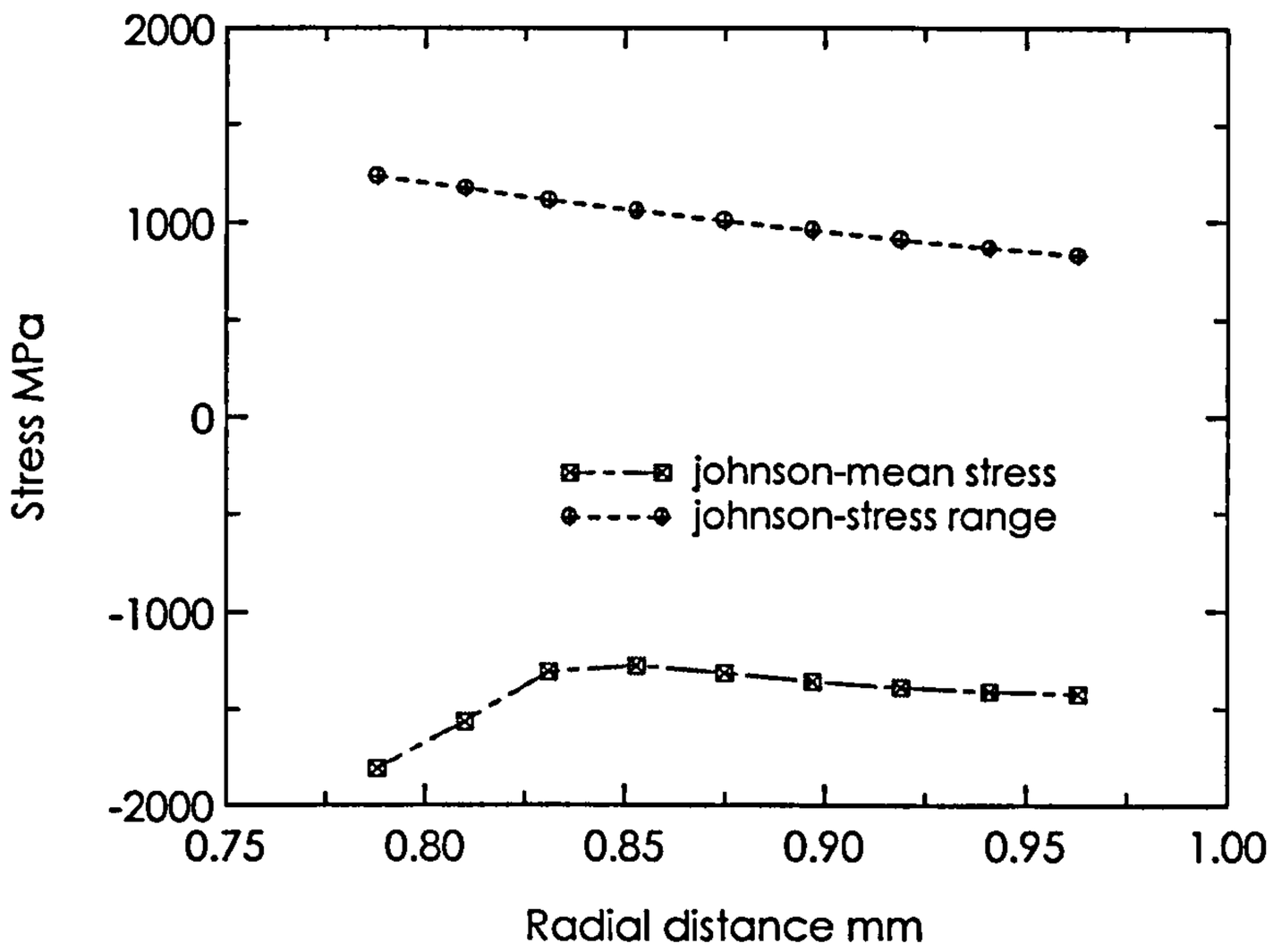

Fig 4.17(f) stress range and mean stress in radial direction with applied load of 12 kN. Radius of contact area is 0.78 mm

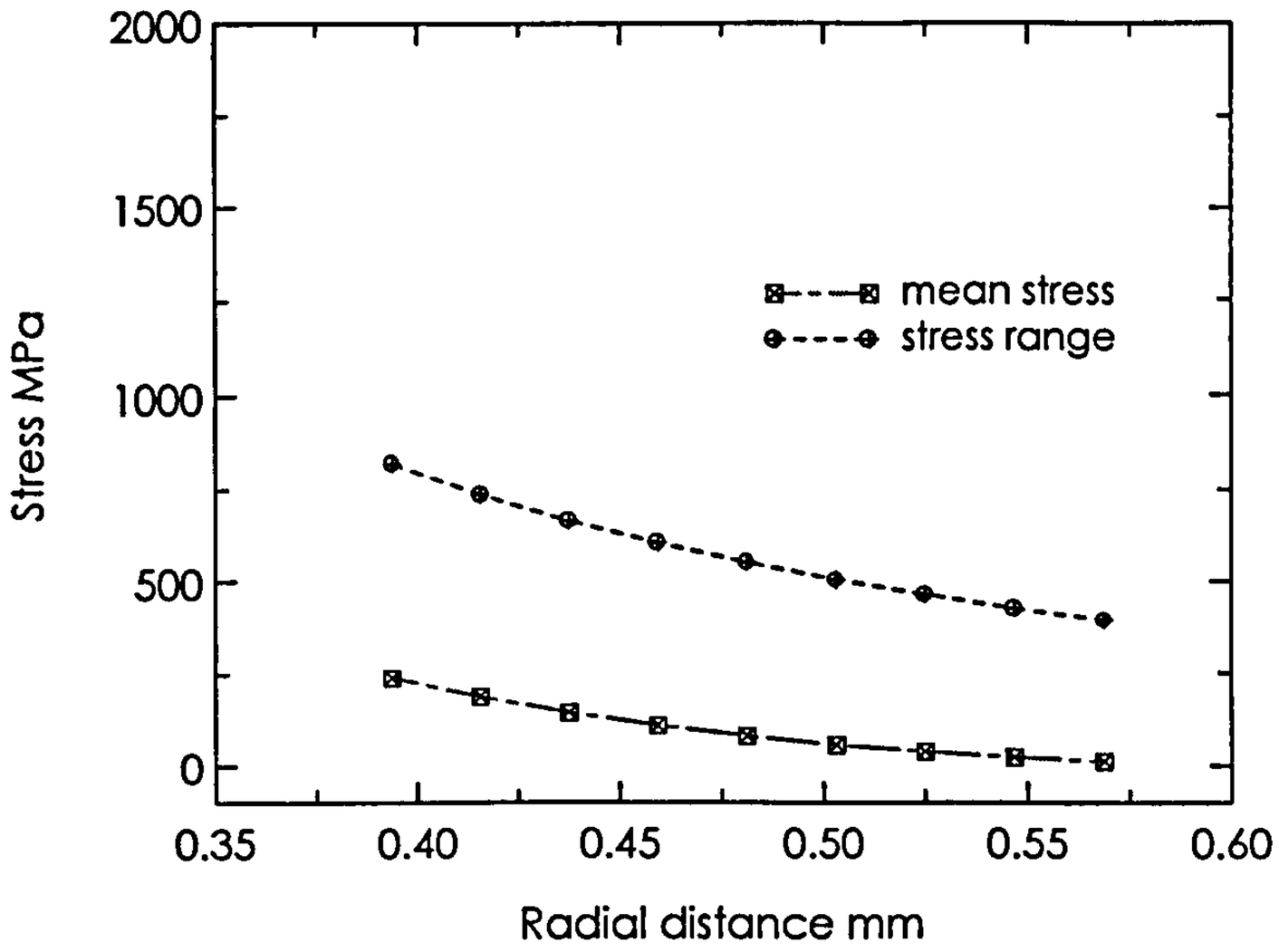

Fig 4.18(a) stress range and mean stress in hoop direction with applied load of 2 kN. Radius of contact area is 0.38 mm

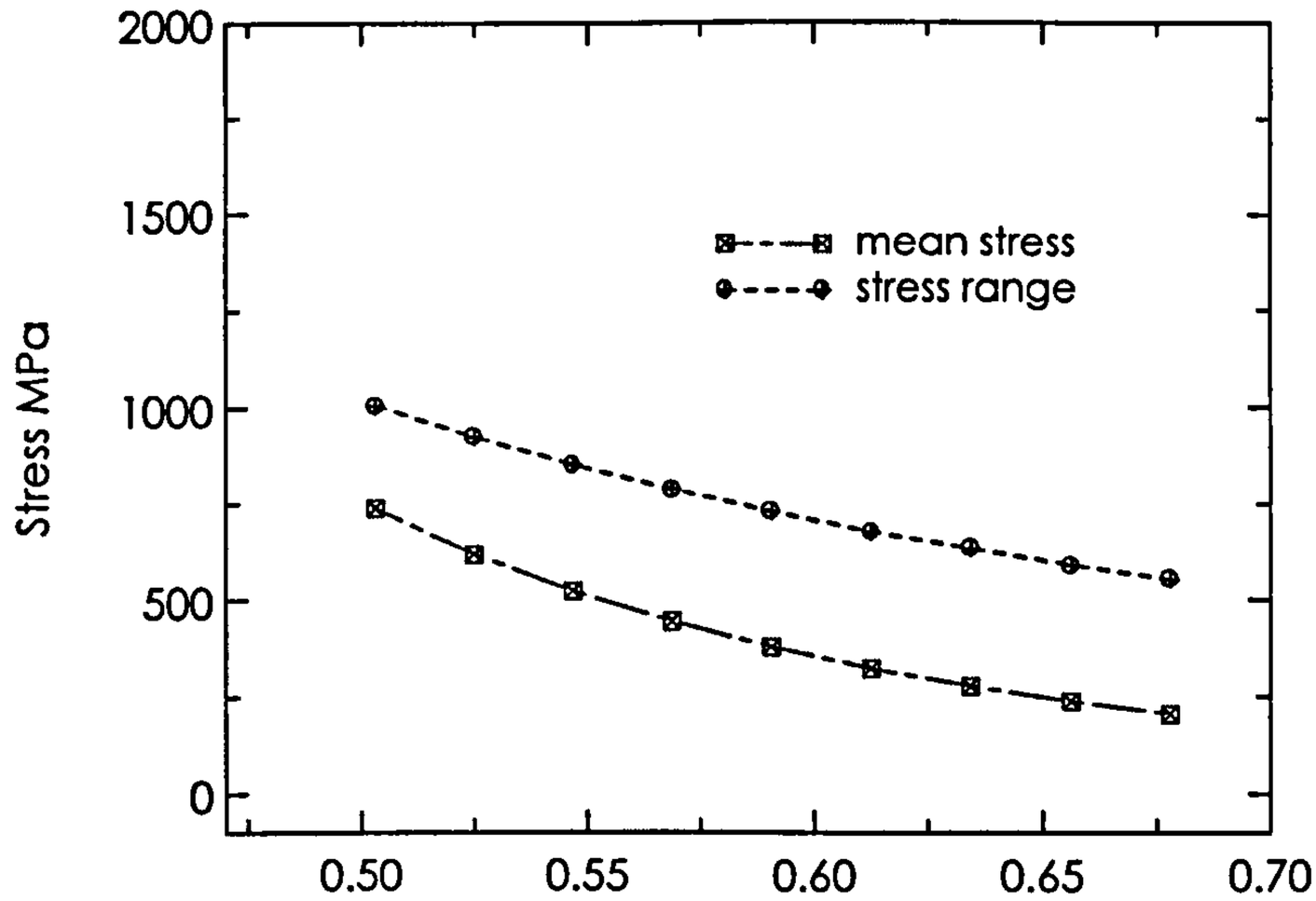

Fig 4.18(b) stress range and mean stress in hoop direction with applied load of 4 kN. Radius of contact area is 0.51 mm

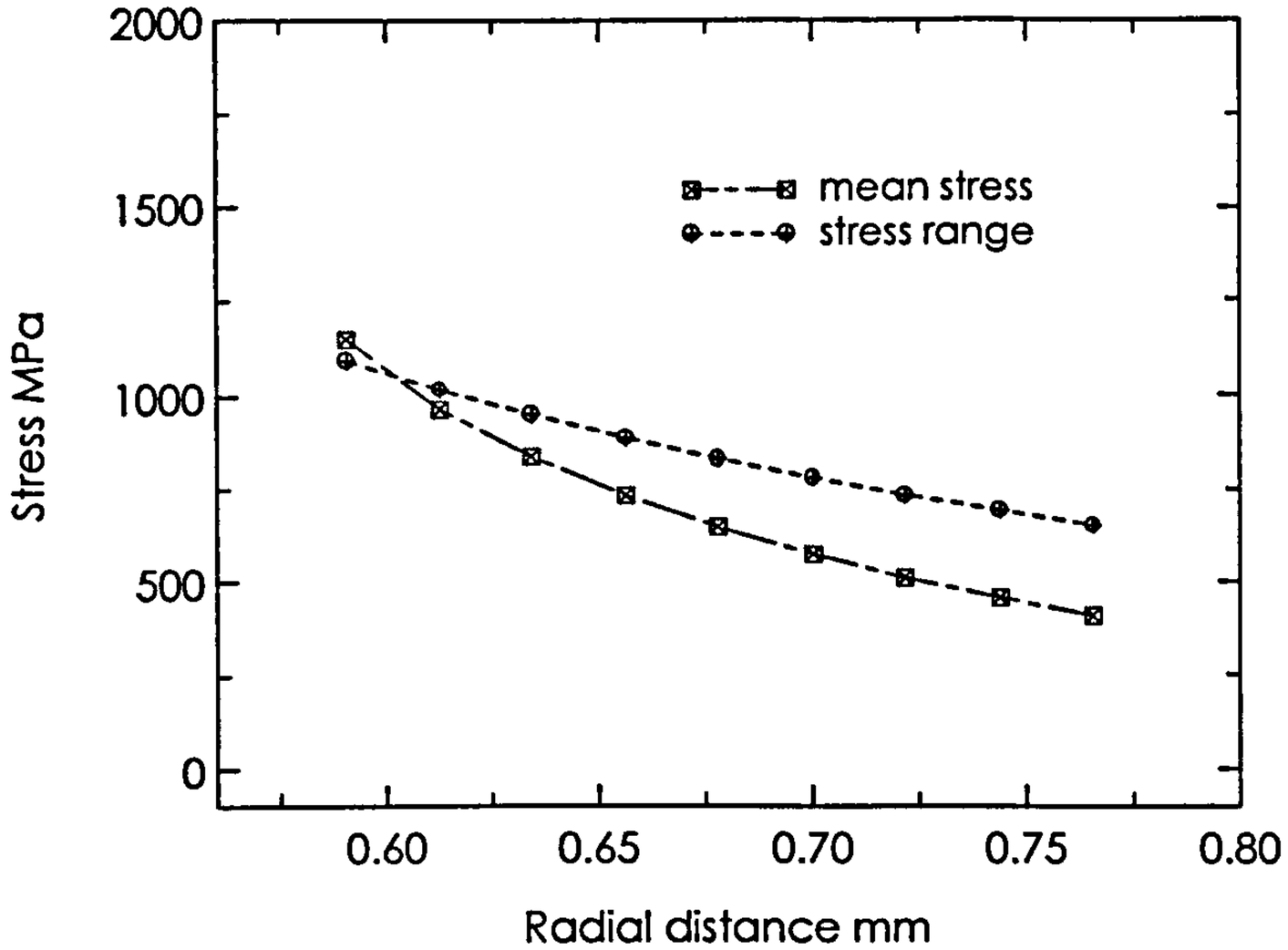

Fig 4.18(c) stress range and mean stress in hoop direction with applied load of 6 kN. Radius of contact area is 0.6 mm

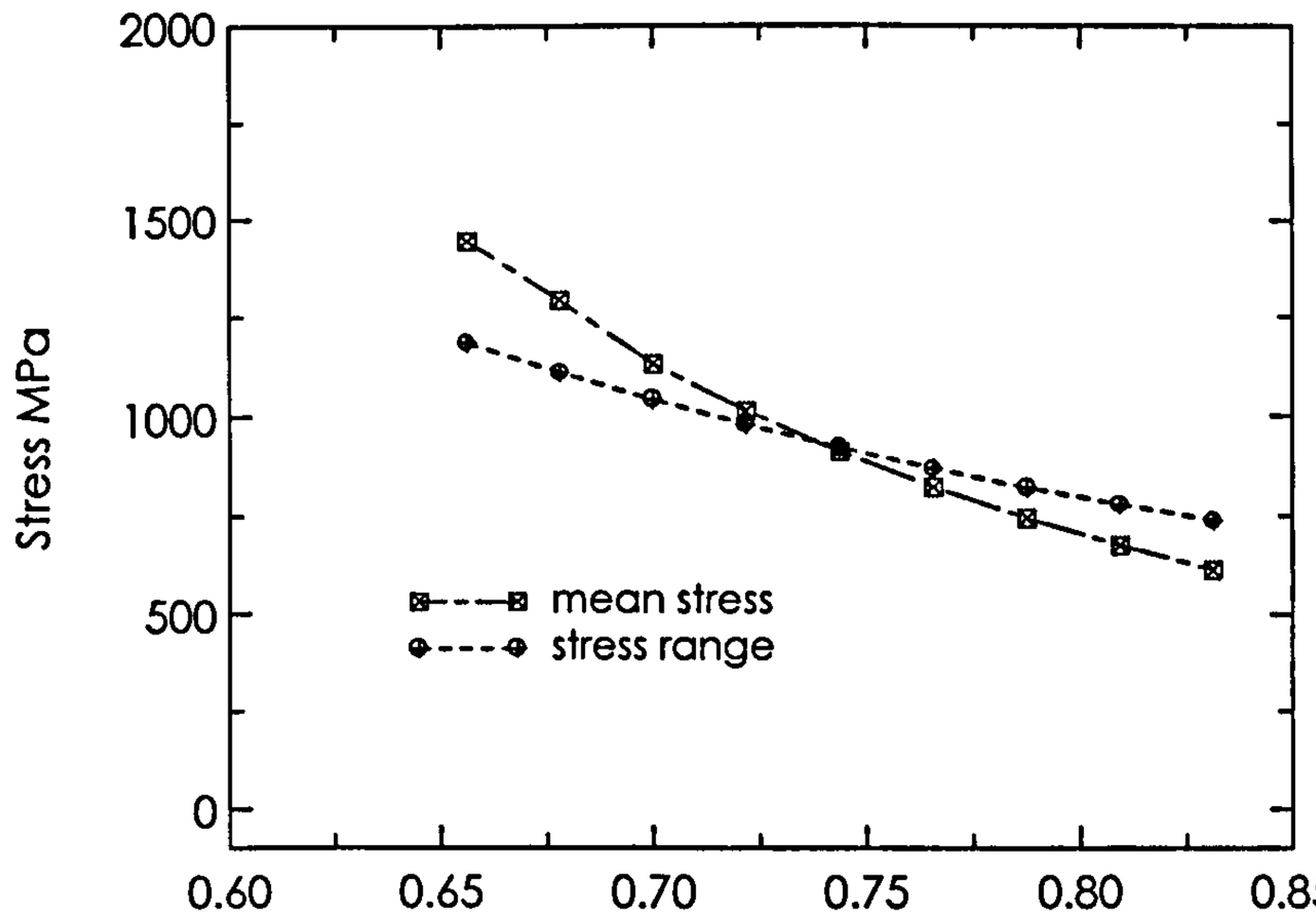

Fig 4.18(d) stress range and mean stress in hoop direction with applied load of 8 kN. Radius of contact area is 0.66 mm

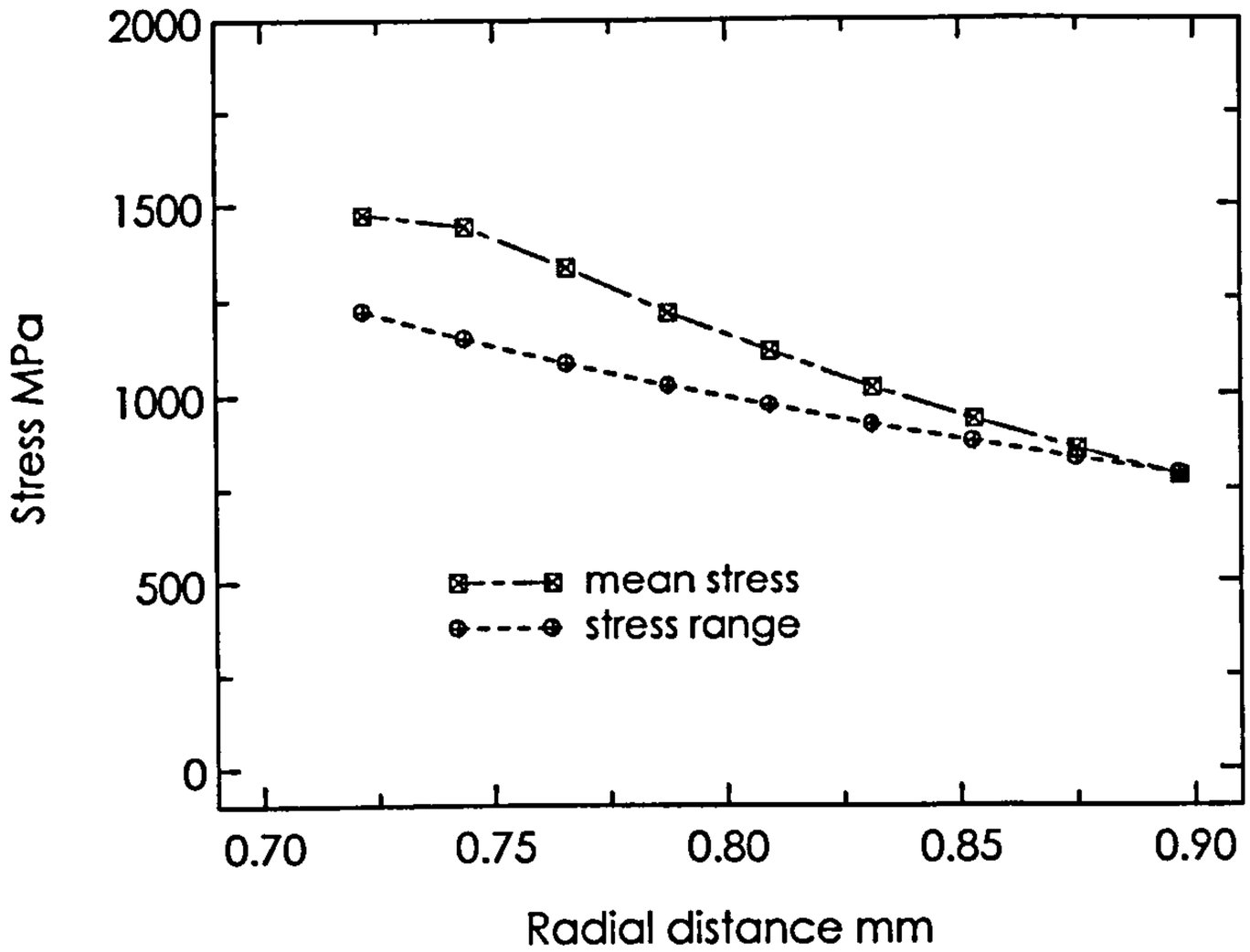

Fig 4.18(e) stress range and mean stress in hoop direction with applied load of 10 kN. Radius of contact area is 0.72 mm

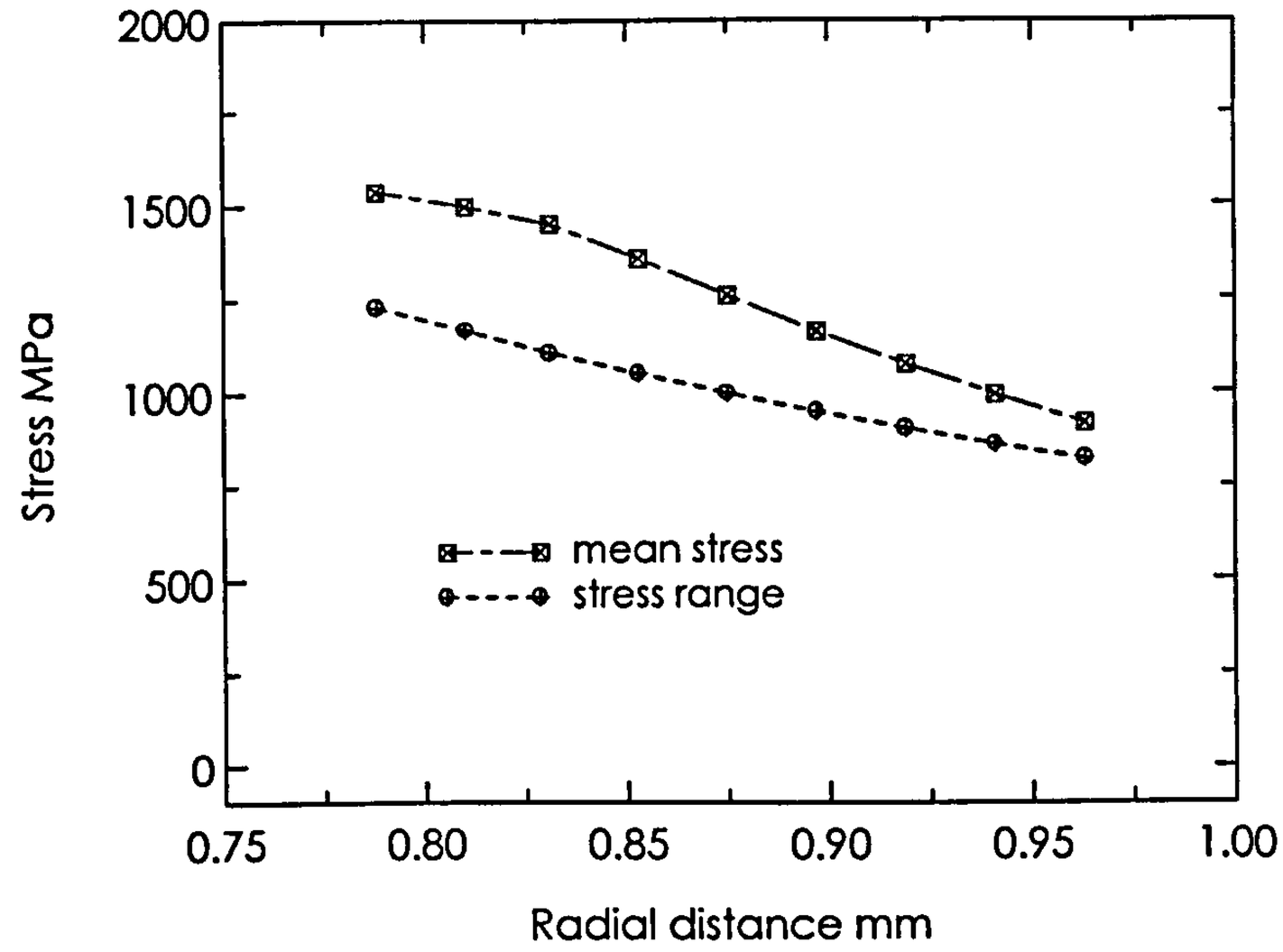

Fig 4.18(f) stress range and mean stress in hoop direction with applied load of 12 kN. Radius of contact area is 0.78 mm

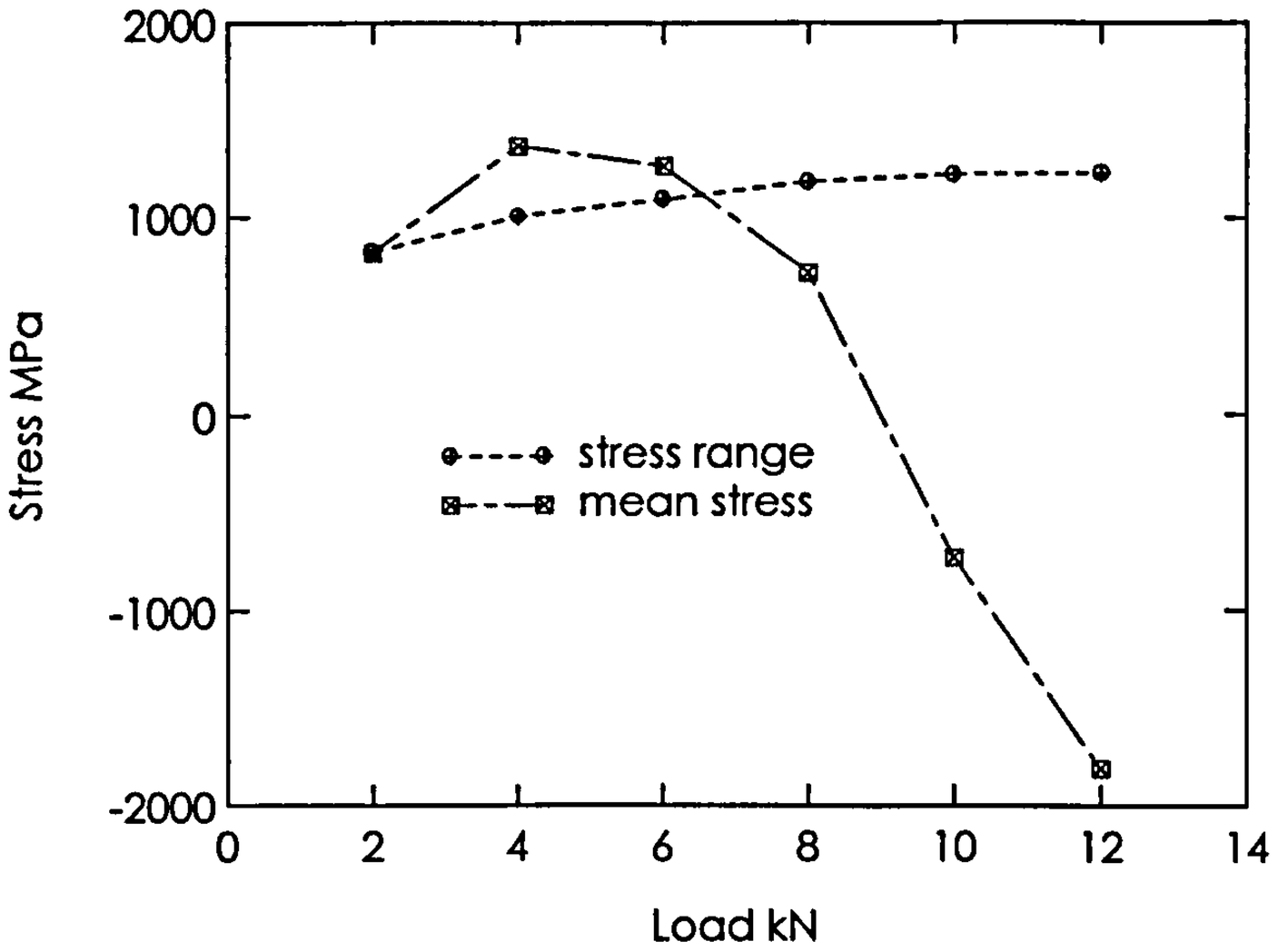

Fig.4.19 variation of mean stress and stress range at indentations peripheries with applied load in the radial direction

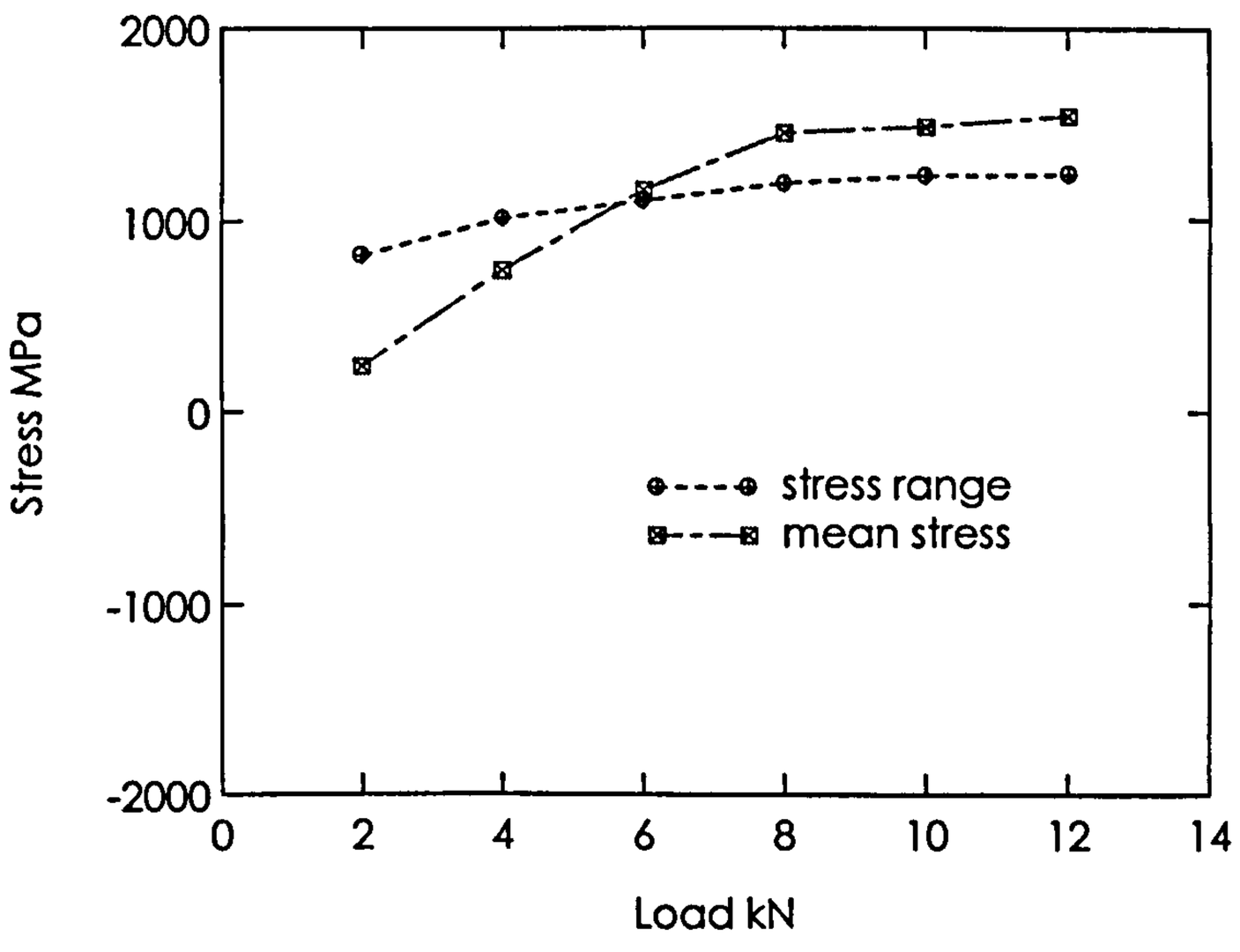

Fig.4.20 Variation of mean stress and stress range at indentations peripheries with applied load in the hoop direction

The variations of mean stress and stress range with applied load at indentations peripheries are shown in figures 4.19 and 4.20 for radial and hoop stress components respectively. These changes in mean stress resulted from changes in stresses at maximum load. This is evident by comparing figures 4.19 and 4.20 with Fig.4.13. The effect of stress at maximum load on stress range is less apparent. This is because changes of residual stresses follow a similar trend to changes in stresses at maximum load.

Hoop stresses are responsible for radial crack initiation and propagation. These results are not in contradictions with results presented in (Chapter 3 Fig.3.48). which shows that rate of crack propagation of radial cracks increases with increasing applied load.

For the radial stress component the mean stress at loads of 4kN or higher decreases with increasing applied load. The mean stresses at 10 and 12 kN become compressive. It has been pointed out earlier that ring cracks in the experiments were very shallow and could be introduced due to plastic deformation of the pressed indenter against the specimen surface in the standing contact fatigue test, i.e. due to factors that have not been properly modelled in the FEA presented above.

In purely elastic indentation, the radial stress is tensile outside the contact area whilst the hoop stress is compressive. The situation is reversed in elastic-plastic indentation and in the fully plastic regime. Here, the radial stress is compressive whilst the hoop stress is tensile as illustrated in Fig. 4.21.

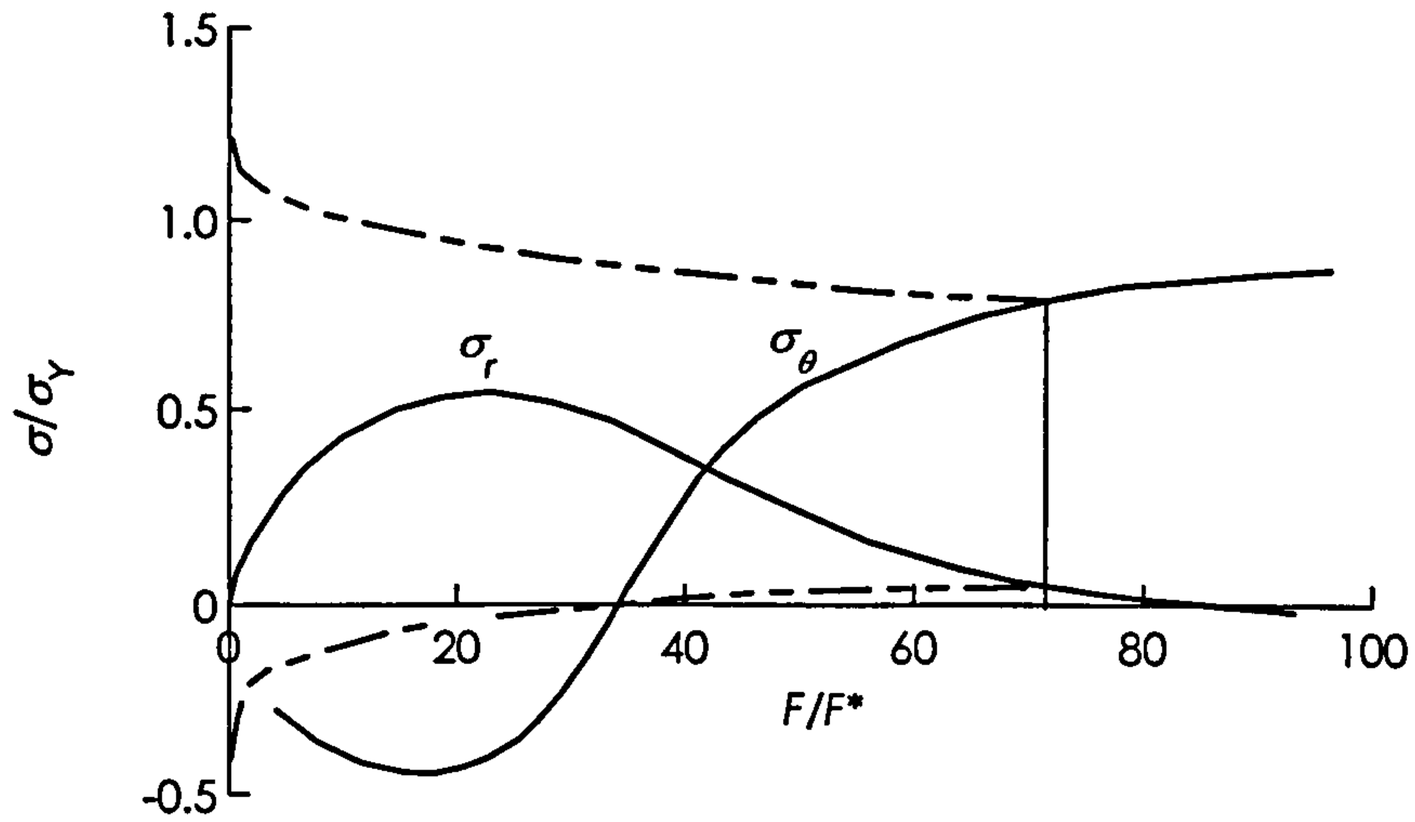

Fig.4.21 Schematic illustration of the proposed variation of surface radial and hoop stresses at indentation edge with increasing contact load as proposed by Studman and Field.(1977)

CHAPTER 5

The Austenite to Martensite Transformation and Residual Stress

It is often stated that when carburised steels are heat treated, sub-zero cooled or shot peened, the transformation of austenite to martensite contributes significantly to the residual stresses that are developed. Despite the fact that the austenite to martensite transformation in steel produces a volume dilatation, there is, in our experience, little unequivocal evidence that the transformation is the source of the development of significant residual stress. Thus, it is worth considering the theoretical background so that estimates of residual stress can be compared with experimental measurements. The following treatment was developed from Mura's (1998) textbook on micromechanics.

We wish to estimate the residual stress induced by martensite transformation in case carburised steel. If the transformation occurs during quenching from the austenite region at high temperatures, thermally activated plastic relaxation could interfere with the development of residual stress. To avoid this complication, consider transformation at low temperatures, either by strain or stress-induced transformation (e.g. during shot peening) or by sub-zero cooling. In practice this could occur by the transformation of *retained* austenite by one or all of these mechanisms. It is shown below that residual stresses are induced in the case region principally because of the *dilatation* that accompanies the martensite transformation. Under this circumstance the development of the residual compressive stress in the case is analogous to the transient thermal stress developed in the surface layers when a solid is heated and can be calculated in the same way.

5.1 Background

It is generally accepted that the basic atom movements involved in the austenite-to-martensite transformation in ferrous alloys are described by the resulting Bain strain (Bain, 1924). The Bain strain is best defined using the body centred tetragonal cell that can be picked out within a pair of structure cells in the fcc. austenite. The cell shown in Fig.5.1 has dimensions $b = a_0/\sqrt{2}$ and $c = a_0$, where a_0 is the lattice parameter of the

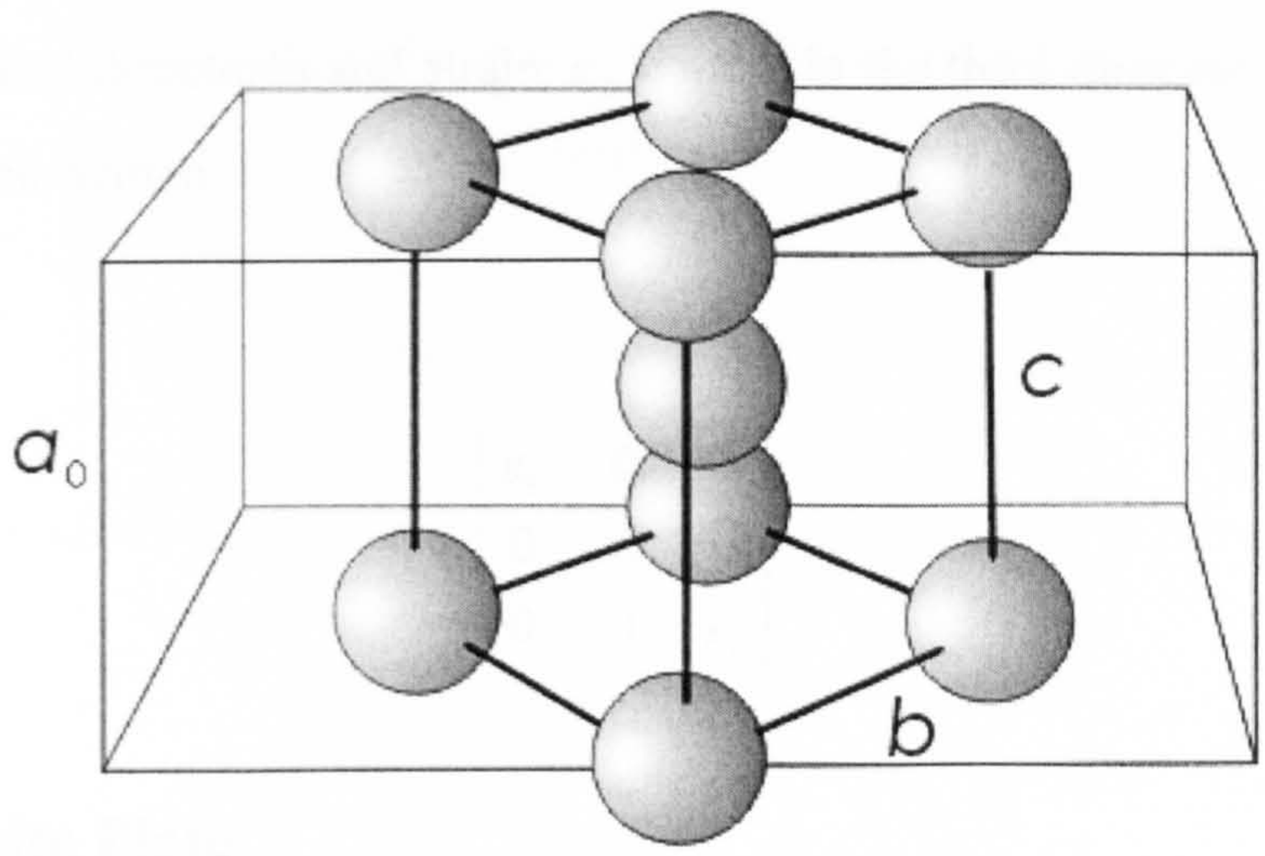

Fig. 5.1. Body centred tetragonal cell within a pair of face centred cubic cells

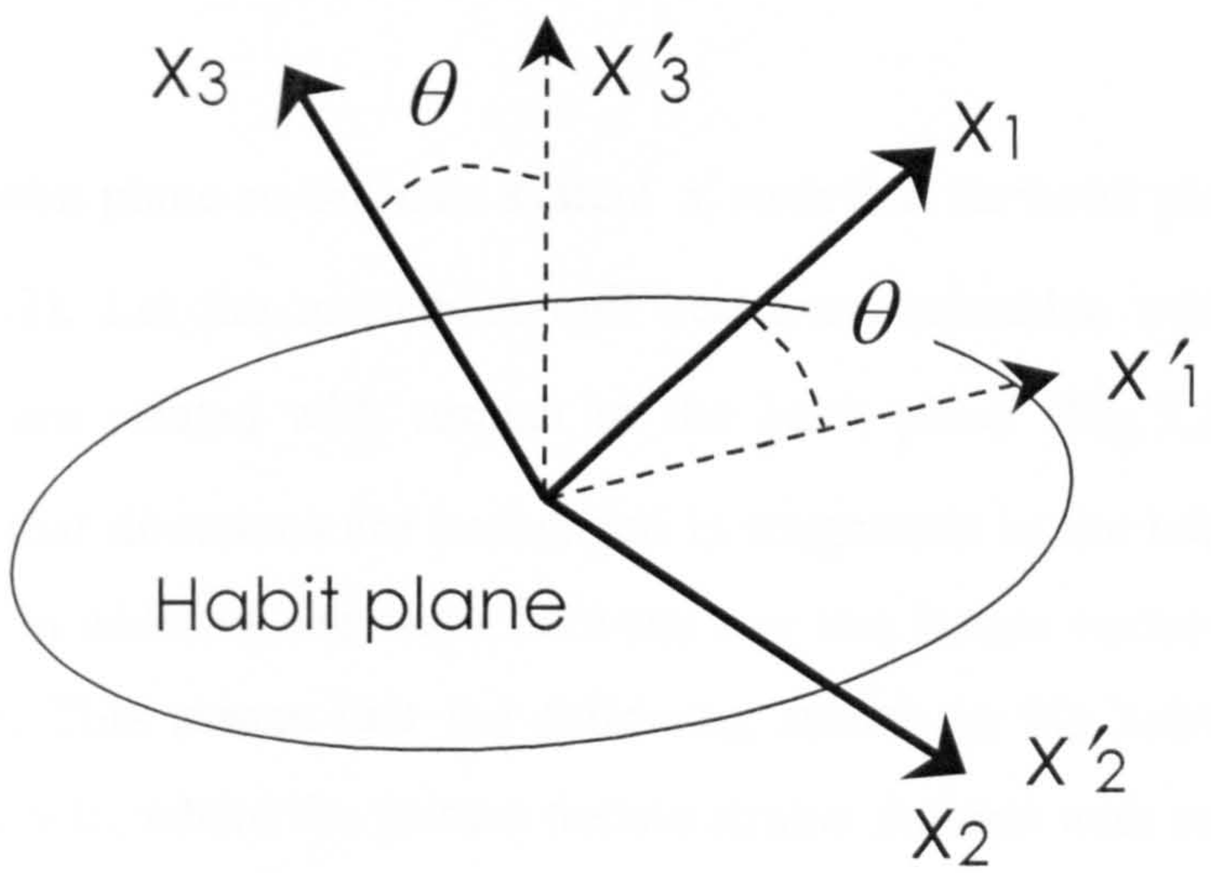

Fig. 5.2. Rotated co-ordinate system.

austenite. To form the martensite unit cell the c dimension must contract by about 20 % and the b dimension must expand by about 12 %. This corresponds to a strain $\varepsilon_1 = 0.12$ in two orthogonal directions and strain $\varepsilon_2 = -0.2$ in the third direction. In matrix form the strain can be written

$$e_{ij} = \begin{bmatrix} \varepsilon_1 & 0 & 0 \\ 0 & \varepsilon_2 & 0 \\ 0 & 0 & \varepsilon_1 \end{bmatrix} \tag{5.1}$$

5.2 Martensite Plate

The martensite transformation is observed to occur initially in regions in the form of plates within the austenite matrix. The crystal plane on which the martensite forms is called the habit plane (e.g. $\{225\}_f$ in steels with less than 1.4 % C). The Wechsler, Lieberman and Read (1953) model explains the relation between the Bain strain and the habit plane.

Designate the habit plane co-ordinate system x_i' such that the habit plane lies in the x_1'-x_2' plane (Fig.5.2). Let the martensite unit cell axes coincides with the co-ordinate axes x_i, which are rotated with respect to the habit plane (Fig.5.2). It is observed experimentally that directions are unchanged in magnitude in the habit plane after the transformation. In addition, the angle between any two lattice vectors is unchanged in the habit plane. This means that the following strains in the habit plane are zero: $e_{1'1'} = e_{2'2'} = e_{1'2'} = 0$, where the primes denote strains defined with respect to the x_i' co-ordinate system. The Wechsler, Lieberman and Read model explains this observation (Wayman, 1964). However, we also wish to consider the stress associated with the transformation. When a martensite plate is created within the austenite the Bain strain is constrained by the surrounding austenite. If there were no constraint the Bain strain would occur without producing any stress. Such strains are called eigenstrains. They have also been termed "transformation" strains or "stress-free" strains.

To understand the Bain strain in the martensite plate, we note that the martensite plates are internally twined. That is, alternating regions (region 1 and region 2) exist in the martensite plate, where the material in region 2 is the crystallographic twin of the material in region 1 (Fig.5.3). Mura (1998) calculated the stress in the martensite plate. Imagine that the plate is an ellipsoid and let the volume ratio be f in region 1 and $(1-f)$ in region 2.

The eigenstrain in the two regions with respect to the local crystal axes x_i are given by

$$e^{p}{}_{ij} = \begin{bmatrix} \varepsilon_1 & 0 & 0 \\ 0 & \varepsilon_2 & 0 \\ 0 & 0 & \varepsilon_1 \end{bmatrix} \qquad \text{(region 1)}$$

$$= \begin{bmatrix} \varepsilon_2 & 0 & 0 \\ 0 & \varepsilon_1 & 0 \\ 0 & 0 & \varepsilon_1 \end{bmatrix} \qquad \text{(region 2)} \qquad (5.2)$$

The strain is now averaged according to the formulae

$$\begin{aligned} \bar{e}^{p}_{11} &= f\varepsilon_1 + (1-f)\varepsilon_2 \\ \bar{e}^{p}_{22} &= f\varepsilon_2 + (1-f)\varepsilon_1 \\ \bar{e}^{p}_{33} &= f\varepsilon_1 + (1-f)\varepsilon_1 = \varepsilon_1 \end{aligned} \qquad (5.3)$$

The strains in the co-ordinate system of the martensite plate x_i' are obtained using the tensor rotation procedure

$$e^{p}{}_{i'j'} = a_{ki'}a_{lj'}e^{p}{}_{kl}$$

The value of f and the rotation are now selected to match the empirically observed strains in the habit plane.

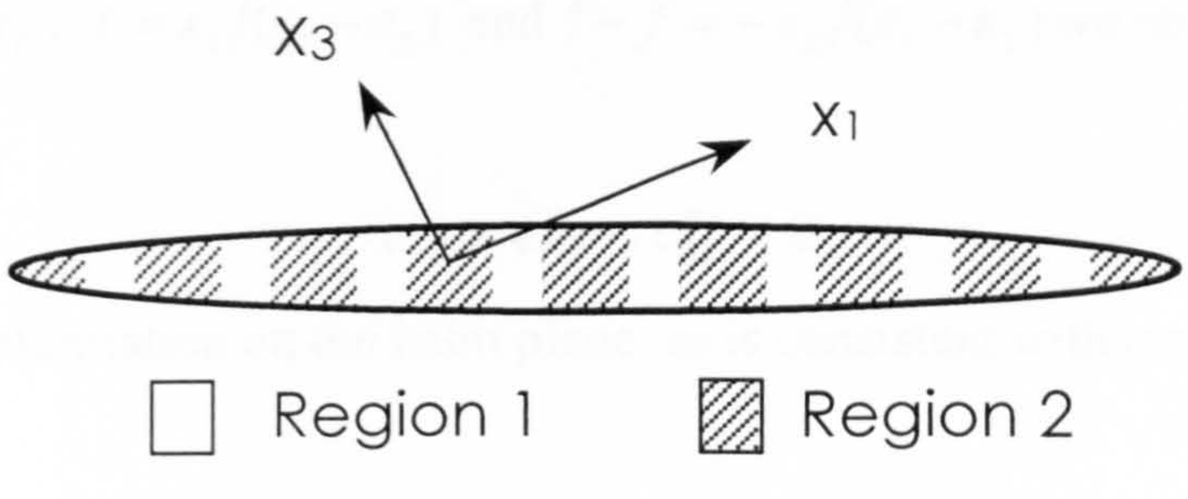

Fig. 5.3. Internally twinned martensite plate.

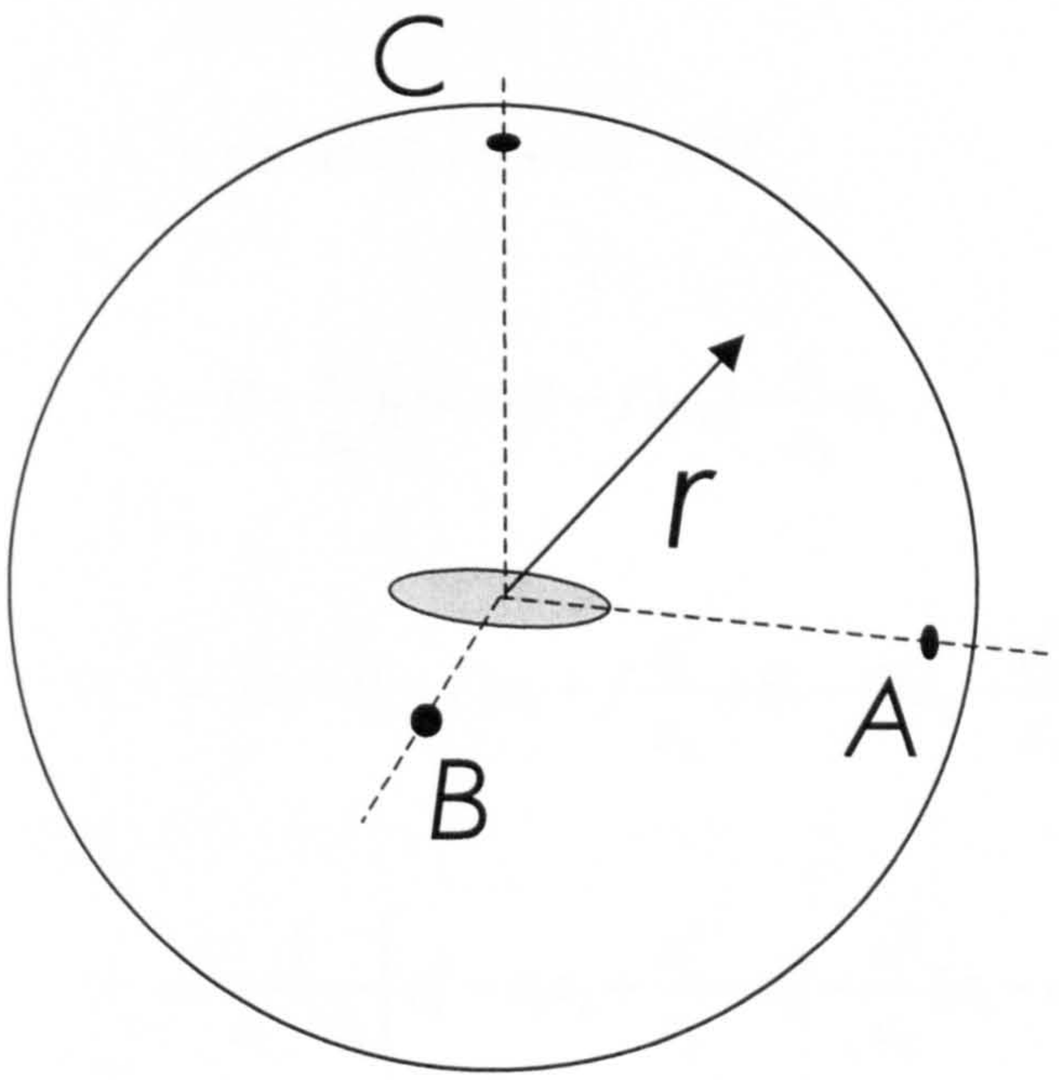

Fig. 5.4. Dilatation of a volume due to formation of a martensite plate within it.

Let the rotation occur about the x_2 axis (Fig.5.2). Then we have $a_{22'}=1$, $a_{i2}=a_{2i'}=0$, $a_{33'}=\cos\theta$, $a_{13'}=\sin\theta$, $a_{31'}=-\sin\theta$, $a_{11'}=\cos\theta$. If we take $\cos\theta=\sqrt{-\varepsilon_1/\varepsilon_2}$, $\sin\theta=\sqrt{1+\varepsilon_1/\varepsilon_2}$, $f=\varepsilon_1/(\varepsilon_1-\varepsilon_2)$ and $1-f=-\varepsilon_2/(\varepsilon_1-\varepsilon_2)$ we obtain the result

$$e^p_{1'1'}=e^p_{2'2'}=e^p_{1'2'}=0,$$

i.e. there is no deformation on the habit plane, as is consistent with experimental observation.

Now calculate $e^p_{3'3'}$, $e^p_{1'3'}$ and $e^p_{2'3'}$.

$$e^p_{2'3'}=a_{12'}a_{13'}\bar{e}^p_{11}+a_{22'}a_{23'}\bar{e}^p_{22}+a_{32'}a_{33'}\bar{e}^p_{33}=0$$

$$e^p_{3'3'}=a^2_{13'}\bar{e}^p_{11}+a^2_{23'}\bar{e}^p_{22}+a^2_{33'}\bar{e}^p_{33}$$

$$=\sin^2\theta.\bar{e}^p_{11}+0+\cos^2\theta.\bar{e}^p_{33}$$

$$=(1+\frac{\varepsilon_1}{\varepsilon_2})[f\varepsilon_1+(1-f)\varepsilon_2]-\frac{\varepsilon_1}{\varepsilon_2}\varepsilon_1$$

$$=f\varepsilon_1+(1-f)\varepsilon_1+f\frac{\varepsilon_1^2}{\varepsilon_2}+(1-f)\varepsilon_2-\frac{\varepsilon_1^2}{\varepsilon_2}$$

$$=\frac{1}{\varepsilon_1-\varepsilon_2}\left[\varepsilon_1^2-\varepsilon_1\varepsilon_2+\frac{\varepsilon_1^3}{\varepsilon_2}-\varepsilon_2^2-\frac{\varepsilon_1^2}{\varepsilon_2}(\varepsilon_1-\varepsilon_2)\right],$$

$$=\frac{1}{\varepsilon_1-\varepsilon_2}\left[\varepsilon_1^2-\varepsilon_1\varepsilon_2+\varepsilon_1^2-\varepsilon_2^2\right],$$

$$=\frac{1}{\varepsilon_1-\varepsilon_2}(2\varepsilon_1+\varepsilon_2)(\varepsilon_1-\varepsilon_2)\quad.$$

Thus

$$e^{p}_{3'3'} = 2\varepsilon_1 + \varepsilon_2 \tag{5.4}$$

$$e^{p}_{1'3'} = a_{11'}a_{13'}\bar{e}^{p}_{11} + a_{21'}a_{23'}\bar{e}^{p}_{22} + a_{31'}a_{33'}e^{p}_{33}$$

$$= \sqrt{\frac{-\varepsilon_1}{\varepsilon_2}}\sqrt{1+\frac{\varepsilon_1}{\varepsilon_2}}\,\bar{e}^{p}_{11} - \sqrt{\frac{-\varepsilon_1}{\varepsilon_2}}\sqrt{1+\frac{\varepsilon_1}{\varepsilon_2}}\,\bar{e}^{p}_{33}$$

$$= \sqrt{\frac{-\varepsilon_1}{\varepsilon_2}}\sqrt{1+\frac{\varepsilon_1}{\varepsilon_2}}\left[f\varepsilon_1 + (1-f)\varepsilon_2 - \varepsilon_1\right]$$

$$= \sqrt{\frac{-\varepsilon_1}{\varepsilon_2}}\sqrt{1+\frac{\varepsilon_1}{\varepsilon_2}}\left[\varepsilon_1 + \varepsilon_2 - \varepsilon_1\right]$$

$$= \frac{\sqrt{-\varepsilon_1(\varepsilon_2+\varepsilon_1)}}{\varepsilon_2}\varepsilon_2$$

Thus

$$e^{p}_{1'3'} = \sqrt{-\varepsilon_1(\varepsilon_2+\varepsilon_1)} \tag{5.5}$$

To sum up

(i) Internally twinned martensite gives a habit plane with invariant lattice vector provided that $\cos\theta = \sqrt{\frac{-\varepsilon_1}{\varepsilon_2}}$, $\sin\theta = \sqrt{1+\frac{\varepsilon_1}{\varepsilon_2}}$ and $f = \frac{\varepsilon_1}{\varepsilon_1 - \varepsilon_2}$.

This corresponds with experimental observation.

(ii) On average, the eigenstrain within the martensite plate consists of a shear $e^{p}_{1'3'} = \sqrt{\frac{-\varepsilon_1}{\varepsilon_2}}\sqrt{1+\frac{\varepsilon_1}{\varepsilon_2}}\varepsilon_2$ superimposed on a tensile extension $e^{p}_{3'3'} = 2\varepsilon_1 + \varepsilon_2$

In matrix form the strains are

$$e^{p}_{i'j'} = \begin{bmatrix} 0 & 0 & e^{p}_{1'3'} \\ 0 & 0 & 0 \\ e^{p}_{1'3'} & 0 & e^{p}_{3'3'} \end{bmatrix}$$

The dilation of the material within the transformed ellipsoid is $= e^{p}_{1'1'} + e^{p}_{2'2'} + e^{p}_{3'3'} = e^{p}_{3'3'} = 2\varepsilon_1 + \varepsilon_2 \cong 2\times 0.12 - 0.2 = 0.04$. This is superimposed on a shear strain $e^{p}_{1'3'} = \sqrt{\frac{0.12}{0.2}}\sqrt{1-\frac{0.1}{0.2}} \times 0.2 \cong 0.1$ These two components constitute the eigenstrain which, if it occurred in an unconstrained plate, would produce no stress. However, the full development of the eigenstrain strain is restricted by the matrix, which produces counteracting stress and reduces the strain produced in the martensite plate.

5.3 Stress in an Inclusion

The stress produced by the eigenstrain can be calculated by the method of Eshelby (1957) (see also the more detailed treatment by Mura (1998)).

Consider an isolated martensite plate. If there were no matrix the eigenstrain would consist of an extension (on average) in the x_3' direction combined with a shear. In an unconstrained plate this strain would produce no stress. However the matrix will resist deformation, giving rise to a compressive stress in the ellipsoid and a counteracting shear stress. To calculate these stresses assume that the ellipsoid is penny-shaped i.e. $a = b >> c$. The stresses then can be obtained using Eshelby's method (see Mura for details). Take the eigenstrain to be

$$e^{*}_{11} = e^{p}_{1'1'} = 0 \quad e^{*}_{22} = e^{p}_{2'2'} = 0 \quad e^{*}_{12} = e^{p}_{1'2'} = 0 \quad e^{*}_{23} = e^{p}_{2'3'} = 0$$

$$e^{*}_{33} = 2\varepsilon_1 + \varepsilon_2 \quad e^{*}_{13} = \sqrt{-\varepsilon_1(\varepsilon_2 + \varepsilon_1)}$$

From (Mura, 1998. p 81) we have

$$\sigma_{11} = \sigma_{22} = 2\mu\left[-\frac{2\nu+1}{8(1-\nu)}\pi\frac{c}{a}e_{33}^{*}\right]$$
$$\sigma_{33} = 2\mu\left[-\frac{1}{4(1-\nu)}\pi\frac{c}{a}e_{33}^{*}\right] \qquad (5.6)$$
$$\sigma_{13} = 2\mu\left[-\frac{2-\nu}{4(1-\nu)}\pi\frac{c}{a}e_{13}^{*}\right]$$

All other components are zero. Here μ is the shear modulus and ν is Poisson's ratio.

Note that as $c \to 0$ all stresses go to zero.

As an example, take 2μ=154 GPa, ν= 0.3, e_{33}^{*}= 0.04, e_{13}^{*} = 0.1 and $c/a = 10^{-2}$, we have the values $\sigma_{11} = \sigma_{22} \cong -55$, $\sigma_{33} \cong -70$ and $\sigma_{13} \cong -172$ MPa.

Thus, for thin martensite plates in steel the residual stresses associated with transformation of an isolated plate in an un-transformed matrix are modest compared with the yield strength of the martensite (> 2000 MPa). As shown by (5.6), the internal stresses are limited by the small *c/a* ratio. However, these are not the residual stresses we expect to develop in a case-carburized component.

5.4 Dilatation and Residual Stress in Case-Carburized Steels

We assume that martensite transformation occurs at low temperatures in the retained austenite in the case of case-carburised steel. The core is assumed to be an infinite half-plane. If the case were not connected to the core the martensite transformation would produce an expansion or dilatation of the material but no stress would result. However the connection of the case to the core prevents expansion in the $x_1 - x_2$ plane so that residual compressive stress must develop in the case as a result. The first step is to calculate the dilatation that results from the martensite transformation.

Consider a single martensite plate with eigenstrain e_{33}^{*} and e_{13}^{*}, all other strains being zero. The method of Eshelby (1961) can be used to calculate the displacement in the material. To apply this method we use an approximation. That is, we ignore the effect of the shear eigenstrain e_{13}^{*}. The physical basis for this approximation is that the shear

strains produced by martensitic transformations are self-cancelling in that the shear strains produced by the different martensite variants sum to zero. If the shear strains were not self-cancelling on the large scale, the transformation would result in an overall shape change. As is well known, no macroscopic shape change accompanies an austenite to martensite transformation, although dilatation occurs in steels.

The displacement field u_i at a point remote from the martensite plate is given by Eshelby (1961).

$$u_i = V\frac{e^*_{jk}g_{ijk}}{8\pi(1-\nu)r^2}, \tag{5.7}$$

where

$$g_{ijk} = (1-2\nu)[\delta_{ij}l_k + \delta_{ik}l_j - \delta_{jk}l_i] + 3l_il_jl_k\,. \tag{5.8}$$

Here δ_{ij} is the Kronecker delta, l_i denotes a unit vector joining the origin to the point of observation, r is the magnitude of the radial vector joining the origin to the point and V is the volume of the martensite plate. The summation convention is implied. We imagine a sphere centred on the origin and consider a limited number of points on the surface of the sphere. Using the eigenstrain obtained above, we have

$$e^*_{jk}g_{ijk} = e^*_{33}g_{i33} + e^*_{13}g_{i13} \tag{5.9}$$

Now consider the points A, B and C at the intersection of the co-ordinate axes with the surface of the sphere (Fig. 5.4)

At point A $l_1 = 1$, $l_2 = l_3 = 0$; $g_{i33} = (1-2\nu)[\delta_{i3}l_3 + \delta_{i3}l_3 - \delta_{33}l_i] + 3l_il_3l_3 = -(1-2\nu)l_i$; $g_{i13} = (1-2\nu)[\delta_{i1}l_3 + \delta_{i3}l_1 - \delta_{13}l_i] + 3l_il_1l_3 = -(1-2\nu)\delta_{i3}$. With u in units of $8\pi(1-\nu)r^2/V$, we have $u_1 = -e^*_{33}(1-2\nu)$, $u_2 = 0$ and $u_3 = e^*_{13}(1-2\nu)$

At point B, $l_1 = l_3 = 0$, $l_2 = 1$; $g_{i33} = (1-2\nu)[0+0-l_i]+0 = (1-2\nu)l_i$;

$g_{i13} = (1-2\nu)[0+0-0]+3l_i l_1 l_3$. Thus, with u in units of $8\pi(1-\nu)r^2/V$, we have

$u_1 = u_3 = 0$, $u_2 = -(1-2\nu)e^*_{33}$.

At point C, $l_1 = l_2 = 0$, $l_3 = 1$, $g_{i33} = (1-2\nu)[\delta_{i3}+\delta_{i3}-l_i]+3l_i$,

$g_{i13} = (1-2\nu)\,[\,\delta_{i1}+0+0\,]+0$. Thus in units of $8\pi(1-\nu)r^2/V$, $u_1 = e^*_{13}\,(1-2\nu)$, $u_2 = 0$,

$u_3 = e^*_{33}[2(2-\nu)]$.

In summary, the radial displacements are:

$$u_3 = \quad V\frac{2(2-\nu)}{8\pi(1-\nu)r^2}e^*_{33} \quad \text{(point C)}$$

$$u_1 = u_2 = -V\frac{(1-2\nu)}{8\pi(1-\nu)r^2}e^*_{33} \quad \text{(points A and B)} \qquad (5.10)$$

Thus, the sphere expands in the x_3 direction and contracts in the other two. The fractional changes in the radius vector at the three points are

$$\frac{u_3}{r} = \quad V\frac{2(2-\nu)}{8\pi(1-\nu)r^3}e^*_{33} \quad \text{(point C)}$$

$$\frac{u_1}{r} = \frac{u_2}{r} = -V\frac{(1-2\nu)}{8\pi(1-\nu)r^3}e^*_{33} \quad \text{(points A and B)}$$

The dilatation of the inscribed sphere is the sum of these. If V_1 is the volume of the sphere, then

$$\frac{\Delta V_1}{V_1} = \frac{V}{8\pi(1-\nu)r^3}[4-2\nu-1+2\nu-1+2\nu]$$

$$\frac{\Delta V_1}{V} = \frac{V}{8\pi r^3}\frac{2(1+\nu)}{(1-\nu)}e^*_{33}$$

But $V_1 = 4/3\pi r^3$, thus

$$\frac{\Delta V_1}{V_1} = \frac{V}{V_1}\frac{1}{3}\frac{(1+\nu)}{(1-\nu)}e^*_{33} \tag{5.11}$$

However, $V/V_1 = f_M$ is the transformed volume fraction. Therefore

$$\frac{\Delta V_1}{V_1} = f_M \frac{1}{3}\frac{(1+\nu)}{(1-\nu)}e^*_{33} \tag{5.12}$$

The same result would obtain by averaging the effect of all martensite variants within the inscribed sphere i.e. martensite plates of various orientations would produce the same dilatation. If these are averaged, the strain in each of the x_1, x_2 and x_3 directions is 1/3 $\Delta V_1 / V_1$, i.e.

$$e = f_M \frac{1}{9}\frac{(1+\nu)}{(1-\nu)}e^*_{33} \tag{5.13}$$

5.5 Residual Stress in the Case

The strain $e = e_x = e_y = e_z$ in (5.13) is itself a macroscopic eigenstrain. If it occurred homogeneously in an unconstrained layer it would produce no macroscopic stress. However, the material in the case is constrained by the core, which, we assume, undergoes no phase transformation. The effect of constraint on the stresses developed in analogous to the effect of thermal expansion (Timoshenko and Goodier, 1987).

Consider an infinite plate, thickness $2a$, with regions that transform near the two surfaces to a depth h. The resulting stress in the transformed layers is

$$\sigma_x = \sigma_y = -e^* \frac{E}{(1-\nu)} + \frac{1}{2a}\frac{E}{(1-\nu)}\int_{-a}^{a} e^* dz \tag{5.14}$$

If we take $e^* = 0$ when $-(a-h) \le z \le (a-h)$ and $e^* = f_M \frac{1}{9}\frac{(1+\nu)}{(1-\nu)} e^*_{33}$

we obtain

$$\sigma_x = \sigma_y = -e^* \frac{E}{(1-\nu)} + \frac{E}{(1-\nu)} e^* \frac{h}{a} \qquad (5.15)$$

Let $h/a \to 0$. The residual stress in the case is then

$$\sigma_x = \sigma_y = -f_M \frac{E}{9}\frac{(1+\nu)}{(1-\nu)^2} e^*_{33} \qquad (5.16)$$

As an example, let $E = 200$ GPa, $e^*_{33} = 0.04$, $\nu = 0.3$ and $f_M =$ 0.3, then the macroscopic residual stress in the transformed layers is $\sigma_R =$ –700 MPa. This represents a potentially large contribution to the residual stress. For instance, shot peening is routinely observed to produce maximum residual stresses between –800 and –1300 MPa in case carburised steels. At the same time, the shot peening treatment is found to reduce the retained austenite content to low levels in the surface layers, presumably as result of strain induced transformation. Does the strain-induced transformation contribute to the observed residual stress? The above theoretical estimate (eqn. 5.16) indicates that that it may be more important than the contribution from the inhomogeneous plastic strains produced by the indentation of the shot. This idea can be disputed, and the matter is discussed further below, in the light of experimental observations.

5.6 Volume Change due to Austenite to Martensite Transformation in Steel

The observed effects of the transformation of retained austenite on residual stress appears to be less than it should be if the volume expansion was 4 % as is normally assumed. For this reason, some experiments were undertaken to measure the increase in volume induced by the austenite to martensite transformation at low temperatures by sub-zero cooling.

Procedure

Ovako 677 steel bars with paralleled edges were hardened by austenitization and air cooling. Figure 6.1 shows dimensions of specimens used in these experiments. The microstructure consisted of martensite and retained austenite. The deep freeze treatment, by immersion in liquid nitrogen, should transform most of the retained austenite to martensite. This transformation is accompanied by an increase in volume. Therefore, volumetric change can be related to amount of transformed austenite by accurate measurements of retained austenite and specimens volumes before and after deep freezing treatment. The percentage increase in specimens volume were estimated as follow.

- Measurement of the initial amount of retained austenite by X-ray technique
- Accurate measurement of specimens dimensions with dialometrery equipment
- Deep freezing in liquid nitrogen to transform retained austenite to martensite
- Re-measure the retained austenite
- Re-measure the specimen dimensions
- Calculate the percentage of transformed austenite and the volume change
- Calculate the volume change for 100% austenite transformation

Results

Three specimens were used to measure volume change. The first one was 10 mm in thickness with edge length of 20 mm. The dimensions of the other two specimens were 12 mm in thickness and 24 mm in the edge. Figure 5.5 shows schematic drawing for these specimens. Accurate measurements of dimensions with dialometrery equipment were made by measuring the distance between two points on opposite sides. The measurements were taken at different locations. Four points for the thickness and two points for each of the other two dimensions. The measurements were repeated after deep freezing on the same positions. Then the average in each dimension was calculated. The results for the three specimens are given below.

The retained austenite was measured by X-ray diffraction. The percentage of retained austenite phase in specimens before and after deep freezing is shown in Table 5.1

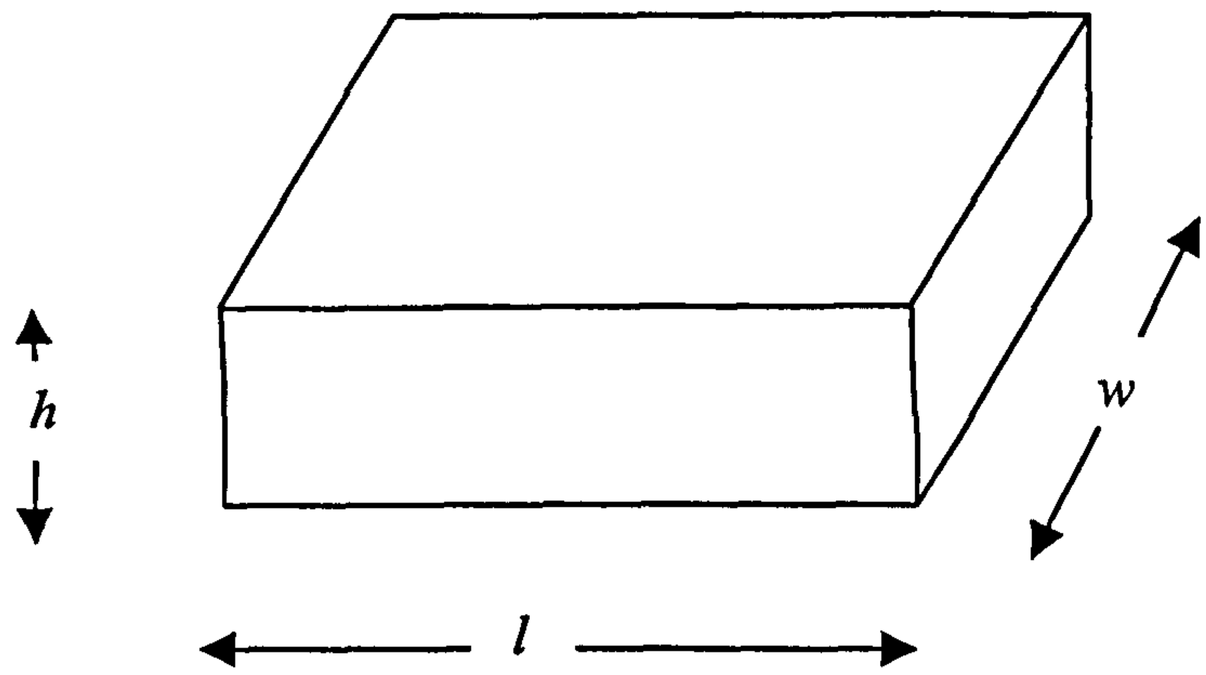

Fig.5.5 shows schematic shape of specimens used to measure the volume change

Table 5.1 percentage of transformed austenite by deep freeze treatment and the corresponding measured increase in volume

Specimen	Initial % retained austenite	% retained austenite after sub-zero cooling	Percentage of austenite transformed	Percentage* increase in volume
1	20.0	13.0	7	4
2	18.5	9.2	9.3	2.28
3	24.4	5.6	18.8	1.84

* Measurements and calculations of percentage of volume change are indicated in Appendix A

The different proportions of retained austenite transformed in the different specimens can be attributed to different degrees of stabilisation. It is known that retained austenite tends to stabilise if it is held at room temperature or above for some time before being sub-zero cooled. Thus specimen 1 was held for 10 weeks before sub-zero cooling, whereas specimen 3 was sub-zero cooled within 100 hours after quenching.

It appears that there is a trend for the volume increase to reduce as the % transformation increases. This may be associated with different carbon contents in the transformed austenite. The volume increase for the austenite to martensite transformation is well documented in literature. The Bain model proposed a 4 % increase in volume. However Bain and Paxton (1966) showed that the percentage of increase in volume decreases with increase in carbon content. The percentage increase in volume decreased to about 3 % when the carbon content was about 1.2 %. However, these volume changes refer to the normal austenite-to-martensite transformation on quenching from the stable austenite field. The results in Table 5.1 are for sub-zero cooling where the austenite is metastable. The question of the carbon content of the austenite arises in this case. It is possible that the carbon content of the retained austenite is larger than the overall carbon content. This could be attributed to carbon enrichment in retained austenite phase. Sarikaya *et al.* (1992) found that carbon partitioning occurs during austenite to martensite transformation in alloy steels with nominal carbon content of 0.1 and 0.3 %

wt. Higher concentration was found at the α′ / γ interface but the general carbon content in the austenite phase was as high as twice the nominal content in the investigated steels. No partitioning was observed for substitutional elements such as Cr, Ni, Mn and Si. However the decrease in percentage of volume change is related to increase in carbon and not to alloying elements. Therefore the increase in carbon content could be the reason for the lower levels of percentage of volume increase measured in the current work compared with quoted values.

5.7 Residual Stresses Produced by Sub-zero Austenite Transformation

In another experiment, an attempted was made to observe the effect of shot peening in specimens with 18.5 % retained austenite as compared with a low level of retained austenite. The low level of retained austenite was achieved by subzero cooling in liquid nitrogen before shot peening. In itself, this sub-zero cooling does not affect residual stress, because the transformation occurs throughout the whole specimen.

After shot peening, the retained austenite in the surface layers is transformed to martensite and this should contribute to the residual compressive stress developed because of the increase in volume that occurs. Residual stress profiles in the two specimens are shown in Fig.5.6. Higher compressive residual stresses were developed in the specimen with higher retained austenite content. The increment was more pronounced near surface layer where transformation of retained austenite took place due to the peening process as shown in Fig.5.6.

The specimen that was deep frozen before shot peening should show a residual stress profile that derives only from the plastic strain introduced by peening. The specimen with 18.5 % retained austenite should show a residual stress that results from the combination of plastic strain plus the volume expansion of the transformed retained austenite. Figure 5.7 shows that all of the retained austenite was transformed by shot peening. Therefore the difference in residual stresses at the surface of the two specimens should be related to the residual stress contributed by the transformation in the retained austenite. From Fig. 5.6, the residual stress difference of 350 MPa. Hence using eqn 5.16 this implies a volume expansion of 3.2 % which is within the range of results shown in Table 5.1.

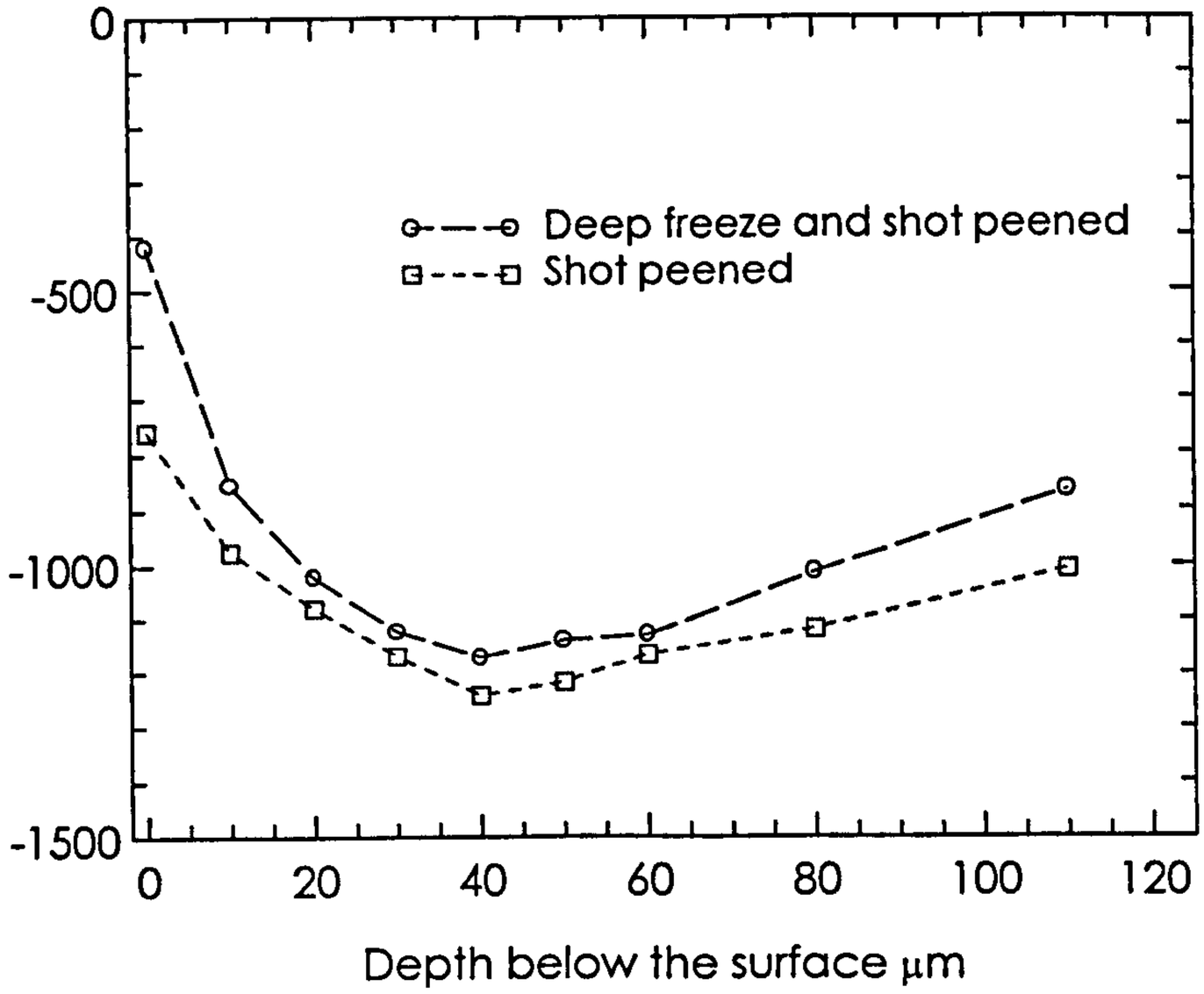

Fig. 5.6 Residual stress profiles after shot peening in two specimens with different retained austenite content

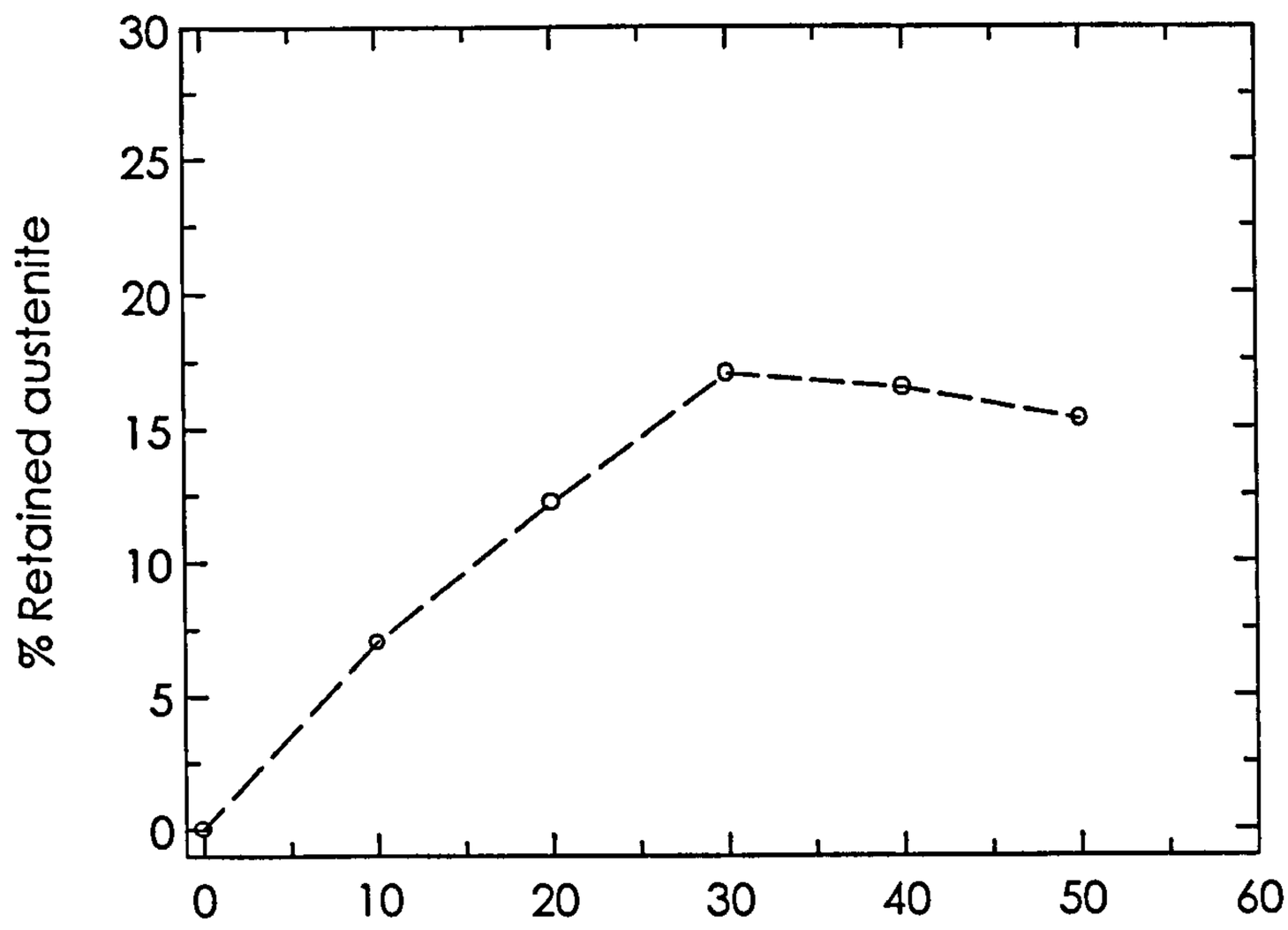

Fig 5.7 Retained austenite profile after shot peening. Initial retained austenite content before shot peening is 18.5%

CHAPTER 6

Discussion

6.1 Effect of Retained Austenite on Fatigue Strength

High duty gears with abnormally high levels of retained austenite were tested for fatigue failure (Chapter 2). Two types of tests were conducted to assess the fatigue performance of these gears. Root bending fatigue was tested by pulsator testing and surface contact fatigue in back-to-back tests. The pulsator test was carried out on spur gears while back-to-back test was done using helical gears. Results of these tests in the form of S-N curves were compared with results obtained from similar gears made with the same steel but with normal content of retained austenite (Chapter 3). Despite the fact that the steel with high retained austenite is softer than the normal steel, the fatigue strength does not seem to be adversely affected by the increased austenite.

6.1.1 Effect of Carbon Content on Austenite Retention

It is not known for certain why one particular batch of 17CrNiMo6 gears had such a high level of retained austenite. The carburization treatment was done commercially by a well-known company, specialising in heat treatment. The experience demonstrates how critical good process control is in producing consistent results in heat treatment. We now speculate on the factors that could explain the high retained austenite level after heat treatment.

The amount of retained austenite is strongly dependent on the carbon content of the steel. Other alloying elements which affect the M_s temperature also have an effect on the retained austenite level. Jatczak (1979) estimated the percentage of retained austenite, taking in consideration the effect of quench temperature, The retained austenite content is given by the expression

$$\%\mathrm{RA} = 100\exp(-0.011[M_s - T_q])$$

where T_q is the temperature of the quenchant in degrees Celsius

and $M_s(^\circ C) = 539 - 423(\%C) - 30.4(\%Mn) - 12.1(\%Cr) - 17.7(\%Ni) - 7.5(\%Mo)$

Using this equation it can be shown that even in alloys containing 0.4 % carbon, some austenite is retained. When the carbon content is as high as 1% the retained austenite levels in 10xx plain carbon steel and 43xx alloy steel are 20% and 40 % respectively after carburization and quenching to room temperature (Wilson and Weins, 2000). Marder and Krauss (1967) measured the retained austenite content in a series of Fe-C alloys. Retained austenite increased exponentially with carbon content to reach about 40 % at a carbon content of 1.4% after quenching to room temperature. They also showed that as the carbon content increased above 1.0% the martensite structure completely consisted of martensite plates, rather that the mixed lath and plate structure found with lower carbon contents.

In the gears used in the present work, the carbon content in the case material exceeds 1%. Therefore a retained austenite level of 40 to 60 % is not unexpected in the presence of alloying elements such as Ni, Cr, Mn and Mo which also lower the M_s temperature. The morphology of martensite is the type expected in high carbon steel (plate martensite) as shown in Fig.3.9.

As indicated above, the retained austenite content was higher than the levels specified in the standard heat treatment. This can be attributed to the high carbon level in the carburised case. Figure 3.3 shows the carbon content profile through the carburised case obtained with LECO Glow Discharge Spectroscopy chemical analyser where it can be seen that the maximum carbon content is about 1.5 wt. % which is much higher than the specified level. Clearly, the carburization treatment was incorrectly performed due, possibly to poor temperature or gas composition control. Whatever the reason, the incorrect heat treatment gears provided the opportunity of investigating the fatigue properties of steel with high retained austenite. It should be noted that high levels of retained austenite are avoided at all costs in the gearing industry. In contrast, high retained austenite is often used in the bearing industry (we have been assured of this by research collaborators in a large bearing manufacturing company).

Retained austenite is a metastable phase. It is softer and more ductile than martensite phase and has higher fracture toughness. From the point of view of fatigue performance any microstructural changes producing a decrease in strength is thought to be likely to cause the fatigue strength to deteriorate. Therefore the presence of retained austenite in substantial amounts might be considered to impair to the fatigue performance if no other changes occurred during fatigue. However transformation of retained austenite to martensite can take place. Parameters, which stimulate transformation, include tensile stress, plastic strain and temperature. The transformation reaction also results in change of residual stress distribution induced by increase in volume accompanied by the reaction. Thus, if transformation of retained austenite occurs as a result of fatigue loading, the presence of retained austenite initially in the steel may not result in lower fatigue strength.

6.1.2 Results of Fatigue Tests

Comparison of fatigue strength for steels with high and normal retained austenite content for surface contact fatigue and root bending fatigue tests are shown in figures 3.2 and 3.3 respectively. The S-N curves show some enhancement in fatigue strength in the low cycle range regime in both tests ($N \approx 10^4$). However in the high cycle, low strain fatigue regime, results for surface contact fatigue test showed that the endurance limits for both steels were approximately the same and fatigue properties were not much affected. For the root bending fatigue test, the fatigue properties of the steel with high retained austenite showed slight deterioration toward the high cycle fatigue regime. Experiments results showed more scatter in the high cycle fatigue for root bending fatigue test.

These results would be surprising if the retained austenite were simply a softer second phase. Because of its lower yield strength one might expect that yielding would occur at lower applied stress in fatigue and therefore that the fatigue strength would be reduced. However, retained austenite is capable of stress induced and strain induced transformation to martensite and clearly this changes the way the material reacts to cyclic loading. We now examine the evidence from other work in the literature for the

effect of retained austenite. In many cases the effects ascribed to the presence of retained austenite in the published literature are contradictory.

6.1.2.a Bending Fatigue and Fatigue Crack Growth

Studies on the effect of retained austenite on fatigue performance were carried out by a number of investigators on case carburized specimens and specimens with simulated case carburized chemical composition. The effect of retained austenite was studied in bending fatigue, cyclic stress-strain, and contact fatigue as well as on fatigue crack growth rate. Zaccone *et al.* (1989) performed cyclic stress-strain and low cycle bending fatigue tests on high carbon steel simulating microstructure in case carburized steels. The low cycle bending fatigue was conducted in four–point bending test on notched specimens at stresses of 862 MPa and 1655 MPa. Five series of 0.8C-Cr-Ni-Mo steel specimens were heat treated in two different thermal cycles to obtain a variety of austenite-martensite microstructure. Direct quench heat treatment and reheated and quench heat treatment were applied to simulate the range of tempered microstructure formed in the case carburized steels. The composition of the steels was constant except for Cr which increased from 0.0% to 1.3%. Increasing Cr content affects the retained austenite content by lowering of M_s temperature and increases the carbide content, which affects structure refining in reheated specimens. Thus the retained austenite content varied from 20% up to 39% in the various specimens. Before carrying the fatigue tests, tensile and compression tests in the macrostrain and microstrain ranges were carried out for direct quench and reheated specimens. The purpose of these tests was to assess the effect of retained austenite and structure refining on the stress-strain behaviour. The amount of transformed austenite is higher in microstructures with higher initial austenite content. There is a critical strain to induce strain-induced transformation. In the direct quench specimens this critical strain is independent of retained austenite level. Measurement of the volume fraction of transformed austenite as a function of strain showed that an incubation strain is require for transformation unless retained austenite is present in fine grains at high proportions. Retained austenite decreases the elastic limit but refining the austenite increases the elastic limit. At higher strains, transformation of retained austenite was found to increase the strain hardening. High strain hardening rates are maintained until retained austenite stabilises at about 9

to 12 %. The fatigue performance is affected by the presence of retained austenite. Increasing the austenite content increases the stain hardening and the cyclic hardening. In high cycle fatigue where applied stresses are high, cracks are initiated in the early cycles. The induced compressive stresses resulting from the transformation reaction reduces the propagation rates of the transgranular cracks which initiate at embrittled grain boundaries. In high cycle fatigue when fatigue life is controlled by crack initiation, High elastic limit and yield strengths are more favourable to improved fatigue life. Therefore higher proportions of retained austenite decreased the fatigue life unless the retained austenite was finely distributed. The level of applied strains in the high cycle fatigue is below the critical strain to induce austenite transformation. Therefore retained austenite in high cycle fatigue is incapable of retarding crack propagation. In the work carried out by Zaccone *et al.* (1989) the experiments were performed on through hardened specimens. The residual stress distribution produced by heat treatment differs markedly in through hardened steels compared with case carburized steels. Tensile residual stresses are expected to set up in through hardened steels which affect the fatigue life performance. Therefore test specimens simulate the chemical composition of the case material but not the stress distribution. No measurements of residual stresses were made before or after conducting the test.

Da Silva (1999) studied the effect of retained austenite on fatigue crack growth rate in case carburized specimens during low cycle fatigue. Retained austenite contents in the range from less than 6 % up to 37% were produced through various heat treatment routes. da Silva conducted four point bend fatigue test at three different applied loads with stress ratio of 0.1. Results of S-N curves and fatigue crack growth showed that specimens with large amount of retained austenite resulted in a longer life and lower crack growth rate. He found that refining the microstructure increase the crack growth resistance. He attributed the improvement in fatigue life to the capacity of retained austenite to transform during local plastic deformation and the induced compressive stresses generated with transformation.

Szpunar and Bielanik (1984) studied the effect of retained austenite on propagation of fatigue cracks in the case of carburized steel specimens. Two different steel grades were heat treated in five various ways to obtain different hardness combinations in the case and the core and variable proportion of retained austenite. The case depth in all

specimens was about 1 mm thick. Fatigue tests were performed on notched specimens. Toothed wheels made from the same steels and subjected to similar heat treated were tested for fatigue life. All specimens and toothed wheels were tempered at 170 °C for 2 hours. The surfaces of specimens and toothed wheels which were not to be carburised were copper coated by electro-deposition. The non-carburized surfaces of the specimens were then ground and a slit was made in the notch to initiate fatigue cracks. The growth rate was determined by the crack length increment in the carburized case (Δa) to the number of cycles (ΔN). Results from the two steel grades tested at three levels of cyclic amplitudes were not consistent. At low levels of retained austenite the growth rate is higher at higher stress amplitudes in both specimens and the results were comparable in both of them. However the effect of retained austenite on the growth rate was different in either steel. In one steel grade the growth rate was not affected by retained austenite content at medium stress amplitude. At higher stress amplitude the growth rate increases with increasing retained austenite and at the lower stress the growth rate decreases with increasing retained austenite. In the other specimen the trend of retained austenite effect on growth rate in all stress amplitudes was similar. At all stress levels growth rate increases with increasing austenite content up to 23% beyond which the growth rate declines with increasing retained austenite content. The increase of resistance to crack growth rate with increase of austenite content was attributed to the transformation of austenite to martensite in front of the propagating cracks. Thus a large proportion of the external applied work is consumed in transformation and not in crack propagation.

An energy approach for the effect of retained austenite was used by Hu *et al.* (1997). Retained austenite increases fatigue resistance through consumption of supplied energy in the transformation reaction. However when excess energy is available the fatigue resistance is decreased. This is due to the easy formation of microcracks in the brittle transformed martensite. They carried out in situ observation of fatigue crack initiation and propagation using SEM. Three-phase steel (austenite, martensite and ferrite) was used to study the effect of retained austenite on low cycle fatigue. Observations were made for initiation and early propagation stage and propagation stage. Two stress cycles were applied designated as low strain with stress range of σ_{max} = +525 MPa and σ_{min} = -397.5 MPa and high strain with stress range of σ_{max} = +650 MPa and σ_{min} = -

450 MPa. Crack initiation was observed in specimens with retained austenite levels of 23%, 11.8% and 2.1%. In the low strain cycle, austenite was found to increase the resistance for crack initiation and early propagation. This was attributed to the ability of austenite to absorb the strain energy of the crack tip. In the propagation stage the effect of austenite was examined on two samples with austenite contents of 23% and 15.5%. The influence was assessed with the aid of plot of fatigue crack growth rate versus the number of cycles. In the high stress cycle, the high austenite sample shows higher crack growth rate. In the low stress cycle the two growth rate curves intersect at some crack length (a_c). Below the intersection point when crack length $a < a_c$ the higher percentage austenite steel has lower crack grow rate and when crack length $a > a_c$ the higher austenite steel has faster crack grow rate. These results were explained by an energy criterion which compares the energy absorbed in the strain induced austenite to martensite transformation and the energy required for crack propagation. Based on this criterion when transformation energy is lower than propagation energy the austenite will decrease the fatigue resistance. This is because transformation of austenite occurs first to produce twin martensite which is easily cracked. Therefore the higher the austenite content the lower the fatigue resistance. In the low stress cycle the supplied energy is consumed by the transformation reaction and the higher the austenite content the higher the fatigue resistance. However as the stress intensity increases with increasing crack length a point is reached at $a = a_c$ where the propagation energy become higher and a situation similar to high stress cycle sets up. Therefore at $a > a_c$ the higher the austenite the lower the fatigue resistance. Gu *et al.* (1989); Lou *et al.* (1990) performed fatigue crack growth tests in carburized steels and found a reduction in the crack growth rate in specimens with high content of retained austenite in the carburized case. They attributed the retardation of the growth crack to the compressive residual stress generated by the plastic strain austenite to martensite transformation.

We note that much of the work on fatigue of retained austenite focus on crack growth, however this may not be particularly related to the bending fatigue strength of gears where no crack growth can be tolerated, i.e. gears are required to operate for more than 10^{10} many cases. The rate of macroscopic crack growth in this case is not significant since most of the life is consumed in the crack nucleation stage. However, it is possible

that transformation of retained austenite at the tip of a microcrack may be important in suppressing fatigue, although there is very little evidence for this.

The findings in the literature show some contradictions about the beneficial effect of retained austenite on bending fatigue. Retained austenite decreases the strength and hardness and causes deterioration of fatigue life. The presence of retained austenite becomes advantageous only when transformation of retained austenite to martensite occurs. This beneficial effect was attributed to the compressive stresses induced with the transformation reaction. However, the effect of the produced un-tempered martensite on fatigue life was a point of debate among investigators. The root bending fatigue test in the current investigated gears showed improved fatigue life in low cycle fatigue. This is believed to be due to the strain-induced transformation of austenite to martensite. In the high cycle fatigue, the fatigue strength for gears with high retained austenite content was slightly inferior to gears with normal content of retained austenite. In fact, the level of stress used in high cycle bending fatigue is too low to produce plastic deformation on anything other than on a highly local (microscopic) scale. Thus the hardness difference between high and low retained austenite content may not be very significant as an indication of fatigue strength difference. For instance Fig.1.2 (Chapter 1) shows that, at the lower bound of the scatter band, tensile strength or hardness is not correlated with fatigue strength at tensile strength levels greater than 1200 MPa. Steels with both high and low levels of retained austenite have tensile strengths larger than 1200 MPa (Hv $\approx$ 450).

6.1.2.b Contact Fatigue

There is very little work on retained austenite in back-to-back gear tests in the literature. Thus, we rely on observations on bearing tests or disc tests for other observations on the effect of retained austenite. Investigations in the literature about the effect of retained austenite on contact fatigue reveal contradictory results as discussed below. Dong *et al.* (1985) carried out contact fatigue test on specimens with retained austenite in the range of 7 to 50 %. Hertzian stresses of 2800 and 3000 MPa and 20 % sliding were applied in a roller bearing test. They found that increasing retained austenite increased the contact fatigue resistance. The enhancement was attributed to

the strain-induced transformation and the accompanying compressive stresses. They noticed that crack initiation took place beneath the surface at the depth of maximum orthogonal shear stress and only later at the surface due to surface tensile stress. It should be noted that subsurface crack nucleation is rarely observed in back-to-back gear tests. The enhancement mechanism is due to delayed crack initiation and propagation. In the absence of such transformation actual measurements of residual stresses in carburized steel show a decrease in compressive stresses during cycling loading (Panhans and Fournelle, 1981). It should be noted that the stress levels quoted above are much higher than those used in back-to-back gear testing.

Vinokur (1981) carried out disc tests to study the effect of retained austenite on contact fatigue in low alloy steel. Two variants were used in the study, the first with uniform carbon through the entire volume and the second were case carburized with carbon content of 0.19% at the core. In each series four grades were produced with carbon content of 0.55, 0.7, 0.8 and 0.95%. Increasing the austentizing temperature from 725 to 850 ° C at steps of 25 ° C result in increased levels of retained austenite in both variants. Contact endurance tests were carried out at contact load of 350 kg/mm^2. Contact endurance was determined from the number of load cycles to start pitting. The contact fatigue strength was higher in case hardened specimens due, it is claimed, to the compressive residual stresses generated in the case layer. The general trend in both variants was as such, for hypoeutectoid steels (eutectoid point was shifted to just above 0.6%C) fatigue resistance increases with increasing quenching temperature and the concomitant retained austenite. For hypereutectoid steels the fatigue strength increases with increasing temperature within the intercritical range and then declines when the austentizing temperature exceeds the upper critical point. As the amount of retained austenite was temperature dependent, the fatigue strength showed initial increase with increase in retained austenite followed by small decline after passing a peak point. Therefore it was concluded that presence of retained austenite is not the direct reason for improving the contact fatigue, rather the improvement was attributed to the dissolution of the carbide and the enrichment of the austenite and martensite with alloying elements and the decrease in the amount and distribution of the detrimental carbides. However Vinokur (1981) did not measure the retained austenite content after tests. Therefore it is not indicated if any transformation took place or not. Thus the phenomenon of induced transformation can not be judged in this work. The detrimental

effect of retained austenite was examined by comparing identical steels with progressively lower levels of retained austenite obtained by cold treatment. Six specimens were treated in the temperature range of +20 to -196°C. The retained austenite level decreased with decreasing temperature but the amount and size of carbides unchanged. Endurance limit increased progressively with decreasing austenite and increasing martensite content.

Muro and Tsushima (1970) in roller bearing tests found that no residual stresses develop below a threshold Hertzian stress of 3500 MPa. In the current work the highest applied Hertzian stress in the low cycle fatigue was 1824 MPa in the back-to–back tests. This stress is much lower than the threshold stress proposed by Muro and Tsushima (1970) and the estimated stress for transformation of about 3400 MPa calculated in the attached Appendix. In bearing tests carried out by Voskamp *et al.* (1980) the applied surface Hertzian stress was in the range of 3280 and 3720 MPa. And in disc tests carried out by Dong *et al.* (1985) the applied Hertzian stress was in the range of 2800 to 3000 MPa. The required stress for transformation depends on the yield strength of the material. This could be the reason why Dong *et al.* (1985) detected subsurface transformation at this level of applied stress. Voskamp *et al.* (1980) did not detected surface changes. This could be due to the already high compressive stresses present at the surface produced by the grinding operations or the good finish of the surfaces which reduces localised stresses. However Dong *et al.* (1985) found that surface transformation and induced stresses occur in addition to subsurface transformations. Compressive residual stress of about 700 MPa was measured at the surface accompanied by surface transformation. Measurement of residual stress on contacted flanks in the present work showed that an increment in compressive residual stress of up to 600 MPa took place at the surface as shown in Fig. 4.8. These are comparable values as these values represent the highest stresses obtained in either study. However, austenite transformation is not the only source for induced surface stresses. Plastic deformation at the asperities of contact surfaces also induces residual stresses. The level of induced compressive residual stress due to transformation depends on the retained austenite carbon content before transformation (da Silva *et al.*, 1999). The carbon contents were similar as these stresses are induced in carburized layers in both studies.

Many authors reported that retained austenite is beneficial when its content is in the order of 30 % (Zaccone *et al.*, 1989; Richman and Landgraf, 1975). Rakhit (2000) reported that retained austenite in the range of 15 to 20 % increases the bending fatigue resistance of gear teeth but lowers the surface hardness which is not desirable for contact fatigue. He claimed deleterious effects on service life of gears with retained austenite in excess of 20 % are due to the dimensions changes and brittleness of un-tempered martensite produced by transformation of the retained austenite. Szpunar and Bielanik (1984) concluded from analysis of published work that the presence of retained austenite in the range of 30-50 % exerts beneficial effects on contact fatigue and bending fatigue. The retained austenite level in the current investigated steel is in the range of 40 to 60 %. This means that the upper boundary of the beneficial or non-harmful range should be extended to higher limits.

The observations reported in the literature on the effect of retained austenite on surface contact fatigue are somewhat contradictory and often confusing. We now summarise the following observations based on the tests done in the present work.

1. Although retained austenite may improve fatigue strength at low cycles, it has very little effect on fatigue strength at high cycles (10^8) (Figures.3.2 and 3.3). This in itself is surprising because retained austenite is softer than martensite. It follows that the transformation from retained austenite to martensite must have an influence in maintaining fatigue strength.
2. There is no austenite-to-martensite transformation below the contacting surfaces at the depth of maximum shear stresses (smooth surfaces). This is because the applied stresses are too low in this region to produce plastic deformation. (Chapter 3.Fig. 3.9-b).
3. There is good evidence that retained austenite to martensite transformation occurs at a shallow depth from surface (Chapter 3 Fig.3.9-b) on the scale of asperity deformation. We believe that this transformation prevents the high retained austenite gears having reduced fatigue strength. Asperity deformation always occurs in surface contact and if transformation is induced as a result, the resulting increase in hardness protects the surface from premature fatigue failure.
4. There is little evidence that the generation of residual stress from the austenite to martensite transformation is a special factor in elevating fatigue strength. There is

evidence that residual compressive stress increases during surface contact fatigue (Chapter 3 Fig.3.8), but this occurs anyway even if there is no transformation. The increase in residual compressive stress at the surface follows from plastic deformation of asperities as is regularly observed in specimens with low retained austenite contents (Shaw, 2002).

Finally we note the various claims in the literature for generation of compressive residual stress by inhomogeneous transformation of retained austenite (e.g. in the case or near the surface). Our experience is that the residual stress change produced by transformation of retained austenite is relatively small. This was discussed further in (Chapters 5).

6.2 Through-Hardened Air-Quenched Steel

We now review the advantages and disadvantages of developing a through-hardened air-hardening (Ovako 677) steel for applications such as gears.

Heavy duty gear steels are manufactured starting from a lower carbon composition (e.g. 0.2 %). Upon carburization the gears acquire high hardness at the surface while maintaining high toughness in the core to resist brittle and catastrophic fracture. However long carburization cycles and the amount of energy consumed render carburization expensive and time consuming. Additional costs add up when closer case depth tolerances and deeper cases are required (Rakhit, 2000). The necessity for using quenchant and its disposal adds to the process cost. Gear distortion and oxidation are common problems in case hardened gears. Other problems encountered in gear carburization are due to differences in carbon content along tooth flank. For example, convergence of carburizing gas flow at teeth tips can result in non-uniform case thickness along the tooth and inhomogeneity of microstructure such as production of intergranular carbides at the teeth tips. A schematic comparison of conventional carburization versus heat treatment of Ovako 677 is shown in Fig.6.1.

Through-hardening steels posses the potential to overcome some of the drawbacks listed above. The use of through-hardening steels is desirable because of its low cost heat treatment operations compared with carburization heat treatments. The production of inexpensive air-hardening steels and elimination of the use of quenching mediums

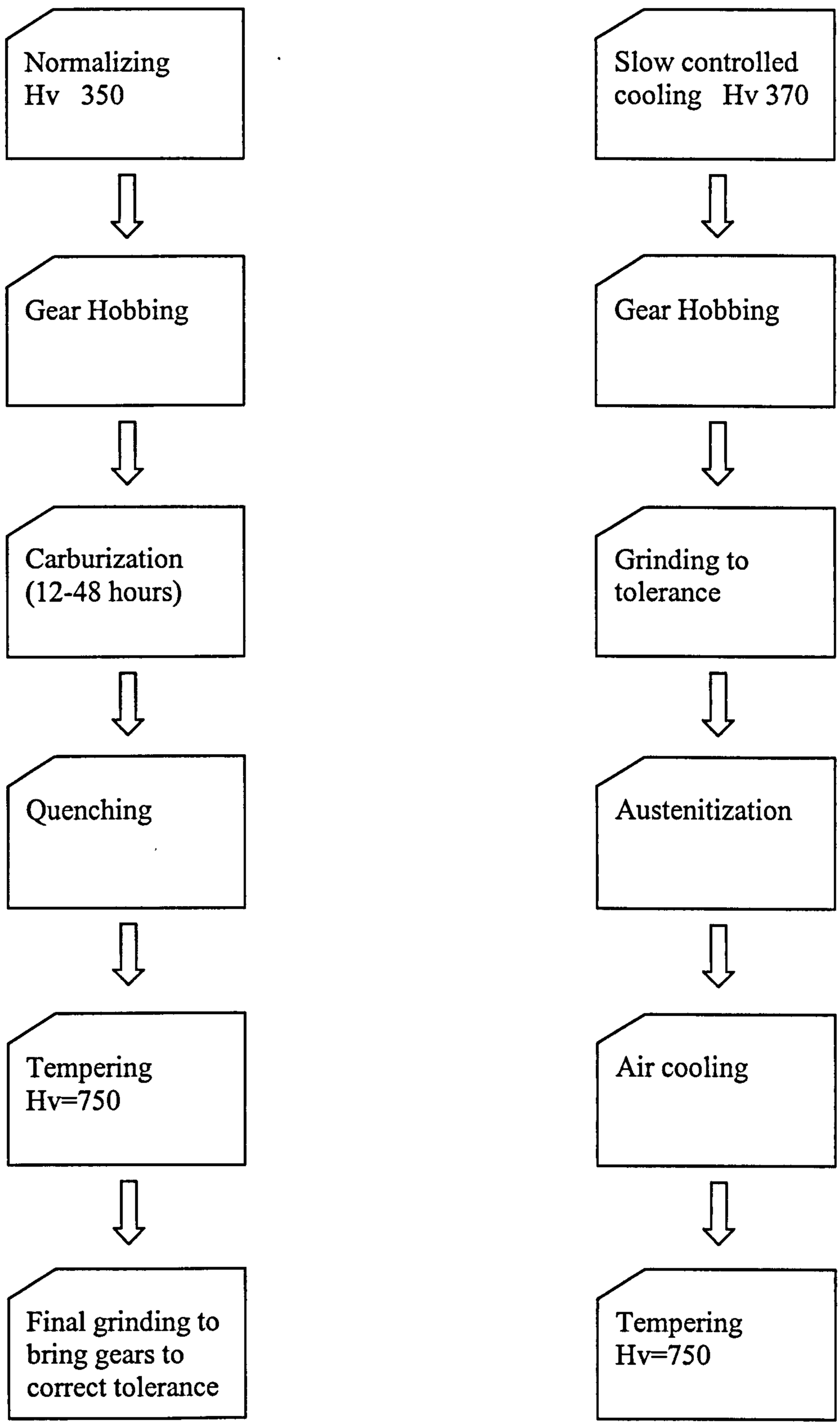

Fig.6.1 Comparison of heat treatment for conventional carburization steel and Ovako 677 steel for gear production

for hardening make this steel an economic alternative for conventional gear steels. Because of short time cycles required to heat treat through-hardening steels, problems like selective internal oxidation should be less serious. In addition, air quenching produces much less distortion than oil quenching. Consequently, much less post-heat treatment grinding will be required. However toughness and ductility are inferior compared with the core of carburized steel. The other disadvantage of through-hardening steels is the surface tensile residual stresses induced after hardening heat treatment (reported in Chapter 3). The latter disadvantage could be detrimental for a material intended for use as a gear material unless shot peening is employed.

6.2.1 Characterisation of Ovako Steel 677

6.2.1.a Hardness and Microstructure

Ovako steel specimens with diameter of 32 mm were hardened by air cooling from the austenite field. Hardness measurements and metallography examinations (Figures 3.16 and 3.18) showed that martensitic transformation took place through the specimen cross section at the moderate cooling rate. Thus the entire section of test specimen was hardened to about 750 Hv. The high carbon content (Fig.3.15) also resulted in retention of austenite phase of about 20 % through out the section, but this did not affect the hardness level.

Specimens tempered for 1 hour at various tempering temperatures (Fig.3.17) showed a gradual decrease in hardness, the behaviour that is expected for carbon and low alloy steels. Tempering affects also the content of the austenite phase (Fig.3.19) but the decomposition occurred at a tempering temperature above 400 °C.

6.2.1.b Residual Stress

The Ovako steel was found to have residual tensile stress at the surface. This is not seen in conventional case carburized steels and is discussed below.

Rapid cooling of steel components from high temperatures results in residual stresses. The origin of the residual stresses is the mutual effect of constraints produced by

different parts in the component to maintain coherency and compatible strains in the whole component. These constraints arise when different parts in the component undergo differential change in volume. Thermal contraction occurs during cooling as the temperature decreases. However phase transformation may occur during cooling at certain temperatures. Phase transformation is usually accompanied also by change in volume. As surface material cools faster than the interior, the final state of residual stress depends on the sequence of events taking place during the cooling process. In case carburized components, the higher carbon content in the case material depresses the M_s temperature and delays the martensite transformation in the case relative to transformations in the core material. The core material resists the late increase in volume at the case due to martensitic transformation. This induces compressive residual stresses at the surface and tensile counterpart stresses at the interior of the component. However, in the through hardening steel, the carbon content and other alloying elements are homogeneously distributed throughout the component thickness. Therefore it is expected that martensitic transformation proceed from the outer surface toward the interior. The later transformed interior tries to expand to accommodate the larger martensite volume. This expansion is constrained by the previously transformed outer surface. Therefore tensile stresses are induced in the outer surface and compression in the interior (Ebert, 1978). Measurements of residual stress profile carried out on through hardening Ovako steel are shown in Fig.3.21. Tensile residual stresses were found in the outer surface. These measurements were carried out on small specimens with 10 mm thickness. In real components with thicker sections the size may influence residual stress distribution. The level of tensile residual stresses at the surface was in the range of 300 MPa. It decreases beneath the surface. As explained earlier surface tensile residual stresses are harmful to fatigue performance of steel gears. This state of residual stress distribution is unlike the one produced in case carburized components where compressive residual stresses of the same order of magnitude are induced at the surface.

6.2.1.c Fracture Toughness

The K_{Ic} value of the hardened and un-tempered specimen was about 20 MN $m^{-3/2}$. This low value of fracture toughness is typical for high carbon steels and compares the

toughness of case carburized material quoted in the literature (Hyde *et al.* 1992). In these cases the fracture path is intergranular (Fig. 3.23-a). Tempering at lower temperatures did not increase the K_{Ic} values. Therefore fracture in hardened Ovako steel is expected to proceed with little plastic deformation. Increases in fracture toughness were only found after tempering temperatures higher than 400 °C. After tempering at a high temperature more fracture energy is absorbed during fracture. This is associated with transgranular crack growth by microvoid coalescence (Fig.3.22 and 3.23-d) although no gross plastic deformation accompanied the fracture. The toughness of the Ovako 667 steel is similar to that of the case material in conventionally carburised steels. The major danger in using the through-hardened steel is the possibility of secondary modes of failure. For instance, if a conventionally carburized gear is shrunk fit onto a shaft, the toughness of the core material guards against possible failure from the fitting operation. The through-hardened steel would not be as tolerant as the carburized steel.

6.3 Standing Contact Fatigue Test

As explained earlier in (Chapter 2) this type of test (SCF test) (in which a ball is pressed against a polished surface) tries to simulate asperities contact on surfaces of teeth flanks. There were substantial differences in our findings in standing contact fatigue compared with those obtained by Alfredsson and Olsson (1999). These are discussed below. Despite these differences, the major idea in this test is that fatigue is most likely in regions where the mean stress is tensile. This follows from the Goodman relation which correlates stress amplitude for fatigue with mean stress.

6.3.1 Test Results

Test specimens are considered in three groups for testing. The first group was tested after heat treatment without repolishing (direct testing), the second after repolishing and the third after shot peening of the repolished surface.

6.3.1.a Directly Tested Specimens

Figures 3.31-3.33 shows a large number of tiny surface cracks that become visible after fatigue loading. These small intergranular cracks are thought to be associated with oxidation of the prior austenite grain boundaries during heat treatment. The heat cycle was about 1 hour long but it seems that surface oxidation occurred at this relatively short austenitization cycle.

6.3.1.b Repolished Specimens

Surface polishing after heat treatment eliminated the small surface cracks. This means that oxidation was limited to a shallow depth during austenitization and that this layer was removed by polishing.

Examinations of test specimens under the applied load range from 2 kN to 12 kN showed that there were mainly two types of cracks produced in test specimens by the ball indenter. These are ring (or tangential) cracks around indentations and radial cracks emanating from indentations. Figures 4.48 and 4.49 show fatigue crack growth versus the number of cycles for radial and ring cracks respectively. No cracks were observed at applied load of 2 kN. At applied load of 4 kN only radial cracks were produced. At higher loads both types of cracks were observed. These figures revealed that both types of cracks were initiated early in the test after about 10^3 to 10^4 cycles. Cracks with length of 10 μm were considered as the initiation point in this test. This is the same criterion set by Alfredsson and Olsson (1999). The stress range affects the crack growth rate significantly. The higher the stress ranges the higher the fatigue crack growth rate. Cracks depths were found to differ significantly between ring and radial cracks, while ring crack were very shallow in depth, radial cracks propagate deeply beneath the surface. Both crack types were surface initiated. No subsurface cracks of any type were observed in the current tests.

Alfredsson and Olsson (1999) carried out standing contact fatigue test on case-hardened steels. Three relatively similar case-carburized steels with case depth of about 1.1 mm and surface hardness of about 750 Hv were examined. The surface oxide layer on specimens surfaces were removed by 'rubbing with cloth' before testing. Applied loads were cycled between maximum loads and nearly zero loads. The maximum

applied load was in the range from 5 kN to 20 kN using a 5 mm steel ball indenter. The influence of residual stress was investigated by testing two different plate thicknesses of 5 and 10 mm. The compressive residual stresses in the thin and thick specimens were 185 MPa and 254 MPa respectively. The tests were terminated after a predetermined number of cycles. They carried out also finite element simulation for the test which will be discussed separately. Alfredsson and Olsson (1999) presented their results as P-N plot for crack initiation for the different steel types. The number of cycles for crack initiation decreases as the applied load increase. The lowest load that gave crack initiation in any test was 7.42 kN. Ring type cracks resulted in this test. These cracks were found to grow initially perpendicular to the specimen surface and then with an inclination to give a cone shape as shown in cross section cut through specimens. Therefore these cracks were described as ring/cone cracks. At a higher number of load cycles (5-10 times the cycles for ring/cone crack initiation) another type of crack was developed. This is lateral subsurface crack usually formed at a depth of about of 0.65 mm beneath the contact surface and the crack location is unrelated to applied load level. The lateral crack diameter increases with increasing applied load. No radial cracks were reported in tests carried out with the 5mm ball indenter. Alfredsson and Olsson (2000) detected some small radial cracks when they used indenter with radius of 1.575 mm.

The formation of ring and cone cracks in Alfredsson and Olsson experiments correspond exactly with the ring and cone cracks observed in monotonic loading of glass (Frank and Lawn, 1967). This corresponds with entirely elastic deformation in both cases. However, this can not be correct for SCF of an elastic-plastic material across the entire loading range. The cracks follow a ring and cone path in a purely elastic material because these are the planes on which the tensile stress is a maximum. In an elastic-plastic material, the maximum tensile stress develops on radial planes at higher loads, when plasticity is well developed. This corresponds with the radial cracks observed in the present work.

The Finite Element simulation analysis for the standing contact fatigue test in the current investigation work confirms that plastic deformation occurred during the test. Based on real data from compression test, the simulation is more realistic than the simulation carried out by Alfredsson and Olsson (1999). As explained in (Chapter 4)

the data that Alfredsson and Olsson (1999) used as input in their FE simulation must be in error. It appears that they used data from a tensile test to which was fitted a power law expression. Of course, the ductility of high strength steel in tension is limited and extrapolation of a slightly non-linear stress-strain curve obtained in a tensile test is certain to be in error when applied to indentation. Effectively, therefore, their input data was not much different from linear elastic, Of course they ought to have obtained their stress-strain data from a compression test, as was done in the present work.

As an indication of agreement between results from SCF test and FE simulation, two different results from both methods were compared. These results are the increase of indentation sizes with increased applied loads and the type and amount of residual stresses left around indentations after load removal. However, it was more convenient to use a Brinell type indention test (application of one load cycle, as explained in (Chapter 3) for this purpose. Test results from indentation test and SCF test were in good agreement with prediction from the FE simulation for the two test results. The relation between applied load and indentation size from real test and FE simulation were very close as shown in Figs.3.27 and 4.14. The results in Fig.3.27 show the mean pressure under spherical indenter tending to saturate at $P_m \cong 3\sigma_y$ with increasing indentation size.

The simulation results in the current work showed that deformation is no longer restricted to a small contained volume beneath the surface. Figures 4.9 show the growth of the plastic zone with increasing applied load. The plastically deformed zones reach the contact surface at load of 2.8 kN. Therefore at applied load of 2 kN with the plastic zone is completely contained within elastically deformed material beneath the surface, the state of stress is similar to the Hertzian elastic solution. However at an applied load of 4 kN or higher the elastic-plastic solution is the appropriate one to adopt in this test and not the elastic solution.

After the first cycle of loading, residual stresses are developed inside and around indentations. The residual stresses affect the level of mean stress and therefore the fatigue crack initiation and propagation. The effect of residual stresses was discussed in (Chapter 4). The analysis supports the formation and propagation of radial cracks.

However, the estimated state of stress is not in favour of formation of ring cracks at high applied loads of 12 kN. Ring cracks were observed but were found to penetrate for only shallow depths beneath the surface. The exact mechanism for these cracks is unclear but it may be produced at the periphery of the contact area due to highly localised deformation in the contact areas that is not properly modelled by the FEA model which ignored any friction.

6.3.1.c Shot Peened Specimens

Shot peening is a well known method of inducing surface compressive residual stresses to enhance fatigue life. High levels of compressive residual stresses were produced in hardened specimens of Ovako steel by shot peening as shown in Fig.3.29. The peak of the compressive residual stress of about 1400 MPa was obtained at a shallow depth of about 40 μm below the surface. High levels of compressive residual stresses are induced by the shot peening process in materials with high strength. Standing contact fatigue showed that shot peening suppressed the formation of radial cracks. This shows that radial cracks are nucleated at the surface and that nucleation is suppressed by the compressive residual stress. The ring cracks produced in these specimens were arrested at shallow depths corresponding with the depth of the peak compressive residual stress. The absence of radial cracks means that the compressive residual stresses induced by the shot peening process were high enough to overcome any tensile stresses induced by the applied contact loads.

6.4 FE Analysis for Stresses near an Indentation

Development of fatigue cracks is affected by the stress range and the mean stress. Estimation of mean stresses should take in consideration any residual stresses existing in the material. In the current work residual stresses are produced as a consequence of plastic deformation during first loading. Therefore there is relatively little cyclic plastic deformation. Therefore the results obtained by FEA simulation were represented to show the effect of these two parameters on fatigue cracking. Equations defining the stress range and mean stress are shown in (Chapter 4). The maximum and minimum stresses in these equations correspond to stresses at loading and after load removal (or residual stress based on the Johnson assumption) respectively. The residual stresses left

after load removal based on this assumption were obtained by subtracting the elastic stress from the maximum stress attained during loading. The extreme stresses in these calculations are the maximum loads stress obtained by FEA and the residual stress obtained based on Johnson assumption. Results for stress range and mean stress are shown over a small distance just outside the indentation area where cracks initiate. Results obtained by FEA give good explanation for development of radial cracks. Figures 4.18 (a-f) showed that the highest levels of mean stress and stress range (in hoop direction) occurs at the outer edge of indentation where cracks initiate. The mean stress increase progressively with increasing applied load. This shows the importance of the plasticity induced stresses on development of fatigue cracks. With increasing applied load the crack growth rate increases with increase in mean stress. The increase in stress range with increase in applied load is less apparent. This is not in contradictions with equations shown in (Chapter 4) for estimation of stress range and mean stress. The FEA also predicted that the mean stress in the radial direction decreases with increasing applied load. However even at high loads when the estimated mean stress is negative the experimental tests showed that ring cracks were produced. As mentioned earlier these cracks were shallow cracks and might be attributed to plastic deformation and frictional effects that are not properly modelled by FEA.

6.5 Standing Contact Fatigue Related to Empirical Fatigue Models

Alfredsson and Olsson (1999) proposed that the SCF test could give information relevant to surface contact fatigue on the scale of surface asperities. To understand this approach, it is worth noting that it is not possible to understand surface contact fatigue in gears, say, based on the stresses produced by ideally smooth surfaces. The stress field produced by contacting cylinders is compressive. Large shear stresses occur below the surface, but any cracks that might exist will be closed by the equally large direct stress components that are compressive. There is no evidence of subsurface crack nucleation in gears run at the stress levels relevant to normal operation conditions. Nucleation of cracks at the surface is also difficult to understand without invoking interaction between asperities. No tensile stress components occur in smooth cylindrical contact unless a significant tangential force is added (Smith *et al.*, 1953). Since gears are well lubricated in operation, it is possible to conceive of significant tangential, frictional forces only on the microscale, i.e. at asperities.

The above argument assumes that a degree of tension or Mode I crack opening is required for growth of fatigue cracks on any scale. The same problem arises in the indentation fracture of brittle materials in monotonic loading (Frank and Lawn, 1967). The largest stresses produced in indentation of an elastic material by a spherical indenter are compressive. Nevertheless, tensile stresses of smaller magnitude occur on planes outside the contact area and it is on these planes that ring and cone cracks develop, i.e. the fracture path follows the plane of maximum principal stress, as has been observed in glass by many observers (Frank and Lawn, 1967). The same thing should also occur in fatigue if the stress field is similar to that in an elastic material. However, although the stress field is similar in steel at low loads, where the plastic zone is small, the stress field changes profoundly as the load increases and the plastic zone size approaches the fully plastic condition. Then, radial cracks are favoured because these planes experience the largest tensile stress. The observations of fatigue cracks in the SCF tests are generally in line with the finite element calculations, in that radial cracks dominate at higher loads.

These observations do not provide a detailed link with the cracks developed in micropitting or macro-scale pitting in back-to-back tests in gears, but they do illustrate the importance of localised tensile stresses in generating fatigue in these cases. We now consider some of the empirical models of fatigue in relation to the observations made in the SCF tests.

Manson-Coffin Model

The Manson-Coffin model of fatigue focuses attention on cyclic plastic deformation in fatigue. The implication is that purely elastic cyclic deformation could not produce fatigue cracks and that even if a plastic component is not discernible on a macroscopic scale it must occur on a microscopic scale for fatigue to occur. Based on controlled amplitude strain cycling tests on ductile materials such as copper, aluminium, alpha brass etc., Manson (1965) and Coffin (1954)) proposed the following relation between the number of cycles to failure N and the cyclic plastic strain Δe_p in a cycle

$$N = \left(\frac{\Delta e_p^0}{\Delta e_p} \right)^c , \tag{6.1}$$

where Δe_p^0 is the strain for failure in a single cycle and the exponent c is approximately equal to 2. The Manson-Coffin relation was found to hold for a wide range of ductile alloys, independent of yield strength.

The Manson-Coffin equation holds in low cycle fatigue, where $N < 10^4$. At larger values of N the cyclic plastic strain becomes much smaller than the elastic component and is generally impossible measure independently. In these circumstances, fatigue data is often fitted with Basquin's (1910) empirical equation. This is

$$N = \left(\frac{3.5\sigma_u}{\Delta\sigma} \right)^{8.3} , \tag{6.2}$$

where σ_u is the tensile strength and $\Delta\sigma$ is the cyclic stress range.

The importance of the Manson-Coffin model, as distinct from Basquin's more empirical equation, is that it focussed attention on the importance of cyclic plastic deformation in producing fatigue. As such, it links with possible micro-mechanisms better than does a purely empirical approach.

Goodman's Equation

Neither of the above models takes account of the influence of mean stress on fatigue, yet a basic rule of metal fatigue is that, after the nucleation stage a fatigue crack grows on the plane of the maximum principal stress. For instance, a fatigue crack nucleated in a shaft subject to cyclic torsion grows at 45 degrees to the axis of the shaft because this is the plane subject to the maximum principal stress. In the present work, the effect of mean stress is critical in accounting for crack path and location and in explaining the effect of the residual stress produced by shot peening.

Goodman (1899) proposed a semi-empirical equation to account for the effect of mean stress on fatigue. If $\Delta\sigma$ is the fatigue strength or the stress range required to produce

failure after, say, 10^8 cycles, Goodman argued that $\Delta\sigma$ must be zero when the mean stress is equal to the tensile strength. Linear interpolation then gives the relation between mean stress σ_m and $\Delta\sigma$, i.e.

$$\Delta\sigma = \Delta\sigma_0\left[1-\sigma_m/\sigma_u\right], \tag{6.3}$$

where $\Delta\sigma_0$ is the fatigue strength with zero mean stress (fully reversed loading). An alternative way of representing this relation is in terms of the maximum or minimum stress versus σ_m. This gives the two curves

$$\begin{aligned}\sigma_{\max} &= \tfrac{1}{2}\Delta\sigma_0+(1-\alpha)\sigma_m \\ \sigma_{\min} &= -\tfrac{1}{2}\Delta\sigma_0+(1+\alpha)\sigma_m\end{aligned}, \tag{6.4}$$

shown schematically in Fig.6.2. Here, the parameter α is the ratio $\frac{1}{2}\Delta\sigma_0/\sigma_u$.

It is clear that a superimposed compressive stress allows an alloy to tolerate a much larger range of cyclic stress. However, the compressive region of the graph in Fig.6.2 has been relatively little explored in previous work (Frost, Marsh and Pook, 1974).

Fatigue Crack Growth

The process of fatigue crack nucleation and crack growth is difficult to study in high strength steels using conventional methods. Because the toughness of the material is low, fatigue cracks of only about 150 μm diameter can be produced under uniform tensile loads before unstable fracture occurs. It is possible to deduce the details of fatigue only after the event by painfully detailed SEM inspection of the fracture surfaces (e.g. Hyde *et al.* 1992). Thus, one has to rely on the evidence of the behaviour of more ductile materials to deduce by analogy what nucleation and growth processes might occur.

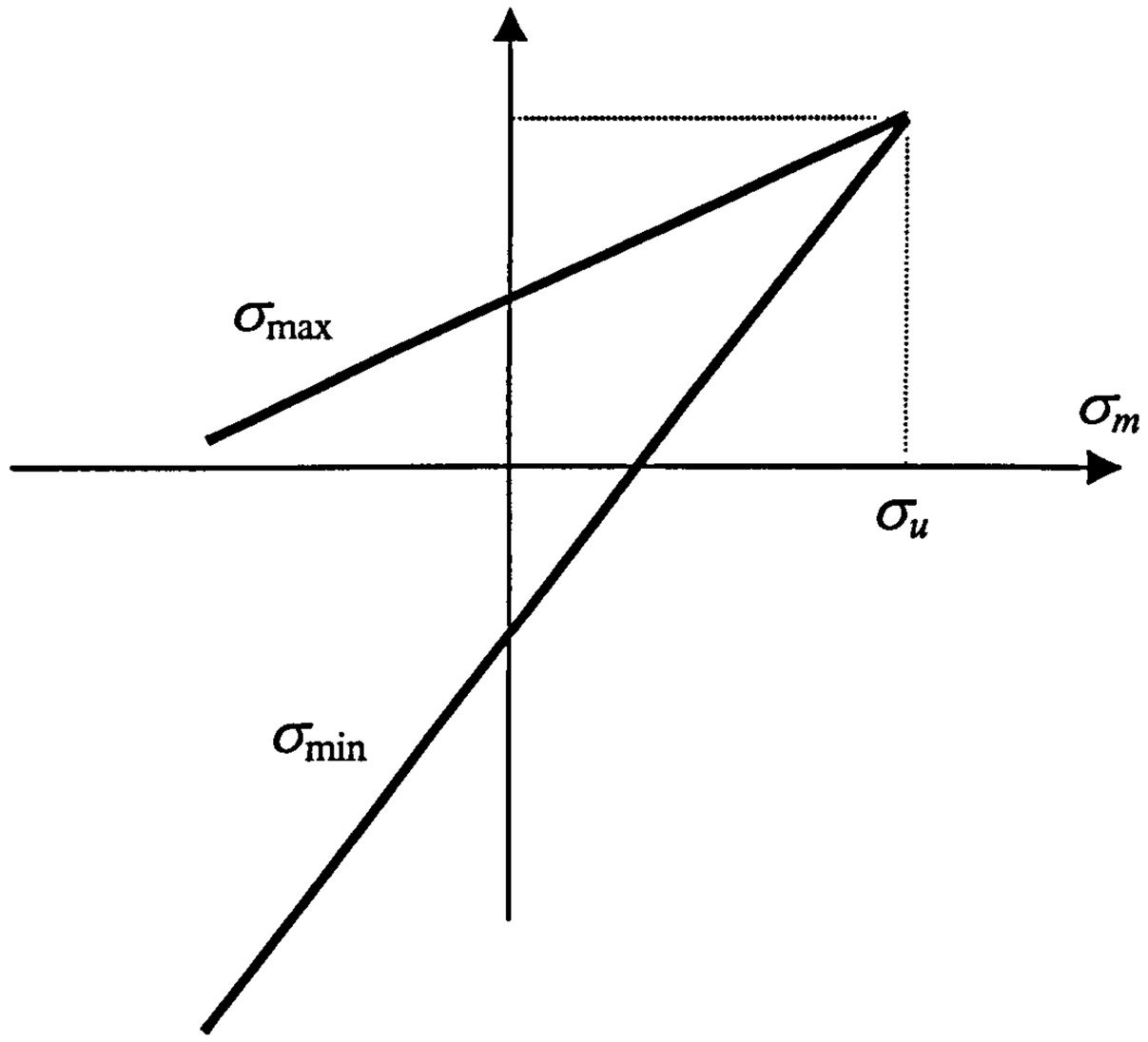

Fig.6.2. Goodman relation for maximum and minimum stress in fatigue.

It is possible to study the processes of nucleation and fatigue crack growth in more ductile alloys (e.g. Tetelman A.S., McEvily, A.J., 1967). The general pattern of behaviour is as follows.

1. Persistent slip bands form in surface grains on slip planes inclined at an angle of about 45 deg. to the maximum principal stress axis.
2. Stage I cracks form on slip planes in the persistent slip bands and grow from the surface until the crack tip intersects the nearest grain boundary.
3. The Stage I crack then provides the nucleus of a Stage II crack that continues to grow on a plane normal to the principal stress axis. Growth of the Stage II crack continues with an increment in each load cycle until overload failure results.

Experimental observations show that most of a specimen's life in high cycle fatigue is spent in nucleating and growing the Stage I cracks. Once Stage II crack growth starts, failure follows in relatively few cycles.

Of course, Stage II crack growth has been extensively studied in deeply notched fracture toughness and the results are normally expressed in terms of the well-known Paris law that relates the crack growth increment per cycle $\mathrm{d}a/\mathrm{d}N$ to the variation in stress intensity factor ΔK:

$$\frac{\mathrm{d}a}{\mathrm{d}N} = A\Delta K^m, \tag{6.5}$$

where A and m are constants. Relatively little quantitative information is available on the growth of Stage I cracks.

Relation to the SCF Tests

The maximum stress variation in the SCF that occurs beneath the indenter, but even though the values are very large there, fatigue cracks nucleate outside the contact area where $\Delta\sigma$ is smaller but the values of σ_{max} are positive. Thus, mean stress is a key factor in producing fatigue.

When the combination of mean stress and stress variation are favourable for fatigue cracks nucleation and growth, it is apparent that nucleation is relatively easy and occurs below 10^4 cycles, corresponding to the low cycle fatigue regime in conventional fatigue testing. This is to be expected since plasticity is well developed locally around the indentation. If we estimate a single cycle ductility $\Delta e_p^0 = 0.02$ for the material, the Manson-Coffin relation predicts that a cyclic plastic strain of only 0.02% is required to produce a fatigue crack in 10^4 cycle. After nucleation, the radial cracks grow in Stage II mode, on planes perpendicular to the direction of the maximum principal stress.

The results in Fig.3.48 and 3.49 show that the major effect of the applied load is on the rate of crack growth, since the number of cycles for nucleation is between 10^3 and 10^4 in all cases where cracks are observed to nucleate before run out. The difficulty in quantifying fatigue in the SCF test is that the stresses and the stress range in the region outside the contact zone are due to second order effects such as the residual stress present on unloading. For instance, the stresses outside the contact zone do not increase monotonically with applied load as explained in (Chapter 4).

In order to make an estimate of the relative effect of the maximum and minimum stress one needs to adopt an indicator stress σ_I that combines stress range and mean stress. One simple possibility is to use the combination

$$\sigma_I = \frac{\Delta\sigma}{1-\sigma_m/\sigma_u}, \tag{6.6}$$

derived from the Goodman relation. It is envisaged that, the larger the value of the indicator stress, the more rapidly fatigue develops. Taking $\sigma_u = 3000$ MPa, values of the indicator stress, obtained from the FEA, as a function of applied load are shown in Fig.6.3.

The results here are only broadly in line with the experimental results from the SCF tests. At loads above 6 kN, the hoop stress indicator shows that radial cracks will dominate any development of fatigue damage, as is observed. Cracks were not modelled in the FEA of indentation, because full three dimensional analyse is required

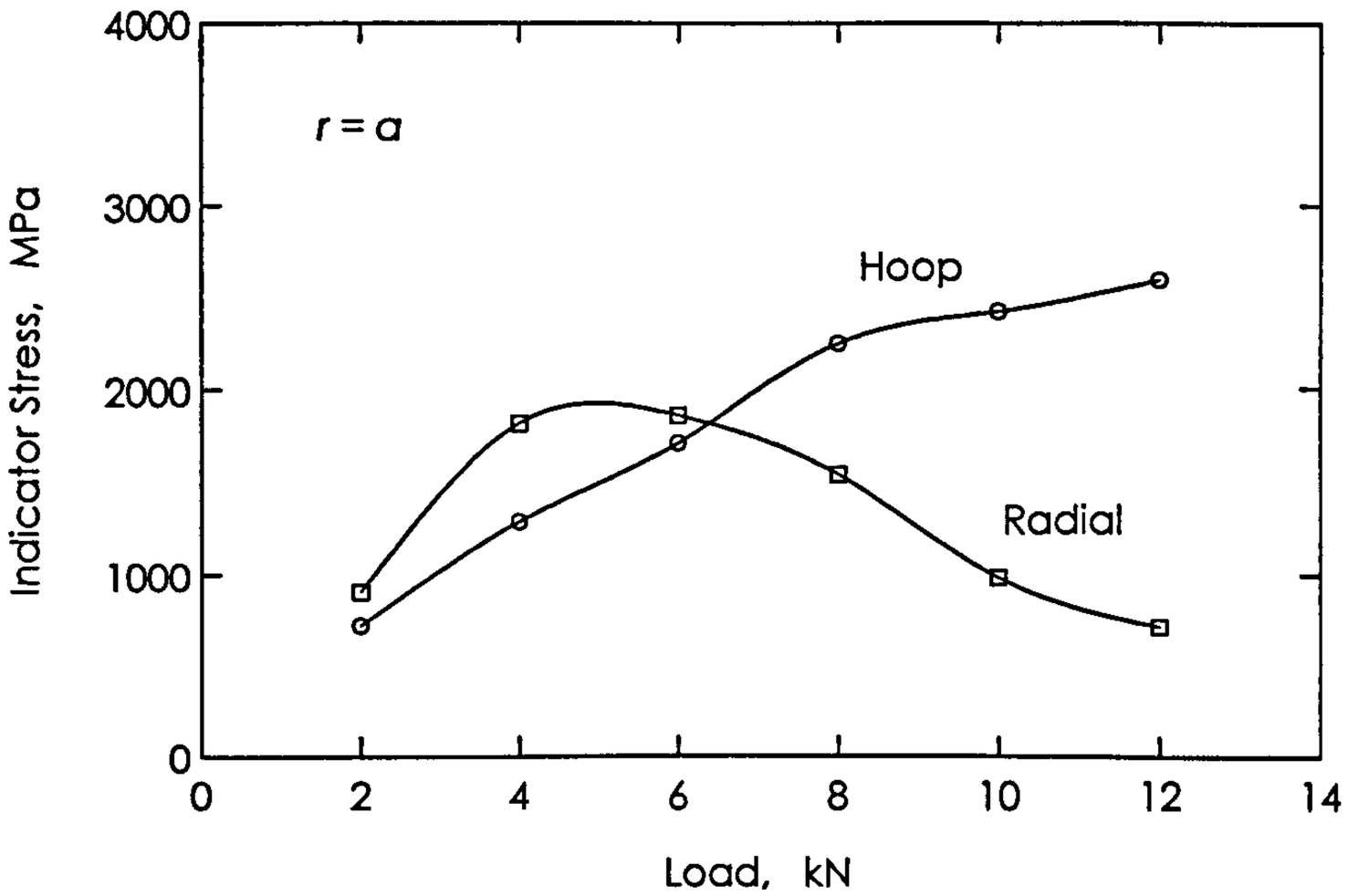

Fig.6.3. FEA results showing indicator stress at $r = a$ as a function of applied load

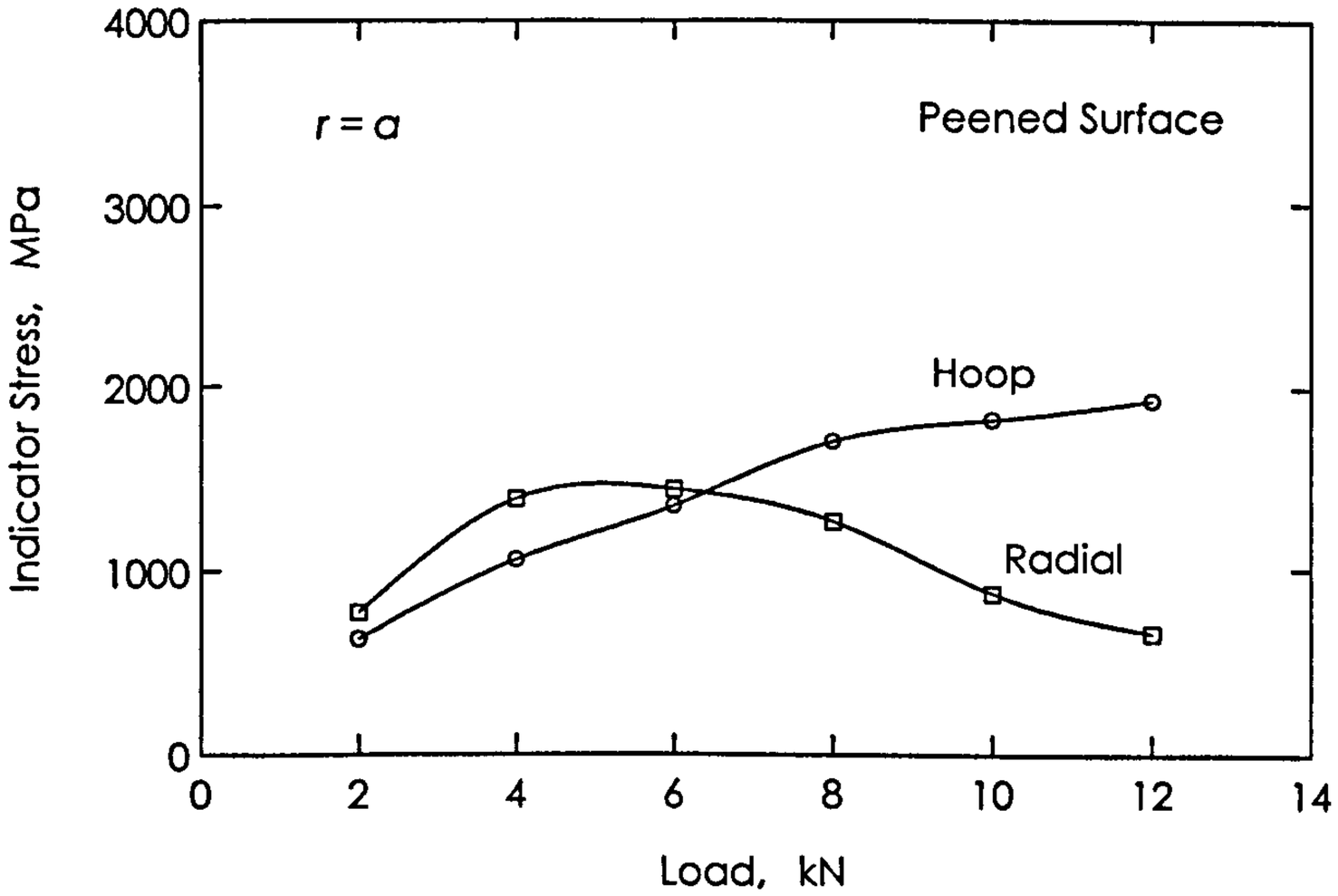

Fig.6.4. FEA results showing indicator stress at $r = a$ as a function of applied load when the residual stress from shot peening is incorporated.

to model the radial cracks near the indentation. Since the major difference between the effects of different loads is in the rate of crack growth, it is likely that calculation of the stress field alone is not sufficient to distinguish between different stress levels in the SCF tests.

The radial stress indicator in Fig.6.3 generally declines with increasing loads after reaching a maximum between 4 and 6 kN load. Thus, the occurrence of ring cracks at higher loads remains unexplained. It has been noted previously that the ring cracks that do form at higher loads do not penetrated very far from the surface and seem to have been arrested early on in the test. It must be concluded that this phenomenon remains to be explained and that the FE models used do not take account of all the interactions between the contacting surfaces, e.g. friction between the indenting sphere and the surface was not included in the model.

It was reported in (Chapter 3) that shot peening a specimen before SCF testing was effective in suppressing the formation of radial cracks. The residual compressive stress induced by shot peening changes the mean stress in the same way for all loads, but it does not affect the cyclic stress. Thus, the effect of shot peening might be included by adding a residual stress component to the mean stress in the expression for σ_I. This modification produces the result shown in Fig.6.4. The residual compressive stress reduces the indicator stress, but not sufficiently to explain the suppression of radial cracks in a relative sense. For instance, if a load of 6 kN is sufficient to produce radial cracks in the un-peened state (Fig.3.37), then a load of 10 or 12 kN should produce cracks in the peened specimen. One implication is that the simple empirical models of fatigue are not adequate to explain all the details of fatigue under more complex loading systems.

Fatigue cracks nucleate in the region just outside the contact area. As the cracks grow in some cases they may become unstable while they are still small. This can be estimated by considering the stress intensity factor K_I of a surface-breaking crack as a function of local stress σ and crack length a (Fig.6.5).

$$K_I = 1.12\frac{2}{\pi}\sigma\sqrt{\pi a}\,. \tag{6.7}$$

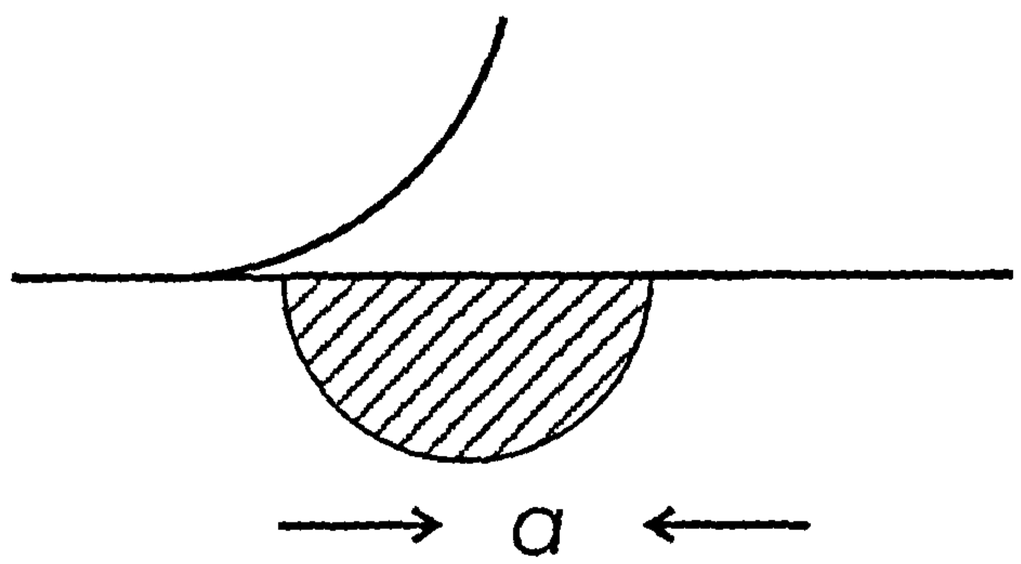

Fig. 6.5. Crack near an indent.

The crack will extend unstably when $K_I = K_{Ic}$. It follows that the critical crack length where this will occur is given by

$$a_c = \frac{1}{\pi}\left[\frac{1}{1.12}\frac{\pi}{2}\frac{K_{Ic}}{\sigma}\right]^2 . \qquad (6.8)$$

Of course, the unstable crack is likely to arrest because it grows into a region of reducing stress. In addition, the presence of a longer crack will itself change the stress distribution. However, a full three-dimensional FE analysis would be required to study crack extension of longer cracks and this was not attempted in the present work.

Estimates of the critical crack radius a_c as a function of load, calculated from the maximum stress just outside the contact area, are shown in Table 6.1. In order to provide an indication of scale, the ratio of crack radius to the indentation radius a_c/a is also shown in Table 6.1.

Clearly, when the ratio a_c/a is small, the cracks could become unstable before they grow into the diminishing stress field. In these cases crack growth in fatigue could be discontinuous or much more rapid than predicted by the ordinary Paris relation. Thus, the growth of radial cracks is probably discontinuous for loads of 8 to 12 kN. Further, the growth occurs in the unloaded state, i.e. they will be driven by the residual stress field. In fact, Studman and Field (1977) observed growing radial cracks near an indent in high strength steel after unloading.

Table 6.1. Critical crack size a_c. Note that a here is the indentation radius.

Load kN	Radial			Ring		
	a_c μm	a_c/a	Condition	a_c μm	a_c/a	Condition
2	590	1.55	unloaded	152	0.4	Loaded
4	162	0.32	unloaded	71	0.14	Loaded
6	87	0.15	unloaded	73	0.14	Loaded
8	60	0.09	unloaded	226	0.33	Loaded
10	57	0.08	unloaded	>1000	>1.4	Loaded
12	54	0.07	unloaded	-		Loaded

6.6 Stresses due to Austenite to Martensite Transformation

Estimation of induced compressive stresses in relation to transformed austenite volume fraction was made in the model presented in (Chapter 5). Experiments were made to measure compressive stresses due to austenite transformation in order to support the finding obtained in the model. In this experiment the process of shot peening was used as a mean to transform retained austenite on the surface of steel specimens. Shot peening induces compressive stresses in surface layers as a result of the plastic deformation. Strain induced transformation of retained austenite to martensite will also occur in the specimen surface layers. Therefore in order to distinguish the effect due to the austenite transformation alone from the effect due to plastic deformation in producing stress, the results from two specimens were compared. One specimen had almost no retained austenite and the other contained about 18.5 % retained austenite. Comparison of residual stress profiles obtained for the two specimens showed that the specimen with retained austenite produced higher compressive residual stress. Therefore the difference in compressive residual stress is attributed to the strain induced transformation of austenite to martensite. Austenite transformation of volume fraction $f_M \approx 0.18$ causes an induced compressive stress of about 350 MPa. This result is in good agreement with the estimation from the mathematical model although it is lower than the estimated value by about 70 MPa based on 4 % change in volume in the austenite-martensite reaction. The estimated value can be regarded as the upper limit for the stresses generated due to the austenite-martensite transformation. This is

because the percentage of volume change could be lower than 4 % particularly when the carbon content is high. Therefore the developed stresses due to the austenite-martensite reaction should be lower than the levels estimated in the mathematical model.

Stresses generated in contacted flanks of helical gears tested for surface contact fatigue were presented in (Chapter 3) (Figure 3.8). These are assessed in the light of the estimation obtained by the mathematical model. Contact loading on run flanks causes retained austenite to transform to martensite. The strain induced transformation was confined to a thin layer where compressive tresses are also generated due to the transformation reaction. The induced stress due to the transformation of austenite volume fraction f_M of about 0.3 was about -500 to -600 MPa (measured along the longitudinal tooth direction Fig.3.8. This level of compressive stress is less than the value estimated by the mathematical model by about 100 to 200 MPa. Reasons for this are similar to ones quoted above. The carbon content in the carburized case of those helical gears was higher than the conventional level. Figure 3.4 showed that the carbon content in the case material was about 1.5 %. This means that the percentage increase in volume due to the austenite-martensite reaction in the transformed layer could be less than the quoted value of 4 %. Therefore compressive stresses generated due to the strain induced austenite transformation should be lower than the estimated value.

Thus by taking the value of 4 % as the upper limit for the percentage of volume change and with a correlation between the percentage volume change and the carbon content, the adopted mathematical model is capable of a reasonable estimate of stresses generated by the austenite-martensite transformation.

CHAPTER 7

Conclusions

Conclusions obtained from this work are summarised below. The work in this investigation consists of two parts. Conclusions points are given separately for each part of the work.

Effect of retained austenite in the case of carburized gears on fatigue life

The effect of retained austenite in the levels of 40-60 % in carburized gears on bending fatigue and surface contact fatigue strength was studied. This level of retained austenite was much higher than the usual specified limits for such applications. The results can be summarised in the following points.

1. High levels of retained austenite do not appear to be detrimental to fatigue life of gears. In fact, retained austenite improved the low cycle fatigue life slightly. In high cycle fatigue (10^8 cycles) no effect was discernible.
2. Transformation of retained austenite to martensite occurs during testing. The transformation was confined to a surface layer of shallow thickness ($\approx$ 10 μm) and could be due to strain induced transformation mechanism. The depth of the transformed layer is related to the deformation of surface asperities in surface contact.
3. Compressive residual stresses were also induced in thin surface layer. However these stresses more likely to be generated due to the plastic deformation which the surface asperities undergo during contact loading.
4. The hard transformed martensite phase and the induced compressive residual stresses could be the reason for preventing premature failure in gears with high retained austenite content.
5. There is no austenite to martensite transformation below the contacting surfaces at the depth of maximum shear stresses (smooth surfaces) occurs. This is because the applied stresses are too low in this region to produce plastic deformation.

Standing Contact Fatigue test for through-hardened Ovako 677 steel

1. Because the steel is a new formulation, a basic characterisation for the heat treatment, hardness, toughness and residual stress was carried out. It was found that properties equivalent to those of case-carburized steel could be developed by air cooling from the austenitizing temperature followed by tempering. Unlike case carburized steel, tensile residual stress is developed in the surface layers.
2. Fatigue of the material was investigated. For this purpose a test method known as the Standing Contact Fatigue Test (SCF test) was adopted. It is aimed through this test to simulate asperities contact on surfaces of mating gear flanks. The following points were concluded.
3. It is postulated that a mean tensile stress is required for fatigue crack formation. Thus, fatigue cracks are nucleated outside the contact area between the spherical indenter and the specimen surface.
4. Both radial and ring cracks are generated in SCF. These results were at variance with results obtained by other workers because radial cracks were observed to be dominant in the present work
5. The SCF results were supported by the results of finite element analysis, which also supports the idea that a mean tensile stress is required for easy fatigue crack nucleation. It is believed that a previous analysis by other workers is in error because an incorrect constitutive equation was used.
6. Shot peening process produced high levels of compressive residual stresses at and near surface material. This residual stress suppressed radial fatigue cracks although very shallow ring cracks were observed. The mechanism for nucleation of the shallow ring cracks is not fully understood at the present time.
7. A mathematical model to estimate compressive stresses generated by the austenite to martensite transformation was proposed. Estimation based on the proposed formula was found in good agreement with measurements obtained from experiments designed for this purpose provided it is assumed that the volume expansion for the sub-zero transformation of retained austenite is less than the 4 % figure often quoted in the literature.

Suggestion for Further Work

A number of particular observations have been made in the course of this research which are not entirely understood and for which insufficient time was available to follow up. The following are some ideas for investigations that might be taken up in the future.

1. The transformation of retained austenite in the surface layers of a specimen was observed to produce a smaller residual compressive stress than would be expected if the volume expansion accompanying transformation is 4 %, as is often assumed. We have explained this by suggesting that the volume expansion is less than 4 % because of the possibility of higher carbon levels in the retained austenite. However, we did not have time to investigate this systematically. Indeed, an investigation of retained austenite in steel with model compositions could be the subject of a whole PhD thesis. It would be interesting to study the subject in much more detail than was possible in this work. The phenomenon is of great metallurgical interest and there is an important practical consequence. That is, the contribution of the transformation of austenite is considerably less than the calculations suggest it should be. It would be satisfying to understand this on a sound scientific basis.
2. The dominance of radial cracking in the standing contact fatigue tests has been explained on the basis of the stress field generated in elastic-plastic indentation. Nevertheless, shallow ring cracks are generated even when radial cracking is suppressed by shot peening prior to testing. This is not explained by the Finite Element results. It is possible that the FE analysis has missed a subtle point in the deformation near an indent. Further work might be done on this aspect of the SCF test.
3. The SCF test shows that fatigue cracks are readily nucleated under compressive loading provided that some regions are in tension. Thus we expect cracks to form near spherical indents but not in cylindrical contact. Since gear contact involves macroscopic cylindrical contact it follows that micropitting in gears must arise from asperity contact on the microscale. The geometry of these contacts is likely to give elliptical contact patches rather than circular ones, i.e. the microcontacts are likely to lie between spherical and cylindrical indentation. This has not been studied in the

present work. However, it is possible to envisage a standing contact fatigue test involving an elliptical contact patch. This could be achieved using crossed cylinders, where the aspect ratio of the ellipse is controlled by varying the angle between the axes of the cylinders. Designing a testing rig to do this would not be easy, but it is suggested that further work could be done on this aspect of fatigue.

References

Alfredsson, B. and Olsson, M., 1999, *Fatigue Fract. Engng. Mater. Struct.* **22,** p.225.

Alfresson, B and Olsson, M. 2000, *Engng. Fracture Mech.* **65,** p.89.

Ando, T. and Krauss, G., 1981, *Met. Trans.* **12A,** p.1283.

Apple, C.A and Krauss, G., 1973, *Met.Trans.* **4,** p.1195.

Bailey, E.F. and Harris, W.J., 1952, *Trans. Amer. Soc. Metals.* **44,** p.204.

Bain, E.C., 1924, *Trans.AIME* **70,** pp.25.

Basquin, O.H., 1910, *Proc. ASTM* **10,** p.625.

Berth, D., Flamand, L. and Godet, M., 1980, *Trans. ASME, J. Lubric. Technol.* **102,** p.478.

Bowen, D.K., Capus, J.M., and Silverstone, C.E., 1967, *Phil. Mag.* **15,** p.1041.

Bull, S.J., Evans, J.T., Shaw, B.A. and Hofmann, D.A., 1999, *Proc. Instn. Mech. Engrs.*. **213,** part J, p. 305.

Calik, Y., Evans, J.T. and Shaw, B.A., 1996, *Scripta mater.* **34,** p.1101

Castleman, L.S., Averbach, B.L. and Cohen, M., 1952, *Trans. Amer. Soc. Metals.* **44,** p.240.

Cavallaro, G.P., Wils, T.P, Subramanian, C., Strfford, K.N, French, P. and Allison, J.E., 1995, *Surface and Coatings Technol.* **71,** p. 182.

Chilton, J.M. and Kelly, P.M., 1968, *Acta. Metall.* **16**, p.637.

Coffin, L.F., 1954, *Trans ASME*, **76**, p.931.

Cohen, M., 1968, *Trans. JIM, Supplement.* 9 xxiii.

Cullity, B.D., 1978, Elements of X-ray diffraction 2nd edition, Addison-Wesley Publishing, INC., Reading.

da Silva, V.F., Canale, L.F., Bose-Filho, W.W. and Crukovic, O.R.,1999, *J. Mat. Eng. and Perfor.* **8(5)**, p.543.

Dickinson, P. 2001, private communication.

Diesburg, D.E., 1978, High cycle and impact fatigue behavior of carburized steels, SAE. Publication 780771

Dong, Z., Fu-xing, W., Qi-gong, C., Ming-xin, Z. and Yin-quian, C., 1985, *Wear* **105**, p.223

Dowling Jr, W.E., Donlon, W.T., Copple, W.B., and Darragh, C.V., 1995, "Fatigue Behaviour of Two Carburized Low Alloy Steels" Conference Proceeding, Carburizing and Nitriding with Atmospheres, eds. Grosch, J., Morral, J., Schneider, M., ASM International, Cleveland, OH, p.55.

Dudley's Gear hand book, 2nd edition, 1992, chapter 15, Lewis Research Centre, NASA

Ebert, L.J., 1978, *Metall. Trans.* **A9**, p.1537.

Emmert, S., 1994, Untersuchungen zur Zahnflankeneermüdung (Graufleckigkeit, Grübchenbildung) schnellaufender Stirnradetriebe. Diss. TU München

Evanson, K.C., Krauss, G., and Matlock, D.K., 2000, "Surface Oxides and Bending Fatigue in Gas-Carburized SAE 4320 Steels" 20th ASM Heat Treating Society

Conference Proceedings 2000, eds. Funatani, K. and Totten, G.E., St. Louis, MO, ASM, p.249.

Eshelby, J.D, 1957, *Proc.Roy.Soc.* **A241**, p.376.

Eshelby, D.J., 1961, "Elastic Inclusions and Inhomogeneities", in *Progress in Solid Mechanics* **2**, eds. Sneddon, N.I. and Hill, R., North-Holland, Amsterdam, p.89.

Fernandes, P.J.L., 1996, *Eng. Failure Anal.* **3 No.3**, p.219.

Fischer, C., 1978, *Metall. Trans.* **9A**, p. 1552.

Frank, F.C.,1953, *Acta Metall.* **1**, p.15.

Frank, F.C. and Lawn, B.R., 1967, *Proc. R. Soc. Lond.* A **299**, 291.

Frankel, H.E., Benett, J.A. and Pennington, W.A., 1960, *Trans. Amer. Soc. Metals*. **52**, p.257.

Frost, N.E., Marsh, K.J. and Pook., L.P., 1974, Metal Fatigue, Oxford Engineering Science Series, Editors: Woods, L.C., Wittrick, W.H. and Cullen, A.L., Clarendon Press Oxford.

Goodman, J., 1899, Mechanics Applied to Engineering, Longmans Green, London.

Gu, C., Lou, B., Jing, X. and Shen, F., 1989, *J. Heat Treat.* **7 No.2**, p.87

Hardy, C.,Baronel,C.N. and Tordino,G.V., 1977, *Int.J.Num.Meth.Engng*. **3**, p.451.

Hertzberg, R.W., 1996, Deformation and Fracture Mechanics of Engineering Materials, John Wiely & Sons, INC. New York.

Hoeprich, M.R, 2000, Tribology 2000-plus 12th Int Colloquium, Ostfilden, Germany.

Hohn, B.R., Oster, P. and Emmert, S.,1996, VDI BERICHTE NR.**1230**, p.331.

Honeycombe, R.W.K., 1981, Steels, Microstructure and Properties, E. Arnold, London.

Hu, Z.Z., Ma, M.L., Liu, Y.Q and Liu, J.H., 1997, *Int. J. Fatigue* **19 No.8-9**, p.641

Hyde, R.S., Cohen, R., Krauss, G. and Matlock D.K., 1992, "Bending Fatigue Characterization and Fracture Toughness of Gas Carburized SAE 4320 Steel", SAE Paper 920534, Society of Automobile Engineers, Warrendale Pa.

Hyde, R.S., Matlock, D.K. and Krauss, G., ,1998, "Quench Embrittlement: Intergranular Fracture Due to Cementite and Phosphorus in Quenched Carbon and Alloy Steels" in Proceedings of the 40th Mechanical Working and Steel Processing Conference, ISS, Warrendale, PA, p. 921.

Jatczak, C.F., 1979, "Retained Austenite and Its Measurement of X-Ray Diffraction, Manual", *Society of Automotive Engineers* **SP-453**.

Johnson, K.L. 1985, Contact Mechanics, Cambridge University Press.

Johnson, K.L. 1968, "An Experimantal Determination of the Contact Stresses Between Plastically Deformed Cylinders and Spheres", Engineering Plasticity, Cambridge, March 1968, eds. J. Hayman and F.A. Leckie, Cambridge University Press.

Johnson, K.L., 1989, Contact Mechanics, Cambridge University Press, NewYork.

Karaman, I., Sehitoglu, H., Maier, H.J. and Balzer, M., 1998, *Meta. Mater. Trans.* **29A**, p.427.

Kern, R.F., 1968, *Metal Progr.* **94(6)**, p.71.

Kinsman, K.R., and Shyne, J.C., 1966, *Acta Metal.* **14**, p.1063.

Krauss, G., 1991, "Microstructure and Properties of Carburized Steels", in Metals Handbook **4**, Heat Treating, *ASM International*, Materials Park, Ohio, p. 363.

Krauss, G., 1999, *Mat. Sci. Eng.* **A273-275**, p.40.

Laufer, E. E., and Roberts, W.N., 1966, *Phil. Mag.* **12**, p. 67.

Leslie, W.C, 1981, The Physical Metallurgy of Steels, McGraw-Hill, Washington.

Leslie, W.C. and Sober, R.J., 1967, *Trans. Amer. Soc. Metals* **60**, p.459.

Lou, B., Jing, X., Gu, C., Shen, F. and He, L., 1990, "Fatigue Crack Growth and Closure Behaviors in Carburized and Hardened Case", Proceedings of International Conference on Fatigue and Fatigue Tresholds, Fatigue'90, Honolulu, Hawaii, eds. Kitagawa, H. and Tanaka, T., Materials and Component Engineering Birmingham, p.1161.

Makinson, J.D., Weins, W.N., Xu, Y., DeAngelis, R.J., Ferber, M.K., Riester, L. and Lawrence, R.V. in: K. Inoue, 1998, "Displasive Phase transformations and Their Application in Materials Engineering", eds. Mukherjee, K., Otsuka, K. and Chen, H., *TMS*, Warrendale. PA, p.391.

Manson, S.S., 1965, *Exp. Mech.* **5**, p.193.

Marder, A.R. and Benscoter, A.O., 1968, *Trans. Amer. Soc. Metals* **61**, p.293.

Marder, A.R. and Krauss, G., 1967, *Trans. Amer. Soc. Metals* **60**, p.651.

Maxwell, P.C., Goldberg, A. and Shyne, J.C., 1974-a, *Met. Trans.* **5**, p.1305.

Maxwell, P.C., Goldberg, A. and Shyne, J.C., 1974-b, *Met. Trans.* **5**, p.1319.

Mesarovic, S.Dj and Fleck, N.A., 1999, *Proc. R. Soc. Lond.* **A 455**, 2707.

Metal hand book, 1980, 9th edition **3**, p.427.

Metal hand book, 1982, 9th edition **5**, p.138.

Mohanty, O.N., 1995, *Mater.Scie.and Eng.* **32B**, p.267.

Mura, T., 1998, Micromechanics of Defects in Solids, Martinus Nijhoff, Dordrecht Netherlands.

Muro, H. and Tsushima, N., 1970, *J. Lubric. Technol. (Trans. ASME, F)*, **25**, p. 345

Neu, R.W. and Sehitoglu, H., 1991, *Meta. Trans.* **22A**, p.1491.

Neu, R.W. and Sehitoglu, H., 1992, *Acta Metall. Mater.* **40 No.9**, p.2257.

Nishiyama, Z., 1978, Martensitic transformation, NewYork: Academic press.

Norstrom, L.A., 1976, *Scand. J. Metall.* **5**, p.159.

Okamoto, M., and Odaka, R., 1952, *J. Jpn. Inst. Met.* **16**, p.81.

Olson, G.B. and Cohen, M., 1972, *J. Less Common Metals* **28**, p.107.

Olson, G.B., 1982, "Transformation Plasticity and the Stability of Plastic Flow", in Deformation, Processing and Structure papers presented at the 1982 *ASM Materials Science siminar* , ed. Krauss, G., p.391.

Olver, A.V., 1995, "Micro-pitting of Gear Teeth: Design Solution", Proc. of IMechE congress, Autotech 95, Birmingham, p.1.

Olver, A.V.,1984, "Micropitting and asperity deformation", Development in numerical and experimental methods applied to tribology, Proceeding of the 10th Leeds-Lyon Symposium on Tribology, eds. Dowson, D., Taylor, C.M., Godet, M. and Berthe, D. Lyon-France 1983, p.319.

Panhans, M.A. and Fournelle, R.J., 1981, *J. Heat Treat.* **2**, p.45

Patel, J.R. and Cohen, M., 1953, *Acta metall.* **1**, p.531.

Rakhit, A.K.,2000, Heat Treatment of Gears: A Practical Guide for Engineering, *ASM International,* Materials Park, OH.

Richman, R.H. and Landgraf, R.W., 1975, *Met. Trans.* **6A**, p.955.

Sarikaya, M., Thomas, G., Steeds, J.W., Barnard, S.J. and Smith, G.D.W., 1982, "Solute Element Partitioning and Austenite Stabilization in Steels" in Proceeding of an International conference on solid-solid phase transformations, eds. Aaronson, H.I., Laughlin, D.E., Sekerka, R.F. and Wayman, C.M., *Metallurgical Society of AIME* 1982, p.1421.

Schönnenbeck, G., 1984, Einfluß der Schmierstoffe auf die Zahnflankenermüdung (Graufleckigkeit und Grübchenbildung) hauptsächlich im Umfangsgeschwindiggkeitsbereich 1 ...9 m/s. Diss. TU München

Shaw, B.A., 2002, private communication

Sinclair, G.B., Follansbee, P.S. and Johnson, K.L. 1985, *Int. J. Solids Structures*, **21**, p.865.

Smith, J.O. and Cang Keng Liu, 1953, *J. Appl. Mech.* **20**, p.157.

Speich, G.R. and Warlimont, H., 1968, *J. Iron Steel Instit.* **206**, p.385.

Studman, C.J. and Field, J.E., 1977, *J. Mater. Sci.* **13**, p.215.

Sung-Ki Lyu, Inoue, K., Deng, G. and Kato, M., 1998, *KSME Intern. J* **12**, p.206.

Szpunar, E. and Bielanik, J., 1984, "Influence of Retained Austenite on Propagation of Fatigue Crack in Carburized Case of Toothed Elements". Proceeding of International Conference Heat Treatment' 84, *The Metal Society*, London, p.39.1

Tetelman A.S., McEvily, A.J., 1967, Fracture of Structural Materials, John Wiley and Sons, NewYork.

Thelning, Karl-Eric, 1975, Steel and its heat treatment. Bofors Handbook, Butterworths London; Boston.

Timoshenko, S.P. and Goodier, J.N., 1987, Theory of Elasticity, Mcgraw-Hill Book Company, London.

Turkdogan, E.T., 1989, "Causes and Effects of Nitride and Carbonitride Precipitation During Continuous Casting" Transaction of the ISS, May, p.61.

Vinokur, B.B., 1981, *Russian Metall.* **6(1)**, p.162.

Voskamp, A.P., österlund, R., Becker, P.C. and Vingsbo, O., 1980, *Metals Technol.* **Jan**, p. 14

Way, S., and Pittsbugh, E., 1935, *Trans. ASME, J. Appl. Mech.* **2**, p.49.

Wayman, C.M., 1964, Introduction to the Crystallography of Martensite Transformations, Macmillan, NewYork.

Wechsler, M.S., Leiberman, D.S. and Read, T.S., 1960 *Trans.AIME*, 218, p.202.

Wilson, B.M. and Weins, W.N., 2000, "International. Retained Austenite and Tooling Failure Case Studies" 20th *ASM Heat Treating Society* Conference Proceedings 2000, eds. Funatani, K. and Totten, G.E., St. Louis, MO, ASM, p.566.

Winchell, R.G., and Cohen, M., 1962, *Trans. ASM.* **55**, p.347.

Winter, H. and Weiss, T.,1981, *J. Mech. Design* **103**, p.499.

Zaccone, M.A., Kelley, J.B. and Krauss, G., 1987, "Fatigue and Strain-Hardening of High Carbon Martensite-Austenite Composite Microstructure", Heat Treatment'87, Proceeding of the International Conference Included in Materials' 87, *Institute of Metals*, London, p.93.

Zaccone, M.A., Kelly, J.B. and Krauss, G., 1989, "Strain Hardening and Fatigue of Simulated Case Microstructures in Carburized Steel", in Carburizing: Processing and Performance, ed. Krauss, G., *ASM International*, Metals Park, OH, p.249.

Appendix A

Calculations of percentage of volume change in four test specimens are shown in tables A.1 to A.3. Retained austenite was transformed to martensite by sub-zero cooling in liquid nitrogen. Specimens' dimensions were measured before and after the sub-zero cooling

Table A.1 Dimensions change in Ovako 677 specimen I after sub-zero cooling

Dimension	Initial measurement	Final measurement	Change in length(ΔL)	Percentage change in length (%ΔL)
Thickness	10.042	10.052	0.01	0.1
	10.042	10.050	0.01	0.1
	10.038	10.048	0.01	0.1
	10.042	10.051	0.01	0.1
Length	19.942	19.962	0.021	0.1
	19.960	19.982	.021	0.1
Width	20.190	20.212	0.021	0.1
	20.190	20.210	0.021	0.1

The percentage increase in edge length is 0.1 %

The percentage volume change $\Delta V = 3\times 0.1 = 0.3$ %

This volume change is for 7 % transformation. For 100 % transformation the volume change would be $\Delta V = 0.3 \times (100/7) = 4$ %

Table A.2 Dimensions change in Ovako 677 specimen II after sub-zero cooling

Dimension	Initial measurement	Final measurement	Change in length(ΔL)	Percentage change in length (%ΔL)	average
Thickness	12.001	12.021	0.02	0.166	0.125
	12.014	12.027	0.013	0.108	
	12.010	12.023	0.013	0.108	
	12.013	12.027	0.014	0.116	
Length	25.115	25.143	0.028	0.111	0.11
	25.110	25.137	0.027	0.108	
Width	24.484	24.527	0.043	0.176	0.154
	24.484	24.516	0.032	0.131	

The percentage volume change $\Delta V = 0.125 \times 0.11 \times 0.154 = 0.212\ \%$

This volume change is for 9.3 % transformation. For 100 % transformation the volume change would be $\Delta V = 0.212 \times (100/9.3) = 2.28\ \%$

Table A.3 Dimensions change in Ovako 677 specimen III after sub-zero cooling

Dimension	Initial measurement	Final measurement	Change in length(ΔL)	Percentage change in length (%ΔL)	average
Thickness	12.018	12.035	0.017	0.141	0.154
	12.012	12.032	0.02	0.166	
	12.020	12.034	0.017	0.141	
	12.025	12.043	0.02	0.166	
Length	24.858	24.894	0.036	0.145	0.15
	24.854	24.891	0.037	0.148	
Width	24.605	24.642	0.037	0.150	
	24.602	24.640	0.038	0.154	

The percentage volume change $\Delta V = 0.154 \times 0.15 \times 0.15 = 0.347$ %

This volume change is for 18.8 % transformation. For 100 % transformation the volume change would be $\Delta V = 0. \times (100/18.8) = 1.84$ %

This will be taken as the upper limit because the measurements of retained austenite become not very accurate when the percentage of retained austenite is about 5 % or less. If all the retained austenite in this specimen has been transformed. i.e if the final percentage of retained austenite is 0 %. Then % $\Delta V = 0.347 \times (100/24.4) = 1.42$ %

Therefore the percentage increase in volume calculated earlier can be taken as an upper limit. This means that the predicted induced stress could be 50 % lower in magnitude than what had been estimated.

Appendix B
Calculation of Contact Stresses

Calculating radius of curvature of involutes at the Pitch line

Construction

(i) Draw the base circle of a pair of gears separated by the centre separation

(ii) Draw a line touching the two circles at tangents. The curvatures of the involutes at the pitch are obtained from the lengths of the bisected line.

Assume equal size gears

The equation of the circle is

$$(y-y_0)^2+x^2+R^2$$

R is the radius of base circle

The equation of the tangent line is

$$y=kx$$

The point of contact is given by substitution

$$(kx-y_0)^2+x^2+R^2$$

$$k^2x^2-2kxy_0+y_0^2+x^2+R^2$$

$$(k^2+1)x^2\_2kxy_0+(y_0^2-k^2)=0$$

One solution only for x occurs when

$$4k^2y_0^2-4(k^2+1)(y_0^2-R^2)=0$$

$$4k^2y_0^2-4k^2y_0^2+4k^2R^2-4y_0^2+4R^2=0$$

$$4k^2R^2=4(y_0^2-R^2)$$

$$k=\sqrt{\frac{y_0^2}{R^2}-1}$$

The length of the tangent line follows

$$r=\frac{x}{\cos\alpha}$$

r is the radius of curvature at pitch line

$$x = \frac{2ky_0}{2(k^2+1)}$$

$$x = \frac{ky_0}{k^2+1}$$

$$x = \frac{ky_0}{y_0^2/R^2}$$

$$x = k\frac{R^2}{y_0}$$

$$x = \frac{R^2}{y_0}\sqrt{\frac{y_0^2}{R^2}-1}$$

$\tan\alpha = k$ and $\cos\alpha = \frac{R}{y_0}$

$$\therefore r = \frac{y_0}{R}\frac{R^2}{y_0}\sqrt{\frac{y_0^2}{R^2}-1}$$

$$r = R\sqrt{\frac{y_0^2}{R^2}-1}$$

For the helical gears used in the present investigation, radius of the base circle,

$R = 73.45\ mm$ and $y_0 = 80mm$

$$r = R\sqrt{\frac{y_0^2}{R^2}-1} \quad = 31.7\,mm$$

Surface stress for two cylinders in contact

Assume $R_1 = R_2$

$$P_0 = 0.591\sqrt{\frac{PE'}{K_D}}$$

where $K_D = \frac{4R_1R_2}{2R_1+2R_2}$

If $R_1 = R_2$, $K_D = R$

$$P_0 = 0.591\sqrt{\frac{PE'}{R}}$$

$$2a = 2.15\sqrt{\frac{PK_D}{E}}$$

$$E' = \frac{E}{(1-v^2)}$$

$$\therefore \frac{2a}{P_0} = \frac{2.15}{0.519}\frac{R}{E}$$

$$\therefore a = 1.819\frac{P_0}{E}R$$

for $P_0 = 1455$ MPa, $E = 200\times10^3$ MPa

$a = 0.013\times R$

for R=31 mm, a=403 μm

Normal load without friction (macroscopic friction in gears should be low because of the lubrication). The stress field can be obtained from the expression given by Smith and Liu (1953). However we need some means of judging when yielding occur. The uniaxial yield strength can be estimated from the hardness number (converted to correct units). Johnson (1989) quotes

$$\sigma_Y = \frac{Hv}{2.8}$$

where σ_y is the uniaxial flow strength at a plastic strain of 8 %. However Hv is normally quoted in units of Kgf/mm^2 . Converting to MPa, thus

$$\sigma_Y = \frac{9.81}{2.8}Hv$$

To be conservative we may take a reduced proportionality

$$\sigma_Y \approx 3Hv$$

Thus if Hv=600 (Kgf/mm^2) $\sigma_Y \cong 1800$ MPa.

Now assume plane strain deformation. Thus the third direction stress is given by

$$\sigma_y = \nu(\sigma_x + \sigma_y)$$

where ν is the Poison's ratio.

To judge when yielding occurs we need to use a yield criterion. The most convenient is Von Misses. First define the hydrostatic σ_m and deviatoric stress components.

$$\sigma_m = (\sigma_x + \sigma_y + \sigma_z)/3$$

Deviatoric stresses are

$$S_x = \sigma_x - \sigma_m \qquad S_y = \sigma_y - \sigma_m \qquad S_z = \sigma_z - \sigma_m$$

The shear stress components are unchanged

The Von Mises equivalent stress is

$$\sigma_v = \sqrt{3}\left[\frac{1}{2}(S_x^2 + S_y^2 + S_z^2) + \tau_{xs}^2\right]^{1/2}$$

Yield will occur when $\sigma_v = \sigma_Y$ (the uniaxial yield strength).

The MathCad document shows computation of Von Mises stress, directional stresses, hydrostatic pressure and Von Mises stress contours normalised by maximum pressure

The maximum Von Mises stress occurs below the surface as shown in contour map at

$z/a \approx 0.7$, $x/a = 0$

The maximum value is $\frac{\sigma_v}{P_0} \approx 0.53$

Estimated value of P_0 required for yielding

If Hv=600 Kgf/mm^2 $\sigma_Y \cong 1800$ MPa

At yield the maximum value $\sigma_Y \cong 1800$ MPa

$$\therefore P_0 = \frac{1800}{0.53} \approx 3400 \text{ MPa}$$

Thus there should be no yielding under the applied load of about 1450 MPa. If yielding does occur it would be occur first at a depth $\cong 0.7 \times 400 = 280 \mu$m below the surface.

Thus any plastic flow must be due to other factors. We have assumed that surfaces are perfectly smooth. In fact surfaces are rough on microscale. Thus any plastic deformation that occurs must be confined to a very narrow region of a size that is of the order of the peak to trough height of the surface i.e $<10\mu$m

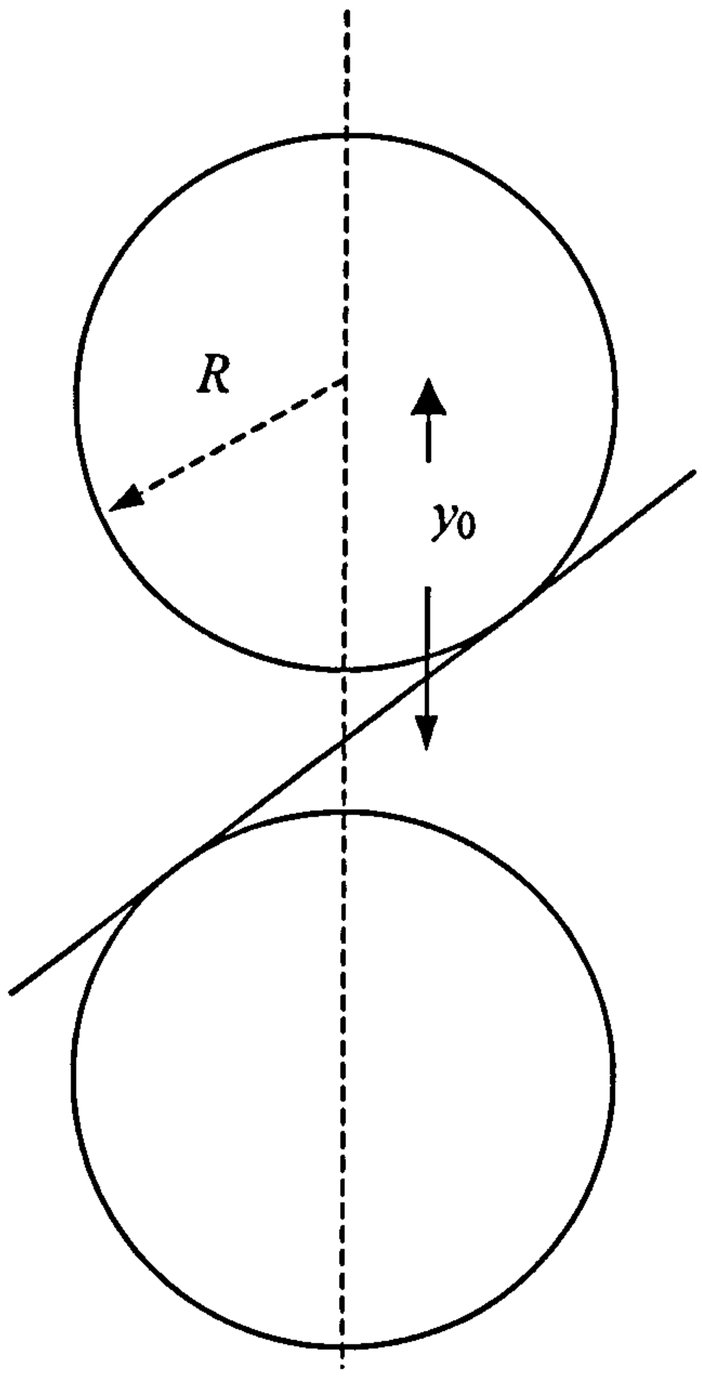

Schematic drawing shows the Basic circles for two gears in contact

Smith and Liu- contact stresses between cylinders. No friction
All stresses in units of maximum pressure p0

$$K(x,z) := \frac{(1-x)^2 + z^2}{(1+x)^2 + z^2}$$

$$L(x,z) := \frac{1}{\left[(1+x)^2 + z^2\right]}$$

$$F(x,z) := \pi \cdot L(x,z) \cdot \left[\frac{1 + \sqrt{K(x,z)}}{\sqrt{K(x,z)} \cdot \sqrt{2 \cdot \sqrt{K(x,z)} + (1 + K(x,z) - 4 \cdot L(x,z))}} \right]$$

$$G(x,z) := \pi \cdot L(x,z) \cdot \left[\frac{1 - \sqrt{K(x,z)}}{\sqrt{K(x,z)} \cdot \sqrt{2 \cdot \sqrt{K(x,z)} + (1 + K(x,z) - 4 \cdot L(x,z))}} \right]$$

$$\sigma x(x,z) := \text{if}\left[(z=0), \text{Re}\left(\sqrt{1-x^2}\right), \frac{z}{\pi} \cdot \left[\left(1 + 2 \cdot x^2 + 2 \cdot z^2\right) \cdot F(x,z) - 2 \cdot \pi - 3 \cdot x \cdot G(x,z) \right] \right]$$

$$\sigma z(x,z) := \text{if}\left[(z=0), \text{Re}\left(\sqrt{1-x^2}\right), \frac{z}{\pi} \cdot (F(x,z) - x \cdot G(x,z)) \right]$$

$$\sigma xz(x,z) := \text{if}\left(z=0, 0, \frac{z^2}{\pi} \cdot G(x,z) \right)$$

Plane Strain

$\nu := 0.3$

$$\sigma y(x,z) := \nu \cdot (\sigma x(x,z) + \sigma z(x,z))$$

Hydrostatic and Deviatoric Components

$$\sigma m(x,z) := \frac{(\sigma x(x,z) + \sigma z(x,z) + \sigma y(x,z))}{3}$$

$$sx(x,z) := \sigma x(x,z) - \sigma m(x,z)$$

$$sz(x,z) := \sigma z(x,z) - \sigma m(x,z)$$

$$sy(x,z) := \sigma y(x,z) - \sigma m(x,z)$$

Von Mises component

$$\sigma v(x,z) := \sqrt{3}\cdot\left[\frac{\left(sx(x,z)^2 + sz(x,z)^2 + sy(x,z)^2\right)}{2} + \sigma xz(x,z)^2\right]^{\frac{1}{2}}$$

Maximum Principal Stress

$$\sigma 1(x,z) := \frac{\sigma z(x,z) + \sigma x(x,z)}{2} + \sqrt{\left(\frac{\sigma z(x,z) - \sigma x(x,z)}{2}\right)^2 + \sigma xz(x,z)^2}$$

$z := 0, 0.1 .. 1.1$

$x := 0$

Stress

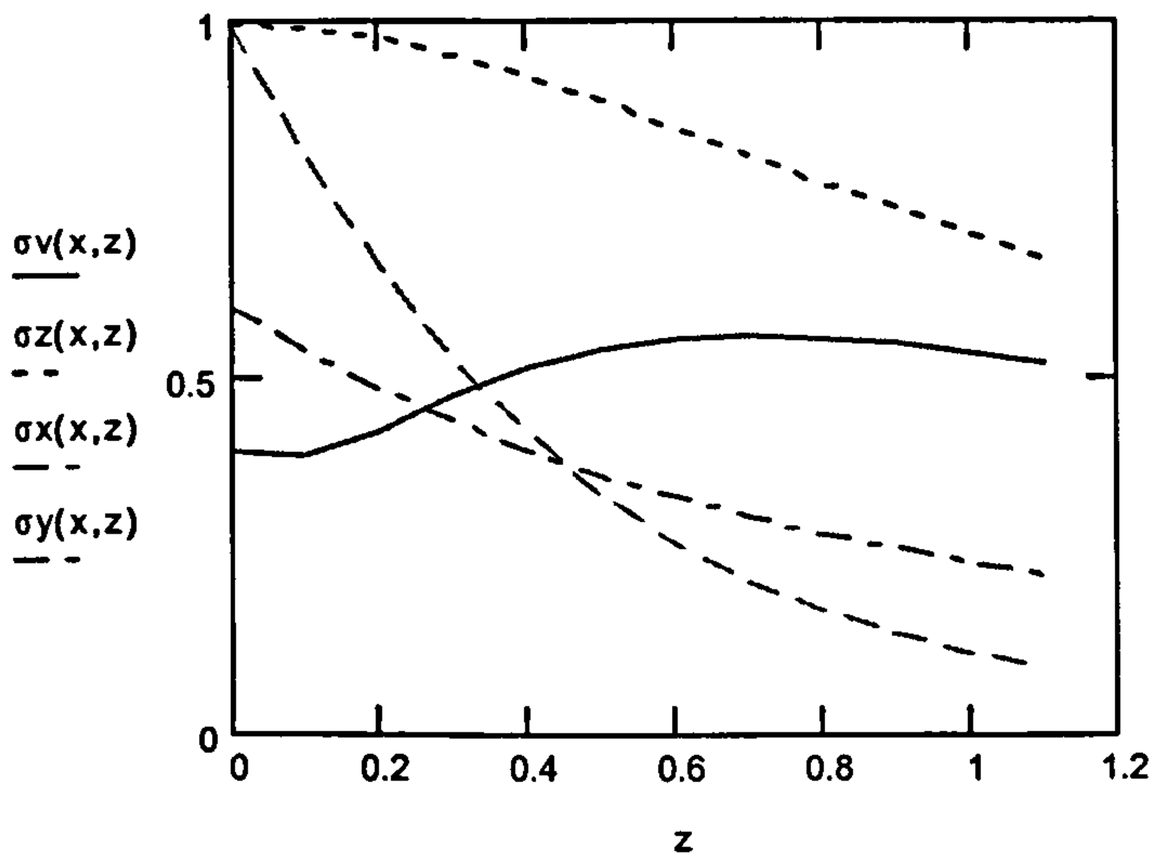

Hydrostatic pressure

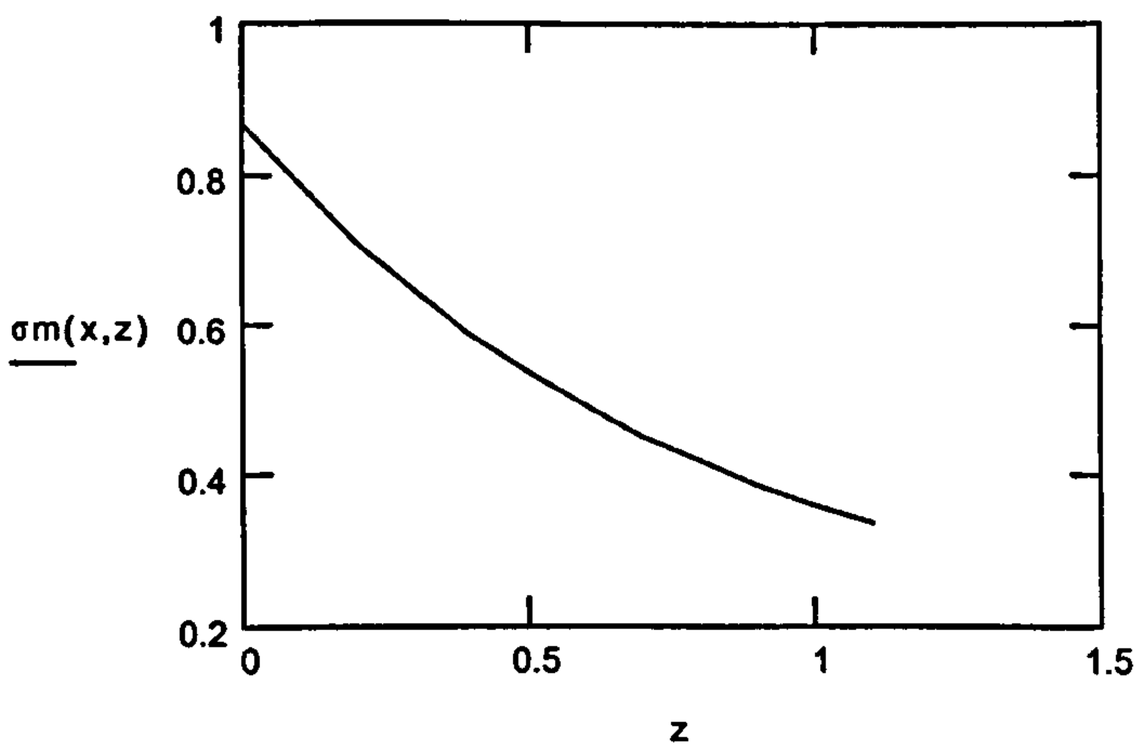

Contour Plot

$N := 20$

$i := 0..N$

$j := 0..N$

$x_i := \frac{2 \cdot i}{N}$

$z_j := \frac{2 \cdot j}{N}$

$M_{i,j} := \sigma v(x_i, z_j)$

$M_{0,0} = 0.4$

$\sigma z(0,0) = 1$

$J_{i,j} := \sigma 1(x_i, z_j)$

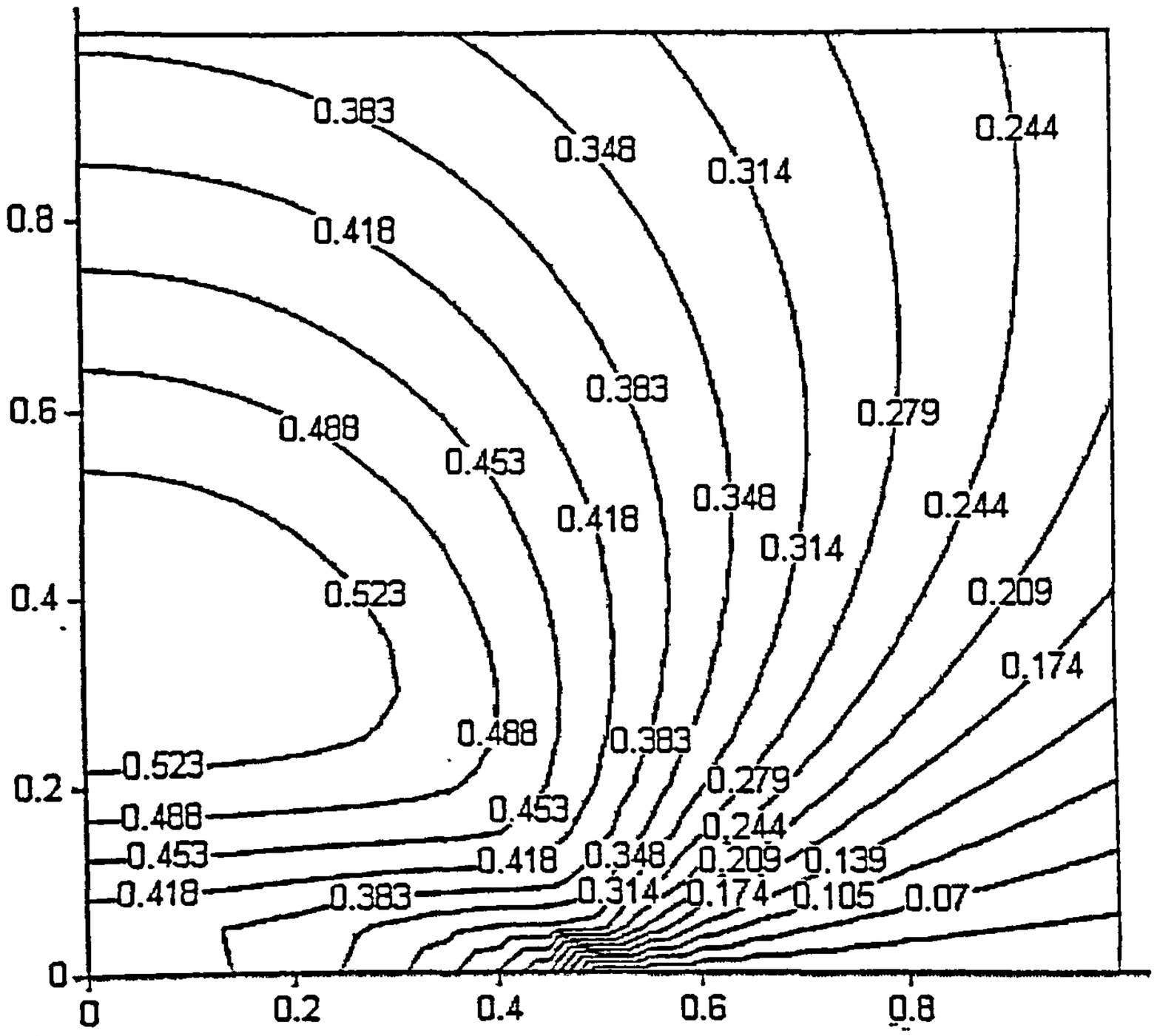

M

Contour plot of von Mises stress

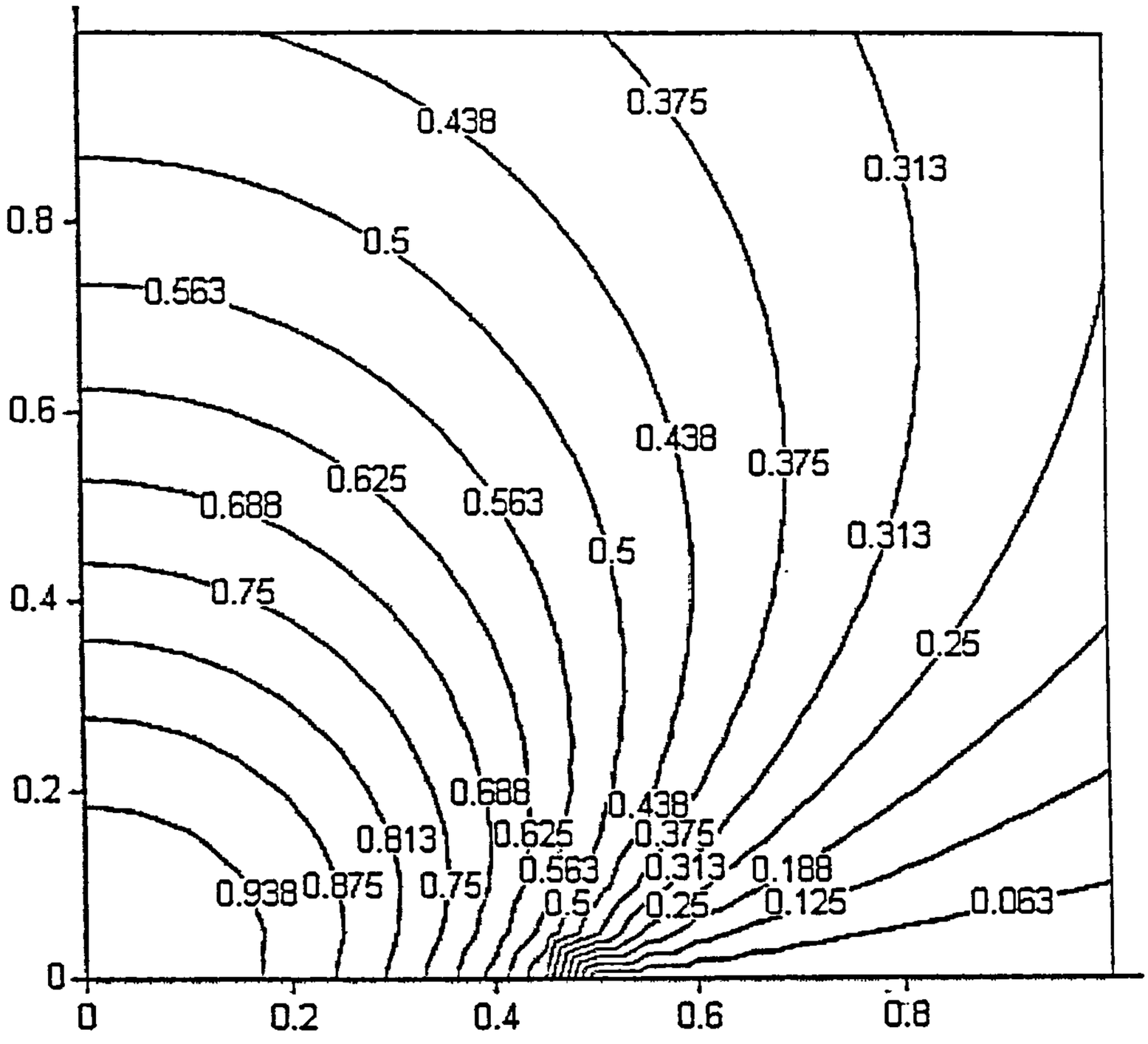

J

Contour plot of maximum principal stress